STOCHASTIC FLOW AND TRANSPORT THROUGH MULTIFRACTAL POROUS MEDIA

by

Albert Essiam

Bachelor of Science in Mining Engineering
University of Idaho, Moscow, Idaho (1991)

Master of Science in Civil and Environmental Engineering
Massachusetts Institute of Technology, Cambridge, Massachusetts (1995)

Submitted in Partial Fulfillment of the
Requirements for the Degree of
Doctor of Philosophy in Civil and Environmental Engineering

at the

MASSACHUSETTS INSTITUTE OF TECHNOLOGY

September 2001

Signature of Author.....
Department of Civil and Environmental Engineering
August 17, 2001

Certified by.....
Daniele Veneziano
Professor of Civil and Environmental Engineering
Thesis Supervisor

Accepted by.....
Oral Buyukozturk
Chairman, Departmental Committee on Graduate Studies

STOCHASTIC FLOW AND TRANSPORT THROUGH MULTIFRACTAL POROUS MEDIA

By
ALBERT ESSIAM

Submitted to the Department of Civil and Environmental Engineering
On August 17, 2001
in partial fulfillment of the requirements for the Degree of Doctor of Philosophy in Civil and Environmental Engineering

ABSTRACT

Stochastic theories of flow and transport in aquifers have relied on the linear perturbation approach that is accurate for flow fields with log-conductivity variance σ_F^2 less than unity. Several studies have found that the linear perturbation ignores terms that have significant effects on the spectra of the hydraulic gradient ∇H and specific discharge $\underline{q}$ when σ_F^2 exceeds unity. In this thesis we study flow and transport when the hydraulic conductivity K is an isotropic lognormal multifractal field. Unlike the perturbation approach, results obtained are nonlinear even though several simplifying assumptions are made. The spectral density of $F = \ln(K)$ for this type of field is $S_F(\underline{k}) \propto |\underline{k}|^{-D}$ where D is the space dimension. It is found that under this condition, the hydraulic gradient ∇H and specific discharge $\underline{q}$ are also multifractal; whose renormalization properties under space contraction involve random scaling and random rotation of the fields. Analytical expressions that are functions of D and the codimension parameter of F, C_K are obtained for the renormalization properties and marginal distributions of ∇H and $\underline{q}$. Because of the boundary conditions, the fields ∇H and $\underline{q}$ are anisotropic at large scales but become isotropic at very small scales. The mean specific flow decreases as the scaling range of F increases, at a rate that is dependent on D and C_K. Flow simulations on a plane validate the analytical results.

The multifractal properties of ∇H and $\underline{q}$ are used to derive their spectral density tensors, the macrodispersivities, and the effective conductivity of the medium. The spectra obtained account for the random rotation of the ∇H and $\underline{q}$ at smaller scales. Spectra for ∇H and $\underline{q}$ are anisotropic at large scales but become isotropic at small scales. The scale of isotropy depends on D and C_K. The linear perturbation approach does not capture this important feature and further gives incorrect amplitudes and power decays of the spectral density tensors. Using the spectra of $\underline{q}$ the macrodispersivities are computed and compared with results from the linear perturbation approach. Reflecting the properties of the spectral density of $\underline{q}$, the macrodispersivities for the nonlinear theory are isotropic at small travel distances and are anisotropic at large travel distances.

In the ergodic case when the spatial averages of all fields of interest are close to their ensemble averages, it is found that our expression for effective conductivity K_{eff} corresponds to a formula conjectured by Matheron [1967].

Using the scaling properties of the inverse of the velocity field (also known as slowness), we derive expressions for the first passage time distribution FPTD and mean plume concentration for transport in a multifractal K field. The theoretical results of FPTD for the nonlinear theory are fitted by regression methods to data from field experiments and from numerical simulations and compared with results from the continuous time random walk CTRW and two-phase transport model. Results of the nonlinear theory are found to be more suitable for predicting non-Fickian transport. The CTRW model is more suited for transport in statistically inhomogeneous media. Both the CTRW and two-phase models are suitable for modeling Fickian transport.

Since most subsurface flow occurs in anisotropic K fields, the conditions of isotropy are relaxed to consider flow in anisotropic multifractal K fields. Unlike the isotropic case, closed form results for the hydraulic gradient ∇H and specific discharge $\underline{q}$ fields are not obtained. However, an expression that can be evaluated numerically for the statistical properties of the hydraulic gradient ∇H is obtained. The scaling properties of flow in geometrically anisotropic fields are also considered and the renormalization properties of ∇H are obtained.

Thesis Supervisor: Daniele Veneziano
Title: Professor of Civil and Environmental Engineering

TABLE OF CONTENTS

ABSTRACT 2
TABLE OF CONTENTS 4
LIST OF FIGURES 7
LIST OF TABLES 14

CHAPTER 1: INTRODUCTION
1.1 Review of flow theories and motivation for the present work 15
1.2 Field Heterogeneity 18
1.3 Flow analysis when K is an isotropic lognormal multifractal field 22
1.4 Thesis organization 24

CHAPTER 2: REVIEW OF FIRST-ORDER AND HIGHER-ORDER APPROACHES

Introduction 27
2.1 First-order solution of spectral perturbation equations. 29
2.2 Higher-order approaches 36
2.3 Effective hydraulic conductivity expressions for isotropic media (first- and second-order models) 48
2.4 Macrodispersivity 55
2.5 Fractals and Self-Similar Models 74
2.6 Multifractal characterization of random resistor and random superconductor networks 84

CHAPTER 3: MULTIFRACTAL SCALING OF HYDRAULIC CONDUCTIVITY

Introduction 90
3.1 A review of multifractal theory for subsurface flow. 91
3.1.1 Isotropic multifractality 92
3.1.2 Generalized Multifractality (Generalized Scale Invariance GSI) 99
3.1.3 Bare/dressed and conservative/non-conservative measures 105
3.2 Multifractal Measures – Empirical Evidence 106

CHAPTER 4 – SCALING OF THE HYDRAULIC GRADIENT AND THE SPECIFIC DISCHARGE FIELDS

	Introduction	122
	4.1.1 Assumptions made in the flow analysis	130
	4.1.2 Multifractality of ∇H and $J=\lvert\nabla H\rvert$	134
	4.1.3 Distribution of the Scaling Parameters J_r and $\underline{e}_r$	142
4.2	Multifractal Scaling of bare $\underline{q}$ and q	153
	4.2.1 Multifractality of $\underline{q}$ and q	154
	4.2.2 Distribution of the Scaling Parameters B_r and $\underline{e}_r$	156
	4.2.3 Marginal distributions of bare flows	160
	4.2.4 Moment Scaling Function of q	164
	4.3.1 Problem Formulation and solutions from exact 1D analysis and from FOSM	167
	4.3.2 Comparison with K_{eff} in the case of finite-resolution multifractal K	171
4.4	Comparison of the current approach with the results of random electrical conductivity networks by Bin Lin et al. (1991) and Archangelis et al. (1985)	173

CHAPTER 5: SPECTRAL ANALYSIS OF THE HYDRAULIC GRADIENT AND SPECIFIC DISCHARGE FIELDS

	Introduction	177
5.1	Spectral analysis of ∇H and $\underline{q}$: First- and second-order analyses	179
5.2	Isotropically multifractal measures and their logarithms	183
5.3	Spectral energy tensors under generalized scale invariance	189
5.4	Nonlinear spectral analysis of ∇H	191
5.5	Nonlinear spectral analysis of specific discharge $\underline{q}$	198

CHAPTER 6: FLOW SIMULATIONS IN SATURATED AQUIFERS WITH MULTIFRACTAL HYDRAULIC CONDUCTIVITY

		214
6.1	Construction of the K field and its scaling properties	230
6.2	Computing the Head Field	233
6.3	The Head Field	243
	6.3.2 Scaling of the hydraulic gradient	6.4 Sca lin

	g of Specific Discharge Field	252
6.5	Properties of the rotation angle	267
6.6	Scaling of Bare Fields	275
6.7	The relation between the log conductivity F and the hydraulic Gradient	285
6.8	Flow simulation for a K field with a high variability $(C_K = 0.8)$	292

CHAPTER 7 – SOLUTE TRANSPORT IN RANDOM POROUS MEDIA

Introduction		305
7.2	Ensemble and plume scale dependent macrodispersivity	313
7.3	A review of the continuous time random walk (CTRW) model	330
7.4	Scaling properties of the Velocity Field	340
7.5	Comparison of the Nonlinear Theory Model, the CTRW and the Two-Phase Models	356

CHAPTER 8: FLOW IN AQUIFERS WITH HOMOGENEOUS ANISOTROPIC LOGNORMAL HYDRAULIC CONDUCTIVITY FIELDS

Introduction		369
8.1	Marginal distribution of the hydraulic gradient ∇H for homogeneous anisotropic lognormal hydraulic conductivity	373
8.2	An approximate scheme to deal with geometric anisotropy	380

CHAPTER 9 – SUMMARY AND CONCLUSIONS

9.1	Summary	386
9.2	Conclusions	393
9.3	Recommendations for future research	394

REFERENCES 397

LIST OF FIGURES

Figure		Page
1.1	Dispersivities measured at different sites – compiled by Pickens and Grisak (1981) and Lallemand-Barres et al (1978).	20
2.1	Comparison of calculated head variances versus prediction by the small perturbation approximation and by a second-order correction [From Dagan, 1995 and Lent and Kitanidis, 1996].	77
2.2	Calculated head variances for individual log-conductivity realizations. As the correlation length relative to the domain size decreases (increasing the domain size), the variance in the head variance increases (from Lent and Kitanidis, 1996).	78
2.3	Spectrum of head fluctuations, $S_{hh}(\underline{k})$: (a) spectrum cross-section along the k_1 axis and (b) spectrum cross-section along k_2 axis; the small perturbation approximation is exactly zero along the $k_2 = 0$ axis and hence is not shown in the diagram. The difference between the small perturbation approximation and the simulations is the growth of the large-scale components [From Lent and Kitanidis, 1996].	79
2.4	The effects of the variance of log-conductivity on the head variogram of head fluctuations, $\gamma_{hh}(\xi)$: (a) variogram cross-section along the ξ_1 axis, in the direction of flow, and (b) variogram cross-section along the ξ_2 axis, perpendicular to the direction of flow.	80
2.5	Comparison of the variogram of the specific discharge fluctuation in the direction of flow, $\gamma_{q_1q_1}(\xi)$ to the small perturbation approximation: (a) cross section of $\gamma_{q_1q_1}(\xi)$in the ξ_1 direction (b) cross section of $\gamma_{q_1q_1}(\xi)$in the ξ_2 direction (c) cross section of $\gamma_{q_2q_2}(\xi)$in the ξ_1 direction and (d) cross section of $\gamma_{q_2q_2}(\xi)$in the ξ_2 direction [From Lent and Kitanidis, 1996].	81
2.6	Comparison between effective permeabilities obtained by the effective medium theory (labeled self-consistent in the figure), the perturbation method (labeled small perturbation), the moment method and Matheron's conjecture [From Dykaar and Kitanidis and Renard, 1992 and Marsily, 1996]	82

2.7	Difference between ensemble average concentration of a plume and the ensemble average of a plume relative to the center of mass position (From Rajaram, 1991).	83
2.8	Tracer particles spreading in a perfectly stratified aquifer	84
2.9	Illustration of three self-similarity conditions for a process on the real line: (a) self-similarity of X(t), Eq. 2.77 (b) self-similarity of the increments of X(t), Eq. 2.78 and (c) local self-similarity of the increments of X(t), Eq. 2.79	85
2.10	Apparent longitudinal dispersivities versus scale of study excluding numerical model calibration results. Results of Neuman's regression analysis.	86
2.11	Hierarchical model of L de Archangelis et al. (1985) for $(h_b, v_b) = (2,1)$, where h_b and v_b are the horizontal and vertical bonds respectively.	87
2.12	An illustration of the duality of series and parallel resistors.	88
3.1	Measured one-dimensional spectrum of log-conductivity at a borehole (circles) in the Mount Simon aquifer, from Bakr (1976)	108
3.2	Profiles of hydraulic conductivity data obtained from vertical boreholes in an eolian sandstone formation in Arizona (from Goggin, 1988)	112
3.3	One-dimensional spectral density of measured log-conductivity for the vertical transect (Trans1)	113
3.4	One-dimensional spectral density of measured log-conductivity for the vertical transect (Trans2)	117
4.1	An illustration of the spectrum of an isotropic lognormal multifractal K field	125
4.2	An illustration of quantities as one moves from a coarse resolution r in domain Ω to a finer resolution in a contracted region Ω / r	127
4.3	Illustration of a hypothetical Brownian motion path on a 3D sphere	151

5.1	Spectral contour of the head field for the linear and nonlinear theory	197
5.2	Spectral contours of the longitudinal specific flow $S_{q_1q_1}$	207
6.1	An illustration of the flow domain and the imposed boundary conditions.	212
6.2	A lognormal multifractal hydraulic conductivity field with $C_K = 0.1$ and 0.3	219
6.3	An illustration of how a K field at resolution r = 4 is averaged to obtain a K field with resolution r = 2	221
6.4	The scaling of a lognormal hydraulic conductivity field K with $C_K =$ 0.1.The straight lines on the graph are obtained by performing a linear regression against the data points.	223
6.5	The scaling of a lognormal hydraulic conductivity field K with $C_K =$ 0.3.The straight lines on the graph are obtained by performing a linear regression against the data points.	224
6.6	Comparison between the results of the numerical (empirical) simulation and the theoretical scaling relations for K fields with $C_K = 0.1$ and 0.3.	225
6.7	The scaling moments for 20 simulations of lognormal multifractal K fields with $C_K = 0.1$. Moments for s = 1 have not been shown because they all have a value of 1. Due to the overlap of some points one cannot clearly see all the 20 points.	226
6.8	The scaling moments of the average values of the moments shown in Figure 6.7. This is the average scaling moment of 20 realizations of K fields with $C_K = 0.1$.	227
6.9	A perspective view of the head field computed from a hydraulic conductivity field with (a) $C_K = 0.1$ and (b) $C_K = 0.3$.	235
6.10	The head contours from K fields with (a) $C_K = 0.1$ and (b) $C_K = 0.3$.	237
6.11	The hydraulic gradient field computed from a K field with $C_K = 0.1$.	239
6.12	An illustration of how the hydraulic gradient vectors change with resolution.	240
6.13	The scaling of moments for the hydraulic gradient amplitude for $C_K =$ 0.1. The lines on the graph are obtained by performing a linear regression on the points.	244

6.14 The scaling of moments for the hydraulic gradient amplitude for C_K = 0.3. The lines on the graph are obtained by performing a linear regression on the points. 245

6.15 Comparison of the numerically obtained scaling moments of the hydraulic gradient field with the theoretically derived values for fields with C_K = 0.1 and 0.3. 246

6.16 Scaling of the amplitude of the hydraulic gradient field for the C_K = 0.1 fields shown in Fig. 6.7. 249

6.17 The scaling of the average values of the hydraulic gradient amplitude shown in Fig. 6.16 for fields with C_K = 0.1. 250

6.18 The velocity field computed for a hydraulic conductivity field with C_K = 0.1. 253

6.19 Scaling of the magnitude of the velocity vectors for a field with C_K = 0.1. 256

6.20 Scaling of the magnitude of the velocity vectors for a field with C_K = 0.3. 257

6.21 Comparison between the theoretical and empirical scaling moments for the specific discharge amplitude for C_K = 0.1 and 0.3. 258

6.22 The scaling of the specific discharge amplitudes for fields with C_K = 0.1. 261

6.23 The scaling of the average of the specific discharge amplitudes for fields with C_K = 0.1 shown in Fig. 6.22. 262

6.24 The scaling of the slowness for a field with (a) C_K = 0.1 and (b) C_K = 0.3. 264

6.25 A plot of the angle of rotation α_r versus the magnitude of the hydraulic gradient J_r for different resolution for a field with C_K = 0.1. 268

6.26 The increments of the rotation angles as one moves from a coarser to a finer resolution versus the original rotation angles at the coarser resolution. 270

6.27 A plot of the variance of the rotation angles of the hydraulic gradient vectors versus resolution. 271

6.28 A normal probability plot of the normalized values of $\ln(J_{256})$ and α_{256}. The values of α_{256} have a mean of 1 and variance 1 to better display the data. 273

6.29 The scaling of K fields developed to resolutions of 64, 128, 256 and 512. 277

6.30 Comparison the scaling of bare multifractal K fields and theoretical scaling of multifractal K fields with $C_K = 0.1$. 278

6.31 The scaling of hydraulic gradient fields with resolutions 32, 64, 128 and 256 from K fields with $C_K = 0.1$. 279

6.32 Comparison of the scaling moments of the magnitude of the hydraulic gradient fields of K fields with $C_K = 0.1$ developed to resolutions of 64, 128, 256 and 512 with the theoretical moment scaling function $W_J(s) = C_K\left(0.125s + 0.375\left(s^2 - s\right)\right)$. 280

6.33 The scaling of velocity fields obtained from K fields developed to resolutions of 64, 128, 256 and 512. 283

6.34 Comparison of the slopes of lines in Fig. 6.33 with the theoretical scaling function $W_{q,b}(s) = C_K\left(-0.875s + 0.375\left(s^2 - s\right)\right)$. 284

6.35 A scatter plot of the log hydraulic conductivity F versus the log hydraulic gradient amplitude J. 286

6.36 The effective conductivity for K fields with $C_K = 0.1$ and 0.3. 290

6.37 The scaling of a K field with $C_K = 0.8$. 293

6.38 A comparison of the moment scaling of a K field with $C_K = 0.8$ with the theoretical moment scaling function of $C_K(s^2 - s)$. 294

6.39 A contour plot for the head field computed from a K field with $C_K = 0.8$ 297

6.40 The hydraulic gradient field computed for a K field with $C_K = 0.8$. 298

6.41 The scaling of the hydraulic gradient amplitude for K fields with $C_K = 0.8$. 299

6.42 A comparison of the moment scaling of the hydraulic gradient amplitude and the theoretical moment scaling function for a K field with $C_K = 0.8$. 300

6.43 The scaling of the specific flow amplitudes for a K field with $C_K = 0.8$. 301

6.44 A comparison of the moment scaling of the specific flow amplitude and the theoretical moment scaling function for a K field with $C_K = 0.8$. 302

6.45a The scaling of the specific flow amplitudes for fields with $C_K = 0.8$ 303

6.45b The scaling of the average of the specific flow amplitudes for fields with $C_K = 0.8$ shown in Fig. 6.45a 304

6.45c Comparison between the theoretical and empirical scaling moments for the average specific flow amplitude for $C_K = 0.8$ 305

7.1 Comparison of the linear and nonlinear ensemble macrodispersivities for $C_K = 0.1$ and 0.3 318

7.2 Growth of plume second moments for linear and nonlinear theories for plumes with initial sizes of (a) .002ko and (b) .2ko 319

7.3 Relative macrodispersivities for linear and nonlinear theories for plumes with initial sizes of (a) 0.002ko and (b) 0.2ko 320

7.4 Evolution of a plume with initial size .1ko through a flow field with C_K = 0.1 and 0.3; $k_{max} = 512$, $k_o = 1$ and the times are t = time/k_{max}*E[V] 328

7.5 Cumulative FPTD for $0 < \alpha < 1$ for the CTRW model 339

7.6 Cumulative FPTD for $1 < \alpha < 2$ for the CTRW model 340

7.7a PDF of Slowness for $C_K = 0.1$ and 0.2, $k_o = 1$ and $k_{max} = 512$ 347

7.7b CDF of Slowness for $C_K = 0.1$ and 0.2, $k_o = 1$ and $k_{max} = 512$ 348

7.8a PDF of FPTD for $C_K = 0.1$ and 0.2, $k_o = 1$ and $k_{max} = 512$ 350

7.8b CDF of FPTD for $C_K = 0.1$ and 0.2, $k_o = 1$ and $k_{max} = 512$ 351

7.9a PDF of particle location for $C_K = 0.1$ and 0.2, $k_o = 1$ and $k_{max} = 512$ 352

7.9b CDF of particle location for $C_K = 0.1$ and 0.2, $k_o=1$ and $k_{max} = 512$ 353

7.10a Variance of the first passage time for a flow field with $C_K = 0.1$, $k_{max} = 1024$, $k_o = 1$ 354

7.10b Variance of the first passage time for a flow field with $C_K = 0.3$, $k_{max} = 1024$, $k_o = 1$ 355

7.11 (a) The flow path idealized as a sine function (b) Variance of the mean slowness at different sampling intervals along the sine curve in (a). 356

7.12 Comparison of models and their fit to the Mobile Site data by Huyakorn et al. (1986) 360

7.13 Comparing the models to experimental data from Berkowitz and Scher (2000) 361

7.14 FPTD for the CTRW and NL models fitted to data obtained from numerical simulations in fields with multifractal hydraulic conductivity with $C_K = 0.1$, $k_o = 1$ and $k_{max} = 512$ 362

7.15 Comparison of the CTRW and nonlinear theory (NL). The CTRW model was fitted to the NL model in the near field and using the fitted parameters was compared to the NL model in the far field. 363

7.16 Comparison of the CTRW and nonlinear theory (NL). The CTRW model was fitted to the NL model in the near field and using the fitted parameters was compared to the NL model in the far field. 364

7.17 Concentration variance versus time 367

LIST OF TABLES

Table 3.1	Results of regression analysis of the log spectral density versus log frequency for various sections of the vertical transects Trans1 and Trans2 from Goggin (1988)	113
Table 6.1	Slopes of $\log\{\langle K^S \rangle\}$ versus $\log\{\text{resolution}\}$ for K fields with $C_K = 0.1$	229
Table 6.2	Slopes of $\log\{E[J^S]\}$ versus $\log\{\text{resolution}\}$ for K fields with $C_K = 0.1$	251
Table 6.3	Correlation coefficients between F_r and $\ln(J_r)$ for different resolutions r. The theoretical value for D = 2 is $\rho = -0.817$.	287
Table 7.1a	Evolution of plumes: $\beta = 2$, $C_K = 0.3$, $\Sigma_{Small} = 0.0004k_o^2$, $\Sigma_{Large} = 0.04k_o^2$ and $k_o = 1$	321
Table 7.1b	Ensemble macrodispersivity: $\beta = 2$, $C_K = 0.3$, $\Sigma_{Small} = 0.0004k_o^2$, $\Sigma_{Large} = 0.04k_o^2$ and $k_o = 1$	322
Table 7.2	The evolution of plumes with initial sizes $\Sigma_o = 0.0061k_o^2$ and $\Sigma_o = 0.0015k_o^2$, $\beta = 2$, $C_K = 0.3$ and $k_o = 1$	327
Table 7.3	Values of λ obtained by various authors	363
Table 8.1	A comparison of K_{eff} from an anisotropic K field compared to the K_{eff} from an isotropic K field but on a rectangle with aspect ratio determined by a_1 and a_2.	385

CHAPTER 1: INTRODUCTION

1.1 Review of flow theories and motivation for the present work

The flow of water through a saturated porous medium is governed by Darcy's law [Bear, 1972; Gelhar, 1993]

$$\underline{q} = -K.\nabla H \tag{1.1}$$

where $\underline{q}(\underline{x})$ is the specific discharge vector, $K(\underline{x})$ is the hydraulic conductivity, and $H(\underline{x})$ is the hydraulic head. For a zero-divergence flow field, the hydraulic head H and the log hydraulic conductivity $F = \ln K$ must satisfy

$$\nabla^2 H + \nabla F.\nabla H = 0 \tag{1.2}$$

Over the past three decades, there has been much interest in the statistical properties of the hydraulic gradient ∇H and the flow $\underline{q}$ that result from Eqs. (1.1) and (1.2) when K in the domain of interest is a random field. Part of the interest stems from the growing concern over contamination of groundwater sources that culminated in the passage of the Comprehensive Environmental Response, Compensation and Liability Act (CERCLA), by the US Congress in 1980. Gelhar and co-workers (Gelhar and Axness, 1983; Gelhar et al., 1984; Gelhar 1987; Ababou and Gelhar, 1990) developed the first-order spectral theory that led to closed form relations between the power spectrum of F and the spectral

density tensors of ∇H and $\underline{q}$. The spectral density tensor of $\underline{q}$ has been used to explain how a plume spreads with travel time or distance. Variants of this approach have been developed by Dagan (1985), Koch and Brady (1988), Dagan and Neuman (1991), Glimm et al. (1993), Zhan and Wheatcraft (1996) and Neuman (1996).

First-order analysis simplifies the problem by replacing Eq. (1.2) with linear approximations in the fluctuations $f = F - E[F]$ and h=H-E[H] and Eq. (1.1) with approximations in the fluctuation $\underline{q}' = \underline{q} - E[\underline{q}]$ and writing $K = \exp(f + E[F])$. The spectral density tensors of the head h and flow $\underline{q}'$ fluctuations are obtained in Fourier space by assuming that the log conductivity variances are far less than unity, so that higher order terms in f and h can be ignored. This approach leads to exact results, as the variance of the log-conductivity field tends to zero. However, there has been an interest in examining the effects of the higher order terms of f on the power spectra of ∇H and $\underline{q}$ when flow occurs in a medium with highly fluctuating hydraulic conductivity field K. Using mainly perturbation methods, several authors have examined the effects of higher-order terms in f and h on the power spectra of ∇H and $\underline{q}$; see Dagan (1985), Deng and Cushman (1995, 1998), Hsu et al. (1996), Hsu and Neuman (1997) and Lent and Kitanidis (1996), among others. In general, these studies found that the inclusion of second-order terms has significant effects on the spectra of ∇H and $\underline{q}$ when the variance of F = lnK exceeds unity. The theoretical approaches by Dagan (1985), Deng and Cushman (1998) and Hsu and Neuman (1997) are limited by the fact that the mathematical expressions obtained by considering higher order terms in f and h become very complex and limit the extent to which higher-order exponents can be incorporated

into the analysis. The numerical solutions, for example that of Lent and Kitanidis do not provide any predictive tools in studying flow behavior in high contrast K fields, although they reveal the deficiencies of the first-order solution. Moreover, for large-conductivity variances, Ababou et al. (1988) have found that the higher order theories are not necessarily more accurate than first-order solutions. Hence, it is desirable to devise alternatives to the perturbation approach that can deal directly with the nonlinearities of the problem and avoid the computational limitations encountered when one relies on say the exponential expansion of terms in the perturbation approach. The work presented in this thesis is one such alternative. Results are obtained by assuming that the flow occurs in a saturated porous medium with an isotropic lognormal multifractal hydraulic conductivity K. For a scalar quantity like K, multifractality means that the average values $\overline{K}(S)$ in regions S of $\mathbb{R}^D$ are statistically invariant under isotropic space contraction by any given factor $r \geq 1$ and multiplication by a non-negative random variable A_r, i.e.

$$\overline{K}(S) \overset{d}{=} A_r . \overline{K}(rS)$$

where $\overset{d}{=}$ denotes equality of all finite dimensional distributions and A_r has a lognormal distribution [Veneziano, 1999]. We exploit the scaling properties of the hydraulic conductivity K to derive the properties of the hydraulic gradient ∇H and specific flow $\underline{q}$. The application of a multifractal K field allows one to obtain interesting results about the properties of the flow field that cannot otherwise be obtained. Moreover, assuming

that K is an isotropic multifractal field allows one to obtain results whose applications extend beyond the field of hydrology and can be applied in the study of random electrical networks. The study of random electrical networks is analogous to that of flow through heterogeneous K fields. In fact, both problems are mathematically the same, with K being analogous to random resistors, the hydraulic gradient ∇H similar to the voltage across the resistors, and the specific discharge $\underline{q}$ analogous to the current. What makes both problems interesting is the inherent randomness of the hydraulic conductivity or the resistance. Some models used in representing the heterogeneity of K fields are discussed next.

1.2 Field Heterogeneity

Heterogeneity of porous media, as expressed through a mathematical model of K or F, has been recognized as a difficult problem in groundwater hydrology. Various models, for example geostatistical models [Journel and Huijbregts, 1978; Isaaks and Srivastava, 1989] and spatial point process models by Ripley (1981) have been used in modeling K fields. During the past decade, there has been growing emphasis on the case when the hydraulic conductivity is a broad-band field with some type of scale invariance (Arya et al., 1988; Wheatcraft and Tyler, 1988; Ababou and Gelhar, 1990; Neuman, 1990; Dagan, 1994; Rajaram and Gelhar, 1995; Zhan and Wheatcraft, 1996; Di Federico and Neuman, 1997). These representations of the hydraulic conductivity field were mostly spurred by the need to explain the observed scale-dependence of macrodispersivities [Gelhar et al.,

1985 and 1992; Neuman, 1990] shown in Figure 1.1. In these analyses it is typically assumed that F=lnK is a homogeneous Gaussian field with spectral density S_F that decays like a power law along any given direction in Fourier space. In the isotropic case, this means that $S_F(\underline{k}) \propto k^{-\alpha}$, where k is the length of $\underline{k}$ and α is a constant. For example, when α is between D+1 and D+3 the log-conductivity $F(\underline{x})$ is a fractional Brownian surface (fBs), but values of α close to D have also been reported, for example Ababou and Gelhar (1990) and the analysis of Goggin (1988) data presented in Chapter 3 of this thesis.

Several authors have explained the observed data in Figure 1.1 with fractal models, with perhaps the most comprehensive contributions by Glimm and coworkers (Glimm and Jaffe, 1985; Glimm and Sharpe, 1991), Furtado et al. (1990, 1991), Zhang (1992) and a summarizing article by Glimm et al. (1993). These fractal models represent the scale-invariance of the log-conductivity fields F as deterministically self-similar that satisfy

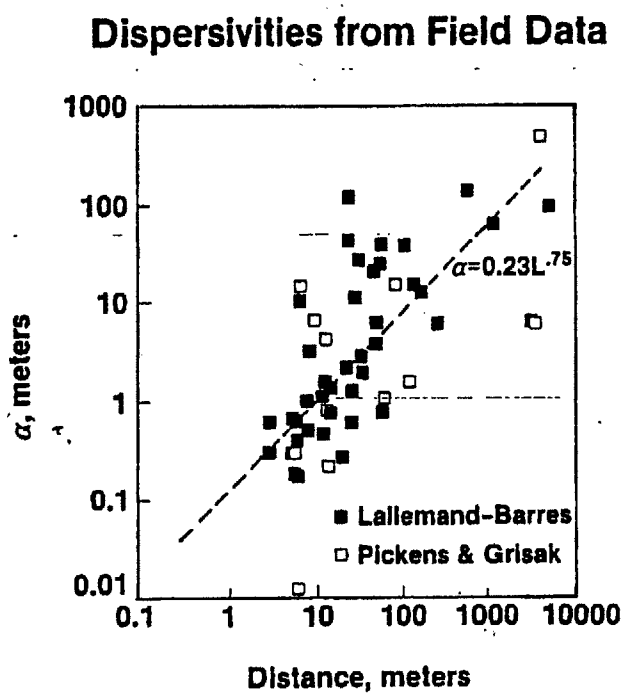

Figure 1.1 - Dispersivities measured at different sites – compiled by Pickens and Grisak (1981) and Lallemand-Barres et al (1978).

$$F(\underline{x}) \overset{d}{=} r^{-H} F(r\underline{x}) \tag{1.3}$$

where H is some real number and $r \geq 1$, or as processes with a weaker form of self-similarity when only its increments are self similar and satisfy,

$$F(x_1) - F(x_2) \overset{d}{=} r^{-H}\left[F(rx_1) - F(rx_2)\right], \quad x_1, x_2 \in \mathbb{R} \tag{1.4}$$

Neuman (1990) assumed that the hydraulic conductivity field was of the type expressed in Eq. (1.4), and using a regression analysis on Fig. 1.1, obtained H = 0.25. He assumed a universal relationship for the self-similar hydraulic conductivity in Eq. (1.4), which means that all aquifers at a given scale should have the same degree of heterogeneity. Data from the Borden site by Sudicky (1986) and the spectral analysis of the data by Robin et al. (1991) contradict the results of Neuman (1990). Neuman's notion of a universal model ignores the fact that different aquifers have varying degrees of heterogeneity at different scales. Moreover, Neuman's result depends on the reliability of the data shown in Fig. 1.1. Some of the data has been shown to be unreliable by Gelhar (1986). Hence, a model based on inaccurate data leads one to question the correctness of the results.

The model of hydraulic conductivity K proposed in this thesis presents a more realistic picture of aquifer heterogeneity. We model the K field as an isotropic lognormal multifractal. This model generalizes the notion of self-similarity to account for the randomness one would expect in aquifers. The real world application of this model may

be limited because one would expect aquifers to have anisotropic hydraulic conductivities. Moreover, the scales over which one would find multifractality of K may be limited. Yet, the application of a multifractal K field allows one to obtain a solution of the zero divergence Darcy equation that is entirely different in approach from the perturbation method and provides interesting results for the properties of the hydraulic gradient ∇H and specific discharge $\underline{q}$. The method of analysis is presented below.

1.3 Flow analysis when K is an isotropic lognormal multifractal field.

This thesis obtains a solution for zero divergence flow equation (Eq. 1.2) under the assumption that the hydraulic conductivity K is an isotropic lognormal multifractal field. Thus, the log hydraulic conductivity $F = \ln(K)$ is a Gaussian random field with spectral density

$$S_F(\underline{k}) = \begin{cases} \frac{2}{S_D} C_K k^{-D}, & k_o \le k \le r k_o \\ 0 & \text{otherwise} \end{cases} \qquad (1.5)$$

where $k = |\underline{k}|$ is the length of the wavenumber vector, S_D is the area of the unit D-dimensional sphere, C_K is the codimension parameter of K, k_o is the minimum wavenumber and r is the resolution to which the K field is developed. It is assumed that Eq. (1.5) holds for $k_o \gg 1$ and $C_K \ll 1$.

To study the possible multifractality of ∇H and $\underline{q}$, we consider a cascade of hydraulic gradient and flow fields at different resolutions $r \geq 1$. The ∇H and $\underline{q}$ fields at resolution r are obtained by considering flow through a log-conductivity field F_r in which all Fourier components with wavenumbers $k > rk_o$ have been filtered out. Using subscript r to denote quantities derived under $F = F_r$, the hydraulic gradient ∇H_r and specific flow $\underline{q}_r$ satisfy Darcy and no-divergence conditions

$$\begin{cases} \underline{q}_r = -K_r \nabla H \\ \nabla^2 H_r + \nabla F_r . \nabla H_r = 0 \end{cases} \tag{1.6}$$

The random fields ∇H_r and $\underline{q}_r$ for different r are compared using Eq. 1.6 under two assumptions, that through simulation have been found to be accurate:

1. In spaces of dimension $D > 1$, high frequency zero-mean fluctuations of the head and flow along the boundary of Ω affect the hydraulic gradient and flow only in a narrow region near the boundary.
2. Consider a sub-region Ω' of Ω and split F into a low-frequency component F_{LF} and a high frequency component F_{HF}. Inside Ω' the low frequency component F_{LF} may be considered constant. It is assumed that hydraulic gradient inside Ω' can be obtained accurately by replacing F with F_{HF} while subjecting Ω' to a large-scale hydraulic gradient equal to $\nabla H'_{LF}$.

Details of the analysis are presented in Chapter 4. The main results of these analyses are that the hydraulic gradient fields and specific discharge fields are also multifractal. In addition, the distributional properties of these parameters are provided in Chapter 4 and the accompanying numerical validation for the two-dimensional case is provided in Chapter 6.

1.4 Thesis Organization

This dissertation consists of nine chapters, including this introductory chapter. Chapter 2 contains a brief review of the first- and second-order perturbation theories and how these theories have been used in deriving the spectral density tensors of the hydraulic gradient ∇H and the specific flows $\underline{q}$. The spectral density tensor of $\underline{q}$ is used in computing the macrodispersivities [Rajaram and Gelhar, 1995]. In addition, the perturbation method has been used in computing the effective hydraulic conductivity of both isotropic and anisotropic heterogeneous media. For media with log-conductivity variances exceeding unity, the second-order theories have studied the effect of the higher-order terms on the spectra of ∇H and $\underline{q}$. These theories are also reviewed in Chapter 2. Chapter 2 also contains a brief review of fractal and self-similar models that have been used in characterizing the heterogeneity of aquifers.

Chapter 3 discusses the properties of multifractal measures. The properties of scalar and vector multifractal fields are presented in addition to the justifications for modeling

hydraulic conductivity fields as multifractals. Chapter 4 obtains the nonlinear solution of flow under the condition that the hydraulic conductivity field is an isotropic multifractal field. Properties of the hydraulic gradient and specific discharge field are obtained theoretically. Using the scaling results in Chapter 4, the spectral density properties of the hydraulic gradient and specific discharge field are obtained in Chapter 5.

The theoretical results presented in Chapter 4 are validated through numerical simulations and presented in Chapter 6. Results from the numerical simulations show that in spite of the numerical errors one expects in flow computations, the theoretical results of Chapter 4 accurately predict the behavior of flow in isotropic lognormal multifractal media.

The results of Chapters 4 and 5 are restricted to flow in fields with isotropic multifractal hydraulic conductivity K. Chapter 7 extends the results to include flow in anisotropic lognormal multifractal K fields. Unlike the isotropic K fields, the anisotropic multifractal K fields scale differently in the horizontal and vertical directions. The marginal distributions of the hydraulic gradient fields for anisotropic multifractal K fields are derived in Chapter 7.

Chapter 8 discusses issues related to the transport of solutes in isotropic multifractal K fields. The first passage time distribution, mean plume concentration and macrodispersivity of a solute in a multifractal flow field are presented.

The results of this thesis and their significance are discussed in Chapter 9. In addition, recommendations for future research that will help in understanding flow and transport in highly heterogeneous media are presented.

CHAPTER 2 –REVIEW OF FIRST-ORDER AND HIGHER-ORDER APPROACHES

Introduction

A compilation of over 130 dispersivity values from various sources at scales ranging from 10cm to 100km shown in Figure 1.1 [Arya, 1988; Gelhar et al., 1985, 1992] indicate an increase of the dispersivity with scale. Regarding these data as valid for single formations is debatable [Neuman 1993a, b; Gelhar 1993] and has cast doubt on certain theories based on the analysis of the data. At any rate, based on a regression analysis, Neuman [1990] suggested a power-law dependence of the longitudinal dispersivity A_L with the scale (or travel distance) L

$$A_L \propto L^{\beta} \tag{2.1}$$

where $\beta \simeq 1.5$. Several authors have explained the scale-dependent behavior in Figure 1.1 with fractal models [J. Glimm et al.; 1990, 1991, Zhang, 1992; Zhan and Wheatcraft, 1996; Rajaram and Gelhar, 1995; Ababou and Gelhar, 1990]. These fractal models represent log-conductivity field F as non-stationary self-similar processes with stationary increments that have spectra of the form

$$S_F(\underline{k}) \propto k^{\alpha} \tag{2.2}$$

where k is the length of $\underline{k}$ and α is some constant. For example, when α is between D+1 and D+3, where D is the spatial dimension, the log-conductivity F is a fractional Brownian surface (fBs). The spectrum of $F = \ln K$ is related to the velocity field via the linear perturbation results of Gelhar and Axness (1983). The results of Gelhar and Axness simplify the solution of the zero-divergence Darcy equation by substituting the flow variables head H, log-conductivity F and specific discharge q with linear approximations in the fluctuations $f = F - E[F]$, $h = H - E[H]$ and $q' = q - E[q]$. Spectral densities of the hydraulic gradient ∇H and specific discharge $\underline{q}$ are obtained by assuming that the variance of $F \ll 1$. This assumption allows the higher-order terms in h and f to be discarded. Several authors have examined the effects of the higher-order terms in f and h on the spectra of ∇H and $\underline{q}$ when the variance of F exceeds unity. And have found that including the higher-order terms have significant effects on the spectra of ∇H and $\underline{q}$. For large variances of F, the second-order solutions may not necessarily be more accurate than the first-order solutions [Ababou et al., 1988]. Hence, for highly heterogeneous media, alternate methods are needed that will avoid the expansions involved in the perturbation approach and deal directly with the nonlinearities.

This chapter reviews the first and higher-order theories and presents in detail the shortcomings of these approaches. An understanding of these theories will give a context for the goals and approaches of this research, which studies the properties of the hydraulic gradient and flow fields when the hydraulic conductivity is an isotropic lognormal multifractal field. Instead of the perturbation approach, a renormalization approach that exploits the scaling properties of the hydraulic conductivity field will be

used in deriving the distributions of the hydraulic gradient and specific discharge fields. The theories reviewed in this chapter, especially results of the first-order theory, will be compared and contrasted with the results of the nonlinear theory.

This chapter is organized as follows. Section 2.1 reviews the linear perturbation approach, followed in section 2.2 with a review of higher-order theories and numerical solutions used in studying the effects of higher-order terms. Section 2.3 reviews approaches used in computing the effective permeability. In section 2.4 macrodispersivity theories used in explaining how solutes spread are reviewed. Section 2.5 reviews the fractal and self-similar models that have been used in characterizing the heterogeneity of aquifers. The relevance of the results presented in this thesis extends beyond applications in hydrology and has applications in electrical engineering. Hence, section 2.6 contains a review of work done on multifractal conductor networks, which is a mathematical analogue to the problem of flow through heterogeneous K fields.

2.1 First-order solution of spectral perturbation equations

There are many types of geological or natural earth materials through which water can flow. This thesis studies the flow through non-fractured porous media. A sedimentary aquifer is an example of such a medium. An important characteristic of porous media is the porosity. The total porosity expresses the total averaging volume represented by interstices. A more significant measure for fluid flow is the connected porosity n, in

which only those voids that provide connections among averaging volumes are considered. In this thesis, the term "porosity" refers to the connected porosity and materials with a finite amount of porosity are described as permeable. The effects of porosity variations have been considered and found secondary relative to the effects of the hydraulic conductivity [Warren and Skiba, 1964; Naff, 1978]. Therefore, the porosity is treated as constant in this thesis.

The classical description of flow in permeable materials is based on a continuum representation of mass and momentum balances applied at a scale that averages over a large number of flow passages to produce a continuous description of flows and concentrations. This averaging is done over a so-called representative elementary volume (REV), which is large compared to the fine-scale variability and small compared to overall scale of the problem.

The conservation of momentum corresponding to Newton's law is the Darcy equation [Bear, 1972; Gelhar, 1993]

$$q_i = -K\frac{\partial H}{\partial x_i} \quad i = 1, 2, 3 \tag{2.3}$$

where q_i = specific flow vector [L/T]

K = hydraulic conductivity tensor [L/T]

H = piezometric head [L]

Each of the variables in Eq. (2.3) represents an average over an REV that can be viewed as a point in space. The Darcy equation strictly applies to relatively slow flows (or flows with a small Reynolds number) that do not change rapidly over time [Gelhar, 1993].

Flows in many naturally occurring aquifers are expected to satisfy this condition with a few exceptions such as flow in karstic limestone, basalt or coarse gravel.

For saturated groundwater flow, the conservation of mass of a non-reactive species is [Bear, 1972; Gelhar, 1993]

$$n\frac{\partial c}{\partial t}+\nabla\left(\underline{q}c\right)=\nabla\left(nDc\right) \tag{2.4}$$

where D = dispersion coefficient tensor $\left[L^2/T\right]$

c = concentration of the species $\left[M/L^3\right]$

For a zero-divergence flow field, Eq. 2.3 is written as

$$\nabla K\nabla H+K\nabla^2 H=0 \tag{2.5}$$

Dividing through Eq. (2.5) by K and expressing it in terms of F = lnK gives

$$\nabla^2 H+\nabla F\nabla H=0 \tag{2.6}$$

The hydraulic conductivity K is a stationary random function with a lognormal distribution. Justification for the lognormal representation of the K fields has been presented by Hufschmied (1985) and Sudicky (1986) who analyzed extensive data of conductivities and found the lognormal distribution to an accurate representation.

Gelhar and Axness (1983) obtain the first-order solution to Eq. (2.6) by assuming that small random perturbations about the mean occur in the specific discharge, log hydraulic conductivity and head, so that

$$\begin{aligned} F &= \bar{F} + f & E[f] &= 0 \\ q_i &= \bar{q}_i + q_i' & E[q_i'] &= 0 \quad i = 1, 2, 3 \\ H &= \bar{H} + h & E[h] &= 0 \end{aligned} \tag{2.7}$$

where the bar indicates the mean of these quantities. Substituting Eq. (2.7) into Eq. (2.6) and expanding terms gives

$$\nabla^2\bar{H} + \nabla^2 h + \nabla\bar{F}\nabla\bar{H} + \nabla\bar{F}\nabla h + \nabla f\nabla\bar{H} + \nabla f\nabla h = 0 \tag{2.8}$$

Taking the ensemble average of the above equation we obtain

$$\nabla^2\bar{H} + \nabla\bar{F}\nabla\bar{H} + E[\nabla f\nabla h] = 0 \tag{2.9}$$

Subtracting Eq. (2.9) from Eq. (2.8) gives

$$\nabla^2 h + \nabla\bar{F}\nabla h + \nabla f\nabla\bar{H} = -\{\nabla f\nabla h - E(\nabla f\nabla h)\} \tag{2.10}$$

Assuming the mean log-conductivity $\bar{F}$ is constant, Eqs (2.9) and (2.10) become respectively,

$$\begin{aligned} &\text{(i)}\ \ \nabla^2\overline{H}+E[\nabla f\nabla h]=0 && \text{(mean eq.)} \\ &\text{(ii)}\ \nabla^2 h+\nabla f\nabla\overline{H}=-\{\nabla f\nabla h-E(\nabla f\nabla h)\} && \text{(perturbation eq.)} \end{aligned} \tag{2.11}$$

Since the perturbations are assumed small the products of the perturbed terms $\{\nabla f\nabla h-E(\nabla f\nabla h)\}$is dropped. Moreover, the mean hydraulic gradient in the longitudinal direction is assumed constant such that $J=-\nabla\overline{H}$, then Eq (2.11) can be written as

$$\nabla^2 h=\sum_{i=1}^{3} J_i\frac{\partial f}{\partial x_i} \tag{2.12}$$

In addition, Eq. (2.3) is expressed in terms of the perturbations as follows:

$$\begin{aligned} \overline{q}_i+q_i^{'} &= -K_o\exp(f)\left(\nabla\overline{H}+\nabla h\right) \\ &= -K_o\left\{1+f+\frac{f^2}{2}+.....\right\}\left(\nabla\overline{H}+\nabla h\right) \end{aligned} \tag{2.13}$$

where $K_o=\exp\left(\overline{F}\right)$ and the dots represent the higher-order terms. Under the condition that the perturbations f and h are small so that higher-order terms may be neglected, the mean value of q_i is $E[q_i]=-K_o\nabla\overline{H}$ and the mean-corrected specific discharges $q_i^{'}=q_i-E[q_i]$ are given by

$$q_i' = -K_o\left[J_i f - f\frac{\partial h}{\partial x_i}\right] \tag{2.14}$$

By using the Fourier- Stieltjes representations for f, h and q_i' as shown below:

$$f(\underline{x}) = \int_{-\infty}^{\infty}\int e^{i\underline{k}\underline{x}} dZ_f(\underline{k})$$

$$h(\underline{x}) = \int_{-\infty}^{\infty}\int e^{i\underline{k}\underline{x}} dZ_h(\underline{k})$$

$$q_i'(\underline{x}) = \int_{-\infty}^{\infty}\int e^{i\underline{k}\underline{x}} dZ_{q_i}(\underline{k})$$

Eq. (2.12) can be written as

$$\begin{aligned} (ik)^2 dZ_h &= \sum_{j=1}^{3} J_j (ik_j) dZ_f \\ \Rightarrow dZ_h &= \sum_{j=1}^{3} -\frac{iJ_j k_j}{k^2} dZ_f \end{aligned} \tag{2.15}$$

Also, from Eq. (2.14)

$$dZ_{q_i} = K_o\left(J_i - \frac{J_j k_i k_j}{k^2}\right) dZ_f \tag{2.16}$$

With $\bar{q}_2 = \bar{q}_3 = 0$ and a statistically isotropic lnK field, the transverse mean hydraulic gradients $J_2 = J_3 = 0$, the spectrum of the specific discharge becomes

$$S_{q_i q_j} = J_1^2 K_o^2 \left(\delta_{1i} - \frac{k_1 k_i}{k^2} \right) \left(\delta_{1j} - \frac{k_1 k_j}{k^2} \right) S_{ff} \tag{2.17}$$

where the indices vary from 1 to D (the dimension of space). This is a second-rank symmetric tensor. Also from Eq. (2.15) the power spectral density of the hydraulic head fluctuation h is

$$S_{hh} = J_1^2 \left(\frac{k_1}{k^2} \right)^2 S_{ff} \tag{2.18}$$

The first-order perturbation approach presented above has the advantage of producing closed form results. However, a key assumption is that the variance of the log-conductivity field is small such that second and higher order terms in the log-conductivity fluctuations can be neglected. A question that has been much researched deals with the effects of the neglected higher order terms on the spectral solution of the head, hydraulic gradient and specific discharge.

2.2 Higher-order approaches

Dagan (1985) developed a higher order perturbation expansion to examine the effects of the discarded higher order terms on the spectrum of the head fluctuations. Hsu and Neuman (1997) followed an approach similar to Dagan's but instead of an exponential covariance function, modeled the log-conductivity field F with a Gaussian autocovariance function. In addition whereas Dagan's derivation is based on Fourier transforms, Hsu and Neuman obtain their results in physical space. The focal point of Hsu and Neuman's analysis is the velocity covariance function, unlike the covariance functions for head and log-conductivity as was in the case of Dagan. In fact, the analysis of Hsu and Neuman is similar to that of Deng and Cushman (1995) but differs in details. Deng and Cushman's derivation was done in Fourier space and evaluates the velocity covariance terms numerically, whereas Hsu and Neuman evaluate terms that are first-order in hydraulic head analytically and higher-order terms numerically. Moreover, Deng and Cushman model the log-conductivity field with an exponential covariance function while Hsu and Neuman use a Gaussian covariance function.

Lent and Kitanidis (1996) and Bellin et al. (1992) applied numerical techniques to investigate the range of validity of the small perturbation approximation for head and specific discharge in finite two-dimensional domains. Lent and Kitanidis perform the flow simulations in Fourier space, while Bellin et al. simulate the flow and transport processes in physical space. Lent and Kitanidis investigate the range of validity of the linear perturbation for the head and specific discharge moments in 2D finite domains whereas Bellin et al. investigate the accuracy of the linear perturbation for both flow

(specific discharge moments) and transport (longitudinal and transverse displacement variances) variables. While Lent and Kitanidis perform their computations on a regular grid, Bellin et al. apply a finite element approach in which the grid is subdivided into triangles. Results of the various higher-order approaches are presented below.

Dagan (1985) begins by using $\nabla H = -J + \nabla h$, $\nabla F = \nabla f$ and $\nabla^2 H = \nabla^2 h$ in Eq. (2.6) to obtain

$$\nabla^2 h + \nabla f . \nabla h = J . \nabla f \tag{2.19}$$

By taking the Fourier transform (FT) of Eq. (2.19), using the FT of derivatives and products below,

$$\begin{aligned} FT\left[\nabla u(\underline{x})\right] &= -i \begin{bmatrix} k_1 \\ k_2 \\ k_3 \end{bmatrix} \hat{u}(\underline{k}) \\ FT\left[u_1(\underline{x}) u_2(\underline{x})\right] &= (2\pi)^{D/2} \int \hat{u}_1(\underline{k}_1) \hat{u}_2(\underline{k} - \underline{k}_1) d\underline{k}_1 \end{aligned} \tag{2.20}$$

where $\hat{u}(\underline{k}) = (2\pi)^{-D/2} \int u(\underline{x}) e^{i\underline{k}\cdot\underline{x}} d\underline{x}$ and D is the space dimension, Dagan obtained

$$\begin{aligned} -k^2 \hat{h}(\underline{k}) + (2\pi)^{-D/2} \int \underline{k}_1 . (\underline{k} - \underline{k}_1') \hat{h}(\underline{k}_1) \hat{F}(\underline{k} - \underline{k}_1) dk_1 \\ = i (\underline{J} . \underline{k}) \hat{F}(\underline{k}) \end{aligned} \tag{2.21}$$

where k is the amplitude of the wavenumber vector $\underline{k}$. The solution of Eq. (2.21) is obtained in recursive form as

$$\hat{h}_1(\underline{k}) = i\frac{\underline{J}.\underline{k}}{k^2}\hat{F}(\underline{k})$$

$$\hat{h}_n(\underline{k}) = \int \frac{k_1^2}{k^2}\beta(\underline{k}_1,\underline{k})\hat{F}(\underline{k}-\underline{k}_1)\hat{h}_{n-1}(\underline{k}_1)d\underline{k}_1 \qquad (2.22)$$

where $\beta(\underline{k}_1,\underline{k}_2) = -(2\pi)^{-D/2}\frac{\underline{k}_1.(\underline{k}_2-\underline{k}_1)}{k_1^2}$. The first-order approximation $\hat{h}_1$ is the same as the solution obtained in Eq. (2.18). Substituting $\hat{h}_1$ into the recursive Eq. (2.22) and so on for further approximations and summing up the results, Dagan obtains for $\hat{h}$ up to third-order terms

$$\begin{aligned}\hat{h}(\underline{k}) = \hat{h}_1 + \hat{h}_2 + \hat{h}_3 = i\underline{J}.\Bigg\{&\frac{\underline{k}}{k^2}\hat{F}(\underline{k}) \\ &+\int \frac{\underline{k}_1}{k^2}\beta(\underline{k}_1,\underline{k})\hat{F}(\underline{k}-\underline{k}_1)d\underline{k}_1 \\ &+\int\int \frac{\underline{k}_2}{k^2}\beta(\underline{k}_1,\underline{k})\beta(\underline{k}_2,\underline{k}_1)\hat{F}(\underline{k}_2)\hat{F}(\underline{k}_1-\underline{k}_2) \\ &.\hat{F}(\underline{k}-\underline{k}_1)d\underline{k}_1 d\underline{k}_2\end{aligned} \qquad (2.23)$$

The cross-spectrum of h and f is obtained by multiplying $\hat{h}(\underline{k}_2)$ by $\hat{F}(\underline{k}_1)$ and averaging

$$S_{fh}(\underline{k}_2)=\left\langle \hat{F}(\underline{k}_1)\hat{h}(\underline{k}_2)\right\rangle = i\underline{J}.\left\{\frac{\underline{k}_2}{k_2^2}\left\langle \hat{F}(\underline{k}_1)\hat{F}(\underline{k}_2)\right\rangle \right.$$
$$+\iint \frac{k_2}{k^2}\beta(\underline{k}_1,\underline{k}_2)\beta(\underline{k}_2,\underline{k}_1) \qquad (2.24)$$
$$\left.\cdot\left\langle \hat{F}(\underline{k}_2)\hat{F}(\underline{k}_1-\underline{k}_2)\hat{F}(\underline{k}_2-\underline{k}_1)\hat{F}(\underline{k}_1)\right\rangle\right\} d\underline{k}_1 d\underline{k}_2$$

To simplify Eq. (2.24) Dagan replaces the second- and fourth-order moments of $\hat{F}$ with their expanded expressions (see Eq. 18 in Dagan, 1985), integration over $\underline{k}_2$ is performed, and terms that cancel out by symmetry are dropped. The detailed calculations are given in the Appendix of Dagan, 1985. The final result is

$$S_{fh}(\underline{k}_2)=i\frac{\underline{J}.\underline{k}_2}{k_2^2}\left[1+L(k_2)\right]S_{ff}(\underline{k}_2)$$
$$\text{where } L(k_2)=-(2\pi)^{-D/2}\int \frac{\left[\underline{k}_1.(\underline{k}_1+\underline{k}_2)\right](\underline{k}_2.\underline{k}_1)}{(k_1^2+k^2)k^2}\left(1+\frac{\underline{k}.\underline{k}_1}{k_1^2}\right)S_{ff}(k_1)d\underline{k}_1 \qquad (2.25)$$

Using a method similar to the one described above Dagan obtains the spectrum of the head fluctuations as

$$S_{hh}(\underline{k}_2)=\frac{(\underline{J}.\underline{k}_2)}{k_2^4}\left[1+2L(k_2)\right]S_{ff}(\underline{k}_2) \qquad (2.26)$$

The function L is the second-order correction. If one leaves out L in Eqs. **(2.25)** and **(2.26)** the first-order approximation by Gelhar and Axness is obtained. Hence, the validity of the first-order approximation depends on the smallness of L compared to unity. To grasp the magnitude of the second-order correction, Dagan analyzes the spectra for a log-conductivity field with an exponential covariance and found the maximum value of $-L/\sigma_f^2$ to be 0.08 and concluded that the first-order spectra S_{fh} and S_{hh} are quite accurate for values of σ_f^2 as large as unity. In fact, Dagan found that the inclusion of the second-order terms had little effect on the spectra S_{fh} and S_{hh} for log-conductivity variance σ_f^2 on the order of unity. This indicates that the head variance is relatively unaffected by high order interactions. To understand the effects of the second-order correction in F=lnK fields with spectra of the type $S_F(\underline{k}) \propto k^{\alpha}$ where α is a constant, the behavior of the integral in L (Eq.2.25) is examined near the origin and at infinity, by setting $\underline{k} = k\underline{e}$ and $\underline{k}_1 = k_1\underline{e}_1$, where $\underline{e}$ and $\underline{e}_1$ are unit vectors. Then $L(\underline{k})$ can be written as

$$
\begin{aligned}
L(k_2) &= -(2\pi)^{-D/2} \int \frac{(k_1^2 k)\left[\underline{e}_1 \cdot (k_1\underline{e}_1 + k\underline{e})\right](\underline{e}.\underline{e}_1)}{(k_1^2 + k^2)k^2}\left(1 + \frac{k_1 k}{k_1^2}(\underline{e}.\underline{e}_1)\right) S_{ff}(k_1)\, d\underline{k}_1 \\
&= -(2\pi)^{-D/2} \int \frac{k_1^2}{k_1^2 + k^2}\left(\frac{k_1}{k} + (\underline{e}.\underline{e}_1)\right)(\underline{e}.\underline{e}_1)\left(1 + \frac{1}{(k_1/k)}(\underline{e}.\underline{e}_1)\right) S_{ff}(k_1)\, d\underline{k}_1
\end{aligned}
\qquad (2.27)
$$

For isotropic K fields $S_{ff}(\underline{k}_1)$ is polarly symmetric. Therefore, what matters in Eq. **(2.25)** is the average of the term in Eq. (2.27) for $\underline{e}_1$ a vector on the unit spherical surface

in $\mathbb{R}^D$. Terms in $(\underline{e}.\underline{e}_1)^n$ with n odd do not contribute to this average. Neglecting these terms, Eq. (2.27) reduces to

$$L(k_2) = -(2\pi)^{-D/2} \int 2 \frac{k_1^2}{k_1^2 + k^2} (\underline{e}.\underline{e}_1)^2 S_{ff}(k_1) d\underline{k}_1 \tag{2.28}$$

Notice that $(\underline{e}.\underline{e}_1)^2 = (\cos\alpha)^2$ where α is the angle between $\underline{e}$ and $\underline{e}_1$. The expected value of $(\cos\alpha)^2$ is 1/D. Hence Eq. (2.28) can be written as

$$L(k_2) = -(2\pi)^{-D/2} \int \frac{2}{D} \frac{k_1^2}{k_1^2 + k^2} S_{ff}(k_1) d\underline{k}_1 \tag{2.29}$$

As $(k_1/k) \to \infty$, the ratio $k_1^2/(k_1^2 + k^2) \to 1$, implying divergence of $L(k_2)$ for $S_{ff}(\underline{k}) \propto k^{-\alpha}$ with $\alpha \le D$. Notice that $\alpha = D$ which corresponds to a lognormal multifractal K field is included in this condition. The case $\alpha < D$ corresponds to fractional Gaussian noise (fGn) representations of lnK.

For $(k_1/k) \to 0$, the ratio $k_1^2/(k_1^2 + k^2)$ behaves like k_1^2. Therefore the low-frequency divergence of $L(k_2)$ occurs only for $\alpha \ge D + 2$ which does not include multifractal conductivity cases. Thus for multifractal hydraulic conductivity K the second-order correction factors to S_{fh} and S_{hh} have high frequency divergence. It is worth noting that $k_1^2/(k_1^2 + k^2) \ge 0$. Therefore, in the pre-multifractal case when the scaling range extends to a large but finite wavenumber, L is large negative and the second-order

spectrum S_{hh} is large negative. Thus, the second-order analysis is not applicable to multifractal hydraulic conductivity fields.

A second order correction for the velocity covariance has been obtained by Hsu and Neuman [1996] and Deng and Cushman [1995, 1998]. The starting point for Hsu and Neuman's analysis is Eq. **(2.13)**. Velocity covariance expressions are obtained for the expansion with terms up to the second-order in f. Hsu and Neuman found that the velocity variances are larger when approximated to second-order in f than to the first-order. And that the ratio between the first- and second-order variance approximations is larger in three than in two dimensions. Deng and Cushman [1995] took an approach similar to that of Hsu and Neuman. They initially obtained erroneous results but corrected their results in Deng and Cushman (1998). Their 1998 results agreed with those of Hsu and Neuman.

Numerical Approaches

Lent and Kitanidis (1996) compare results of Monte Carlo simulations to the linear perturbation approximation for head and specific discharge spectra. The discrete Fourier transforms of the head h and log-conductivity fluctuations are expressed as

$$h(\underline{x}) = \sum_{\text{all}\underline{k}} \hat{h}(\underline{k}) \exp(i2\pi \underline{k}.\underline{x})$$

$$f(\underline{x}) = \sum_{\text{all}\underline{k}} \hat{F}(\underline{k}) \exp(i2\pi \underline{k}.\underline{x}) \qquad (2.30)$$

Using Eq. (2.30) in Eq. **(2.19)** the zero-divergence Darcy equation can be written in discrete form as

$$k^2\hat{h}(\underline{k})+k_j\hat{h}(\underline{k})*k_j\hat{F}(\underline{k})=-\frac{i}{2\pi}J_j\Psi_j\hat{F}(\underline{k}) \tag{2.31}$$

where $i=\sqrt{-1}$, $\underline{k}$ is a wavenumber vector composed of integers, Ψ_j is the wave space matrix defined such that $fft^{-1}(\Psi)fft\left(\hat{F}(\underline{k})\right)$ is equivalent to the physical space operation $\partial f/\partial x$ [Lent and Kitandis, 1996], and the * operator denotes a convolution sum defined as

$$G_1(\underline{k})*G_2(\underline{k})=\sum_{\underline{k}=\underline{r}+\underline{s}} G_1(\underline{r})G_2(\underline{s}) \tag{2.32}$$

The spectral formulation of Eq. (2.31) is approximated by truncating the wavenumber domain $\underline{k}$ with cutoff wavenumbers. This is equivalent to limiting the spatial scales of variability that are included in the calculation. Eq. (2.31) then becomes a system of simultaneous, linear algebraic equations. This procedure is known as the numerical spectral method.

The Monte Carlo simulations begin by generating random realizations of the Fourier transform (FT) of the log-conductivity fluctuations $\hat{F}(\underline{k})$. Realizations of $\hat{F}(\underline{k})$ are then used to solve for the FT of the head fluctuations $\hat{h}(\underline{k})$ using Eq. (2.31). The spectrum of the head is then estimated by

$$S_{hh}(\underline{k}) = \frac{1}{N}\sum_{j=1}^{N} \hat{h}_j^*(\underline{k})\hat{h}_j(\underline{k}) \tag{2.33}$$

where the subscript j refers to the $\hat{h}(\underline{k})$ obtained from the jth realization of $\hat{F}(\underline{k})$ and N is the number of Monte Carlo realizations. The specific discharge in direction j is calculated using [see Lent and Kitanidis, 1996 for details]

$$q_j = -K_o \text{fft}\left[\exp\left(\text{fft}^{-1}\left(\hat{F}\right)\right)\left(-J_j + \text{fft}^{-1}\left(\Psi_j \hat{h}\right)\right)\right] \tag{2.34}$$

where fft is the Fast Fourier transform. The spectrum of the specific discharge is then estimated from

$$S_{q_i q_j}(\underline{k}) = \frac{1}{N}\sum_{\ell=1}^{N} q_{i\ell}(\underline{k}) q_{j\ell}^*(\underline{k}) \tag{2.35}$$

where $q_{j\ell}$ is the ℓth realization of the FT of the q_j component. An important consideration in any numerical approach is the assurance of numerical accuracy and appropriate convergence conditions. Methods used in ensuring numerical accuracy and convergence are explained in Lent and Kitanidis (1996) and follow methodologies of Bellin et al. (1992).

Lent and Kitanidis (1996) compared the head and specific discharge spectra computed from the linear perturbation theory and the spectra obtained through numerical

simulations (performed on a 512 x 512 grid) using the log-conductivity covariance by Mizell et al. [1992]. Figure 2.1 compares the Monte Carlo simulation results at two values of λ/L, where λ is the correlation distance and L is the size of the domain, to the linear perturbation approximation and the second-order correction of Dagan (1985). Decreasing λ is equivalent to increasing the domain size. And one can see from Fig. 2.1 that decreasing λ has the effect of significantly increasing the head variance. Another interesting feature of the head variance simulations is that the head fluctuations do not appear to be ergodic. Figure 2.2 shows the calculated head variances for two different values of λ. In Ababou et al.'s [1988, 1989] investigation, the spatial moments are used to approximate the ensemble moments, implicitly assuming ergodic behavior. Lent and Kitanidis' results show that for the head fluctuations at least, increasing the domain size relative to the log-conductivity correlation length will not necessarily insure that ensemble moments will equal the spatial moments. Figure 2.1 suggests that the linear perturbation approach tends to underpredict the head variances as the domain size becomes large. Figure 2.3 shows that the small wavenumber (large spatial scale) components of head variance are significantly larger than the predictions of the linear perturbation approach. Moreover, the small wavenumber components increase with increasing log-conductivity variance, which in turn results in the apparent non-ergodicity of head fluctuations.

The dependence of the head variance on the size of the domain can be also seen from the variograms. Figure 2.4 shows the effects of increased log-conductivity variance on the head variogram for the case when $\lambda = 0.02$. The estimates provided by the Monte Carlo simulations tend to much higher sills, indicating a higher overall variance.

Another interesting observation is that the *hole effect*, a requirement that the head variance should be finite in an infinite 2D domain, disappears as the log-conductivity variance grows.

The analysis of Lent and Kitanidis (1996) shows that the specific discharge variances tend to be ergodic, and tend to decrease as the size of the domain increases. This is true of both the longitudinal and transverse components. Apparently, taking the derivative of the head fluctuations was sufficiently dampens the large-scale effects contributing to the nonergodicity observed in the head [Lent and Kitanidis, 1996]. Lent and Kitanidis find the linear perturbation approach to be a very robust predictor of the covariance of the longitudinal component of the specific discharge vector. However, the perturbation approach tends to under predict the variance of the transverse component of the specific discharge. These results are shown in Figure 2.5. Interestingly, this latter result has been confirmed by Hsu and Neuman (1996) and Deng and Cushman (1998).

Bellin et al. (1992) arrive at a similar conclusion as the above authors. They find the linear perturbation to be robust in predicting the longitudinal specific discharge spectrum but unreliable in predicting the transverse specific discharge spectrum. The unreliability of the transverse velocity spectrum prediction from the small perturbation approach increases with increasing log-conductivity variance. Unlike Lent and Kitanidis, Bellin et al. do not examine the head spectrum. However, they compare predictions of the second-moments of a plume from the small-perturbation approach and from numerical simulations. They find that for σ_f^2 ranging from 0.2 to 1.6 the linear theory overestimates the longitudinal second moment of the plume. Their results do not include an examination of the transverse second moment of the plume, however Hsu et al. (1996)

examine the second-order correction of the transverse second moment and find the linear perturbation to under predict the magnitude of the second moment of the plume. Issues related to the spread of solutes in heterogeneous media are discussed in Section 2.4.

In summary, the second-order and numerical approaches expose the limitations of the first-order approach. The analytical solutions of the second-order corrections are complex and limit the extent to which higher-order exponents can be incorporated into the analysis. Moreover, the second-order theories do not provide information on flow distribution properties other than the second moments. Furthermore, the second-order results find that first-order approach to underpredict the variance of the transverse component of the specific discharge. The second-order approaches also expose the limitations of the perturbation approach. The exponential expansions present mathematical difficulties in trying to obtain second-order covariance terms in the hydraulic head and specific discharge.

The numerical results are illuminating, however they do not provide predictive tools that can be used to characterize flow in highly heterogeneous media. The numerical results of Lent and Kitanidis (1996) and Bellin et al. (1992) reveal the robustness of the first-order theory in predicting the longitudinal second moment of a plume's dispersion. Despite their lack of predictive capability, the numerical results show that the first-order theory tends to under estimate the covariance of the transverse component of the plume and confirm theoretical second-order corrections of Hsu and Neuman (1996) and Deng and Cushman (1998). The second-order theories and the numerical results clearly suggest that the furtherance of knowledge in flow theories for fields with highly variable hydraulic conductivity needs to be pursued with alternate

methods. Theoretical approaches that seek to address the effects of higher-order terms have to incorporate approaches that sidetrack the complications of the exponential expansions involved in the perturbation approach. In effect, these alternate approaches have to embrace a new theoretical framework, such as the current renormalization approaches of Sposito (2000), Christakos et al. (1999) or apply a novel approach as that applied in this thesis. All these approaches do not arrive at an exact solution for the nonlinear zero-divergence flow problem. However, the approach in this thesis for example, presents new results for spectral densities of head, hydraulic gradient and specific discharge which were not found using the linear perturbation approach.

2.3 Effective hydraulic conductivity expressions for isotropic media (first- and second-order models)

Effective hydraulic conductivity, more commonly known as effective permeability, is a term used for a medium that is statistically homogeneous on a large scale. In a stochastic context, it is defined through a form of the mean Darcy equation, such that the effective hydraulic conductivity in a D-dimensional region S is a scalar quantity $K_{eff}(S)$ such that, when an average hydraulic gradient $\nabla H = -\underline{J}$ is applied to S, the mean specific discharge $E\left[\underline{q}(S)\right]$ is given by

$$E\left[\underline{q}(S)\right] = -K_{eff}(S)\underline{J} \tag{2.36}$$

When the hydraulic conductivity is a random field, both K_{eff} and $E\left[\underline{q}(S)\right]$ are random variables. However, for infinitely large domains and ergodic K, $E\left[\underline{q}(S)\right]$ does not depend on the realization and K_{eff} becomes a deterministic quantity.

Gelhar and Axness (1983) obtain expressions for K_{eff} by taking the expectation of Eq. **(2.13)**.

$$E[q_i] = -K_o E\left[\left\{1 + f + \frac{f^2}{2} + ...\right\}\left(\nabla\overline{H} + \nabla h\right)\right] \tag{2.37}$$

let $\nabla\overline{H} = -J_i$ and $\nabla h = \frac{\partial h}{\partial x_i}$ then Eq. (2.37) becomes

$$E[q_i] = K_o\left[J_i\left(1 + \frac{\sigma_f^2}{2}\right) - E\left(\frac{\partial h}{\partial x_i} f\right)\right] \tag{2.38}$$

In Eq. (2.38), terms up to the second order in the perturbations have been retained. The expected value of the product of the perturbations in the head gradient and in log-conductivity is an important term that reflects the relationship between the conductivity

variation and the head perturbation that it produces. This term, $E\left(\frac{\partial h}{\partial x_i} f\right)$ is evaluated as follows:

$$E\left[\frac{\partial h}{\partial x_i} f\right] = \int_{\underline{k}} ik_i E\left[dZ_h dZ_f^*\right] \tag{2.39}$$

from Eq. **(2.15)** $dZ_h = \sum_{j=1}^{3} -\frac{iJ_j k_j}{k^2} dZ_f$, hence Eq. (2.39) becomes

$$E\left[\frac{\partial h}{\partial x_i} f\right] = \int_{\underline{k}} ik_i E\left[-\frac{iJ_j k_j}{k^2} dZ_f dZ_f^*\right] = \int_{\underline{k}} \frac{J_j k_i k_j S_{ff}(\underline{k})}{k^2} d\underline{k}$$
$$= F_{ij} J_j \tag{2.40}$$

where $F_{ij} = \int_{\underline{k}} \frac{k_i k_j S_{ff}(\underline{k})}{k^2} d\underline{k}$

Obtaining expressions for F_{ij} is pivotal in deriving K_{eff} expressions for the small perturbation approach. For example, for 1D flow with a constant mean hydraulic gradient, F_{ij} is,

$$F_{11} = \int_{-\infty}^{\infty} \frac{k_1^2}{k_1^2} S_{ff}(k_1) dk_1 = \sigma_f^2 \tag{2.41}$$

It is worth noting that the evaluation of the integral is not dependent of the form of the spectrum, because variance is simply the integral of the spectrum over wave number. The effective conductivity for 1D flow, then, is

$$K_{eff} = K_o\left[1+\frac{\sigma_f^2}{2}-\sigma_f^2\right] = K_o\left[1-\frac{\sigma_f^2}{2}\right] \tag{2.42}$$

Equation (2.42) is approximate because higher-order terms were discarded in equation (2.38).

The exact effective permeability for a 1D flow system can be obtained as follows: Darcy's equation can be written as $J = qK^{-1}$, where J is the mean hydraulic gradient

$$\Rightarrow J = qE\left[K^{-1}\right] \tag{2.43}$$

Also,

$$q = J/E\left[K^{-1}\right] = K_{eff}J \tag{2.44}$$

where $K_{eff} = \left\{E\left[K^{-1}\right]\right\}^{-1}$ is the harmonic mean of K. If the lnK process is normal, then the harmonic mean is

$$K_{eff} = K_o \exp\left(-\frac{\sigma_f^2}{2}\right) \tag{2.45}$$

It is clear that equation (2.42) cannot be correct for $\sigma_f^2 > 2$ because it predicts a physically impossible negative hydraulic conductivity under those conditions.

For multidimensional flow in isotropic log-conductivity fields, F_{ij} is

$$F_{11} = \int_{\underline{k}} \frac{k_1^2}{k^2} S_{ff}(\underline{k}) d\underline{k} = \frac{\sigma_f^2}{D} = F_{22} = F_{33} \tag{2.46}$$

where D = 2 or 3 is the space dimension. Hence the K_{eff} for two and three dimensions is

$$\begin{cases} \text{(i)} \quad K_{eff} = K_o & \text{for 2D} \\ \text{(ii)} \quad K_{eff} = K_o\left[1 + \frac{\sigma_f^2}{6}\right] & \text{for 3D} \end{cases} \tag{2.47}$$

Equation (2.47)i agrees with Matheron's (1967) conjecture that K_{eff} in an isotropic and stationary porous medium is given by

$$K_{eff} = \left(E[K]\right)^{(D-1)/D} \left(E[K^{-1}]\right)^{-1/D} \tag{2.48}$$

In the case of log-normal conductivity distribution with mean 1 and variance σ_f^2,

$E[K] = \exp\left(1 + \frac{1}{2}\sigma_f^2\right)$, hence K_{eff} in Eq. (2.48) becomes:

$$K_{eff} = E[K]\exp\left(-\frac{1}{D}\sigma_f^2\right) = K_o \exp\left[\sigma_f^2\left(\frac{1}{2} - \frac{1}{D}\right)\right] \qquad (2.49)$$

Several arguments support Eq. (2.49) in the case of isotropic lognormal conductivity. One used by Matheron (1967) and later by King (1989) is that Eq.(2.49) reproduces the exact results for D = 1 and D = 2. Additional support comes from the fact that the first-order linear perturbation results of Gelhar and Axness (1983), Gutjahr et al.(1978) and the second-order results of Dagan (1993) can be seen as the first- and second-order terms of Taylor's series expansions of the exponential in Eq. (2.49). King (1989) and later Noetinger (1994) by elaborate developments of higher-order in σ_f^2 and through certain approximations obtain Eq. (2.49). Dykaar and Kitanidis (1992) found a deviation of only 4% between calculations made with the spectral numerical method and Matheron's conjecture (see Figure 2.6). However, all these procedures are underlain by some approximations and proving equation (2.49) exactly has defied attempts in the past [Dagan, 1993]. Kozlov (1993) using results from random homogenization theory for multiscaled media shows that Matheron's conjecture is asymptotically accurate as the length scales of the media tend to infinity. Abramovich and Indelman (1995) and De Wit (1995) using perturbation expansions show that for correlated isotropic media, Matheron's conjecture is inaccurate.

Kozlov relies on homogenization theory for random media (for details on homogenization theory see Kozlov, 1989, Zhykov et al., 1993). The permeability field K is modeled as an isotropic lognormal multiscale field with a certain number of scales N, so that as $N \to \infty$ the log permeability field converges to a normal distribution:

$$K_N(x) = K_o \exp\left\{\frac{1}{\sqrt{N}} F_N(x)\right\} \qquad F_N(x) = \sum_{k=1}^{N} f_k(x)$$

where $F = \ln(K)$ and the independent, statistically-homogeneous fields are assumed to have correlation lengths $\xi_k \to \infty$, $k \to \infty$ in such a way that the ratio ξ_{k+1} / ξ_k also converges to a finite value. Kozlov's work relies on a result from random homogenization theory that allows a random tensor to be related to a constant matrix whose elements can be expressed in exponential form (see Eqs. 2.2 and 2.9 in Kozlov, 1993). Upper and lower bounds can be obtained for the constant matrix. More importantly, the arithmetic mean serves as the upper bound and the harmonic mean serves as the lower bound of the constant matrix and consequently the random matrix.

Using these results from random homogenization theory Kozlov shows that the random log-permeability can be represented as a random tensor that for $N \to \infty$ its mean equates to Matheron's expression. He shows that the upper and lower limits of the homogenized permeability field converge to the same value that is Matheron's expression.

2.4 Macrodispersivity

The subject of how solutes are transported in groundwater has been studied with great interest for the past thirty years. Descriptors of how a solute spreads with travel time or distance from the point of injection are expressed respectively through two parameters: dispersion coefficient D_{ij} and macrodispersivity, A_{ij}. The dispersion coefficient expresses the growth rate of the second spatial moment of the concentration M_{ij} with respect to time, whereas macrodispersivity quantifies the growth of the second moment of concentration with respect to mean travel distance. In general, when the growth rate of M_{ij} with respect to either time or distance is constant, the nature of the dispersion is described as Fickian.

The dominant mechanism of dispersion of solutes is attributed to the variability of the flow velocities that are in turn associated primarily with the spatial variations in the hydraulic conductivity. Most stochastic theories of dispersion describe transport across an ensemble of aquifers, and the measures of dispersion relate to the ensemble mean concentration. The ensemble theories are assumed valid under ergodic conditions, that is for large contaminant sources or for plumes that travel over large distances. These ensemble theories cannot be applied in predicting the evolution of small plumes in a single realization. Rajaram and Gelhar [1993, 1995] presented a theory that predicts the growth of a plume of a given size. The formula that is presented for the rate of growth of the plumes second moment involves two scales: the plume displacement and the plume size. Figure 2.7 illustrates the difference between the ensemble average concentration of

a plume, and the ensemble average of a plume relative to the center of mass position. If $C(\underline{x},t)$ denotes the concentration field in a single realization, the spatial moments of the concentration field in a single realization are given by

$$\bar{x}_i(t) = \frac{n}{m}\int_{-\infty}^{\infty} x_i C(\underline{x},t)\,d\underline{x} \qquad i=1, 2, 3$$

$$S_{ij}(t) = \frac{n}{m}\int_{-\infty}^{\infty} \left(x_i - \bar{x}_i(t)\right)\left(x_j - \bar{x}_j(t)\right) C(\underline{x},t)\,d\underline{x} \quad i, j = 1, 2, 3 \tag{2.50}$$

$\bar{x}_i(t)$ refers to the $i-$coordinate location of the center of mass at time t.

n = porosity of the medium, assumed constant

$S_{ij}(t)$ = second moment tensor that quantifies the dispersion about the center of mass $\bar{x}_i(t)$.

For non-reactive tracers the concentration field in a single realization of steady flow satisfies the advective dispersion equation (ADE) (Eq. (2.4)). The ensemble-mean concentration is obtained by taking spatial averages of the ADE and assuming uniform flow in the x_1 direction so that the ADE becomes

$$n\frac{\partial \hat{C}}{\partial t} + \hat{q}_1 \frac{\partial \hat{C}}{\partial x_i} - \frac{\partial}{\partial x_i}\hat{q}_1 A_{ij}\frac{\partial \hat{C}}{\partial x_j} = 0 \quad i, j = 1, 2, 3 \tag{2.51}$$

where $\hat{C}(\underline{x},t)=E\left[C(\underline{x},t)\right]=$ ensemble average concentration

$\hat{q}_1$ = uniform mean flow

A_{ij} = macrodispersivity tensor

Also, the second moment of the ensemble average of the concentration is

$$M_{ij}(t)=\frac{n}{m}\int_{-\infty}^{\infty}\left(x_i-\hat{x}_i(t)\right)\left(x_j-\hat{x}_j(t)\right)\hat{C}(\underline{x},t)d\underline{x} \quad i,j=1,2,3 \tag{2.52}$$

and $\hat{x}_i(t)=\frac{n}{m}\int_{-\infty}^{\infty}x_i\hat{C}(\underline{x},t)d\underline{x}=\frac{\hat{q}_1 t}{n}$. A_{ij} is related to M_{ij} as follows

$$A_{ij}(t)=\frac{n}{2\hat{q}_1}\frac{dM_{ij}}{dt}=\frac{1}{2}\frac{dM_{ij}}{d\hat{x}_1} \tag{2.53}$$

A_{ij} quantifies the dispersion of the ensemble mean concentration about the ensemble-mean center position. The second moment M_{ij} is not the same as the ensemble average of the single realization tensor Σ_{ij}. The difference between these two quantities is illustrated in Fig. 2.7. M_{ij} and Σ_{ij} are related by [Rajaram 1992; Rajaram and Gelhar, 1995]

$$M_{ij}(t)=\Sigma_{ij}(t)+R_{ij}(t) \tag{2.54}$$

where $\Sigma_{ij}(t) = E\left[S_{ij}(t)\right]$ is the ensemble average of the second moment tensor in any realization.

$R_{ij}(t) = E\left[\left(\overline{x}_i(t) - \hat{x}_i(t)\right)\left(\overline{x}_j(t) - \hat{x}_j(t)\right)\right]$ is the ensemble average of the product of the derivations of the center of mass in a realization in the i and j directions from the ensemble mean center of mass locations in the same direction.

The ensemble theories are first reviewed and followed by a review of the single-realization theory. Recently renormalization group methods have been applied to derive the ensemble macrodispersivity results. These theories are also reviewed.

Ensemble Theories

For uniform mean flow aligned in the x_1 direction in a heterogeneous porous medium, the growth rate of M_{ij} with mean displacement $\hat{x}_1$ can be described by the following expression, which has been presented in equivalent forms by Dagan (1984, 1988), Gelhar (1983, 1987, 1993, 1995), Neuman (1987) and Koch and Brady (1988)

$$A_{ij}\left(\hat{x}_1\right) = \frac{1}{2}\frac{dM_{ij}}{d\hat{x}_1} = \frac{n^2}{\overline{q}^2}\int_0^{\overline{x}_1}\int_{-\infty}^{+\infty} e^{\left(ik_1 - \alpha k^2\right)\xi} S_{q_i q_j}(\underline{k})\, d\underline{k}\, d\xi \qquad (2.55)$$

where

α is the pore scale dispersion coefficient and

$S_{q_i q_j}(\underline{k})$ is the velocity spectrum

Dagan (1988) presents the derivation of the above equation from the theory of turbulent-diffusion.

$$A_{ij}(t)=\frac{d^2M_{ij}(t)}{dt^2}=\frac{2}{(2\pi)^3}\int\int_{-\infty}^{\infty}E\left[\hat{u}_j(\underline{k})\hat{u}_i^*(\underline{k})e^{i\underline{k}'.\underline{X}'}\right] \\ .\exp\left(ik'.\overline{\underline{U}}t-\alpha k_i'k_j't\right)d\underline{k}d\underline{k}' \quad i,j=1,2,3 \tag{2.56}$$

where X' is the residual of the displacement of a particle defined by $\frac{dX'}{dt}=\underline{u}(X_t)$ where X_t is the total particle displacement and $\underline{u}$ is the residual of the convective fluid velocity. The superscripts ^ and * denote the Fourier transform and conjugate respectively. In fact Dagan shows how various macrodispersivity expressions obtained by Mercado (1967) as well as results obtained by Dagan (1982, 1984), Gelhar and Axness (1983) and Neuman et al. (1987) are particular cases of Eq. (2.56).

Gelhar and Axness (1983) obtain an expression for macrodispersivity in the far-field from the linear perturbation approach by substituting the perturbed terms for C ($C=\overline{C}+c$) and q in Eq. **(2.4)** so that its steady state form is

$$\frac{\partial}{\partial x_i}\left[\left(\overline{q}_i+q_i'\right)\left(\overline{C}+c\right)\right]=E_{ij}\frac{\partial^2}{\partial x_i\partial x_j}\left(\overline{C}+c\right) \tag{2.57}$$

Expanding and taking the mean produces the mean equation

$$\frac{\partial}{\partial x_i}\left[\overline{qC}\right]+\frac{\partial}{\partial x_i}\left(E\left[q_i'c\right]\right)=E_{ij}\frac{\partial^2\overline{C}}{\partial x_i\partial x_j} \tag{2.58}$$

Subtracting Eq. (2.58) from the steady state version of Eq. **(2.4)** produces

$$\frac{\partial}{\partial x_i}\left(\overline{q}_i c+q_i'\overline{c}+q_i'c-E\left[q_i'c\right]\right)=E_{ij}\frac{\partial^2 c}{\partial x_i\partial x_j} \tag{2.59}$$

Assuming the primed quantities are small, the second order term $q_i'c-E\left[q_i'c\right]$ is neglected; hence, the first-order approximation describing the concentration perturbation is

$$\frac{\partial}{\partial x_i}\left(q_i'\overline{c}+\overline{q}_i c\right)=E_{ij}\frac{\partial^2 c}{\partial x_i\partial x_j} \tag{2.60}$$

For convenience, the mean flow direction is aligned in the x_1 direction so that $\overline{q}_1=q\neq 0$ and $\overline{q}_2=\overline{q}_3=0$. The local dispersion tensor E_{ij} may be approximated in the form [Naff, 1978]

$$\left[E_{ij}\right]=\begin{bmatrix}\alpha_L q & 0 & 0\\ 0 & \alpha_T q & 0\\ 0 & 0 & \alpha_T q\end{bmatrix} \tag{2.61}$$

where α_L and α_T are respectively the longitudinal and transverse dispersivities. Expanding the left term of Eq. (2.60) and utilizing the properties of a zero divergence flow and Eq. (2.61), Eq. (2.60) reduces to

$$q_i \frac{\partial \overline{C}}{\partial x_i} + q \frac{\partial c}{\partial x_1} = q\left[\alpha_L \frac{\partial^2 c}{\partial x_1^2} + \alpha_T \left(\frac{\partial^2 c}{\partial x_2^2} + \frac{\partial^2 c}{\partial x_3^2}\right)\right] \tag{2.62}$$

Eq. (2.62) is the approximate stochastic partial differential equation describing the concentration perturbation c produced as a result of specific discharge perturbations q'.

The macrodispersivity expression is obtained by considering the spectral representations for the perturbed quantities and noting that

$$c = \int_{\Re^3} e^{i(\underline{k}\cdot\underline{x})} dZ_c(\underline{k})$$

Making use of the above spectral representation and writing $G_i = -\partial \overline{C} / \partial x_i$, Eq. (2.58) can be expressed in Fourier space as

$$\left[ik_1 + \alpha_L k_1^2 + \alpha_T \left(k_2^2 + k_3^2\right)\right] q dZ_c = G_i dZ_{q_i} = G_j dZ_{q_j} \tag{2.63}$$

Multiplying both sides by the complex conjugate Fourier amplitude $dZ^*_{q_j}$ and taking the expectation of both sides of the equation gives

$$\left[ik_1 + \alpha_L k_1^2 + \alpha_T\left(k_2^2 + k_3^2\right)\right] qS_{cq_i}(\underline{k}) = G_i S_{q_i q_j}(\underline{k}) \tag{2.64}$$

where S_{cq_i} is the cross-spectrum of c and q_j, and $S'_{q_i q_j}$ is the cross-spectrum of the j and i components of the specific discharge.

Eq. (2.64) relates the spectra of flow variation with that of dispersive flux. The mean dispersive flux is evaluated by integrating its spectrum so that

$$\text{(i)}\quad E\left[cq_i'\right] = \int_{-\infty}^{\infty} S_{cq_i}(\underline{k})d\underline{k} = \int_{-\infty}^{\infty} \frac{qG_j S_{q_i q_j}(\underline{k})d\underline{k}}{\beta(\underline{k})q^2} = qA_{ij}G_j$$

where (2.65)

$$\text{(ii)}\quad A_{ij} = \int_{-\infty}^{\infty} \frac{S_{q_i q_j}(\underline{k})d\underline{k}}{\beta(\underline{k})q^2} \quad \text{and} \quad \beta(\underline{k}) = \left[ik_1 + \alpha_L k_1^2 + \alpha_T\left(k_2^2 + k_3^2\right)\right]$$

Eq. **(2.65)**ii is the macrodispersivity tensor, which depends on the covariance function used to describe the heterogeneity of the medium via the velocity spectrum $S_{q_i q_j}$.

The general development of the macrodispersivity expression (Eq. **(2.65)**ii) involves two major assumptions:

1. That the mean concentration gradient $G_i = -\partial \overline{C} / \partial x_i$ can be treated as constant, i.e. the mean concentration is a linear function of the spatial coordinates. This assumption will be strictly valid when the concentration field is relatively smooth. In other words, this assumption will be valid only after the plume has traversed a substantial displacement distance. Consequently, the macrodispersivity Eq. 2.65ii is not expected to valid near solute sources where large concentration gradients and sharp curvature will occur.
2. A second assumption involves the spectral relationship used for the covariance between the concentration fluctuations c and the fluctuations of the specific discharge components q_i' (Eq. **(2.65)**i). This relation holds when c and q_i are stationary fields, so that their measures have orthogonal increments. In the above derivation, whereas q_i is stationary, c is not and Eq. **(2.65)**i should be replaced with

$$\mathrm{Cov}[c, q_i] = \int_{\Re^3} \int_{\Re^3} E\left[dZ_c(\underline{k}_1) dZ_{q_i}(\underline{k}_2) \right]$$

where the cross terms are also included. It is not clear what effect these cross-terms may have on the covariance. However, these cross terms are not taken into consideration in evaluating the macrodispersivity.

Returning to the generalized form of macrodispersivity (Eq. **(2.56)**), Dagan (1987) shows that Gelhar and Axness' expression in addition to those of Dagan (1982) and the

macrodispersivity for a stratified medium by Matheron and Marsily (1980) are all specialized forms of Eq. (**2.56**).

Gelhar and Axness' expression for macrodispersivity (Eq. (**2.65**)ii) can be obtained from Eq. (**2.56**) by integrating over distance to yield

$$A_{ij} = \frac{n}{\bar{q}^2} \int_{-\infty}^{\infty} \frac{-1 + e^{(ik_1 - \alpha k^2)\xi}}{ik_1 - \alpha k^2} S_{q_i q_j}(\underline{k}) d\underline{k} \tag{2.66}$$

In the limit as $x \rightarrow \infty$ the exponential term in Eq. (2.66) can be neglected and thus leads to Gelhar and Axness' expression.

For flow in a stratified medium shown in Figure 2.8, where the aquifer exhibits perfect stratification (i.e. the hydraulic conductivity varies in only the z direction), the following relations can be obtained for the flow variables:

The displacement of a particle is

$$x = qt = \left(\frac{KJ}{n}\right)t \tag{2.67}$$

Assuming the porosity variations to be less than the hydraulic conductivity variations, the mean particle displacement is given by

$$\bar{x} = E[x] = \frac{Jt}{n} E[K] = \frac{\bar{q}}{n} t \tag{2.68}$$

And the variance of the displacement is given by

$$\sigma_x^2(z)=E\left[(x-X)^2\right]=\left(\frac{Jt}{n}\right)^2 E\left[\left(K-\overline{K}\right)^2\right]=\frac{\overline{x}^2}{\overline{K}^2}\sigma_K^2(z) \tag{2.69}$$

Also

$$\sigma_q^2(z)=\frac{\overline{q}^2}{\overline{K}^2}\sigma_K^2(z) \tag{2.70}$$

Dagan obtains Matheron and Marsily's asymptotic results by integrating Eq. **(2.56)** over distance to obtain

$$A_{ij}=\frac{n^2}{\overline{q}^2}\int_{-\infty}^{\infty}\frac{-1+e^{(ik_1-\alpha k^2)\overline{x}_1}}{ik_1-\alpha k^2}S_{q_iq_j}(\underline{k})d\underline{k} \tag{2.71}$$

Ignoring the odd terms Eq. (2.71) becomes

$$A_{ij}=\frac{n^2}{\overline{q}^2}\int_{-\infty}^{\infty}\frac{1-e^{-\alpha k^2\overline{x}_1}}{\alpha k^2}S_{q_iq_j}(\underline{k})d\underline{k} \tag{2.72}$$

For small travel times, the exponential in Eq. (2.72) can be expanded to obtain

$$A_{ij} \rightarrow \bar{x}_1 \int_{-\infty}^{\infty} S_{q_i q_j}(\underline{k})d\underline{k} = 2\bar{x}_1\sigma_q^2 = 2\frac{\sigma_K^2}{\bar{K}^2}\bar{q}^2 t \tag{2.73}$$

Eq. (2.73) is the well-known Taylor short-time limit in which the dispersivity grows linearly with time.

The asymptotic long time limit of Eq. (2.72) is obtained by letting $k \rightarrow 0$, i.e.

$$A_{ij} \rightarrow \frac{n^2}{\bar{q}^2}\int_{-\infty}^{\infty} \frac{S_{q_{11}}(0)\left(1-e^{-\alpha k^2 \bar{x}_1}\right)}{\alpha k^2}dk = \frac{n^2\sigma_K^2\lambda^2}{\alpha\bar{K}^2} = A_\infty \tag{2.74}$$

where λ is the correlation length of the hydraulic conductivity. Note that, because of the k^{-2} power in the integrand, the conductivity spectrum must be of the type

$$S_{KK} = \frac{8\sigma_K^2\lambda^5}{3\pi\left(1+\lambda^2k^2\right)^3}$$

if the macrodispersivity is to approach a constant for large mean displacement [Gelhar, 1993].

The asymptotic behavior for macrodispersivity has been explored by various researchers including Dagan [1984], Rajaram and Gelhar [1995], Neuman [1990],

Neuman and Zhang [1990], Ababou and Gelhar [1990], Zhan and Wheatcraft [1996], Glimm and Sharp [1991] and Glimm et al. [1993]. With slight variations in the spectrum of the hydraulic conductivity, all these researchers relied on the velocity spectrum of the linear perturbation theory and have arrived at similar conclusions; that at short travel times or distances, the longitudinal and transverse macrodispersivities are anisotropic and that this anisotropy is maintained at long travel distances. For example, Dagan found that for a medium with an exponential covariance function of log-conductivity, the following are the asymptotic results for the 2D case:

$$\text{(i)}\quad A_{11} \to \frac{3}{8}\sigma_F^2 \bar{q}^{-2} t; \qquad A_{22} \to \frac{1}{8}\sigma_F^2 \bar{q}^{-2} t \quad \text{for } t \ll 1$$

$$\text{(ii)}\quad A_{11} \to 2\sigma_F^2 \lambda \bar{q} t \left[1 - \frac{3\ln\left(t\bar{q}/\lambda\right)}{2\left(t\bar{q}/\lambda\right)}\right]$$

$$A_{22} \to \sigma_F^2 \lambda^2 \left[\ln\left(t\bar{q}/\lambda\right) + 0.933\right] \quad \text{for } t \gg 1$$

This display in anisotropy at both small travel times and distances between the longitudinal and transverse dispersivities is a marked feature resulting from the linearization of the zero divergence Darcy's law. The validity of these results will be determined when results for nonlinear solution of Darcy's equation are presented.

Plume-scale dependent macrodispersion

Rajaram and Gelhar (1993, 1995) obtained an expression for computing the ensemble average of the second moment Σ_{ij}. They used the so-called "two-particle" approach to derive a formula for Σ_{ij}, given by

$$A_{ij}^{r}(\underline{x}_1) = \frac{1}{2}\frac{d\Sigma_{ij}}{d\bar{x}_1} = \int_0^{\bar{x}_1}\int_{-\infty}^{\infty} e^{ik_1\xi}\left\{1-\tilde{F}\left(\underline{k},\bar{x}_1\right)\right\}S_{q_iq_j}(\underline{k})d\underline{k}d\xi \qquad (2.75)$$

where $\tilde{F}\left(\underline{k},\bar{x}_1\right)$ = Fourier transform of the ensemble average separation distribution function. Various expressions are given for $\tilde{F}$ in Rajaram (1992) for plumes with different configurations. For a plume with an initial Gaussian distribution $\tilde{F}\left(\underline{k},\bar{x}_1\right) = \exp\left(k_i k_j \Sigma_{ij}\right)$. The derivation of Eq. (2.75) is non-trivial and is presented in detail by Rajaram (1992) and involves the following steps:

1. The derivation begins with a definition of Σ_{ij}, which is then expressed in terms of the separation function $F(\underline{\rho},t) = \frac{n^2}{m^2}\int_{-\infty}^{\infty} C(\underline{x},t)C(\underline{x}+\underline{\rho})d\underline{x}$.
2. Results of the probability density of the separation distribution function of particles (from turbulent diffusion) are applied in relating the dispersion coefficient $D_{ij}(\underline{\rho},t)$ to the correlation function of the particle velocities.
3. The velocity correlation function is related to the velocity spectrum via the Fourier transform. Finally, the mean flow is assumed to be aligned in the x_1

direction so that mean velocities in the x_2 and x_3 directions are assumed to be zero. These assumptions are used in arriving at Eq. (2.75).

Eq. (2.75) represents a system of differential equations that must be solved numerically to determine the second moment tensor and consequently the relative macrodispersivity A_{ij}^r. The portion of the integrand in Eq. (2.75) in curly brackets is essentially a low wavenumber filter which is related to the size of the plume as reflected in the second moment term. At large times, as the plume becomes very large, the dispersivity approaches the ensemble result but when the plume is smaller, the relative dispersivity is reduced. Physically, A_{ij}^r represents the fact that, when the plume is small, it is dispersed by only the high frequencies or the high wavenumber fluctuations in the velocity field, but as the plume grows it is progressively dispersed by lower frequencies or wavenumber fluctuations.

Several researchers (Koch and Brady; 1988, Neuman, 1990; Glimm and Sharp, 1991; Kemblowski and Wen; 1993) have evaluated the ensemble macrodispersivities for fGn models and find that the macrodispersivity tends to grow as a power of the mean displacement. When the influence of the plume size is included Eq. (2.75) much smaller macrodispersivities are predicted and simple power law dependence on the displacement is not found (Rajaram and Gelhar, 1995). This result of Rajaram and Gelhar is confirmed in this thesis. However, there are significant differences in macrodispersive behavior when the velocity spectrum from the nonlinear theory in this thesis is compared to that of the linear theory.

Two-phase model

An approach that has been widely used to treat solute transport in heterogeneous porous media is one in which the medium is assumed to consist of different materials, or regions with drastically different velocities. It is then assumed that the convective transport in the low-velocity region is negligible, and that transfer of the solute between the immobile fluid region and the flowing fluid is via molecular diffusion. In this model, it is assumed that there are regions that are poorly connected to the main flow. However, the geometry of these regions is not specified. In this so-called "dead end pore" model (Coats and Smith, 1964) an attempt is made to account for the tailing or asymmetry observed in laboratory concentration profiles by modifying the ADE to include diffusion or mass transfer into stagnant volume. The rate mass increase is decomposed into two components to account for transfer in the mobile and immobile phases. If the ADE (Eq. (2.4)) is augmented by terms accounting for stagnant volume, the result is,

$$\text{(i)}\quad f\frac{\partial C}{\partial t}+(1-f)\frac{\partial C^*}{\partial t}=E\frac{\partial^2 C}{\partial x^2}-v\frac{\partial C}{\partial x}$$

and (2.76)

$$\text{(ii)}\quad (1\text{-}f)\frac{\partial C^*}{\partial t}=K\left(C-C^*\right)$$

where f is the fraction of pore space occupied by mobile fluid [L/L], C^* is the concentration in the stagnant fluid [M/L^3], and K is rate constant or first-order mass transfer coefficient [T^{-1}] and Eq. (2.76)ii presupposes a first-order mass transfer process. In Appendix C, Coats and Smith (1964) obtain the solution of Eq. 2.76

$$\frac{C}{C_o}=\frac{2e^J}{\pi}\int_0^{\infty}\frac{\exp\left(\frac{\gamma}{2}\left(1-\sqrt{\rho}\cos\left(\frac{\phi}{2}\right)\right)\right)}{a_1^2+a_2^2}\left[a_1\cos(ZJ-w)+a_2\sin(ZJ-w)\right]dZ \quad (2.77)$$

where

$J = I/f$ and I is the pore volumes injected, vt/L

$a = KL/v$ $\qquad Z=\frac{af}{1-f}(J-y)$

$\phi=\tan^{-1}(v/u)$

$$u=1+\frac{4}{\gamma}\left(1+\frac{ba+a(1+Z^2)}{(1+b)^2+Z^2}\right)$$

$$v=\frac{4Z}{\gamma}\left(1+\frac{ab}{(1+b)^2+Z^2}\right)$$

$\rho=\sqrt{u^2+v^2}$ $\qquad b=af/(1-f)$

$$a_1=1+\sqrt{\rho}\cos\frac{\phi}{2}-Z\sqrt{\rho}\sin\frac{\phi}{2}$$

$$a_2=Z\left(1+\sqrt{\rho}\cos\frac{\phi}{2}\right)+\sqrt{\rho}\sin\frac{\phi}{2}$$

$$w=\frac{\gamma}{2}\sqrt{\rho}\sin\frac{\phi}{2}$$

In laboratory experiments, where the configuration and properties of the immobile regions are constructed in a known fashion (Rao et al., 1980; Gillham et al., 1984), it has been confirmed that predictions from dual-media models fit the observed breakthrough curves. However, in field situations, the geometry and properties of the

immobile zones are not known, and there are no established procedures for determining these [Gelhar, 1993]. As a result, the additional parameters are usually extracted by curve fitting breakthrough curves. Such curve-fitting procedures are not desirable, especially in the case where, because of the similarity of the shapes of breakthrough curves produced by different conceptual models, one would question the uniqueness of such parameters [Gelhar, 1993]. The more fundamental difficulty with the dual-media model is the assumption that the velocity field can be approximated by the extreme condition assumed in these models: that is, a mobile region with a uniform velocity and an immobile region with zero velocity. Naturally occurring heterogeneous media are more likely to exhibit a wide range of fluid velocities. In that case, it is likely that diffusional transport will be overwhelmed by convective effects, so that the overall transport is no longer diffusionally controlled. Moreover, the two-phase model applies the Fickian assumption and does not account for the variation of the dispersion coefficient with scale. Hence, the two-phase model will be inappropriate for modeling transport in highly heterogeneous media. In spite of these criticisms of the dual-model, it offers insights into the physical mechanisms that may explain the tail behavior of the breakthrough curves.

Renormalization Group Methods for Obtaining Ensemble Macrodispersivity Expressions

Recently results from quantum mechanics have been applied in studying flow and transport in porous media (for example, Christakos, G. et al. 1995; Glimm, J. 1999 and Sposito G, 2001). The renormalization group method (RNG) was developed for dealing with problems in turbulence in fluids. The major difficulty is the simultaneous existence of many different space and time scales of equal importance at high Reynolds number. In broad terms, the RNG is a procedure for integrating small length scales which leads to divergent solutions, so that the remaining unknowns describe the large length scales of the system that lead to convergent solutions [Glimm, J. 1999].

Sposito [2001] applies a key result from quantum field theory (QFT), the Dyson equation, to derive the ensemble macrodispersivity in Eq. 2.55. He concludes that the sophisticated approach of the QFT does not provide any better results than can be obtained through the linear perturbation approach. Although the QFT can provide improved accuracy, this comes at a significant physical cost, which from Sposito's point of view is not justifiable.

Christakos et al. [1995] use the so-called diagrammatic approach to solve the stochastic flow equations. Instead of the symbols used in the flow equations, diagrams are used to represent terms. Christakos et al. show how this approach can be used to solve flow equations. In fact, a comparison of the solution obtained from the diagrammatic approach for the 1D case shows that it performs worse than the second-order perturbation result (see Figs. 2 and 3 in Christakos et al. 1995).

2.5 Fractals and Self-Similar Models

Over the past twenty years, there has been an increasing application of scale-invariant models to study the heterogeneity and flow through porous media. This discussion is prefaced with a review of self-similar models and how they differ from multifractal models. The classical notion of self-similarity for a random process X(t) in $\Re$ is that there exists a sequence of positive real numbers a_r such that, for any $r > 0$,

$$X(t) =^{d} a_r X(rt) \qquad t \in \Re \tag{2.78}$$

where $=^{d}$ denotes equality of all finite-dimensional distributions . Eq. (2.78) is a statement of invariance of X(t) under the group of positive affine transformations { $X \rightarrow a_r X$, $t \rightarrow rt$; $a_r > 0$ }. Since a_r satisfies $a_{r_1 r_2} = a_{r_1} a_{r_2}$ for any $r_1, r_2 > 0$ and $a_1 = 1$, a_r must have the form r^{-H} for some real H and Eq. (2.78) may be stated more explicitly as [Veneziano, 1999]

$$X(t) =^{d} r^{-H} X(rt), \qquad t \in \Re \tag{2.79}$$

Random processes that satisfy Eq. 2.79 are said to be self-similar (ss) or more specifically H-ss.

A process can have a weaker form of self-similarity when only its increments are self-similar. That is,

$$\left[X(t_1)-X(t_2)\right] \overset{d}{=} r^{-H}\left[X(rt_1)-X(rt_2)\right], \qquad t_1,\ t_2 \in \Re \tag{2.80}$$

for some real H and any $r > 0$.

One may further constrain the self-similar and self-similar increment processes in Eqs. (2.79) and (2.80) to have stationary increments. Such processes satisfy the condition

$$\left[X(t_0+\tau)-X(t_0)\right] \overset{d}{=} r^{-H}\left[X(t_0+r\tau)-X(t_0)\right] \tag{2.81}$$

for any given $t_0 \in \Re$ and $r > 0$ [Veneziano, 1999]. The types of invariance expressed by Eqs. (2.79), (2.80) and (2.81) are illustrated in Figure 2.9.

A multifractal process can be considered a more general form of a self-similar process and is obtained by replacing the deterministic scaling factors $a_r = r^{-H}$ in Eqs. (2.78) and (2.79) with real non-negative random variables A_r, independent of the process X(rt). Then Eq. (2.78) becomes

$$X(\underline{t}) \overset{d}{=} A_r \cdot X(r\underline{t}) \qquad t \in \Re^d \tag{2.82}$$

where $\cdot$ denotes the product of independent quantities and $=^d$ denotes equality of all finite-dimensional distributions.

The interest in and application of self-similar or fractal concepts in hydrology has been motivated by a desire to explain the behavior of increasing dispersivity with scale (see Fig. 1.1).

Philip (1986) applied Taylor's (1921) result for dispersion

$$D = \frac{1}{2}\frac{dM}{dt} = \frac{\bar{q}^2}{n^2}\int_0^t R_q(\tau)d\tau \qquad (2.83)$$

where R_q is the velocity correlation function. Philip suggested that a correlation function of the form

$$R_q(\tau) = \left(1+\frac{\tau}{T}\right)^{-1+\alpha} \qquad 0<\alpha<1 \qquad (2.84)$$

where T is a constant and represents the minimum time scale, will explain the scale dependent dispersivity in Fig. 1.1. Philip also suggested that any R_q with a similar power-law behavior at large time will yield an asymptotic power-law growth of the dispersion coefficient. This approach by Philip cannot be used to predict dispersivities because the velocity covariance function is not expressed as a function of the hydraulic conductivity field.

Neuman [1990] and Di Federico and Neuman [1998] used fractal models in explaining Figure 1.1. Neuman begins by modeling the log-conductivity field as a superposition of separate contributions of log-conductivity at different scales. So that

$$F^i(\underline{x}) = \sum_{j=0}^{i} F_j(\underline{x}) \tag{2.85}$$

where F^i is the log-conductivity at a particular resolution, and F_j are the log-conductivity contributions at resolutions finer than i. Each of the contributing log-conductivity fluctuations F_j has a distinct variance $\sigma^2_{F_j}$ and tensor of integral scales $\underline{L}_j$. Spatial increments of the contributions are mutually uncorrelated so that the semivariogram of $F^i(\underline{x})$, $\gamma^i_F(\underline{s})$ where $\underline{s}$ is a displacement vector, becomes simply the sum of semivariograms contributing by $F_j(\underline{x})$,

$$\gamma^i_F(\underline{s}) = \sum_{j=0}^{i} \gamma_{F_j}(\underline{s}) \tag{2.86}$$

If each distinct scale has an exponential covariance

$$R_F(\underline{x}) = \sigma^2_F \exp\left[-\left(\frac{x_1^2}{L_1^2} + \frac{x_2^2}{L_2^2} + \frac{x_3^2}{L_3^2}\right)\right] \tag{2.87}$$

where L_1, L_2 and L_3 are the integral scales in the principal directions of anisotropy x_1, x_2 and x_3, then the semivariogram that corresponds to Eq. (2.86) is

$$\gamma_F(s, L_v) = \sigma_F^2(L_v)\left[1-\exp\left(-\frac{s}{L_v}\right)\right] \tag{2.88}$$

where L_v is the directional integral scale and associated variance $\sigma_F^2(L_v)$. Integrating Eq. (2.88) over all possible integral scales L_v yields

$$\gamma_F(s) = \int_0^\infty \sigma_F^2(m)\left(1-e^{-ms}\right)dm \tag{2.89}$$

where m is defined as $m = \frac{1}{L_v}$ is a wave number representing the spatial frequency of log-conductivity fluctuations in the direction v. In the special case where

$$\sigma_F^2(m) = \frac{C}{m^{1+2\omega}} \qquad 0 < 2\omega < 1 \tag{2.90}$$

and C is a positive constant, then the integral in Eq. (2.89) becomes

$$\gamma_F(s) = C_0 s^{2\omega} \tag{2.91}$$

where C_0 and ω are positive constants. In other words, the semivariogram of log-conductivity grows as a power of the distance s. Next, Neuman relates Eq. (2.91) to the asymptotic values of macrodispersivity derived in Neuman and Zhang [1990] from the macrodispersivity expression, Eq. **(2.55)**. For long travel times Neuman and Zhang obtained

$$A_L(s) = c_0 s(t) \sigma_F^2 \tag{2.92}$$

where s(t) is the mean travel distance. Next Neuman relates Eq. (2.92) to results of the linear regression performed on the data in Figure 1.1. His fitted lines are shown in Figure 2.10 and he obtains a relation between macrodispersivity and travel distance of the form,

$$A_L = 0.0175 L_s^{1.5} \tag{2.93}$$

with a regression coefficient $R^2 = 0.74$ and 95% confidence intervals [0.0113, 0.0272] about the coefficient 0.0175 and [1.30, 1.61] about the exponent 1.5. Neuman explains Eq. **(2.1)** by relating σ_F^2 in Eq. (2.92) to Eq. (2.93). And further explains the dependence of σ_F^2 on travel distance L via the variogram in Eq. (2.91). The variance σ_F^2 is given by the semivariogram in Eq. (2.91). Finally Neuman obtains the ω as 0.75 and regards it as "universal."

Neuman's methodology and derivation suffers from a number of setbacks and is critiqued by Gelhar et al. [1993]. The highlights of the critique are:

1. Neuman's derivation depends heavily on the reliability of the data shown in Figure 1.1. Some of the data have been shown to be unreliable by Gelhar [1986]. Hence, a model derived a priori on assumptions of the reliability of the data leads one to question the correctness of the results.
2. Secondly, Neuman's notion of a universal model ignores the fact that different aquifers have degrees of heterogeneity at a given scale [Gelhar, 1993].
3. Neuman's results are based on an asymptotic approximation of the macrodispersivity equation **(2.55)**, which in a sense is equivalent to a linearization scheme. Hence may not apply to the small travel times or the intermediate range of travel.

Zhan and Wheatcraft [1996] represent the F = lnK as a fractional Brownian surface (fBs), so that increments of the F field have the form

$$E\left[\left(F(x_1)-F(x_2)\right)^2\right] \propto |x_2 - x_1|^{\alpha} \qquad 0 < \alpha < 2 \tag{2.94}$$

Moreover, F = lnK has a spectral density of the form

$$S_F(\underline{k}) = \frac{S_o}{k^{\beta}} \tag{2.95}$$

where S_o is a constant, $\beta = \alpha + D$, D is the space dimension, k is the magnitude of the wavenumber vector $\underline{k}$. Eq. (2.95) shows that as $k \to 0$, $S_F(\underline{k}) \to \infty$, so $k = 0$ is the singular point of the spectral density function. Since $k = \frac{2\pi}{l}$, where l is the wavelength or the scale of the medium, when $k \to 0$, $l \to \infty$ which implies that the porous medium is infinitely large. However, in nature, the aquifer boundaries will determine the limit of heterogeneity. Therefore, there is always a maximum l, L_{max} and thus a minimum wavenumber k_o. The introduction of L_{max} with no flow boundaries will introduce a low limit cutoff $k_o = \frac{2\pi}{L_{max}}$. The issue of incorporating finite-size effects of the flow domain in the spectrum of log-conductivity has been discussed by Ababou and Gelhär [1990]. In addition to the low wavenumber cutoff, they suggest a high wavenumber cutoff k_{max} that represents the spacing of conductivity measurements or the scale of conductivity measurements. Using the general result in Eq. **(2.55)** Zhan and Wheatcraft show that a spectrum of the type (Eq. (2.95)) leads to a scale-dependent ensemble macrodispersivity.

Rajaram and Gelhar (1995) also show that representing the log-conductivity field as fBs and using Eq. **(2.55)** leads a scale-dependent ensemble macrodispersivity. However, when the plume-scale dependent macrodispersion is computed with fBs representation of the log-conductivity field much smaller macrodispersivities are predicted and a simple power law dependence on displacement is not found.

Ababou and Gelhar [1990] obtained the 1D spectra of log-conductivity data obtained from the Mount Simon aquifer. The domain size was L_{max} = 303 ft and the measurement spacing L_{min} = 1 ft. The log-spectral density was plotted against log-frequency, and the spectrum of the log-conductivity was suggested to behave as Eq. (2.95). Ababou and Gelhar [1990] suggested the data to have $\beta = D$, and for their case D = 1. This spectrum where $\beta = D$ coincides with that of a field with a multifractal conductivity. However, a close examination of the spectra by Ababou and Gelhar [1990] indicates that the fitted slope of 1 is not necessarily accurate. In the low frequency range, the spectra exhibit a distinct curvature, and the high frequency range clearly departs from a slope of one. In fact, the slope of one fits a very small portion of the empirically obtained spectra. This lack of fit of the spectra with a slope of one has been commented on in a note by Tyler and Wheatcraft [1992]. Using this multifractal spectrum of the conductivity field and spectral density of the specific discharge from the linear theory in the ensemble macrodispersivity expression (Eq. **(2.55)**) Ababou and Gelhar obtain the following expression for the longitudinal macrodispersivity

$$A_{11} = \sigma_o^2 \left(L_{max} - L_{min} \right) \tag{2.96}$$

where σ_o^2 is the same as S_o in Eq. (2.95). Eq. (2.96) applies in the far-field and suggests that in the pre-asymptotic regime the macrodispersivity of a plume grows linearly with the size of the plume and should increase in time approximately as:

$$A_{11}(t) \simeq \sigma_o^2 L(t) \tag{2.97}$$

In fact, all the research work done in area of fractal representations of the conductivity field have closely followed the approaches discussed above. The work of Glimm and Sharp (1990) and Glimm et al. (1993) follow the same approach as that of Zhan and Wheatcraft and presenting the details will be redundant.

Questions about the validity of these fBs representations of the log-conductivity field remain. For example, Hewett (1986) analyzed a series of over 2100 values of porosity data from geophysical logs sampled at intervals of 0.16 meters. He found a β value of 2.72. However, it is difficult to judge the reliability of this value since no confidence interval was provided [Gelhar, 1993]. Moreover, these fractal models represent the hydraulic conductivity as nonstationary processes. The representation of conductivity fields as nonstationary processes contradicts the empirical findings of Hufschmied (1985) and Sudicky (1986) who found that hydraulic conductivity fields can be accurately modeled as stationary processes with a lognormal distribution.

This thesis models the hydraulic conductivity field as a stationary lognormal multifractal field. Instead of relying on spectra obtained through the linear perturbation approach, a new approach exploits the scaling properties of the hydraulic conductivity field to derive the distributions of the hydraulic gradient and specific discharge fields. The results will be compared with those of the linear theory in subsequent chapters.

2.6 Multifractal characterization of random resistor and random superconductor networks

The flow of a liquid through a field with a random hydraulic conductivity K distribution, to which a unit hydraulic gradient is applied in the main direction of flow is analogous to problem of defining the voltage distribution on an electrical network with random resistors to which a unit voltage drop is applied. If a unit voltage drop is applied across opposing faces of the network, the total current that will flow I_{tot} is analogous to the effective conductivity K_{eff}. I_{tot} is known as the conductance of the electrical network and this is analogous to the notion of K_{eff} in hydrology.

Several researchers [de Arcangelis et al., 1985; Amitrano et al., 1986; Bin Lin et al., 1991 and Bershadski. A, 1997] have studied the characterization of random resistor networks. These authors (with the exception of Bershadski, who simply presented a summarizing report) have studied the voltage distribution in a discrete cascade of electrical networks on a square lattice with random resistors to which a unit voltage is applied. The electrical network is visualized as a random resistor network on a square lattice of size L x L. Each bond in the network is either a conductor carrying a unit resistance with probability p or an insulator with probability 1 – p.

The moments of the voltage distribution $M(q)$ are given by [de Archangelis et al., 1986]

$$M(q) = \sum_{\text{all } V} n_V V^q \sim L^{-K(q)} \tag{2.98}$$

where $K(q)$ is the moment scaling function, n_V is the number of bonds with a voltage drop V. It is assumed that n_V and V have the following scaling properties

$$\begin{aligned} &(i)\ n_V = B(q)L^{f(q)} \\ &(ii)\ V(q) = A(q)L^{-\alpha(q)} \end{aligned} \tag{2.99}$$

where A and B are slowing varying functions of q. Substituting Eq. (2.99) into Eq. (2.98) and comparing the exponents of the left and right hand sides, one obtains

$$K(q) = q\alpha(q) - f(q) \tag{2.100}$$

Bin et al. (1991) extend the hierarchical model of Archangelis et al shown in Fig 2.11. This model has two key parameters: the number of horizontal bonds h_b and the number of vertical bonds v_b. This lattice is referred to as the (h_b, v_b) lattice. Fig. 2.11 shows an $(h_b, v_b) = (2,1)$ model. For a lattice with a unit potential applied across it, Bin et al. obtain the following results for the voltage distribution:

$$V(j) = \frac{1}{(2h_b + v_b)^N} h_b^j \quad j = 0, 1, ..., N \tag{2.101}$$

where j is the level to which the model has been developed. When j = 0 corresponds to the minimum voltage V_{min} and j = N corresponds to the maximum voltage V_{max}.

The number of bonds with voltage V is given by

$$n_{V(j)} = (h_b v_b)^N \left(\frac{2}{h_b v_b}\right)^j \binom{N}{j}, \quad j = 0, 1, ..., N \tag{2.102}$$

The moment $M(q)$ for the general (h_b, v_b) lattice is

$$M(q) = \left(\frac{2h_b^q + h_b v_b}{(2h_b + v_b)^q}\right)^N \tag{2.103}$$

And the moment scaling function is obtained as

$$K(q) = q - 1 + \left[k \ln\left(1 + \frac{v_b}{2h_b}\right) - \ln\left(1 + \frac{v_b}{2h_b^{q-1}}\right)\right] / \ln 2 \tag{2.104}$$

Using the formulation above, Bin et al. (1991) examine the scaling properties of a superconductor network, in which the configuration of the random resistor network is transposed so that the number of horizontal and vertical number of bonds in the random

resistor network is a transpose of the number of horizontal and vertical bonds in the superconductor network. This dual of the lattice (h_b, v_b), represented by $(h_b, v_b)'$ is shown in Fig.2.12. The random superconductor network in Fig. 2.12 has bonds of infinite conductivity with probability p_c^- (just below the percolation threshold) and unit conductance bonds with probability $1-p_c^-$ (Bin et al., 1991). The same boundary condition $\Delta V = 1$ is imposed across this network and because of duality, the voltage distribution on the dual (or transposed) lattice V_i' is equal to the current distribution $\hat{I}_i$ on the original lattice under the boundary condition $\hat{I}_{total} = 1$. The duality principle can be understood by considering the series and parallel resistor network in Fig. 2.13. If a voltage difference of V is applied across the resistors R_1 and R_2 in series, and the corresponding voltages across the resistors are V_1 and V_2, then from Ohm's law the following Eqs. hold for the series configuration

$$V = (R_1 + R_2)I \tag{2.105}$$

Also,

$$V_1 + V_2 = V \tag{2.106}$$

where $V_1 = R_1 I_1$ and $V_2 = I_2 R_2$, thus $I_1 = I_2 = I$. For the parallel configuration one obtains

$$I = I_1 + I_2 \tag{2.107}$$

Again applying Ohm's law, one obtains

$$\frac{V}{R}=\frac{V_1}{R_1}+\frac{V_2}{R_2}$$

where $V = V_1 = V_2$. Thus, the summation of voltages in series is replaced by summation of current in the parallel configuration. Also, the equality of currents in the series configuration is replaced by equality of voltages in the parallel configuration. This is a simplified explanation of duality. Bin et al. apply the duality principle for the transposed circuit configuration and obtain the following results for the current distribution

$$\hat{I}_i=\frac{v^i/(2v+h)^N}{v^N/(2v+h)^N}=v^{i-N} \qquad i=0,1,\ldots,N \tag{2.108}$$

where v and h are the vertical and horizontal number of nodes respectively. Also, the number of nodes with voltage V' in the transposed circuit n_{V_i} is the same as the number of nodes in the original circuit n_V, and the scaling moments of the current is obtained as

$$E\left[I^q\right]=G^{-q}\sum_V n_V V^q \tag{2.109}$$

where G is the total conductance of the circuit and is given by

$$G=\left(2+\frac{v}{h}\right)^{N} \tag{2.110}$$

Bin et al. point out that this duality representation may not be accurate because it contradicts prior results of Keller (1964) and Straley (1977), who found that for a random two-phase square lattice with conductance σ_1 and σ_2, the following relations hold:

$$G(p,\sigma_1;1-p,\sigma_2)G\left(p,\frac{1}{\sigma_1};1-p,\frac{1}{\sigma_2}\right)=1 \tag{2.111}$$

$$G(p,\sigma_1;1-p,\sigma_2)=(\sigma_1\sigma_2)G\left(p,\frac{1}{\sigma_2};1-p,\frac{1}{\sigma_1}\right) \tag{2.112}$$

where G is the total conductance of the system. Letting $p=p_c$, $\sigma_1=1$, and $\sigma_2=0$, then Eq. (2.109) represents a random resistor network of unit conductance bonds with probability p and zero conductance bonds with probability 1- p. Eq (2.112) relates the conductance in a random resistor network and the random superconductor network. However Eq. (2.110) contradicts the dual relationship calculated by Bin et al. Thus, a random resistor network modeled with a lattice of dimensions (h_b, v_b) may not give a good description of the random superconductor network modeled with $(h_b, v_b)^T$. Bin et al. argue that a dual lattice of the random superconductor network can be approximated by adjusting the values of h_b and v_b.

CHAPTER 3: MULTIFRACTAL SCALING OF HYDRAULIC CONDUCTIVITY

Introduction

Properties of multifractal measures are discussed in this chapter. Section 3.1 contains a review of multifractal theory. Section 3.1.1 presents a discussion on isotropic multifractal measures. These multifractal measures are generally scalars and do not contain the more general features of vectors which in addition to the scaling properties of their magnitudes possess scaling properties associated with their direction. Vectors that possess multifractal properties are presented in section 3.1.2. In addition to the distinction between scalars and vectors, multifractal measures can be grouped into conservative and non-conservative measures or described as a "bare" or "partially dressed measure". When a multiplicative process is terminated at a finite resolution r, the resulting measure $\underline{V}_r$ is called a "bare" measure. When the multiplicative process is continued to infinity, the limiting measure within a region S, $\underline{V}(S)$ is said to be "dressed" [Lovejoy and Schertzer, 1996]. A multifractal measure is said to be conservative if the bare mean $E[\underline{V}_r]$ is also the mean of the dressed measure $\underline{V} = \lim_{r\to\infty} \underline{V}_r$. In the non-conservative case, $E[\underline{V}_r]$ varies as a power function of r and either vanishes or diverges as $r \to \infty$. Properties of conservative and non-conservative measures as well as bare and dressed measures are presented in section 3.1.3. Bare measures

Section 3.2 presents empirical and theoretical justifications for modeling hydraulic conductivity fields as multifractals.

3.1 A review of multifractal theory for subsurface flow

There is a vast literature on the subject of multifractals. Multifractal phenomena were first explicitly found in the analysis of nonlinear dynamical systems (see for example Grassberger, 1983; Hentschel and Procacia, 1983) but had been used implicitly in the study of turbulent flows (Mandelbrot, 1974). Multifractals have been used in characterizing turbulent flows (see for example Frisch and Parisi, 1985; Jensen et al., 1985 and Meneveau and Sreenivasan, 1987). They have also been used in characterizing various geophysical phenomena such as rainfall (e.g. Schertzer and Lovejoy, 1987; Davis et al., 1994; Wilson et al., 1991), topography (e.g. Veneziano and Iacobellis, 2000) permeability (e.g. McCauley et al., 1990) and in the characterization of mineral deposits (e.g. Quiming, 1995). The notations and terminology used vary depending on the field of application. Hence this chapter provides a background on multifractal theory, and explains the symbols and concepts used in this thesis. Most of the properties mentioned here are in physical space. Properties in Fourier space are also presented.

All considerations are for a homogeneous vector field $\underline{V}$ in D-dimensional space. The number of components of $\underline{V}$ is not necessarily equal to the spatial dimension D; hence, the special case of one-component vectors corresponds to scalar fields such as the hydraulic conductivity K. Homogeneous multifractal fields do not have point values, i.e. at any given location $\underline{x}$ the value of $\underline{V}(\underline{x})$ is not defined. However, the measure $\underline{V}(S)$ of a region S of R^D is typically non-degenerate. This is why random measures $\underline{V}(S)$ rather than ordinary fields $\underline{V}(\underline{x})$ are considered.

A vector measure $\underline{V}(S)$ is said to be multifractal if it is statistically invariant under a group of random transformations of the space and the field $\underline{V}$ itself [Veneziano, 1999].

The simplest group of transformations, which is sufficient to describe the symmetries of the hydraulic conductivity model, is isotropic contraction of the support and multiplication of the measure by an independent random variable. Invariance under this group of transformations is called isotropic multifractality and is described shortly. Invariance under more complex space and field transformations is often referred to as generalized scale invariance (GSI; see Lovejoy and Schertzer, 1985, and Schertzer and Lovejoy, 1996) and is reviewed in section 3.1.2.

3.1.1 Isotropic Multifractality

A homogeneous random measure $\underline{V}(S)$ in R^D is isotropically multifractal if there exists a sequence of non-negative random variables $\{A_r, r \geq 1\}$ independent of $\underline{V}$ such that the measure density $\underline{v}(S) = \underline{V}(S)/|S|$ is statistically invariant under the scale transformations $\{\underline{x} \rightarrow \underline{x}/r, \underline{v} \rightarrow A_r\underline{v}\}$ i.e. if

$$\underline{v}(S) \stackrel{d}{=} A_r \underline{v}(rS) \qquad r \geq 1 \tag{3.1}$$

where $\stackrel{d}{=}$ denotes equality of all finite dimensional distributions [Veneziano, 1999]. If $\underline{V}$ has finite nonzero mean, then the expected measure density $E[\underline{v}(S)]$ is constant for all S and $E[A_r] = 1$. Eq. (3.1) relates the statistical properties of a larger region of the field to the properties of the field within a smaller region S. Thus, the field in the smaller region $\underline{v}(S)$ is obtained by isotropically contracting the field in the larger region $\underline{v}(rS)$ and

multiplying it by the non-negative random variable A_r. A field that satisfies Eq. (3.1) is also described as a contractive stochastic self-similar field (c-sss). The random variables A_r in Eq. 3.1 are defined only in terms of their marginal distributions [Veneziano, 1999] From repeated application of Eq. 3.1, first with $r = r_1$ and then with $r = r_2$, one finds that the variables A_r must satisfy the group property

$$A_{r_1 r_2} \overset{d}{=} A_{r_1} A_{r_2} \qquad \text{for any } r_1,\ r_2 \geq 1 \tag{3.2}$$

where the factors A_{r_1} and A_{r_2} on the right hand side are independent. Moreover, from Eq. (3.2), it must be $A_1 = 1$. In the special case when A_r is deterministic, Eq. (3.2) implies $A_r = r^{-H}$ for some real H and Eq. (3.1) becomes the classic condition of self-similarity. Eq. 3.2 is a fundamental consistency relation, with many implications on the random variables A_r and the field $\underline{V}$ (see Veneziano, 1999). Two of them are mentioned below:

1. Distribution of A_r: Eq. (3.2) implies that for any natural n, $\log(A_r)$ satisfies $\log(A_r) \overset{d}{=} \sum_{i=1,n} \log\left(A_{r^{1/n},i}\right)$ where the variables $A_{r^{1/n},i}$ are independent copies of $A_{r^{1/n}}$. Therefore, $\log(A_r)$ must have infinitely divisible distribution [Veneziano, 1999]. For example, the lognormal distribution is an admissible distribution for A_r.

2. Moment Scaling Function: It follows from Eq. (3.2) that the moments of A_r must scale with r as $E\left[A_r^s\right] = r^{W(s)}$ where W(s) is a convex moment scaling

function and is called the moment function $W(s) = \log_r \{E[A_r^s]\}$: see for example Kahane and Peyriere (1976), Schertzer and Lovejoy (1987), and Gupta and Waymire (1993). In the multifractal literature, the function W(s) is usually denoted by K(s). This notation is changed to avoid confusion with the hydraulic conductivity. The function W(s) is of great theoretical and practical importance, since it characterizes the distribution of A_r and hence the scaling properties of $\underline{V}$. Also, W(s) can be inferred from the moments of v(S), where v is the amplitude of $\underline{v}$, because from Eq. (3.1),

$$E[v^s(S)] = r^{W(s)} E[v^s(rS)] \tag{3.3}$$

The function W(s) can therefore be obtained as the slope of the plot of the $\log E[v^s(rS)]$ against $\log(r)$.

An important special case of Eq. (3.1) is when A_r has lognormal distribution. Since $E[A_r] = 1$, in the lognormal case $\ln(A_r)$ must have normal distribution with mean value $-C_K \ln(r)$ and variance $2C_K \ln(r)$, where $C_K = \frac{1}{2}\mathrm{Var}[\ln(A_e)]$ is a constant. The associated moment scaling function W(s) can be found from the moments of the lognormal distribution (see for example Johnson and Kotz, 1970, Chapter 14) and is given by

$$E\left[A_r^s\right] = \exp\left\{-sC_K \ln r + s^2 C_K \ln r\right\}$$

$$= \exp\left\{\ln r^{-sC_K} + \ln r^{s^2 C_K}\right\} = r^{C_K\left(s^2 - s\right)} = r^{W(s)}$$

so that

$$W(s) = C_K\left(s^2 - s\right) \tag{3.4}$$

This lognormal multifractal is used in section 3.2 to represent the hydraulic conductivity field.

If $\bar{v}(S)$ denotes the average measure density of $v(S)$, then $\bar{v}(S)$ has the following Fourier representation

$$\bar{v}(S) = \frac{1}{|S|}\int_{\mathbb{R}^D} \hat{I}_S(\underline{k})\hat{v}(d\underline{k}) \tag{3.5}$$

where $|S|$ is the volume of S, $\hat{I}_S(\underline{k})$ is the D-dimensional Fourier transform of the indicator function S, and $\hat{v}(d\underline{k})$ is a complex measure in Fourier space. Properties of $\hat{v}(d\underline{k})$ are given in Yaglom (1986). Since $\hat{I}_{rS}(\underline{k}) = r^D \hat{I}_S(r\underline{k})$ and the volume of rS is $r^D|S|$, substitution of Eq. (3.5) into Eq. (3.1), a condition satisfied by $\bar{v}(S)$ gives

$$\frac{1}{|S|}\int_{\mathbb{R}^D}\hat{I}_S(\underline{k})\hat{v}(d\underline{k})\overset{d}{=}r^D\frac{1}{r^D|S|}A_r\int_{\mathbb{R}^D}\hat{I}_S(r\underline{k})\hat{v}(d\underline{k})$$
$$\overset{d}{=}A_r\int_{\mathbb{R}^D}\hat{I}_S(\underline{k}')\hat{v}(d\underline{k}'/r) \tag{3.6}$$

where $\underline{k}'=r^D\underline{k}$. Eq. (3.6) holds for any S, hence the spectral measure $\hat{v}(d\underline{k})$ must satisfy

$$\hat{v}(d\underline{k})\overset{d}{=}A_r\hat{v}(d\underline{k}/r)\qquad r\geq 1 \tag{3.7}$$

Eq. (3.7) is dual property in Fourier space of the renormalization property in Eq. (3.1) [Veneziano, 1999]. There are two main differences between Eqs. (3.1) and (3.7):

1. $\bar{v}$ is multifractal under contraction, whereas $\hat{v}$ is multifractal under dilation.
2. v is homogeneous, while $\hat{v}$ is non-homogeneous.

Suppose the spectral density $S_v(\underline{k})=\frac{E\left[\left|\hat{v}(d\underline{k})\right|^2\right]}{d\underline{k}}$ exists. Then from Eq. (3.7)

$$S_v(\underline{k})=r^{-D}E\left[A_r^2\right]S_v(\underline{k}/r) \tag{3.8}$$

Substituting $E\left[A_r^2\right]=r^{W(2)}$ into Eq. (3.8) produces

$$S_v(\underline{k})=r^{-D+W(2)}S_v(\underline{k}/r) \tag{3.9}$$

Replacing $\frac{1}{r} = r'$, $0 < r' < 1$ and in Eq. (3.9), one obtains

$$S_v(r\underline{k}) = r^{-D+W(2)} S_v(\underline{k}) \tag{3.10}$$

In the lognormal case, $W(2) = 2C_K = \mathrm{Var}\left[\log_r(A_r)\right]$.

To determine the spectral density of lnv, the wavenumber components outside the range $k_o \le |\underline{k}| \le rk_o$ are eliminated, so that a field with point values $v_r(\underline{x})$ is obtained. The average value of $v_r(\underline{x})$ in a region S is denoted by $\bar{v}_r(\underline{x})$.

Suppose now that $\bar{v}(S) = \lim_{r\to\infty} \bar{v}_r(S)$ satisfies Eq. 3.1, then at least for large r_1 and any $r \ge 1$,

$$v_{r_1}(\underline{x}) \overset{d}{=} A_r v_{r_1}(r\underline{x}) \tag{3.11}$$

or taking the logs of both sides of Eq. (3.11) gives

$$\ln\left(v_{r_1}(\underline{x})\right) \overset{d}{=} \ln(A_r) + \ln\left(v_{r_1}(r\underline{x})\right) \tag{3.12}$$

It follows that the spectral densities of $\ln(v_{r_j})$ and $\ln(v_{r_i})$ must satisfy $S_{\ln(v_{r_j})}(\underline{k}) = r^D S_{\ln(v_{r_i})}(\underline{k}/r)$. If as $j \to \infty$, the $S_{\ln(v_r)}$ converges to a finite limit $S_{\ln(v)}$, then this implies

$$S_{\ln(v)}(\underline{k}) \propto k^{-D} \tag{3.13}$$

which can also be written as

$$S_{\ln(v)}(r\underline{k}) = r^{-D} S_{\ln(v)}(\underline{k}) \tag{3.14}$$

In the isotropic case, Eq. (3.13) gives

$$S_{\ln(v)}(\underline{k}) = ck^{-D} \tag{3.15}$$

for some c and $k = |\underline{k}|$. Since A_r and $v_{r_i}(r\underline{x})$ are independent, then from Eq. (3.12),

$$\mathrm{Var}\left[\ln\left(v_{r_j}(\underline{x})\right)\right] = \mathrm{Var}\left[\ln(A_r)\right] + \mathrm{Var}\left[\ln\left(v_{r_i}(r\underline{x})\right)\right] \tag{3.16}$$

The spectral density of v_{r_i} is the same as $S_{\ln(v)}$ in Eq. (3.15) in the interval $k_o \le k \le r_1 k_o$ and is zero otherwise. Therefore using Eq. (3.16),

$$\begin{aligned}\mathrm{Var}\left[\ln(A_r)\right] &= \mathrm{Var}\left[\ln\left(v_{m_1}(\underline{x})\right)\right] - \mathrm{Var}\left[\ln\left(v_{r_1}(r\underline{x})\right)\right] \\ &= c\int_{r_1 k_o \le k \le m_1 k_o} k^{-D}\,d\underline{k} \\ &= cS_D \ln(r)\end{aligned} \tag{3.17}$$

where S_D is the surface area of the unit ball in $\mathbb{R}^D$, hence $S_1 = 2$, $S_2 = 2\pi$, $S_3 = 4\pi$. From Eq. (3.17) $c = \dfrac{1}{S_D}\dfrac{\mathrm{Var}\left[\ln(A_r)\right]}{\ln(r)}$. From the review of multifractal fields above, $\dfrac{\mathrm{Var}\left[\ln(A_r)\right]}{\ln(r)} = \mathrm{Var}\left[\ln(A_e)\right]$ is independent of r. Moreover, for A_e lognormal with mean value 1, $\mathrm{Var}\left[\ln(A_e)\right] = \ln E\left[A_e^2\right] = W(2) = 2C_K$. Hence $c = 2C_K/S_D$ and Eq. (3.15) becomes

$$S_{\ln(v)}(\underline{k}) = \frac{2C_K}{S_D}k^{-D} \tag{3.18}$$

3.1.2 **Generalized Multifractality (Generalized Scale Invariance GSI)**

Lovejoy and Schertzer(1985) have extended the notions of scale invariance under isotropic contractions/dilations to include scale invariant transformations of a more general type $\{\underline{x} \to T_{sr}\underline{x},\ \underline{v} \to T_{fr}\underline{v}\}$ where T_{sr} and T_{fr} are the space and field scale-change

operators respectively indexed by the scale change factor r. T_{sr} and T_{fr} can be linear or nonlinear, deterministic or stochastic. Lovejoy and Schertzer call this extended property generalized scale invariance or GSI. In the discussion that follows the space and field subscripts (s and f) will be ignored and the transformation will only be indexed by r.

GSI requires both T_r and a unit scale to be defined, as well as a definition of how the unit scale can be measured. For simplicity, Lovejoy and Schertzer define the unit scale as a unit ball B_1 that defines all the unit vectors. The unit ball is defined implicitly as

$$\begin{aligned} B_1 &= \{\underline{x} : f_1(\underline{x}) < 1\} \\ \partial B_1 &= \{\underline{x} : f_1(\underline{x}) < 1\} \end{aligned} \tag{3.19}$$

where $\{\underline{x} : \text{condition}\}$ denotes the set $\underline{x}$ for which the condition is true, f_1 is a function of position, and ∂B_1 is the so-called "frontier" of the unit ball. The transformations are considered for closed balls. By denoting points in $\mathbb{R}^D$ by $\underline{x} = (x_1, x_2, ..., x_n)$ and $\underline{y} = (y_1, y_2, ..., y_n)$, the closed ball of center $\underline{x}$ and radius r is defined by

$$B_r(\underline{x}) = \{\underline{y} : |\underline{y} - \underline{x}| \le r\} \tag{3.20}$$

Thus, the closed ball contains its bounding sphere. In $\mathbb{R}^2$ a ball B_1 is a disc and in $\mathbb{R}^1$ a ball is an interval [Falconer, 1995].

T_r transforms the scale of a vector by a scale ratio r, and has the following properties. If and only if $r_1 r_2 = r$, then

$$B_r = T_{r_1} B_{r_2} = T_{r_2} B_{r_1} \tag{3.21}$$

Hence T_r has the group properties

$$\begin{aligned} & T_{r_1} T_{r_2} B_{r_1} = B_r = T_{r_1} T_{r_2} B_{r_1} \\ & \Rightarrow T_r = r^{-\underline{G}} \end{aligned} \tag{3.22}$$

where the matrix $\underline{G}$ is called the generator of the group. The negative sign shows reductions by a factor r. The inverse operator (which will be magnifications by a factor r) $T_r^{-1} = T_{r^{-1}}$ only exists when $\underline{G}$ is a matrix [Lovejoy and Schertzer, 1985]. When $\underline{G}$ is an nxn matrix and $\underline{x}$ is an n-dimensional vector, then

$$r^{-\underline{G}} = \exp\left(-\underline{G}\ln(r)\right) = 1 - \underline{G}\ln(r) + \frac{1}{2}\underline{G}^2 \ln^2(r) - \ldots = \sum_{i=0,\infty} (\ln r)^i \frac{\underline{G}^i}{i!} \tag{3.23}$$

and the GSI is described as linear. Moreover, the eigenvalues of $\underline{G}$ must have positive real parts [Lovejoy and Schertzer, 1985]. An ordinary process $v(S)$ in $\mathbb{R}^D$ with the property that

$$v(S) \overset{d}{=} A_r . v\left(e^{\underline{G}\ln r} S\right) \tag{3.24}$$

is said to be $(\underline{G}, A_e)$ stochastically self-similar. Specifically, for any $r \geq 1$, the process is said to be $(\underline{G}, A_e)$ contractive stochastically self-similar process (c-sss). And for $0 < r \leq 1$ the process is described as $(\underline{G}, A_e)$ dilative stochastically self-similar (d-sss) [Veneziano, 1999]. When the matrix $\underline{G}$ is an identity or unit matrix so that $\underline{G} = \underline{I}$, then $\exp\{\underline{I} \ln r\} = r\underline{I}$ and for any $\underline{G}$, Veneziano (1999) proves that there is a one-to-one correspondence between $(\underline{G}, A_e)$-sss and $(\underline{I}, A_e)$-sss processes. This result is very important because it allows one to extend the characterizations of isotropic stochastic self-similar processes in Sec. 3.1.1 to the GSI case.

Nonlinear and Random GSI

When $\underline{G}$ is a nonlinear function and no longer a matrix, the GSI process is described as nonlinear [Lovejoy and Schertzer, 1985]. Similarly, when $\underline{G}$ is random, the GSI process corresponds to a stochastic one. When the GSI is nonlinear, T_r must be transformed into a differential equation before a solution for T_r can be obtained. $T_r = r^{-\underline{G}}$ is written as:

$$\frac{dT_u}{du} = -\underline{G}T_u \tag{3.25}$$

where $u = \ln(r)$. Indexing with u rather than r, and using $T_{u+du} = T_u T_{du}$, $T_{du} = T_{u+du} T_{-u}$ and $T_0 = 1$, Lovejoy and Schertzer obtain:

$$T_{u+du} = T_u + T_{du} \Rightarrow T_{du} = 1 - Gdu,$$
$$\underline{x}_u + d\underline{x}_u = (1 - Gdu)\underline{x}_u \tag{3.26}$$

so that the coefficient $1 - \underline{G}du = 1 + \frac{dT_u}{T_u}$ increases the logarithm of the scale of a vector by the constant amount du independent of the scale of the vector. In other words, if the vector is at scale λ, it is increased by the factor $1 + \frac{d\lambda}{\lambda}$.

In this thesis, we are interested in linear GSI processes. Specifically we are interested in the special case of GSI in which the space and field scale-change operators T_{sr} and T_{fr} respectively satisfy

$$T_{sr}\underline{x} = \frac{1}{r}\underline{R}_r\underline{x}$$
$$T_{fr}\underline{v} = A_r\underline{R}_r\underline{v} \tag{3.27}$$

where $r \geq 1$ is the space-contraction factor, A_r is a random scaling factor for the field $\underline{V}$, $\underline{R}_r$ is a random orthogonal (rotation) matrix, and A_r and $\underline{R}_r$ are independent. Notice that the transformations in Eq. (3.27) rotate the space and field by the same amounts and contract the space isotropically. Although GSI further allows differential rotation between the space and field and different scaling along various directions (affinity transformations), these features are not needed to describe the multifractality of the

vector fields ∇H and $\underline{q}$. Under Eq. (3.27), the measure density $\underline{v}$ and its amplitude v have the following statistical invariance properties:

$$\begin{aligned} &\text{(i)} \quad \underline{v}(S) \overset{d}{=} A_r \underline{R}_r \underline{v}\left(\underline{R}_r^T(rS)\right) \\ &\text{(ii)} \quad \underline{v}(S) \overset{d}{=} A_r v\left(\underline{R}_r^T(rS)\right) \end{aligned} \tag{3.28}$$

where $\underline{R}_r^T(rS) = \left\{\underline{x} : \frac{1}{r}\underline{R}_r \underline{x} \in S\right\}$ is a randomly rotated and scaled version of S. In the case without rotation, $\underline{R}_r = \underline{I}$ and Eq. (3.28) reduces to the isotropic multifractality condition in Eq. (3.1). If $\underline{V}$ has a nonzero mean, then $E[\underline{v}(S)]$ is constant independent of S and Eq. (3.28)i reduces to the isotropic multifractality condition in Eq. (3.1) and $E[\underline{v}(S)]$ is constant independent of S and Eq. (3.28) gives

$$E[A_r \underline{R}_r] = E[A_r]E[\underline{R}_r] = \underline{I} \tag{3.29}$$

In the general case with nonzero rotation $(\underline{R}_r \neq \underline{I})$, Eq. (3.29) implies $E[A_r] > 1$; hence in this case the expected value of v(S) in Eq. (3.28) changes with the size of S.

3.1.3 Bare/dressed and Conservative/non-conservative Measures

This review of multifractal measures is concluded by mentioning the notions of bare/dressed and conservative/non-conservative measures. Homogeneous multifractal measures are generally the result of multiplicative cascade process in which independent rescaled copies of a non-negative homogeneous random field are multiplied; see for example Kahane and Peyriere (1976), Schertzer and Lovejoy (1987), Mandelbrot (1989), and Gupta and Waymire (1993).

When the multiplicative process is terminated at a finite resolution r, the resulting measure $\underline{V}_r$ is sometimes called the "bare" measure at resolution r. When the multiplicative process is continued to infinity, the limiting measure $\underline{V}(S)$ is said to be "dressed"; see for example Schertzer and Lovejoy (1996). A multifractal measure is said to be conservative if the bare mean $E[\underline{V}_r]$ is also the mean value of the dressed measure $\underline{V} = \lim_{r\to\infty} \underline{V}_r$. In the non-conservative case, $E[\underline{V}_r]$ varies as a power function of r and either vanishes or diverges as $r \to \infty$. In the previous review of multifractal theory, we have assumed that the dressed measure $\underline{V}$ has finite nonzero mean. Therefore, the above holds for conservative measures. In the analysis of flow through media with multifractal hydraulic conductivity, we find that the hydraulic gradient ∇H is a conservative field, but the specific discharge $\underline{q}$ is not. This means that for the hydraulic gradient field ∇H, the condition in Eq. 3.32 $E[A_r \underline{R}_r] = I$ is satisfied, whereas for the specific discharge field Eq. 3.32 becomes $E[A_r \underline{R}_r] = r^{-c} \underline{I}$, where c is a positive constant. Thus as resolution to which the flow field is developed r tends to infinity, the mean of the

specific discharge will vanish. In contrast, the mean of the hydraulic gradient field remains constant regardless of the resolution to which the flow field is developed.

It is worth noting that in the non-conservative case, one needs to work with finite-resolution measures like $\underline{V}_r$ rather than the fully developed measure $\underline{V}$, since the latter either diverges or vanishes with probability 1. In practice, this degeneracy is of no great concern since physical processes always have a small-scale cutoff, i.e. they are always of the $\underline{V}_r$ type.

3.2 Multifractal Measures – Empirical Evidence

In this section we present an analysis of hydraulic conductivity data K originally presented by Ababou and Gelhar (1990) and Goggin et al.(1988). The purpose of the analysis is to show that in some cases one can reasonably model the K field as a multifractal.

The hydraulic conductivity data K by Ababou and Gelhar (1990) was obtained from vertical boreholes in the sandstone formation of Mount Simon aquifer in Illinois One-dimensional spectra of the log-conductivity F = lnK reproduced from Ababou and Gelhar (1990) for the three vertical boreholes are shown in Figs. 3.1a, 3.1b and 3.1c. The log spectral density is plotted against log frequency. In each of the figures, a straight line line with a self-similar spectrum of the form:

$$S_{ff}(\underline{k}) = \frac{S_o}{k^{\alpha}} \tag{3.30}$$

where $\alpha = 1$ and S_o is the vertical axis intercept is superimposed on the spectral plots. The solid lines in the figures represent the computed spectra of the F = lnK data and the dashed lines represent the 80% confidence interval of the computed spectra. The spectral curves seem to deviate from the $\alpha = 1$ at both the low and high frequencies. For example between frequencies of 0.02 and 0.15 in Fig. 3.1a, the spectral curve has a slope of 0.22 and between frequencies of 0.2 – 0.6 has a slope of 0.28. For Fig. 3.1b the spectral curve between frequencies of 0.03 – 0.15 has a slope of 0.7 and has a zero slope in the high frequency range of 0.2 – 0.5. For the spectral plot in Fig. 3.1c, the low frequency range of 0.05 – 0.15 has a slope of 0.97 while the high frequency range of 0.15 – 0.5 has a slope of 0.15.

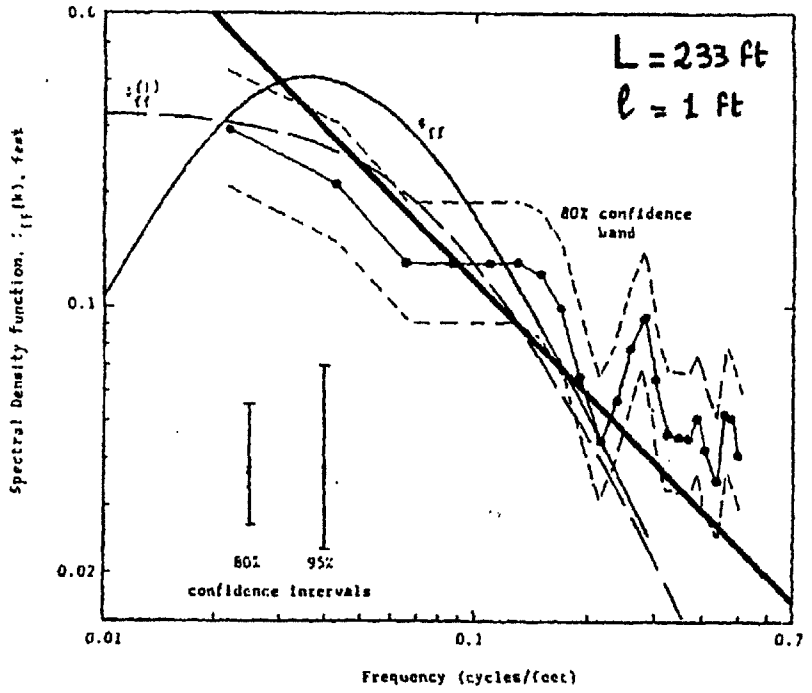

Figure 3.1a - Measured one-dimensional spectrum of log-conductivity at a borehole (circles) in the Mount Simon aquifer, from Bakr (1976). The straight line corresponds to a self-similar spectrum with exponent $\alpha = 1$.

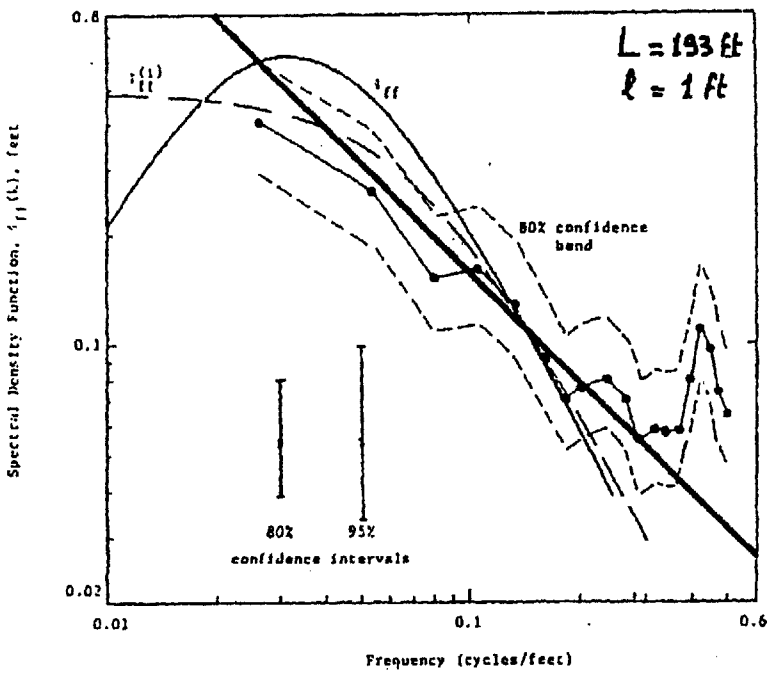

Figure 3.1b – Same as Figure 3.1a for another set of data. The straight line corresponds to a self-similar spectrum with exponent $\alpha = 1$.

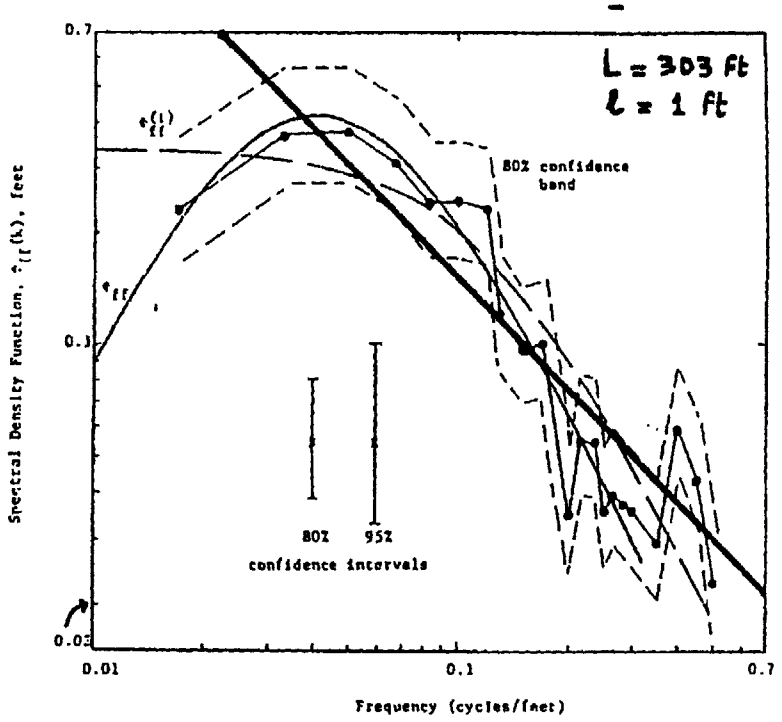

Figure 3.1c – Same as Figures 3.1a and 3.1b for another set of data. The straight line corresponds to a self-similar spectrum with exponent $\alpha = 1$.

The hydraulic conductivity data K by Goggin (1988) is shown in Fig. 3.2. The K data was obtained from an eolian sandstone deposit in northern Arizona with an air minipermeameter. The data in Fig. 3.2 are measurements from two vertical transects obtained at intervals of 0.0125m and labeled Trans1 and Trans2. The data was collected along the vertical transects because it was assumed that variation of the K data in the horizontal direction was insignificant compared to the variance of K in the vertical direction. Boufadel et al. (2000) presented an analysis of this data. The goal of their analysis was to show that the K field could be adequately modeled with a log-levy distribution. They used a double trace method (DTM) to calculate the scaling exponents of the K field can be modeled as a log-levy distribution and that K is non-Gaussian.

In contrast to the analysis of Boufadel et al. (2000), the present analysis is performed on F = lnK instead of K. Moreover, instead of DTM, the spectrum of F = lnK is computed to determine the range of possible exponents α from Eq. 3.30 that can be used to model the data. One can observe from the hydraulic conductivity in Fig. 3.2 that there are some impermeable regions that are clay lenses. Because of the presence of these impermeable regions, one cannot plot the F =lnK profile for Trans1 and Trans2. Consequently, the spectra are computed for various sections of the transects. The spectral plots for Trans1 and Trans2 are shown in Figs. 3.3 and 3.4 respectively. The slopes of the log spectral density versus the log frequency for spectral plots are reported in Table 3.1. The slopes of the spectral curves were obtained by performing a linear regression of the log spectral density versus log frequency. The regression lines are superimposed on the wavy spectral plots.

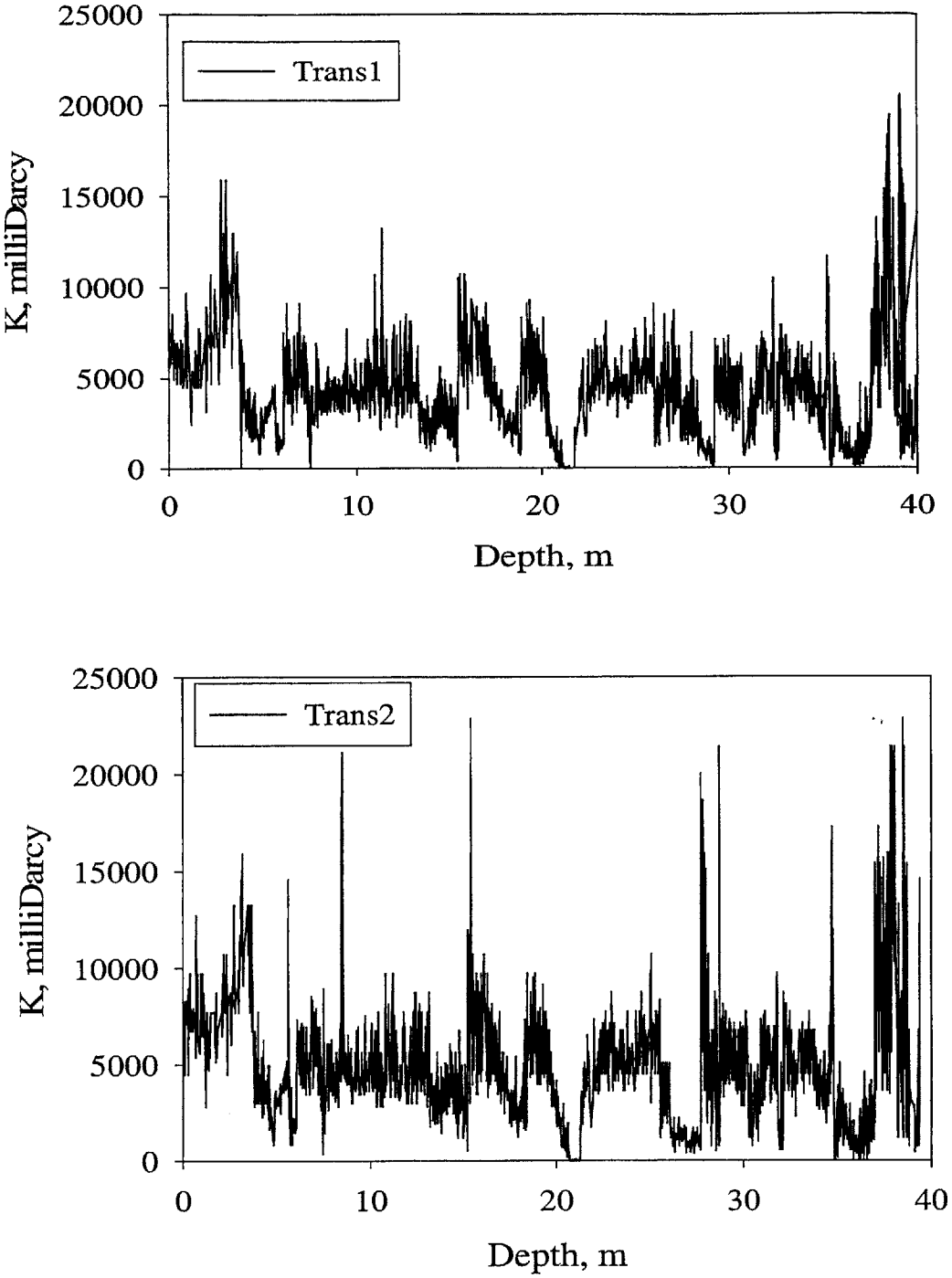

Figure 3.2 – Profiles of hydraulic conductivity data obtained from vertical boreholes in an eolian sandstone formation in Arizona (from Goggin, 1988).

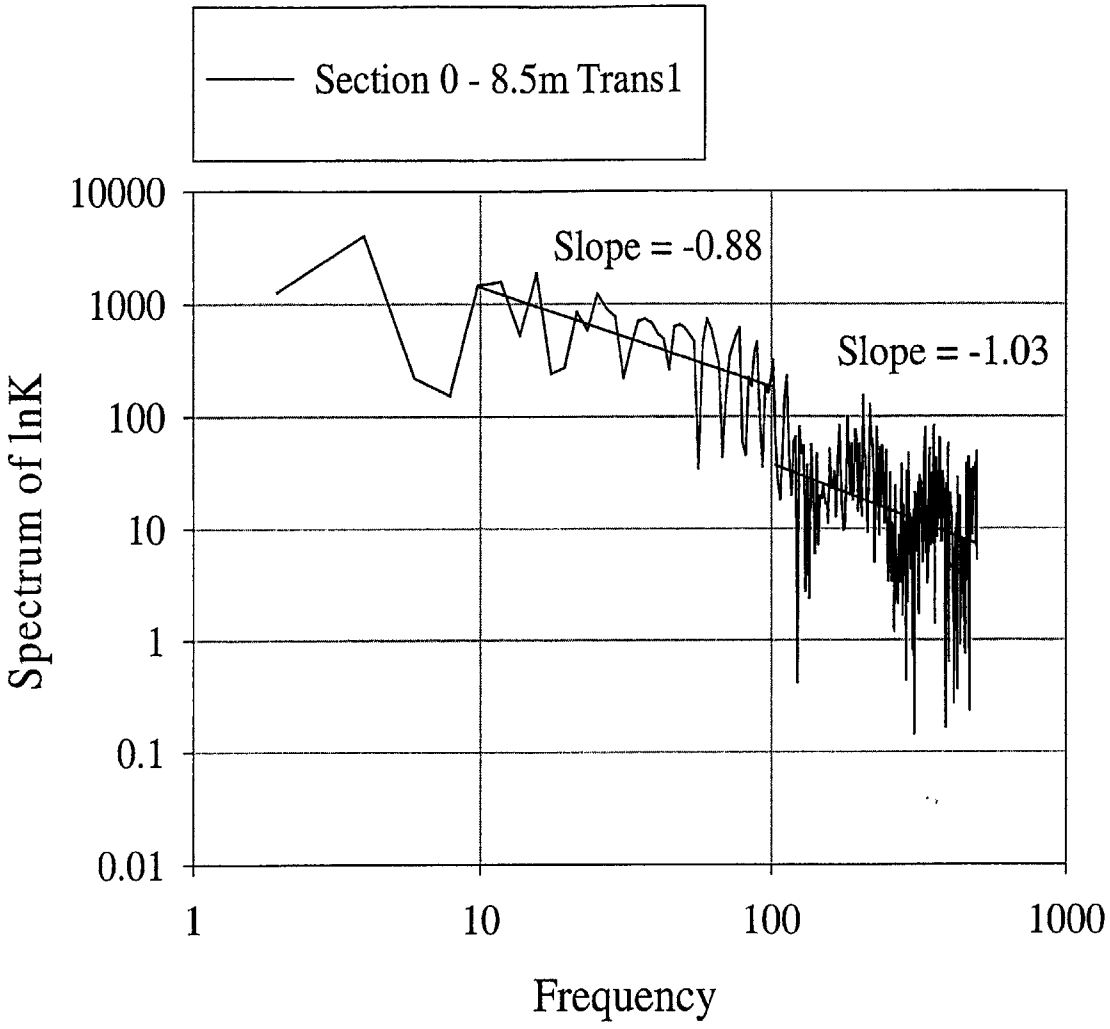

Figure 3.3a – One-dimensional spectral density of measured log-conductivity for the vertical transect (Trans1) for section 0 – 8.5m (from Goggin, 1988)

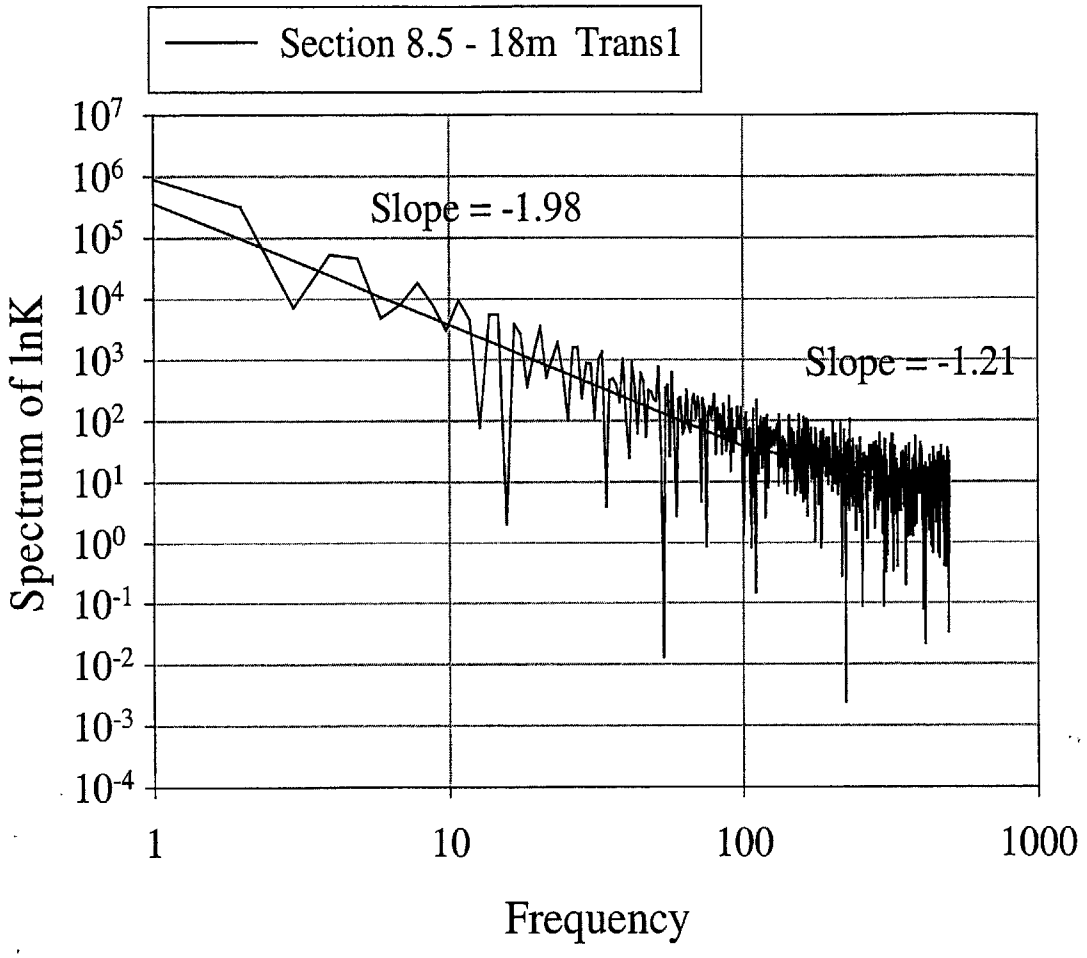

Figure 3.3b – One-dimensional spectral density of measured log-conductivity for the vertical transect (Trans1) for section 8.5 – 18 m (from Goggin, 1988)

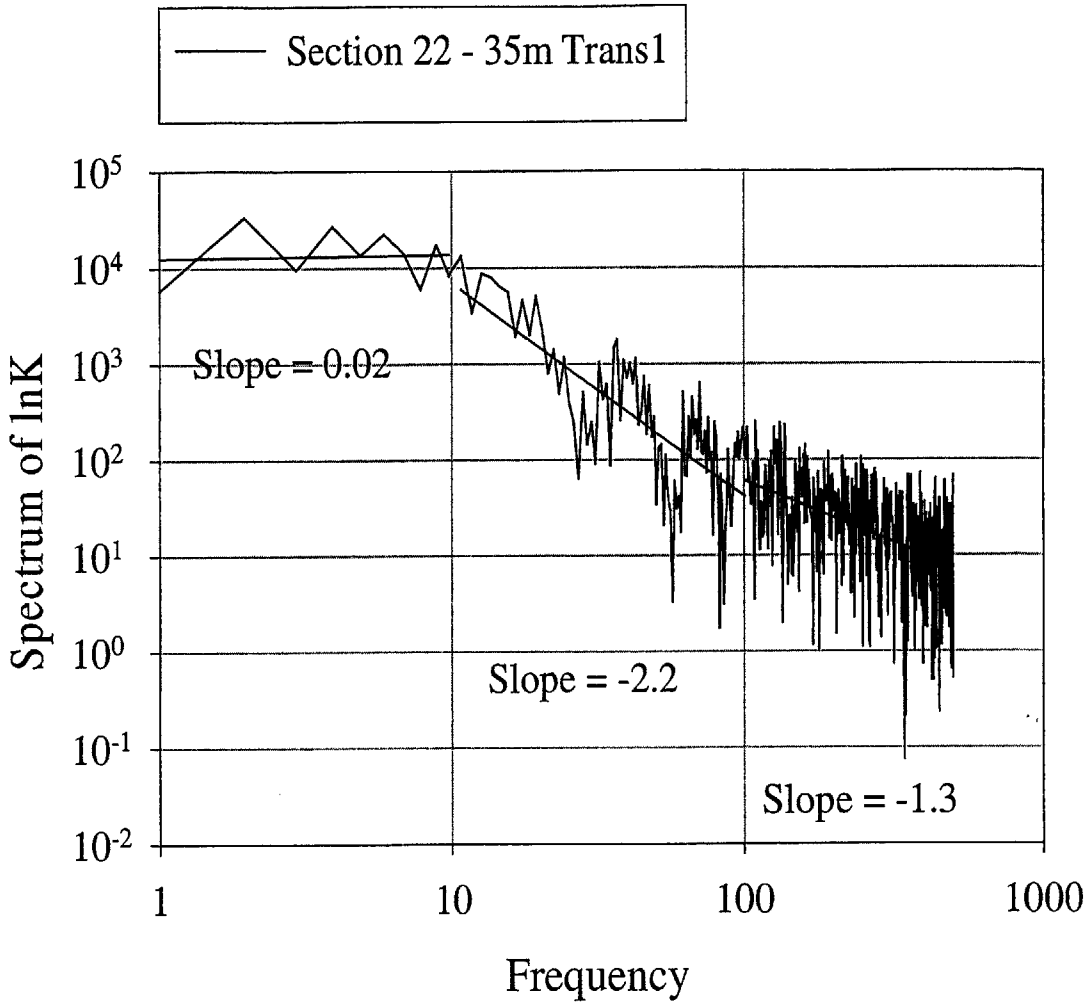

Figure 3.3c – One-dimensional spectral density of measured log-conductivity for the vertical transect (Trans1) for section 22 – 35m (from Goggin, 1988)

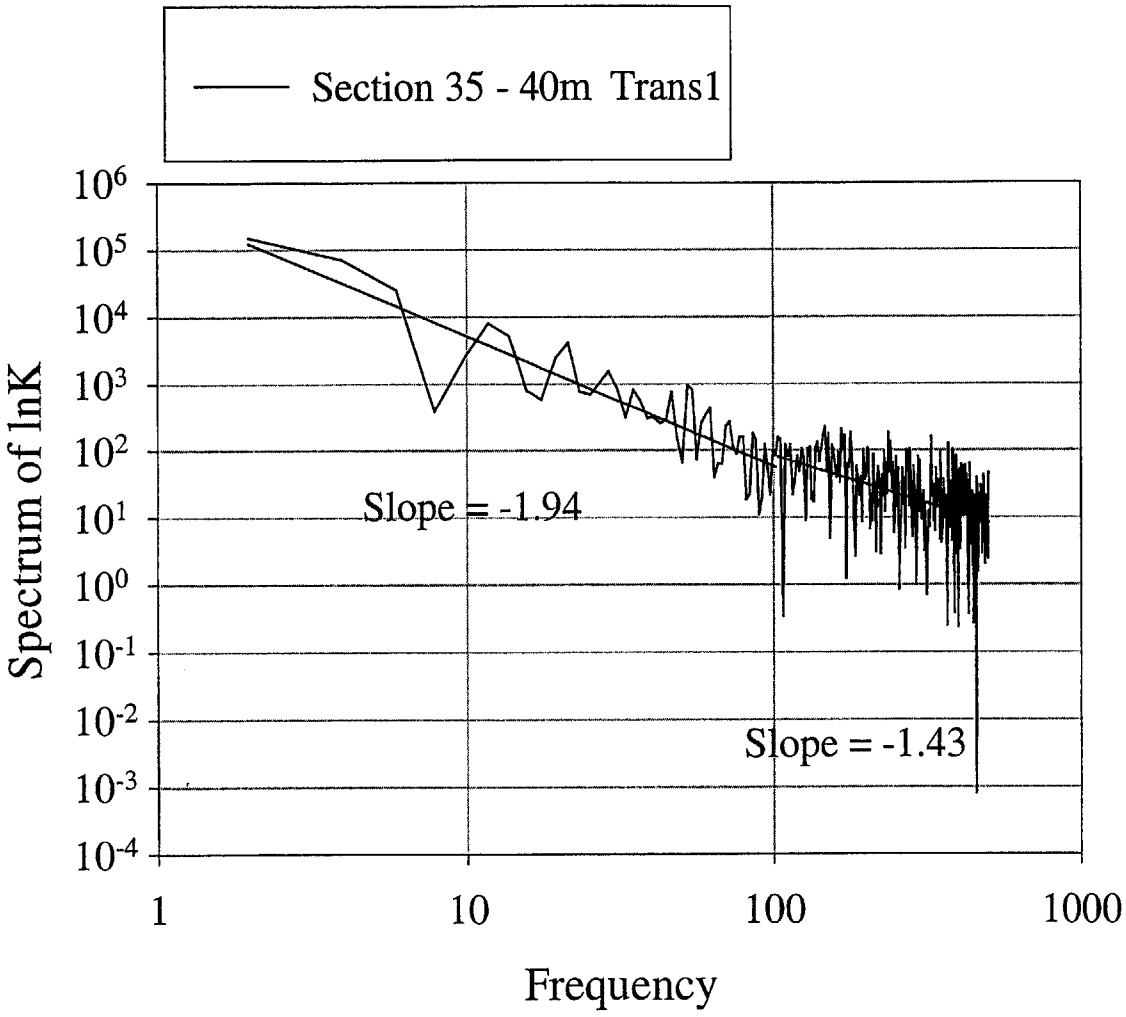

Figure 3.3d – One-dimensional spectral density of measured log-conductivity for the vertical transect (Trans1) for section 35 – 40m (from Goggin, 1988)

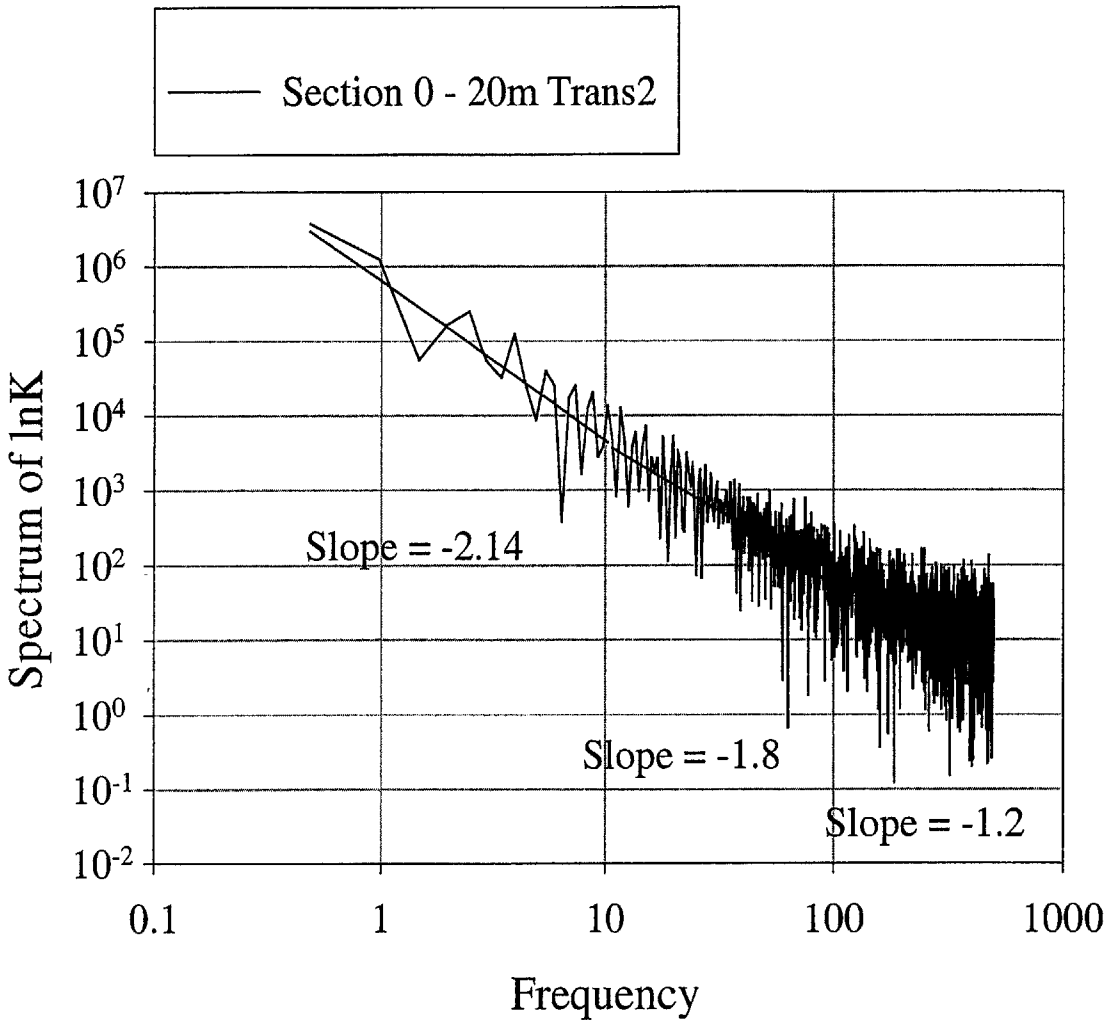

Figure 3.4a – One-dimensional spectral density of measured log-conductivity for the vertical transect (Trans2) for section 0 – 20m (from Goggin, 1988)

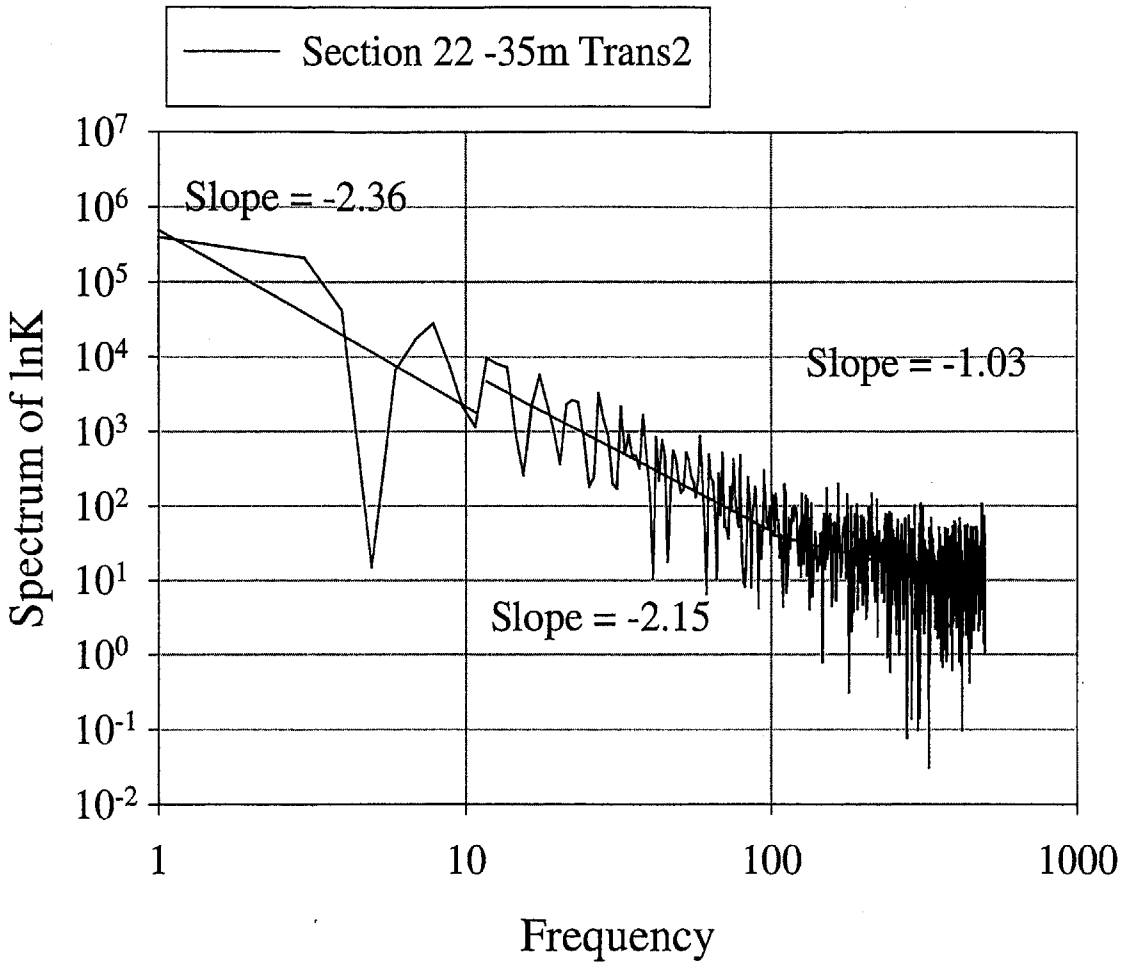

Figure 3.4b – One-dimensional spectral density of measured log-conductivity for the vertical transect (Trans2) for section 22 – 35m (from Goggin, 1988)

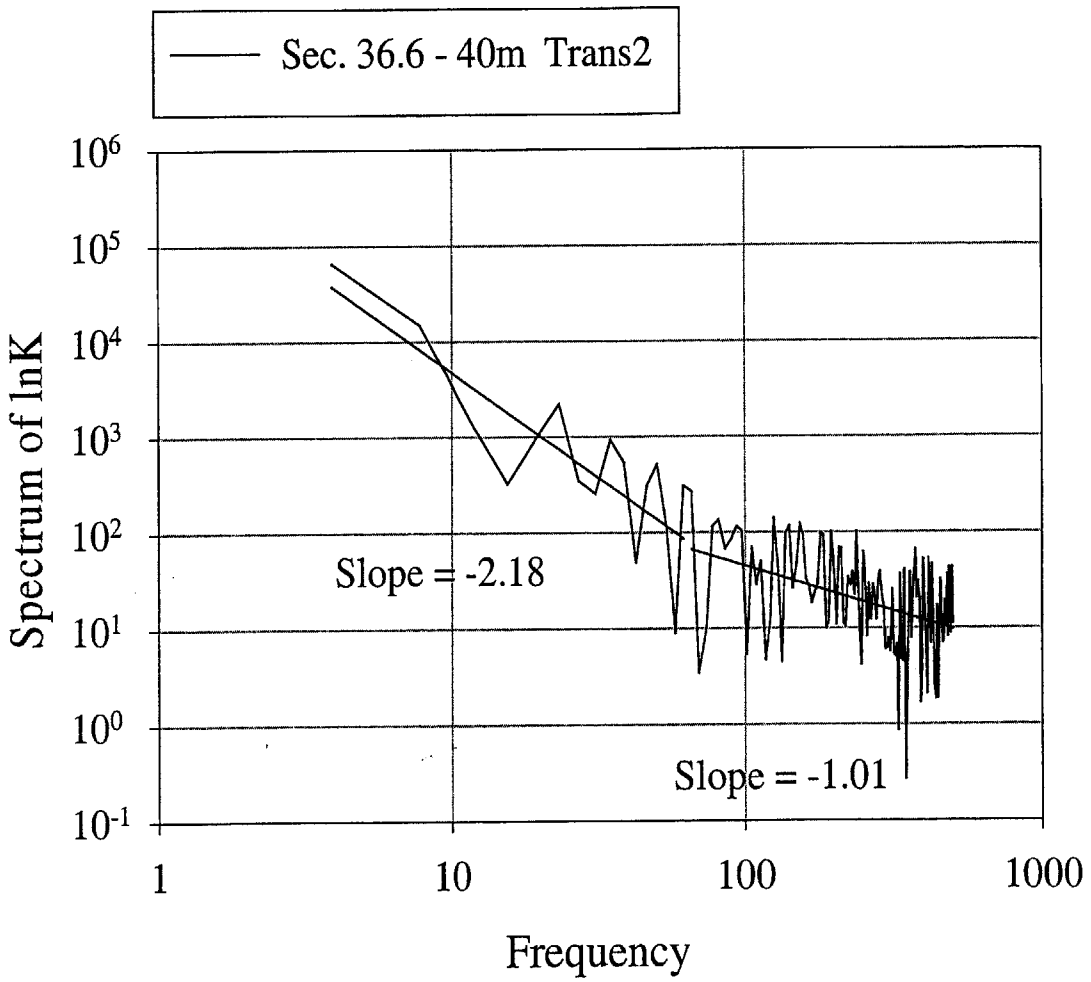

Figure 3.4c – One-dimensional spectral density of measured log-conductivity for the vertical transect (Trans2) for section 36.6 – 40m (from Goggin, 1988)

Table 3.1 – Results of regression analysis of the log spectral density versus log frequency for various sections of the vertical transects Trans1 and Trans2 from Goggin (1988)

Results for vertical section Trans1 shown in Figs. 3.3a – 3.3d		
Vertical Section	Frequency Range	Slope of log spectral density versus log frequency
0 – 8.5m	10 – 100	-0.88
	100 – 500	-1.03
8.5 – 18m	1-100	-1.98
	100-500	-1.21
22 – 35m	1 –10	0.03
	10 – 100	-2.20
	100 – 500	-1.29
35 – 40m	1 – 100	-1.94
	100 – 500	-1.43
Results for vertical section Trans2 shown in Figs. 3.4a – 3.4c		
0 – 20m	0.3 –10	-2.14
	10 – 50	-1.79
	50 - 500	-1.20
22 – 35m	1 – 30	-2.36
	30 – 100	-2.15
	100 - 500	-1.04
36.6 – 40m	3 – 60	-2.19
	60 – 500	-1.01

From Figs. 3.3 - 3.4 we see that the low frequency ranges of the spectra have slopes with values ranging from 0 - -2.40, the mid-frequencies of 50 – 100 have slopes with values between –1.79 and –2.20, and the high frequencies have slopes that range between –1 and –1.43.

The data presented above shows that the spectral density of log conductivity $F = \ln K$, decays like a power-law $S_F(\underline{k}) \propto k^{-\alpha}$, where α is some constant. From the spectral plots in Figs. 3.3 and 3.4 we find that α (which is the negative slope of $\log(S_F)$ versus $\log(k)$) has values between $D+1$ and $D+3$ where D is the space dimension, in some cases and for the high-frequency range $\alpha \approx D$. The case $\alpha = D$ corresponds to hydraulic conductivity fields that are multifractal. For the Goggin data set, we find that this condition of multifractality is satisfied within some range of frequencies. One can argue that modeling the hydraulic conductivity as multifractal is not outside the range of what one may observe in nature. Although, the existence of multifractal hydraulic conductivity may be limited to certain geologic media, the application of this model provides a new way to deal with the nonlinearities of the flow equations. In fact, assuming the hydraulic conductivity to be multifractal allows one to derive the distributional properties of the flow parameters such as the hydraulic gradient ∇H and the specific discharge $\underline{q}$. Moreover, the application of the results of this research extends beyond hydrology and can be applied to the analogous problem of electrical networks with random resistors. This problem is mathematically similar to that of flow through media with highly fluctuating hydraulic conductivity. For these reasons, we model the hydraulic conductivity field K as a multifractal.

CHAPTER 4 – SCALING OF THE HYDRAULIC GRADIENT AND THE SPECIFIC DISCHARGE FIELDS.

Introduction

This chapter presents a novel approach in solving the zero divergence Darcy's equation when the flow occurs in a heterogeneous medium with an isotropic lognormal multifractal hydraulic conductivity field K. The analysis presented exploits the scale-dependent properties of a multifractal K field to obtain the distributions of the hydraulic gradient ∇H and specific discharge $\underline{q}$ fields. For a scalar field like K that is multifractal, its average value $\overline{K}$ within a region S satisfies the scale-invariance property [Veneziano, 1999]

$$\overline{K}(S) \overset{d}{=} A_r . \overline{K}(rS) \tag{4.1}$$

where $\overset{d}{=}$ denotes equality of all finite dimensional distributions, $\overline{K}(S)$ is the average of K within a region S, $r \geq 1$, so that $\overline{K}(rS)$ is the mean value of K within the larger region rS, A_r is non-negative lognormal random variable that is independent of $\overline{K}(rS)$. Eq. (4.1) describes how the statistical properties of a larger region (rS) in a scalar field such as K relate to the statistical properties of the smaller region of K. When the support of a large-scale value of K, $\overline{K}(rS)$ is contracted by a factor r, then the statistical properties of

the scalar quantity on the smaller scale are identical to those on the large scale, if the large scale values are multiplied by a random variable A_r. When K is a multifractal field described by Eq. (4.1), then the log hydraulic conductivity $F = \ln K$ is a Gaussian random field with spectral density

$$S_F(\underline{k}) = \begin{cases} \frac{2}{S_D} C_K k^{-D} & k_o \le k \le k_{max} \\ 0 & \text{otherwise} \end{cases} \qquad (4.2)$$

where k is the amplitude of the wavenumber vector $\underline{k}$, S_D is the surface area of the unit D-dimensional sphere so that $S_1 = 2$, $S_2 = 2\pi$ and $S_3 = 4\pi$, C_K is the so-called codimension parameter of the K field that determines the level of the spectrum of F and k_o and k_{max} define the limits of the multifractal scaling of K. The spectrum of F is shown in Fig. 4.1, the ratio $r = \frac{k_{max}}{k_o}$ is called resolution, and the value C_K determines the level of the spectrum S_F. The notion of resolution is key in understanding the approach used in this thesis and can be better understood if one considers a K field generated over a discrete square grid of size say, 512 x 512. If the maximum size of this grid is 1, so that $k_o = 1$ and k_{max} =512, then the resolution r = 512 refers to the number of pixels over which the K data is generated. As the number of pixels over which the K field is generated is increased, one can gain a more detailed image of the K field. Conversely, when the number of pixels or grid size over which K is generated is reduced, then one observes the large-scale features or a coarser image of the field. How large the K field is

and to what resolution it is developed depend on the spectral cutoffs k_o and k_{max}, which have a physical significance. First, these limits are introduced to ensure that the variance of F = lnK is finite, so that the K field is stationary. Secondly, these limits k_o and k_{max} show that the flow is being considered over a region with defined boundaries and that the flow is being considered over a range of scales. All aquifers in the world have a maximum extent that can be represented by k_o, and the minimum scale at which the flow is considered can be represented by k_{max}. Defining this minimum scale in terms of the physical features of the aquifer is more difficult. For example, the Darcy equation is derived by averaging the flow over several pores, which is called a representative elementary volume (REV). It is difficult to define what constitutes a REV for a heterogeneous medium over which the average properties of the K field change rapidly from one location to the other over the flow domain [Dagan, 1986]. In spite of these complications, the minimum scale of flow k_{max} for a homogeneous medium can be defined, at least mathematically. The isotropic lognormal multifractal K field just described is used to obtain solutions of the hydraulic gradient ∇H and flow $\underline{q}$

$$\begin{cases} \underline{q} = -K\nabla H \\ \nabla^2 H + \nabla F.\nabla H = 0 \end{cases} \tag{4.3}$$

where H is the hydraulic head. We seek a solution to Eq. (4.3) under the condition that F = lnK is a Gaussian random field whose properties have been described. The scheme

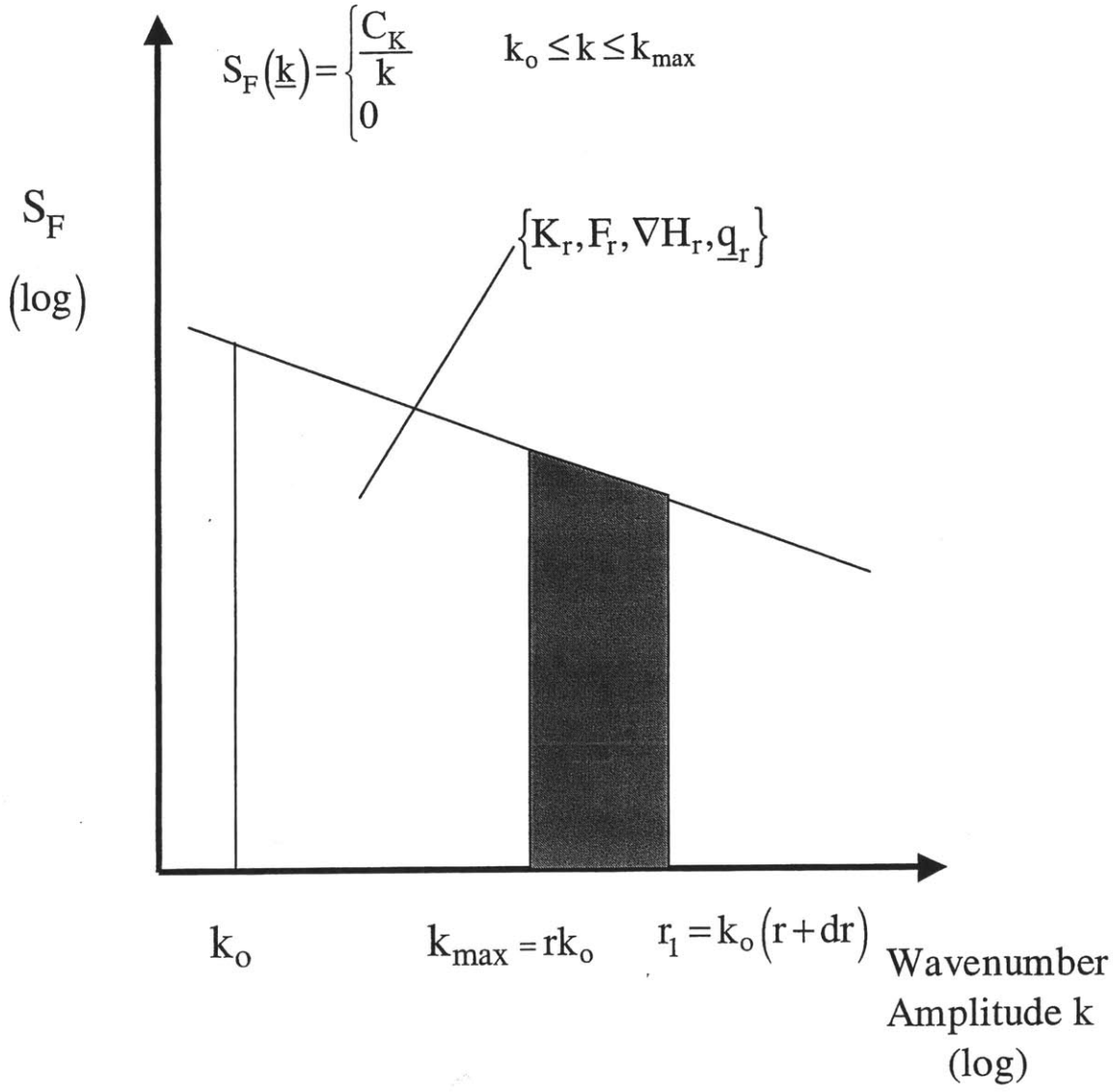

Figure 4.1 – An illustration of the spectrum of an isotropic lognormal multifractal K field.

used in obtaining the solution can be better understood if one considers Figs. 4.1 and 4.2. The analysis begins with a field developed to r (see Fig. 4.1). We denote quantities in this field with a subscript r so that $\nabla H_r, \underline{q}_r$ and F_r are the hydraulic gradient, specific discharge and log-conductivity of the field respectively. A hydraulic gradient J_1 is applied in the x_1 direction and this is denoted as $\nabla H_{LF} = \begin{bmatrix} J_1 \\ 0 \\ 0 \end{bmatrix}$, where the subscript LF denotes low-frequency. The accompanying log-conductivity is F_{LF} is shown in Fig. 4.2. For the K field developed to resolution r, the parameters of the flow field are $\{E[K] = 1, F = F_{LF}, \nabla H = \nabla H_{LF}, \underline{q} = \underline{q}_{LF}\}$. Next, we increase the resolution of the K field by an infinitesimal amount ε $(0 < \varepsilon \ll 1)$, so that we have a new K field that is slightly more random than the K field at resolution r. Because K is multifractal, one can obtain its statistical properties when one moves from a coarser resolution r to a finer resolution $r_1 = r(1+\varepsilon)$. Specifically, we are interested in how the distribution of the hydraulic gradient varies as one moves from $r \rightarrow r_1$. At r_1 the large-scale hydraulic gradient ∇H_{LF} is also incremented by a random quantity $\nabla h_{r \rightarrow r_1}$, a result of the addition of high wavenumber components to the K field so that the large scale ∇F_{LF} is incremented by $\nabla F_{r \rightarrow r_1}$. In other words, $\nabla F_{r \rightarrow r_1}$ directly accounts for the increment in the large-scale hydraulic gradient. At the finer scale r_1, the large-scale component of the hydraulic gradient ∇H_{LF} and ∇F_{LF} can be considered constant within the flow domain so that $\nabla h_{r \rightarrow r_1}$ (shown in Fig. 4.2 as ∇H_{HF}, where the subscript HF connotes high frequency) defines the hydraulic gradient. Thus, it is assumed that the hydraulic gradient ∇H_{HF} can

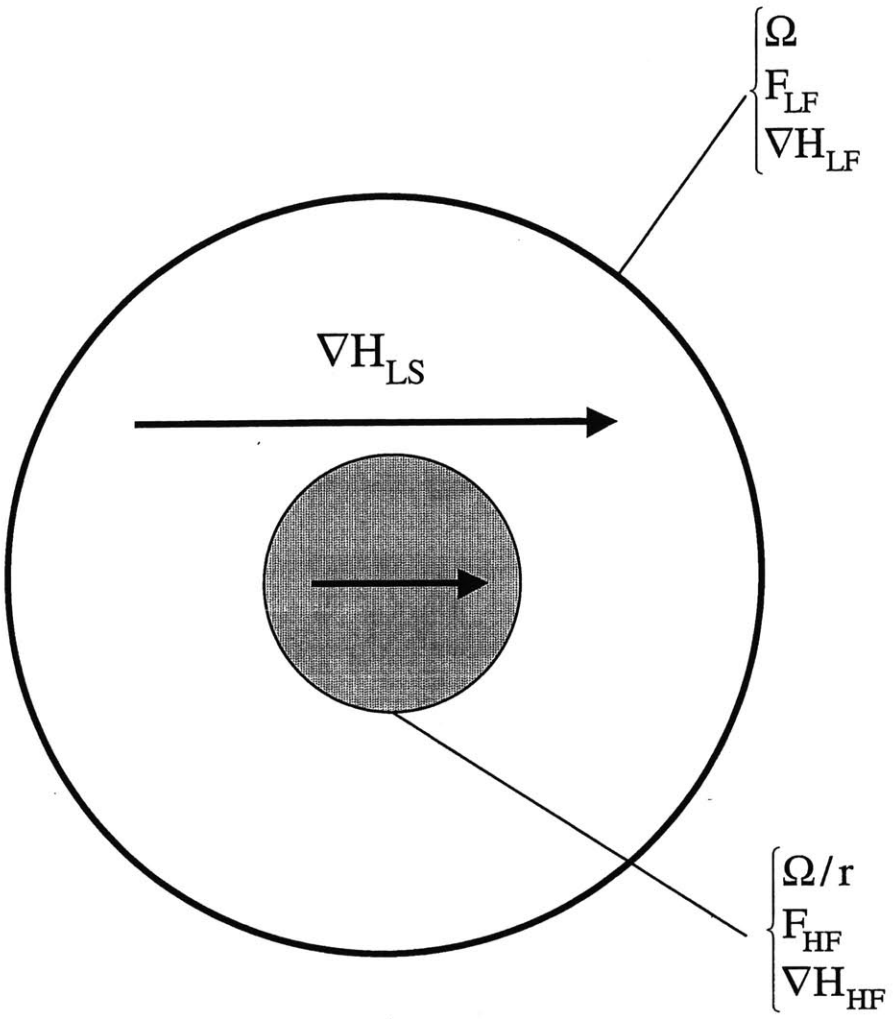

Figure 4.2 – An illustration of quantities as one moves from a coarse resolution r in domain Ω to a finer resolution in a contracted region Ω / r

be obtained by replacing F with F_{HF} while subjecting the field at resolution r_2 (denoted as Ω/r in Fig. 4.2) to a large-scale hydraulic gradient ∇H_{LF}. At this stage, one can write Eq. 4.3 for the r_1 field. Having obtained an expression for the flow at scale r_1, we consider the flow field at a resolution $r_2 = r(1+\varepsilon)^2$. For this finer resolution r_2 field, we consider how the gradient of the F field ∇F and the hydraulic gradient ∇H fields change as one moves from resolution r to this finer scale r_2. At this finer scale r_2, one can obtain an expression for the hydraulic gradient field by taking into consideration that when higher frequency data is introduced into the K field, the hydraulic gradient field at r_2 $\nabla H_{r\to r_2}$ will be inclined in a direction not necessarily aligned in the x_1 direction when we considered the flow at resolution r. Thus, to obtain values of ∇H and ∇F that will satisfy Eq. (4.3) at r_2, the hydraulic gradient field $\nabla H_{r\to r_2}$ has to be rotated and aligned in the direction of the ∇H at resolution r. Just as was done in the case of r_1, an expression for $\nabla H_{r\to r_1}$ is obtained by assuming it to be a sum of the large-scale hydraulic gradient ∇H_{LS} and a component $\nabla h_{r\to r_2}$ that accounts for the added higher frequency components in the F field as one moves from $r \to r_2$. Furthermore, this addition to the large-scale hydraulic gradient $\nabla h_{r\to r_2}$ can be decomposed into two terms: the first component being $\nabla h_{r\to r_1}$ and a second component $\nabla h_{r_1\to r_2}$. Similarly one can obtain expressions $\nabla F_{r\to r_2}$ and hence the zero divergence Darcy equation for flow at r_2. Having obtained the zero divergence expressions for flow at r_1 and r_2, one can compare these expressions to obtain the scaling relation for hydraulic gradient field as one moves from a coarser to a finer resolution.

This is the general approach used in obtaining the distributions of the hydraulic gradient and the specific discharge when the flow occurs in an isotropic lognormal K field. The solutions are obtained as one considers infinitesimal increments in the resolution field and how these increments affect the ∇F and ∇H fields.

The details of the flow analysis are prefaced in Sec. 4.1.1 with a discussion of the key assumptions used in the analysis. The distributions of the hydraulic gradient ∇H and its amplitude $J = |\nabla H|$ are presented in Sec. 4.1.2. In Sec. 4.1.3 the distribution of the scaling parameters of the hydraulic gradient fields and its rotation angles are presented. Sec. 4.2 investigates the scaling of the specific flow field $\underline{q}$. The multifractality of $\underline{q}$ and its amplitude q are presented in Sec. 4.2.1. The scaling parameters of the flow field are presented in Sec. 4.2.2. The marginal distributions of bare flows is presented in Sec. 4.2.3 and is followed in Sec. 4.2.4 with a discussion on the moment scaling function of flow amplitudes. Sec. 4.3.1 presents the problem formulation and solutions of effective hydraulic conductivity K_{eff} from exact one-dimensional analysis and from first-order second moment analysis. A comparison of the results in Sec. 4.3.1 with K_{eff} in the case of finite-resolution multifractal K is presented in Sec. 4.3.2. The final section presents a brief comparison of the results of this chapter with the results of random electrical conductivity networks by Bin Lin et al. (1991) and Archangelis et al. (1985). Results of these authors were reviewed in Chapter 2. Sec. 4.4 presents a brief comparison in their approaches and the one used in this thesis.

4.1.1 Assumptions made in the flow analysis

We study the properties of Darcian flow through a saturated aquifer under the following assumptions:

1. It is assumed that the hydraulic conductivity K is an isotropic lognormal multifractal whose properties have been described in the introduction.

2. It is assumed that in spaces of dimension D > 1, the zero mean high-frequency fluctuations of the head and flow along the boundary of the flow field Ω do not significantly affect the hydraulic gradient and flow away from a narrow region along the boundary of Ω. Neglecting boundary conditions is an assumption that has been made implicitly in the flow analysis of Gelhar and Axness (1983), Ababou and Gelhar (1990) and Dagan (1995). This assumption has been shown to be quite reasonable through results of flow simulations presented in Chapter 6.

3. The third assumption deals with the behavior of flow parameters as one considers flow through a cascade of K fields each of which is developed to a different resolution $r_j = r(1+\varepsilon)^j$ for j = 1, 2,...etc., $0 < \varepsilon \ll 1$, $r_2 = rr_1$ where $r \geq 1$ and $r_2 \geq r_1 \geq 1$. At the large scale, we denote the log-conductivity as F_{LF} and the hydraulic gradient as ∇H_{LF} where the subscript LF is an abbreviation

for low frequency (see Fig. 4.2). The K field at $r_1 = r(1+\varepsilon)$ is obtained by shifting k_{max} to the right of its initial position at resolution r (see Fig. 4.1). This shift in k_{max} adds higher wavenumber components to the K field so that the F field at r_1 consists of two components: the large-scale component F_{LF} and a new added component F_{HF} where the subscript HF denotes high-frequency (see Fig. 4.2), and F_{HF} is a direct result of the added higher wavenumber components added to the K field when the K field at r_1 was created. Also, the hydraulic gradient ∇H in r_1 consists of ∇H_{LF} and ∇H_{HF}, where ∇H_{HF} is a direct consequence of the higher frequencies added to the F field F_{HF}. We assume that the large-scale component of log-conductivity F_{LF} is constant within this new flow field of resolution r_1. And the head field in r_1 can be accurately obtained by replacing F with F_{HF} while subjecting the flow domain Ω to the large-scale hydraulic gradient ∇H_{LF}.

4. The final assumption made in the flow analysis through aquifers with multifractal K deals with the contribution of the term $\nabla F.\nabla h$ in the incremental flow equation as one moves from resolution $r_j \rightarrow r_{j+1}$. At resolution r, the zero-divergence Darcy equation is written as

$$\nabla^2 H_r + \nabla F_r . \nabla H_r = 0 \qquad (4.4)$$

where an average hydraulic gradient $-\underline{J}_o$ is applied in the x_1 direction, and without loss of generality one can set $E[K]=1$ and $\underline{J}_o=\underline{e}=[1,0,...,0]$ the unit vector along the x_1 axis. For the K field developed to resolution r_1 the flow equation inside Ω_1 is obtained by writing $\nabla H_{r_1}=-\underline{e}+\nabla h_{r_1}$, where ∇h_{r_1} is the increment in the hydraulic gradient when higher frequencies are added to the K field in the transition from $r \rightarrow r_1$. Then Eq. (4.4) becomes

$$\nabla^2 h_{r_1}+\nabla F_{r_1}.\nabla h_{r_1}=\frac{\partial F_{r_1}}{\partial x_1} \tag{4.5}$$

We assume that the variance of the term $\nabla F_{r_1}.\nabla h_{r_1}$ is far less than the variance of $\nabla^2 h_{r_1}$ and hence neglect the term $\nabla F_{r_1}.\nabla h_{r_1}$ in the derivation of the distributions of the hydraulic gradient and specific discharge fields. The conditions under which this assumption holds are found by writing Eq. (4.5) in Fourier space as

$$\begin{aligned} &(i)\quad -k^2\hat{h}_{r_1}+i\hat{h}_{r_1}.\left(\underline{k}.\nabla F_{r_1}\right)=ik_1\hat{F}_{r_1} \\ &\Rightarrow \\ &(ii)\quad \hat{h}_{r_1}=\frac{-ik_1\hat{F}_{r_1}}{k^2-i\underline{k}.\nabla F_{r_1}} \end{aligned} \tag{4.6}$$

The variance of the term $(\nabla F_{r_1}.\nabla h_{r_1})$ will be much less than the variance of $\left(\nabla^2 h_{r_1}\right)$ can be neglected if the variance of $|\nabla F|$ in the denominator of Eq. (4.6) is

much less than k^2. From Eq. (4.2) we can write the spectrum of the magnitude of the log-conductivity $|\nabla F|$ as

$$S_{|\nabla F|}(\underline{k}) = \begin{cases} \frac{2}{S_D} C_K k & k_o \le k \le k_{max} \\ 0 & \text{otherwise} \end{cases} \tag{4.7}$$

Hence the variance of $|\nabla F|$ is obtained as

$$\mathrm{Var}\left[|\nabla F|\right] = \int_{k_o}^{k_{max}=rk_o} S_{|\nabla F|}(\underline{k}) d\underline{k} = S_D \int_{k_o}^{rk_o} \frac{2}{S_D} C_K k dk = C_K k_o^2 \left(r^2 - 1\right).$$

Thus the term $(\nabla F_{r_1} . \nabla h_{r_1})$ can be ignored in the flow analysis if

$$\begin{aligned} &\text{(i)} \quad \mathrm{Var}\left[|\nabla F|\right] \ll r^2 k_o^2 \\ &\text{(ii)} \quad \Rightarrow C_K k_o^2 \left(r^2 - 1\right) \ll r^2 k_o^2 \\ &\text{(iii)} \quad C_K \ll \frac{r^2 k_o^2}{k_o^2 \left(r^2 - 1\right)} \end{aligned} \tag{4.8}$$

Since $r \ge 1$, then from Eq. (4.8)iii we can ignore $\nabla F_{r_1} . \nabla h_{r_1}$ for $k_o \gg 1$ and $C_K \ll 1$. From the numerical simulations presented in Table 4.1, we find that the numerical results agree with the theoretical assumptions at least for fields with

$C_K = 0.1$ and 0.3. From Table 4.1, we observe that the variance of $\nabla^2 h_{r_1}$ is significantly larger than the variance of $\nabla F_{r_1}.\nabla h_{r_1}$, especially for $C_K = 0.1$ and 0.3. This can be explained by the fact that ∇F_{r_1} is much less than ∇h_{r_1}. Hence, the variance of $\nabla F_{r_1}.\nabla h_{r_1}$ becomes much smaller than the variance of $\nabla^2 h_{r_1}$.

Table 4.1 – Comparison of the variances of $\nabla^2 h$ and $\nabla f.\nabla h$ computed from numerical simulations on a grid size of 512 x 512.

C_K	$E[\nabla^2 h]$	$E[\nabla h.\nabla f]$	$var[\nabla^2 h]$	$var[\nabla h.\nabla f]$	$\frac{var[\nabla^2 h]}{var[\nabla h.\nabla f]}$
0.1	1.08	0.0020	0.242	0.006	40
0.3	0.88	0.0013	1.709	0.052	32.86
0.8	0.92	0.00062	1.980	0.82	2.4

In deriving the distribution of the hydraulic gradient ∇H and specific discharge $\underline{q}$ fields we study the flow through a series of isotropic lognormal multifractal K fields each of which has been developed to a different resolution $r_j = (1+\varepsilon)^j$ for j = 1, 2, 4 etc. and $0 < \varepsilon \ll 1$. For any $r \geq 1$, we let $\Omega_r \subset \Omega$ be a ball such that, inside Ω_r, fluctuations with wavenumbers $|\underline{k}| < rk_o$ may be considered constant and let $\underline{x}_r$ be any point of Ω_r. In particular, Ω_1 is a ball inside which fluctuations with wavenumbers $|\underline{k}| < k_o$ may be considered constant. With these definitions and assumptions, we now consider the derivation of the scale-invariant properties of ∇H and $\underline{q}$ when the flow occurs in an isotropic lognormal multifractal K field.

4.1.2 Multifractality of ∇H and $J=|\nabla H|$

The derivation of the distributions of ∇H and its amplitude $J = |\nabla H|$ begins by denoting with a subscript r quantities derived for the log-conductivity $F = F_r$ and other flow parameters at a particular resolution, so that the hydraulic gradient ∇H_r and specific flow q_r satisfying the zero-divergence Darcy equations are written as

$$\begin{aligned} &(i) \quad \nabla^2 H_r + \nabla F_r . \nabla H_r = 0 \\ &(ii) \quad \underline{q}_r = -K_r \nabla H_r \end{aligned} \qquad (4.9)$$

As explained in the introduction, we obtain the distributions of the hydraulic gradient by considering flow through a cascade of K fields each of which is developed to a different resolution. The development of the K fields begin at resolution r, and by progressively adding high frequency to the K field, we obtain fields with resolutions $r_j = r(1+\varepsilon)^j$ where $0 < \varepsilon \ll 1$. At resolution r we have a flow problem where a large-scale hydraulic gradient of magnitude $|\nabla H| = \underline{J}_o = \underline{e} = [1,0,...,0]$ is imposed on the flow domain and oriented along the x_1 -axis and we lose no generality by setting $K = E[K] = 1$, $F = F_r$. Next, we consider flow through a K field with resolution r_1 that is obtained by adding high wavenumber components to the K field at r. This is achieved by shifting k_{max} from its original position (see Fig. 4.1) by an amount of $k_o r\varepsilon$ to the right. At resolution r_1, the flow equation inside Ω_1 is given by Eq. 4.11i, writing ∇H_{r_1} as

$$\nabla H_{r_1} = -\underline{e} + \nabla h_{r_1} \tag{4.10}$$

where ∇h_{r_1} is the fluctuation in the hydraulic gradient around its mean value $-\underline{e}$, due to the added variability in the log conductivity F_{r_1}. Also, as a consequence of the spectral density of the log-conductivity, their increments $F_{r\to r_1} = F_{r_1} - F_r$ and their gradients satisfy

$$\text{(i)}\quad F_{r\to r_1}(\underline{x}) \overset{d}{=} F_{r_1}(r\underline{x})$$

$$\text{(ii)}\quad \nabla F_{r\to r_1}(\underline{x}) \overset{d}{=} r.\nabla F_{r_1}(r\underline{x}) \tag{4.11}$$

Substituting Eq. (4.10) and Eq. (4.11) into $\nabla^2 H_r + \nabla F_r.\nabla H_r = 0$ gives

$$\nabla^2 h_{r_1} + \nabla F_{r_1}.\nabla h_{r_1} = \frac{\partial F_{r_1}}{\partial x_1} \tag{4.12}$$

Next, we consider a K field at resolution $r_2 = k_o r(1+\varepsilon)^2$ whose spectrum is obtained by shifting k_{max} to the right of $r k_o$ by a lag of $k_o r\varepsilon(2+\varepsilon)$ in Fig. 4.1. Thus, higher frequencies are added to the K field at resolution r and we obtain a slightly more variable field than was obtained for the K field with resolution r_1. The hydraulic gradient in this field ∇H_{r_2} is the sum of the hydraulic gradient when at resolution r plus an additional term ∇h_{r_2} that is a result of the added fluctuations in the F field F_{r_2}. We can then write expressions for the hydraulic gradient and the gradient of the log-conductivity for the field at resolution $r_2 = rr_1$ as

$$\begin{cases} \nabla H_{rr_1} = \nabla H_r + \nabla h_{r\to r_1} \\ \nabla F_{rr_1} = \nabla F_r + \nabla F_{r\to r_1} \end{cases} \tag{4.13}$$

where $\nabla h_{r\to r_1}$ is the fluctuation in the hydraulic gradient due the added component in the log conductivity field $F_{r\to r_1}$. And the flow equation for the K field at resolution $r_2 = r_1$ is

$$\nabla^2 H_{r_1} + \nabla F_{r_1}.\nabla H_{r_1} = 0 \tag{4.14}$$

Substitution of ∇H_{r_1} and ∇F_{r_1} from Eq. 4.15 into Eq. (4.14) gives

$$\nabla^2 H_r + \nabla^2 h_{r\to r_1} + \left(\nabla H_r + \nabla h_{r\to r_1}\right)\left(\nabla F_r + \nabla F_{r\to r_1}\right) = 0 \tag{4.15}$$

Expanding the terms in the above equation

$$\nabla^2 H_r + \nabla^2 h_{r\to r_1} + \nabla F_r.\nabla H_r + \nabla F_{r\to r_1}.\nabla H_r + \nabla F_r.\nabla h_{r\to r_1} + \nabla F_{r\to r_1}.\nabla h_{r\to r_1} = 0 \tag{4.16}$$

At resolution r, the flow equation is given by

$$\nabla^2 H_r + \nabla F_r.\nabla H_r = 0 \tag{4.17}$$

Subtracting term-by-term Eq. (4.17) from Eq. (4.16) gives

$$\nabla^2 h_{r\to r_1} + \nabla F_{r\to r_1}.\nabla H_r + \nabla h_{r\to r_1}.\left(\nabla F_r + \nabla F_{r\to r_1}\right) = 0, \text{ in } \Omega_r \tag{4.18}$$

The fourth assumption in the previous section showed that for $k_o \gg 1$ and $C_K \ll 1$, the term $\nabla h_{r\to\pi_1}.\nabla F_r$ is small relative to $\nabla^2 h_{r\to\pi_1}$ and may therefore be neglected. Since ∇h_r may be considered constant in Ω/r, one can rotate the coordinate axes inside Ω/r such that the new x_1 coordinate axis is in the direction of the negative hydraulic gradient $-\nabla H_r$. In this rotated reference, $-\nabla H_r^R \equiv J_r \underline{e}$, where the superscript R is used to identify quantities in the rotated reference. Eq. (4.12) becomes

$$\begin{cases} \nabla H_{\pi_1}^R = -J_r \underline{e} + \nabla h_{r\to\pi_1}^R \\ \nabla F_{\pi_1}^R = \nabla F_r^R + \nabla F_{r\to\pi_1}^R \end{cases} \tag{4.19}$$

And the flow equation (4.18) may be written as

$$\nabla^2 h_{r\to\pi_1}^R + \nabla F_{r\to\pi_1}^R.\left(-J_r \underline{e} + \nabla h_{r\to\pi_1}^R\right) = 0, \text{ in } \Omega_r \tag{4.20}$$

Expanding terms and using $\nabla F_{r\to\pi_1}(\underline{x}) \overset{d}{=} r.\nabla F_{\pi_1}(r\underline{x})$ from Eq. (4.11)ii in the above equation, one obtains

$$\nabla^2 h_{r\to\pi_1}^R + \nabla h_{r\to\pi_1}^R.\nabla F_{r\to\pi_1}^R = (rJ_r)\frac{\partial F_{r\to\pi_1}^R}{\partial x_1}, \text{ in } \Omega_r \tag{4.21}$$

Due to the isotropy of the log-conductivity field, one may remove the superscript R from the F terms. Also, from Eq. (4.11)ii $\nabla F_{r\to r_1}(\underline{x}) \overset{d}{=} r.\nabla F_{r_1}(r\underline{x})$, therefore a field statistically identical to $h^R_{r\to r_1}$ in Eq. (4.21) is obtained as the solution of

$$\nabla^2 h^R_{r\to r_1}(\underline{x}) + r.\nabla h^R_{r\to r_1}(\underline{x}).\nabla F_{r_1}(r\underline{x}) = (rJ_r)\frac{\partial F_{r_1}(r\underline{x})}{\partial x_1}, \quad \underline{x}\in\Omega_r \tag{4.22}$$

Recall that for the field at resolution r_1 we obtained the flow equation (Eq. (4.12))

$$\nabla^2 h_{r_1} + \nabla F_{r_1}.\nabla h_{r_1} = \frac{\partial F_{r_1}}{\partial x_1} \tag{4.23}$$

Comparing Eq. (4.23) and (4.22) shows that the solutions of Eq. (4.22) satisfies

$$\nabla h^R_{r\to r_1}(\underline{x}) \overset{d}{=} J_r.\nabla h_{r_1}(r\underline{x}) \qquad x\in\Omega_r \tag{4.24}$$

Finally substituting Eq. (4.24) into $\nabla H^R_{r_1} = -J_r\underline{e} + \nabla h^R_{r\to r_1}$ (which is Eq. (4.19)) gives

$$\nabla H^R_{r_1}(\underline{x}) = J_r\left[-\underline{e} + \nabla h_{r_1}(r\underline{x})\right] \tag{4.25}$$

At resolution r_1 we obtained $\nabla H_{r_1} = -\underline{e} + \nabla h_{r_1}$ which compared to the above equation gives

$$\nabla H^{R}_{\pi_1}(\underline{x}) \overset{d}{=} J_r\left[-\underline{e} + \nabla h_{r_1}(r\underline{x})\right] \overset{d}{=} J_r.\nabla H_{r_1}(r\underline{x}) \tag{4.26}$$

The above equation is fundamental to the analysis in this thesis. It says that a random field in Ω/r identical in distribution to $\nabla H_{\pi_1}(\underline{x})$ is obtained from $\nabla H_{r_1}(\underline{x})$ in Ω by isotropically contracting the space by r, rotating the coordinate axes by a random amount such that the new x_1 axis is aligned with $\underline{J}_r$, and scaling the field $\nabla H_{r_1}(\underline{x})$ by a random factor $J_r = |\underline{J}_r|$. Eq. (4.26) can also be stated as

$$\nabla H_{\pi_1}(\underline{x}) \overset{d}{=} (J_r \underline{R}_r).\nabla H_{r_1}\left(r\underline{R}_r^T \underline{x}\right) \tag{4.27}$$

where $\underline{R}_r$ is an orthogonal random matrix with first column equal to $\underline{e}_r$, and the matrix $(J_r \underline{R}_r)$ is independent of the field ∇H_{r_1}. For D = 1, there is no rotation and for D = 2, $\underline{R}_r = \begin{bmatrix} \cos(\alpha_r) & -\sin(\alpha_r) \\ \sin(\alpha_r) & \cos(\alpha_r) \end{bmatrix}$, where α_r is the random rotation angle with symmetric distribution about zero and $(J_1 \cos\alpha + J_2 \sin\alpha)$ is the first component of $\underline{R}_r^T \underline{J}_r$ and thus the matrix $\underline{R}_r$ is completely by its first column $\underline{e}_r = \begin{bmatrix} \cos\alpha_r \\ \sin\alpha_r \end{bmatrix}$. For D > 2, $\underline{R}_r$ includes arbitrary components of rotation and $\underline{R}_r$ has $\frac{D(D-1)}{2}$ free parameters of which only D – 1 are determined by $\underline{e}_r$. These arbitrary components of rotation do not affect the

statistical properties of the right hand side of Eq. (4.27) and may be left unspecified. Eq. (4.27) implies an analogous scaling relation for the hydraulic gradient amplitude fields $J_r(\underline{x}) = |\nabla H_r(\underline{x})|$, which is

$$J_{rr_1}(\underline{x}) \overset{d}{=} J_r . J_{r_1}(r\underline{R}_r^T \underline{x}) \tag{4.28}$$

As $r \to \infty$, $\nabla H_r(\underline{x})$ does not converge to an ordinary random field $\nabla H(\underline{x})$, because in the limit, the point values of ∇H do not exist. However, the average of $\nabla H_r(\underline{x})$ inside the set S, $\nabla H(S)$ which due to Eq. (4.27) satisfies

$$\nabla H(S) \overset{d}{=} (J_r \underline{R}_r) . \nabla H(r\underline{R}_r^T S) \tag{4.29}$$

The above derivation embodies the essence of scaling analysis that in effect matches the solution of the flow problem at resolution r to the solution as one goes to finer resolutions rr_1. This solution technique is also known as the renormalization method and allows one to obtain an approximate nonlinear solution of the flow equation under conditions that have been presented above.

4.1.3 Distribution of the Scaling Parameters J_r and $\underline{e}_r$

To complete the multifractal characterization of ∇H and J, one needs the joint distribution of J_r and $\underline{e}_r$ or equivalently the marginal distribution of the hydraulic gradient. The vector $\underline{J}_r = -\nabla H_r$ is first considered for resolutions r infinitesimally higher than 1. The distribution of $\underline{J}_r$ is obtained by first characterizing the random field $\nabla H_r(\underline{x})$. From this the marginal distribution of ∇H_r is obtained, which is also the distribution of $-\underline{J}_r$. The flow equation $\nabla^2 h_{r_1} + \nabla F_{r_1}.\nabla h_{r_1} = \frac{\partial F_{r_1}}{\partial x_1}$ for ∇h_r (obtained by replacing r_1 with r in Eq. (4.12)) may be simplified to

$$\nabla^2 h_r = \frac{\partial F_r}{\partial x_1} \tag{4.30}$$

because, for r infinitesimally close to 1, the term $\nabla F_r.\nabla h_r$ is of higher order. In Fourier space, Eq. (4.30) is written as

$$\hat{h}_r(d\underline{k}) = -i\frac{k_1}{k^2}\hat{F}_r(d\underline{k}) \tag{4.31}$$

where $\hat{h}_r$ and $\hat{F}_r$ are the spectral measures of h_r and F_r. Hence the spectral measure of the hydraulic gradient satisfies

$$\nabla \hat{h}_r(d\underline{k}) = (\underline{k}'k'_1)\hat{F}_r(d\underline{k}) \tag{4.32}$$

where $\underline{k}' = \underline{k}/k$ is the unit vector in the direction of $\underline{k}$ and k'_1 is its first component. Eq. (4.32) is approximate because the random function $h_r(\underline{x})$ with spectral measure in Eq. (4.31) does not satisfy the boundary conditions. For example, in one dimension, Eq. (4.30) determines $h_r(\underline{x})$ up to a linear function A + Bx, where A and B are random variables that depend on the random function $F_r(x)$, such that the boundary conditions $h_r(0) = h_r(1) = 0$ are satisfied. The corresponding one-dimensional hydraulic gradient $\nabla h_r(x)$ should contain an extra additive term B that contributes a spectral mass at k = 0. In this analysis, the boundary effects are ignored and the reasons are provided in Sec. 4.1.1. From simulation results presented in Chapter 6 it is found that for D = 2 the neglected terms have negligible effects on the statistics of interest.

Using Eq. (4.32) and the spectral density of F in Eq. (4.2), the spectral density tensor of ∇h_r is

$$\underline{S}_{\nabla h_r}(\underline{k}) = \begin{cases} (\underline{k}'\underline{k}'^T)k_1'^2 \dfrac{2}{S_D} C_K k^{-D} & \text{for } k_o \le k \le rk_o \\ 0 & \text{otherwise} \end{cases} \tag{4.33}$$

where $\underline{k}' = \underline{k}/k$. Since h_r is a homogeneous Gaussian field, its gradient ∇h_r is homogeneous Gaussian with zero mean and is completely characterized by the spectral

tensor in Eq. (4.33). Consequently, the vector $\underline{J}_r = \underline{e} - \nabla h_r$ has joint normal distribution with mean vector $\underline{e}$ and the same covariance matrix as ∇h_r. The covariance matrix is obtained through integration of $\underline{S}_{\nabla h_r}(\underline{k})$ in Eq. (4.33), which gives:

$$\mathrm{Cov}\left[J_{r_i}, J_{r_j}\right] = \mathrm{Cov}\left[\nabla h_{r_i}, \nabla h_{r_j}\right] = 2\underset{D}{E}\left[e_1^2 e_i e_j\right] C_K \ln(r) \qquad (4.34)$$

where $\underset{D}{E}\left[e_1^2 e_i e_j\right]$ is the expected value of $\left(e_1^2 e_i e_j\right)$ when $\underline{e}$ is a random vector with uniform distribution on the surface of the unit sphere in $\Re^D$. The expected values of $e_1^2 e_i e_j$ can be obtained as follows.

Let $\underline{e}_D = [e_1, e_2, ..., e_D]$ be the unit random vector with uniform orientation in R^D. In deriving the scaling properties of the hydraulic gradient and specific flow, one needs to calculate the expected values $\underset{D}{E}\left[e_1^2\right]$, $\underset{D}{E}\left[e_1^4\right]$ for any D and $\underset{D}{E}\left[e_1^2 e_2^2\right]$ for D > 1, where the subscript D reminds one that these quantities depend on the space dimension D. Here these moments are obtained using results from distribution theory.

First, we observe that the vector of squared components $\underline{e}_D^2 = \left[e_1^2, e_2^2, ..., e_D^2\right]$ has the same joint distribution as the vector $\left[\chi_j^2 / \sum_{i=1,n} \chi_i^2,\ j=1,....,D\right]$, where the variables χ_j^2 are independent with chi-square distribution and 1 degree of freedom. Consequently, $\underline{e}_D^2$ has Dirichlet distribution with parameters $\alpha_1 = \alpha_2 = ... = \alpha_D = \frac{1}{2}$ (Johnson and Kotz,

1972, Chapter 40). Let $\alpha = \sum_{i=1,D} \alpha_i = \frac{D}{2}$, then using the results for the moments of the Dirichlet distribution (Johnson and Kotz, 1972; Wilks, 1962), one obtains

$$\begin{cases} \underset{D}{E}\left[e_1^2\right] = \dfrac{\alpha_1}{\alpha} = \dfrac{1}{D} \\ \underset{D}{E}\left[e_1^4\right] = \dfrac{\alpha_1(\alpha_1+1)}{\alpha(\alpha+1)} = \dfrac{3}{D(D+2)} \\ \underset{D}{E}\left[e_1^2 e_2^2\right] = \dfrac{\alpha_1\alpha_2}{\alpha(\alpha+1)} = \dfrac{1}{D(D+2)} \end{cases} \tag{4.35}$$

Using Eq. (4.35), the following relations are obtained for the variances and covariances in Eq. (4.34):

$$\begin{cases} \mathrm{Var}\left[J_{r_1}\right] = \mathrm{Var}\left[\nabla h_{r_1}\right] = \dfrac{6}{D(D+2)} C_K \ln(r) & \text{for } i = 1 \\ \mathrm{Var}\left[J_{r_i}\right] = \mathrm{Var}\left[\nabla h_{r_i}\right] = \dfrac{2}{D(D+2)} C_K \ln(r) & \text{for } i \neq 1 \\ \mathrm{Cov}\left[J_{r_i}, J_{r_j}\right] = \mathrm{Cov}\left[\nabla h_{r_i}, \nabla h_{r_j}\right] = 0 & \text{for } i \neq j \end{cases} \tag{4.36}$$

The factor J_r in Eqs. (4.25) - (4.29) is the length of $\underline{J}_r$, which satisfies

$$J_r = \left|e - \nabla h_r\right| = \sqrt{\left(1 - \nabla h_{r_1}\right)^2 + \sum_{i=2,D} \left(\nabla h_{r_i}\right)^2} \tag{4.37}$$

For r infinitesimally close to 1, ∇h_r is infinitesimal and Eq. (4.37) simplifies to

$$J_r = 1 - \nabla h_{r_1} + \frac{1}{2}\sum_{i=2,D}\left(\nabla h_{r_i}\right)^2 \tag{4.38}$$

with the first two moments (neglecting higher order terms)

$$\begin{aligned} &(i)\quad E[J_r] = 1 + \frac{1}{2}\sum_{i=2,D} \mathrm{Var}\left[\nabla h_{r_i}\right] = 1 + \frac{D-1}{D(D+2)} C_K \ln(r) \\ &(ii)\quad \mathrm{Var}[J_r] = \mathrm{Var}\left[\nabla h_{r_1}\right] = \frac{6}{D(D+2)} C_K \ln(r) \end{aligned} \tag{4.39}$$

The quadratic term had to be included in Eq. (4.38), since that term has a first-order effect (in lnr) on the mean of J_r. The same term makes only a higher-order contribution to the variance of J_r. Since the variability of J_r comes exclusively from the term ∇h_{r_1} in Eq. (4.38) and that term has normal distribution, one concludes that also J_r has normal distribution. However, J_r has positive mean value and infinitesimal coefficient of variation (because $\ln(r)$ is infinitesimal). Therefore, J_r may also be considered to have lognormal distribution. Using expressions for the moments of a lognormal variable in terms of its mean and variance (e.g. Johnson and Kotz, 1970, p. 115) and considering that $\left(E[J_r]-1\right)$ and $\mathrm{Var}[J_r]$ are both infinitesimal, one obtains the s^{th} moment from Eq. (4.39) as

$$E\left[J_r^s\right] = \exp\left\{sm + \frac{1}{2}\sigma^2\right\} \tag{4.40}$$

where $m = E\left[\ln\left(J_r\right)\right]$ and $\sigma^2 = \mathrm{Var}\left[\ln\left(J_r\right)\right]$. Substituting expressions for the mean and the variance of J_r into Eq. (4.40) one obtains

$$E\left[J_r^s\right] = \exp\left\{\left(\frac{D-1}{D(D+2)}C_K \ln(r)\right)s + \frac{1}{2}\left(\frac{6}{D(D+2)}C_K \ln(r)\right)\left(s^2 - s\right)\right\} \tag{4.41}$$

where

$$\begin{cases} E\left[\ln\left(J_r\right)\right] = \dfrac{D-4}{D(D+2)}C_K \ln(r) \\ \mathrm{Var}\left[\ln\left(J_r\right)\right] = \dfrac{6}{D(D+2)}C_K \ln(r) \end{cases} \tag{4.42}$$

D is the space dimension and C_K is the parameter that controls the level of the spectral density of log-conductivity F in Eq. (4.2). Moreover, Eq. (4.41) can be rewritten as

$$E\left[J_r^s\right] = r^{W_J(s)} \tag{4.43}$$

where the moment scaling function $W_J(s)$ is given by

$$W_J(s) = C_K\left[\frac{D-1}{D(D+2)}s + \frac{3}{D(D+2)}(s^2 - s)\right] \tag{4.44}$$

Equation (4.44) has several interesting features. First, one notices that $W_J(s)$ is proportional to the codimension parameter C_K of the hydraulic conductivity. The coefficient s in Eq. (4.44), $C_K\frac{D-1}{D(D+2)}$, measures the expected increase of the hydraulic gradient amplitude J_r as the hydraulic conductivity is developed to higher resolution levels. That is, for two fields developed to resolutions r_1 and r_2 where $r_2 > r_1$, the following relationship holds:

$$\frac{E[J_{r_2}]}{E[J_{r_1}]} = r^{C_K\frac{D-1}{D(D+2)}} \tag{4.45}$$

Eq. (4.45) shows that the expected hydraulic gradient amplitude diverges as the resolution $r \to \infty$. Therefore, the hydraulic gradient amplitude is non-conservative. Since the mean hydraulic gradient $E[\nabla H_r]$ is constant and equal to $-\underline{e}$ for all r, the increase of $E[J_r]$ with r is due to the random rotation of the hydraulic gradient ∇H_r as the resolution r increases. In one dimension, there is no rotation, J is conservative and the coefficient of s is zero. For D = 2, the coefficient is $\frac{1}{8}C_K$ and for D = 3 it has a value of

$\frac{2}{15}C_K$. Thus the hydraulic gradient amplitude is less conservative for D = 3 than for D = 2.

The coefficient of $\left(s^2 - s\right)$ in Eq. (4.44), $C_K \frac{3}{D(D+2)}$ characterizes the increase in the variability of $\log\left[J_r(\underline{x})\right]$ as r increases. Its value depends on the space dimension D. For D = 1, it equals C_K because in one-dimension the hydraulic gradient ∇H is proportional to the hydraulic conductivity K and the variability of $\log\left[\left|\nabla H_r(\underline{x})\right|\right]$ increase with resolution r in a similar fashion as the variability of $\log\left[K_r(\underline{x})\right]$. When $D > 1$, the variability of $\log\left[\left|\nabla H_r(\underline{x})\right|\right]$ increases with resolution at a smaller rate than the variability of $\log\left[K_r(\underline{x})\right]$; this is why the coefficient of $\left(s^2 - s\right)$ is smaller than C_K.

Rotation of the hydraulic gradient ∇H

To obtain the distributional properties of $\underline{e}_r$, consider a resolution r infinitesimally greater than 1. Denote by $\underline{e}$ the unit vector in the direction of the positive x_1 – axis and by $\underline{e}_r$ the unit vector in the direction of the gradient ∇H_r at any given point $\underline{x}$ of the aquifer. Since the difference $\underline{e}_r - \underline{e}$ is infinitesimal, this difference may be considered orthogonal to $\underline{e}$ and described by the coordinates in the sub-space spanned by the $x_2, \ldots, x_D$ axes. These coordinates have values $\nabla h_{r_2}, \ldots, \nabla h_{r_D}$ and, from Eq. (4.36) are iid normal with mean zero

and variance $\frac{2}{D(D+2)}C_K \ln(r)$. For D = 1, there is no rotation; hence $\underline{e}_r$ =1. For D > 1, the unit vector $\underline{e}_r$ has the distribution of Brownian motion (Bm) on the surface of the D-dimensional unit sphere with log-resolution r' = $\ln(r)$ as the time parameter. An important feature of Brownian motion on the sphere is that it asymptotically approaches the uniform distribution, where all directions are equally likely. Moreover the increments in the rotation angle have been found through numerical simulations to be independent (see Chapter 6). The Brownian motion $\underline{e}_{r'}$ starts at $\underline{e}_0 = \underline{e}$, the point on the unit sphere on the positive x_1 axis, and evolves with independent increments $\underline{e}_{r'+\Delta r'} - \underline{e}_{r'}$. For $\Delta r'$ infinitesimal, the increments belong to the hyperplane tangent to the unit sphere at $e_{r'}$. In a local reference on such tangent hyperplanes, these infinitesimal increments are distributed like

$$\left[\frac{2}{D(D+2)}C_K \Delta r'\right]^{1/2} \underline{Z}_{D-1} \qquad (4.46)$$

where $\underline{Z}_{D-1}$ is the standard normal vector with D – 1 components.

The Brownian motion distribution of $\underline{e}_{r'}$ on the unit sphere has rotational symmetry around the point $\underline{e} = [1,0,....,0]^T$. Therefore, an important characteristic of $\underline{e}_{r'}$ is the co-latitude, i.e. the angle $\alpha_{r'}$ between $\underline{e}_{r'}$ and the x_1-axis. Figure 4.3 illustrates the co-latitude and shows a hypothetical Brownian motion path on the 3D sphere. For D = 2, $\alpha_{r'}$ has wrapped normal distribution, with mean zero and variance (before wrapping)

$$\mathrm{Var}[\alpha_{r,\cdot}] = \frac{1}{4} C_K r' \qquad (4.47)$$

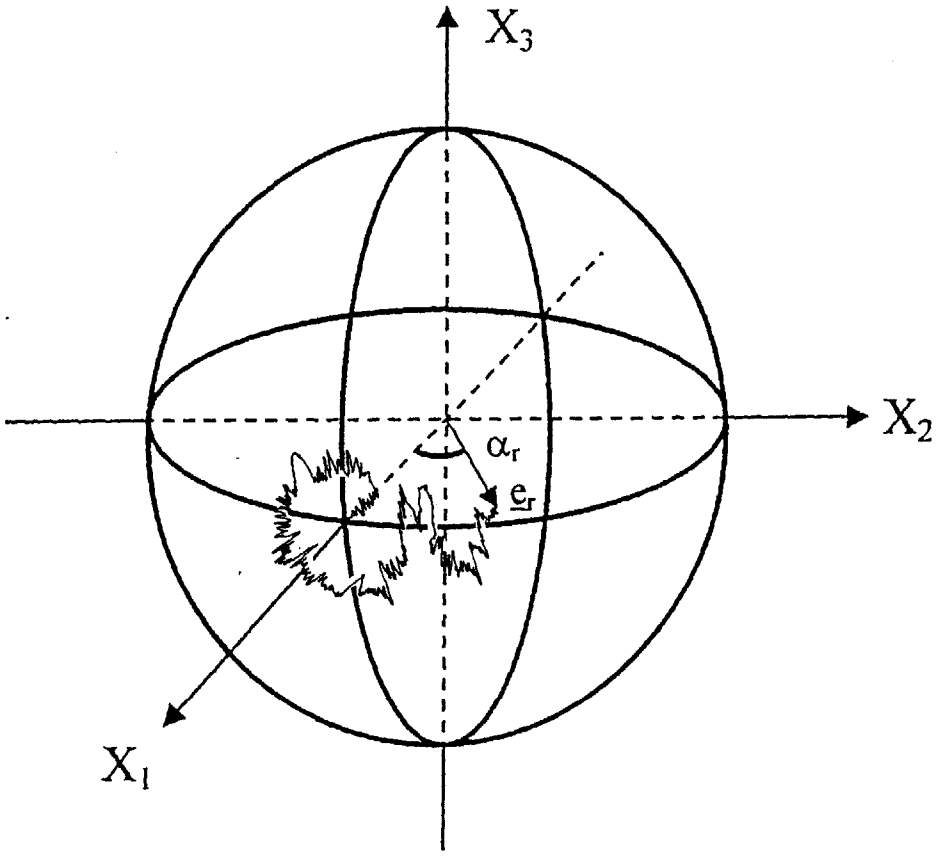

Figure 4.3 - Illustration of a hypothetical Brownian motion path on a 3D sphere

On the wrapped distribution, see Mardia (1972), sec. 3.4.8. The variance of $\alpha_{r'}$ is a measure of the change in local flow direction when the components in the wavenumber range $\left[k, e^{r'}k\right]$, k is any wavenumber larger than k_o, are added to the log hydraulic conductivity F.

For $D \geq 3$, the distribution of Brownian motion on the sphere does not have a simple analytical form (e.g. see Perrin, 1928, for the case D =3), but can be accurately approximated by D-dimensional Fisher distributions (Roberts and Ursell, 1960; Mardia, 1972, 1975). A good approximation to the distribution of the angle $\alpha_{r'}$ may be obtained from these Fisher distributions. When Var $[\alpha_{r'}] \ll 1$, an even simpler approximation based on Eq. (4.46), is

$$\left[\frac{2}{D(D+2)} C_K r'\right]^{1/2} \chi_{D-1} \qquad D > 1 \tag{4.48}$$

where χ_{D-1} is the chi variable with D – 1 degrees of freedom. Since $E\left[\chi^2_{D-1}\right] = D-1$, the second moment of the distribution in Eq. (4.48) is

$$E\left[\alpha^2_{r'}\right] = \frac{2(D-1)}{D(D+2)} C_K r' \tag{4.49}$$

Eq. 4.51 is approximate, but for D = 2 it reproduces the exact result in Eq. (4.48). Equation (4.49) further shows that $E\left[\alpha_{r'}^2\right]$ vanishes for D = 1 and $D \to \infty$ and is maximum with value $\frac{4}{15}C_K r'$ for D =3. In two dimensions, $E\left[\alpha_{r'}^2\right]=\frac{1}{4}C_K r'$, which is only slightly smaller than in three dimensions.

For D > 1, an important feature of Brownian motion on the sphere is that it asymptotically approaches the uniform distribution, where all directions are equally likely. This means that the hydraulic gradient ∇H_r, which is anisotropic at large scales due to boundary conditions, becomes locally isotropic as $r \to \infty$. As this happens, the mean amplitude $E[J_r]$ diverges in such a way that $E[-\nabla H_r]$ remains constant and equal to the unit vector $\underline{e}$ along the x_1-axis.

4.2 Multifractal Scaling of bare $\underline{q}$ and q

This section investigates the scaling of the specific flow $\underline{q}$ by comparing the fields $\underline{q}_r$ in $\underline{q}_r = -K_r \nabla H_r$ (Eq. (4.9)) when the log conductivity $F = \ln(K)$ is developed to different resolutions r. The flow in a K field developed to a resolution r is called a bare field in the multifractal literature. Following the presentation in section 4.1, the multifractality of $\underline{q}$ and its amplitude is first established, followed by a derivation of the scaling parameters. Finally, the marginal distributions of the bare quantities $\underline{q}$ and q are obtained.

4.2.1 Multifractality of $\underline{q}$ and q

From Eq. 4.12 the specific discharge field $\underline{q}_{r_1}$ can be written as

$$\underline{q}_{r_1} = -K_{r_1}\nabla H_{r_1} = K_{r_1}\left(\underline{e} - \nabla h_{r_1}\right) \tag{4.50}$$

Using Eq. (4.13) $\begin{cases} \nabla H_{rr_1} = \nabla H_r + \nabla h_{r\to rr_1} \\ \nabla F_{rr_1} = \nabla F_r + \nabla F_{r\to rr_1} \end{cases}$ the specific discharge field at the finer resolution $r_2 = rr_1$ can be written in the rotated framework as

$$\begin{aligned} \underline{q}^R_{rr_1} &= -K^R_{rr_1}.\nabla H^R_{rr_1} \\ &= \left(K_r K^R_{r\to rr_1}\right)\left(J_r\underline{e} - \nabla h^R_{r\to rr_1}\right) \\ &= \left(J_r K_r\right)K^R_{r\to rr_1}\left(\underline{e} - \frac{\nabla h^R_{r\to rr_1}}{J_r}\right) \end{aligned} \tag{4.51}$$

where, in the above equation

$$\begin{aligned} &\text{(i)}\quad J_r K_r \text{ is independent of } K^R_{r\to rr_1}\left(\underline{e} - \frac{\nabla h^R_{r\to rr_1}}{J_r}\right) \\ &\text{(ii)}\quad \begin{bmatrix} K^R_{r\to rr_1}(\underline{x}) \\ \nabla h^R_{r\to rr_1}(\underline{x}) \end{bmatrix} \overset{d}{=} \begin{bmatrix} K_{r_1}(r\underline{x}) \\ J_r.\nabla h^R_{r_1}(r\underline{x}) \end{bmatrix} \end{aligned} \tag{4.52}$$

Property (i) follows from the independence of hydraulic conductivity fields K_r and $K_{r\to r_1}$ and property (ii) follows from the isotropy of the hydraulic conductivity field (see Eqs. (4.11) and (4.24)). Using these properties, Eq. (4.51) gives

$$\begin{aligned} \underline{q}^{R}_{r_1}(\underline{x}) &\overset{d}{=} (J_r K_r).K_{r_1}(r\underline{x}).\left(\underline{e} - \nabla h_{r_1}(r\underline{x})\right) \\ &\overset{d}{=} (J_r K_r).\underline{q}_{r_1}(r\underline{x}) \end{aligned} \tag{4.53}$$

where $J_r K_r$ is independent of $\underline{q}_{r_1}(r\underline{x})$. Let $\underline{R}_r$ be the orthogonal matrix in Eq. (4.29) with $\underline{e}_r$ the unit random vector in the direction of $-\nabla H_r(\underline{x})$ at any given point in the aquifer. If we denote by B_r a random variable such that $B_r \underline{e}_r \overset{d}{=} -K_r(\underline{x})\nabla H_r(\underline{x}) = \underline{q}_r(\underline{x})$. Then for any r, $r_1 \geq 1$, the specific flows $\underline{q}_r$ satisfy the scaling relation

$$\underline{q}_{r_1}(\underline{x}) \overset{d}{=} (B_r \underline{R}_r).\underline{q}_{r_1}\left(r\underline{R}_r^T \underline{x}\right) \qquad \underline{x} \in \Omega_r \tag{4.54}$$

A direct implication of Eq. (4.54) is that the flow amplitudes q_r scale as

$$q_{r_1}(\underline{x}) \overset{d}{=} B_r.q_r\left(r\underline{R}_r^T \underline{x}\right) \qquad \underline{x} \in \Omega_r \tag{4.55}$$

Equations (4.54) and (4.55) have the form of the generalized scale invariance relations, with random scaling parameters B_r and $\underline{e}_r$. The distribution of these parameters is presented in the next section.

4.2.2 Distribution of the Scaling Parameters B_r and $\underline{e}_r$

The distribution of $\underline{e}_r$ has already been discussed in Sec. 4.1.2 and B_r has the same distribution as $K_r(\underline{x})J_r(\underline{x})$ at a generic point of the aquifer. To derive the joint distribution of the log conductivity F_r and the log hydraulic gradient amplitude $\ln(J_r)$ the variance of F_r is first obtained by integrating the spectral density function of $F_r(\underline{x})$ given in Eq. 4.2. This gives

$$\mathrm{Var}[F_r] = \frac{2}{S_D} C_K \int_{k_o}^{rk_o} k^{-D} d\underline{k} = \frac{2}{S_D} C_K S_D \int_{k_o}^{rk_o} k^{-1} dk = 2C_K \ln(r) \qquad (4.56)$$

Since F_r has normal distribution and $E\left[e^{F_r}\right] = E[K_r] = 1$, it must be

$E[F_r] = -\frac{1}{2}\mathrm{Var}[F_r] = -C_K \ln(r)$. The mean and variance of $\ln(J_r)$ have been previously derived and presented in Eq. (4.42) as

$$\begin{cases} E\left[\ln\left(J_r\right)\right] = \dfrac{D-4}{D(D+2)} C_K \ln(r) \\ \mathrm{Var}\left[\ln\left(J_r\right)\right] = \dfrac{6}{D(D+2)} C_K \ln(r) \end{cases}$$

What remains to be calculated is the covariance between F_r and $\ln\left(J_r\right)$. From Eq. (4.38) and the fact that the terms ∇h_{r_i} in that equation are infinitesimal, one concludes that the variability of $\ln\left(J_r\right)$ is the same as the variability of $-\nabla h_{r_i}$. Using $\nabla \hat{h}_r\left(d\underline{k}\right) = \left(\underline{k}\,'k\,'_1\right)\hat{F}_r\left(d\underline{k}\right)$ (see Eq. (4.32)), the spectral measure of $-\nabla h_{r_i}$ is $-k\,'^2_1 \hat{F}_r\left(d\underline{k}\right)$ where $k\,'_1$ is the first component of the vector $\underline{k}/k$. Therefore,

$$\begin{aligned} \mathrm{Cov}\left[F_r, \ln\left(J_r\right)\right] &= -\frac{2}{S_D} C_K \int_{k_o}^{rk_o} k\,'^2_1 k^{-D} d\underline{k} \\ &= -2 \underset{D}{E}\left[e_1^2\right] C_K \ln(r) = -\frac{2}{D} C_K \ln(r) \end{aligned} \tag{4.57}$$

where e_1 is the first component of a random vector with uniform distribution on the D-dimensional unit sphere and the expectation $\underset{D}{E}\left[e_1^2\right] = \dfrac{1}{D}$ from Section 4.1.2.

The joint normality of F_r and $\ln\left(J_r\right)$ follows from the fact that F_r is normally distributed and $\ln\left|\nabla H_r\right|$ is linearly related to F_r. Hence F_r and $\ln\left|\nabla H_r\right|$ have bivariate normal distribution with parameters

$$\begin{cases} E[F_r] = -C_K \ln(r) \\ E[\ln(J_r)] = \dfrac{D-4}{D(D+2)} C_K \ln(r) \\ Var[F_r] = 2C_K \ln(r) \\ Var[\ln(J_r)] = \dfrac{6}{D(D+2)} C_K \ln(r) \\ Cov[F_r, \ln(J_r)] = -\dfrac{2}{D} C_K \ln(r) \end{cases} \tag{4.58}$$

Hence, B_r has lognormal distribution with parameters

$$\begin{cases} E[\ln(B_r)] = E[F_r] + E[\ln(J_r)] = \left[\dfrac{D-4}{D(D+2)} C_K \ln(r) \right] \\ Var[\ln(B_r)] = Var[F_r] + Var[\ln(J_r)] + 2Cov[F_r, \ln(J_r)] \\ \qquad\qquad = \dfrac{2(D^2-1)}{D(D+2)} C_K \ln(r) \end{cases} \tag{4.59}$$

and initial moments

$$E[B_r^s] = \exp\left\{ E[\ln(B_r)]s + \frac{1}{2} Var[\ln(B_r)]s^2 \right\} = r^{W_{q,b}(s)}$$
$$= r^{C_K\left[-\frac{D+5}{D(D+2)}s + \frac{D^2-1}{D(D+2)}(s^2-s) \right]} \tag{4.60}$$

For s = 1, Eq. (4.60) gives

$$E[B_r] = r^{-\frac{D+5}{D(D+2)}C_K} \tag{4.61}$$

From Eq. (4.61) one observes that $E[B_r] < 1$ and $\lim_{r\to\infty} E[B_r] = 0$ for any finite D. Also, $\lim_{D\to\infty} E[B_r] = 1$ for any given $r > 1$. The fact that $\lim_{r\to\infty} E[B_r] = 0$ is especially important: it implies that the expected flow amplitude vanishes asymptotically as the hydraulic conductivity is developed to infinite resolution. This behavior of q_r can be understood by examining the relation between the log-conductivity $F_r(\underline{x})$ and the log hydraulic gradient amplitude $\ln[J_r(\underline{x})]$ at any given point $\underline{x}$. If we denote ρ as the correlation coefficient between F_r and $\ln(J_r)$, then

$$\rho = \frac{\mathrm{cov}[F_r, \ln(J_r)]}{\sqrt{\mathrm{Var}[F_r]\mathrm{Var}[\ln(J_r)]}} = \frac{-(2/D)C_K \ln(r)}{\sqrt{2C_K \ln(r)(6/D(D+2))C_K \ln(r)}} = -\sqrt{\frac{D+2}{3D}} \tag{4.62}$$

The negative correlation between $F_r(\underline{x})$ and $\ln[J_r(\underline{x})]$ explains why the expected flow amplitude vanishes asymptotically as the hydraulic conductivity is developed to infinite resolution. From Eq. (4.62) one observes that ρ does not depend on the resolution r but varies with the space dimension D. In particular, ρ = -1, -0.817 and –0.745 for D = 1, 2 and 3 respectively. The value ρ = -1 for D = 1 corresponds to the fact that the hydraulic gradient J must balance the hydraulic conductivity K to ensure constant flow. In two and

three dimensions, the correlation between $F_r(\underline{x})$ and $\ln[J_r(\underline{x})]$ is smaller because the fluid can follow alternative paths and can avoid regions of low conductivity. It is interesting to note that ρ does not vanish as $D \to \infty$; rather it asymptotically approaches the value $-1/\sqrt{3} = -0.577$. For numerical validation in two dimensions, ρ has been calculated for K fields with $C_K = 0.1$ and 0.3 as well as for bare and partially dressed fields at lower resolutions r. The results are presented in Chapter 6 and show a very good agreement between the numerical and theoretical results.

4.2.3 Marginal distributions of bare flows

The distributions of B_r and $\underline{e}_r$ derived in Sec. 4.2.2 can be used to find the marginal distribution of the bare flow $\underline{q}_r$ and its amplitude q_r at any finite resolution r. For the flow amplitudes q_r, $q_{r_1}(\underline{x}) \overset{d}{=} B_r . q_r\left(r\underline{R}_r^T \underline{x}\right)$ (Eq. (4.32)) is written in the marginal form

$$q_{r_1}(\underline{x}) \overset{md}{=} B_r . q_{r_1}(\underline{x}) \tag{4.63}$$

where $\overset{md}{=}$ stands for equality of the marginal distributions and $\left(r\underline{R}_r^T \underline{x}\right)$ on the right hand side of Eq. 4.34 has been replaced with $\underline{x}$ because $q_{r_1}(\underline{x})$ is a statistically homogeneous field.

From Eq. (4.63) and the fact that $q_1(\underline{x}) \equiv 1$, where $q_1(\underline{x})$ is the specific flow amplitude for r =1, that corresponds to a constant hydraulic conductivity $K_1(\underline{x}) \equiv E[K] = 1$, one can conclude that the marginal distribution of $q_r(\underline{x})$ is the same as the distribution of B_r, i.e. is lognormal with the moments

$$\begin{cases} E\left[\ln(B_r)\right] = E\left[F_r\right] + E\left[\ln(J_r)\right] = \left[\dfrac{D-4}{D(D+2)} C_K \ln(r)\right] \\ Var\left[\ln(B_r)\right] = Var\left[F_r\right] + Var\left[\ln(J_r)\right] + 2Cov\left[F_r, \ln(J_r)\right] \\ \qquad\qquad = \dfrac{2(D^2-1)}{D(D+2)} C_K \ln(r) \end{cases}$$

which have been given in Eq. (4.59). The marginal distribution of the flow vector $\underline{q}_r(\underline{x})$ can be obtained through a similar argument. Due to the boundary conditions the specific discharge field $\underline{q}$ is anisotropic at large scales and becomes locally isotropic as the resolution $r \to \infty$.

The marginal form of $q_{\pi_1}(\underline{x}) \overset{d}{=} B_r . q_r\left(r\underline{R}_r^T \underline{x}\right)$ is written as

$$\underline{q}_{\pi_1}(\underline{x}) \overset{md}{=} (B_r \underline{R}_r) . \underline{q}_{\pi_1}(\underline{x}) \qquad (4.64)$$

It is worth noting that for $K_1(\underline{x}) \equiv 1$, $\underline{q}_1(\underline{x}) \equiv \underline{e}$ where $\underline{e}$ is the unit vector along the x_1 – axis; these boundary conditions cause the flow field to be anisotropic at the large scale and locally isotropic as $r \to \infty$. Consequently, for any $r \geq 1$, the marginal distribution of

$\underline{q}_r(\underline{x})$ is the same as the distribution of $B_r \underline{e}_r$, where $\underline{e}_r$ is the first column of the random matrix $\underline{R}_r$. From Eq. (4.59), B_r has lognormal distribution and from Eq. (4.46) $\underline{e}_r$ has the Brownian motion distribution on the unit D-dimensional sphere. A simple analytical expression for the marginal distribution of $\underline{q}_r(\underline{x})$ cannot be obtained because the Brownian motion distribution of $\underline{e}_r$ does not have a simple explicit form. However, an explicit expression can be obtained for the mean value of $\underline{q}_r(\underline{x})$, which is directly related to the effective hydraulic conductivity. Since B_r and $\underline{e}_r$ are independent, $E[\underline{q}_r(\underline{x})] = E[B_r]E[\underline{e}_r]$ where $E[B_r]$ is given by Eq. (4.60). Relying on the fact that vector $\underline{J}_r$ has mean value $\underline{e}$, the unit vector in the direction of x_1, $\underline{J}_r$ can be written as $\underline{J}_r = J_r \cdot \underline{e}_r$, where J_r and $\underline{e}_r$ are independent. Taking the expectation of the left and right hand sides of $\underline{J}_r = J_r \cdot \underline{e}_r$ one obtains

$$E[\underline{J}_r] = E[J_r].E[\underline{e}_r] = \underline{e} \tag{4.65}$$

From Eq. (4.43)

$$E[J_r] = r^{\frac{D-1}{D(D+2)}C_K} \tag{4.66}$$

Substituting Eq. (4.66) into (4.65) one can obtain an expression for $E[\underline{e}_r]$ as

$$E[\underline{e}_r] = r^{-\frac{D-1}{D(D+2)}C_K}\underline{e} \tag{4.67}$$

The expression for $E\left[\underline{q}_r(\underline{x})\right] = E[B_r]E[\underline{e}_r]$ is obtained by substituting the expression for $E[B_r]$ from Eq. (4.61) and $E[\underline{e}_r]$ from Eq. (4.67) so that $E\left[\underline{q}_r(\underline{x})\right]$ is given by

$$E\left[\underline{q}_r(\underline{x})\right] = r^{-\left[\frac{D+5}{D(D+2)}+\frac{D-1}{D(D+2)}\right]C_K}\underline{e} = r^{-\frac{2}{D}C_K}\underline{e} \tag{4.68}$$

and its length is

$$\left|E\left[\underline{q}_r(\underline{x})\right]\right| = r^{-\frac{2}{D}C_K} \tag{4.69}$$

The above equation shows that the mean flow amplitude decreases as the resolution of the conductivity field r increases. In fact, the flow is non-conservative and vanishes asymptotically as $r \to \infty$. The mean flow amplitude $r^{-\frac{2}{D}C_K}$ may be interpreted as the effective conductivity of the medium. It is worth noting that the expected value of the flow amplitude, $E\left[q_r(\underline{x})\right] = E\left[\left|\underline{q}_r(\underline{x})\right|\right]$ (which is the same as $E[B_r] = r^{-\frac{D+5}{D(D+2)}C_K}$ in Eq. (4.61)) and the amplitude of the expected flow vector $\left|E\left[\underline{q}_r(\underline{x})\right]\right|$ in Eq. (4.69) scale differently with the resolution r and that, for $D > 1$, the latter quantity has a larger negative decay exponent. For D = 1, the two quantities coincide and $E\left[q_r(\underline{x})\right] = E\left[\left|\underline{q}_r(\underline{x})\right|\right] = \left|E\left[\underline{q}_r(\underline{x})\right]\right| = r^{-2C_K}$.

4.2.4 Moment Scaling Function of q

In this section, the moment scaling function of the flow amplitude fields $q_r(\underline{x})$ is derived. In this derivation one must account for the non-conservative nature of the flow vector $\underline{q}$, that is, the average flow $E[\underline{q}_r(\underline{x})]$ vanishes asymptotically as $r \to \infty$. Consequently, the bare and partially dressed flows have different moment scaling properties and different moment scaling functions, which are denoted by $W_{q,b}(s)$ and $W_{q,d}(s)$, respectively.

We begin with the bare moments, which are moments of the flow fields $q_r(\underline{x})$ developed to different resolutions r. From Eq. (4.60) we have

$$W_{q,b}(s) = \left[-\frac{D+5}{D(D+2)}s + \frac{D^2-1}{D(D+2)}(s^2 - s) \right] C_K \tag{4.70}$$

The interpretation of $W_{q,b}(s)$ in Eq. (4.70) is similar to that of $W_J(s)$ in Eq. (4.44). However, the coefficients of s and $(s^2 - s)$ in the two equations are different. For example the coefficient in Eq. (4.70) is negative because $E[q_r]$ decreases with increasing r, whereas the same coefficient in Eq. (4.44) is positive because $E[J_r]$ increases with r.

The moment scaling function in Eq. (4.70) is non-observable, since it refers to flow fields at different resolutions. What one can observe is the field $\underline{q}_{r_o}(\underline{x})$ at some fixed resolution r_o, from which partially dressed flow fields at lower resolutions can be obtained through spatial averaging.

Next, we consider the scaling of partially dressed flow fields. These fields are obtained by taking a bare flow field $\underline{q}_{r_o}(\underline{x})$ at some fixed resolution r_o and spatially averaging it to obtain fields of lower resolution. The variability and orientation of the bare field $\underline{q}_{r_o}(\underline{x})$ and the partially dressed fields are similar. However, main difference between the two is that the for bare flows the average flow depends on the resolution to which the field is developed (see Eq. (4.68)), and as the resolution $r \to \infty$ the mean flow tends to zero. The dependence of the mean flow on the resolution is described as a non-conservative property of the bare flow field. The mean flow for the partially dressed flow field depends on the resolution r_o of the bare field from which lower resolution flow fields will be obtained. These lower resolution fields are obtained by spatially averaging the original bare flow field and have the same mean value. Thus, the partially dressed flow field is conservative because the mean flow does not change as the higher resolution field is spatially averaged to obtain lower resolution flow fields. Therefore a good approximation to the moment scaling function for the partially dressed flow amplitudes, $W_{q,d}(s)$, results from dividing B_r by the non-conservative factor $r^{-\frac{2}{D}C_K}$ in Eq. (4.69). This corresponds to changing $E[\ln(B_r)]$ in Eq. (4.59) to

$$\left[\frac{D-4}{D(D+2)}-1+\frac{2}{D}\right]C_K \ln(r)=-\frac{D-1}{D+2}C_K \ln(r) \tag{4.71}$$

In particular Eq. (4.59) becomes

$$\begin{cases} E\left[\ln(B_r)\right]=\left[-\dfrac{D-1}{D+2}C_K \ln(r)\right] \\ Var\left[\ln(B_r)\right]= \dfrac{2(D^2-1)}{D(D+2)}C_K \ln(\gamma r) \end{cases} \tag{4.72}$$

where γ is a factor that measures the variance of the partially dressed field when r = 1. It has been found through numerical simulations that $\gamma \approx 1+2C_K$. The introduction of the factor γ does not allow one to obtain an explicit expression for moment scaling function of partially dressed flow fields $W_{q,d}(s)$.

A numerical validation of the theoretical results for the scaling of bare and dressed flow fields is presented in Chapter 6, where the empirical and partially dressed moment scaling functions of q are obtained for two-dimensional flow simulations for C_K values of 0.1 and 0.3 and compared with the theoretical results in this section. The results show a good agreement between the simulation and theoretical results.

Next, we consider in detail Eq. (4.69), $\left|E\left[\underline{q}_r(\underline{x})\right]\right| = r^{-\frac{2}{D}C_K}$ which is the effective hydraulic conductivity. The problem of determining the effective hydraulic conductivity is fundamental to the efficient numerical analysis of flow through heterogeneous media. In

the case of isotropic K, the effective hydraulic conductivity in a D-dimensional region S is a scalar quantity $K_{eff}(S)$ such that, when an average hydraulic gradient $\nabla H = -\underline{J}$ is applied to S, the mean specific flow $\underline{\bar{q}}(S)$ is given by

$$\underline{\bar{q}}(S) = K_{eff}(S)\underline{J} \tag{4.73}$$

It has long been recognized that $K_{eff}(S)$ differs from the mean conductivity $\bar{K} = E[K]$ and has been extensively researched (see reviews by Sanchez-Vila et al. (1995); Wen and Gomez-Hernandez (1996), and Renard and de Marsily (1997)). In the next section classic solutions of $K_{eff}(S)$ from exact 1D analysis and from first-order second moment analysis (FOSM) will be presented. These results will be compared with the $K_{eff}(S)$ in the case of finite resolution multifractal K in section 4.3.2.

4.3.1 Problem Formulation and solutions from exact 1D analysis and from FOSM

For a one-dimensional flow system, for example the flow through a saturated porous column, the zero-divergence Darcy equation is written as

$$\frac{d}{dx}\left(K\frac{dH}{dx}\right) = 0 \tag{4.74}$$

If it assumed that the specific discharge q through the column is known exactly from independent measurements, Eq. (4.74) can be integrated once, and after dividing through by the nonzero hydraulic conductivity:

$$\frac{dH}{dx} = -qK^{-1} \tag{4.75}$$

The goal is to find the solution for the head, H, when the hydraulic conductivity, or in this case its inverse, the hydraulic resistivity, varies in an irregular fashion of x, the distance along the column. Therefore, the hydraulic resistivity, $1/K$, will be regarded as a spatial stochastic process. Eq. (4.75) then becomes a stochastic differential equation in which the solution H will also be a random process. The random processes H and $1/K$ are written in terms of their expected value, or mean, plus a zero-mean perturbation, as follows:

$$\begin{aligned} H &= \overline{H} + h \qquad \overline{H} = E[H] \quad E[h] = 0 \\ 1/K &= \overline{P} + p \quad E[1/K] = \overline{P} \quad E[p] = 0 \end{aligned} \tag{4.76}$$

When the decompositions are substituted in Eq. (4.75), and we take the expected value of that equation,

$$E\left[\frac{dH}{dx}\right] = \frac{d\overline{H}}{dx} = -J = -qE\left[1/K\right] = -q\overline{P} \tag{4.77}$$

where J is the mean hydraulic gradient. Eq. (4.77) can be written in the form

$$q = J/E\left[K^{-1}\right] = K_{eff}J; \quad K_{eff} = \left\{E\left[K^{-1}\right]\right\}^{-1} \tag{4.78}$$

The above equation provides the classic solution for K_{eff} for the 1D case [Gelhar, 1993].

For $D > 1$ a form of the mean Darcy equation that applies to large-scale flow in heterogeneous porous media can be found by taking the expected value of the Darcy equation in the following form:

$$\begin{aligned} E[q_i] &= -E\left[K\frac{\partial H}{\partial x_i}\right] = -e^F E\left[e^f\left(\frac{\partial \overline{H}}{\partial x_i} + \frac{\partial h}{\partial x_i}\right)\right] \\ &= -K_o E\left[\left(1 + f + f^2/2 + \ldots\right)\left(\frac{\partial \overline{H}}{\partial x_i} + \frac{\partial h}{\partial x_i}\right)\right] \\ &= K_o\left[J_i\left(1 + \frac{\sigma_f^2}{2}\right) - E\left(\frac{\partial h}{\partial x_i} f\right) + \ldots\right] \end{aligned} \tag{4.79}$$

where hydraulic conductivity has been expressed in terms of the mean and perturbation forms of lnK:

$$\ln K = F + f; \quad E[\ln K] = F = \ln K_o; \quad E[f] = 0$$

and the exponential function expanded in the Taylor series [Gelhar, 1993]. The expected value of the product of the perturbations in the head gradient and lnK reflects the relationship between the conductivity variation and the head perturbation that it produces. This term can be evaluated using the spectral representation as follows:

$$E\left[\frac{\partial h}{\partial x_i} f\right] = \int_{\underline{k}} ik_i E\left[dZ_h dZ_f^*\right] = J_j \int_{\underline{k}} \frac{k_i k_j}{k^2 - iA_j k_j} S_{ff}(\underline{k}) d\underline{k} \tag{4.80}$$

where A and J are regarded as slowly varying functions of space that are treated as being locally constant [Gelhar, 1993]. The mean Darcy equation then can be written in the form

$$E[q_i] = K_o J_j \left[\left(1 + \sigma_f^2/2\right)\delta_{ij} - F_{ij}\right] = K_{eff} J_j \tag{4.81}$$

where $F_{ij} = \int_{\underline{k}} \frac{k_i k_j}{k^2 - iA_j k_j} S_{ff}(\underline{k}) d\underline{k}$, and the effective hydraulic conductivity tensor K_{eff} .

For a given flow situation, K_{eff} is determined by evaluating the F_{ij} integral.

For two-dimensional flow,

$$F_{ij} = \sigma_f^2 \delta_{ij}/2; \quad \delta_{ij} = 1 \text{ for } i = j \text{ and } 0 \text{ for } i \neq j \tag{4.82}$$

and the corresponding result is

$$K_{eff} = K_o \delta_{ij}; \quad i, j = 1, 2 \tag{4.83}$$

which shows that the effective conductivity is simply the geometric mean in the two-dimensional case.

4.3.2 Comparison with K_{eff} in the case of finite-resolution multifractal K

Suppose that the hydraulic conductivity K is lognormal multifractal field developed to resolution R beyond the scale of the region S. If the average value of K in S is denoted by $\overline{K}(S)$, then $\ln\left[K(\underline{x})\right]$ has normal marginal distribution,

$$\ln\left[K(\underline{x})\right] \approx N\left(\ln\left(\overline{K}\right) - C_K \ln(R),\ 2C_K \ln(R)\right) \tag{4.84}$$

where $C_K = \frac{1}{2}\mathrm{Var}\left[\ln(G_e)\right]$ and G_e is the multifractal scaling factor A_r in Eq. (4.1) for r = e. In this case Eq. (4.78) becomes

$$K_{eff} = \left\{E\left[K^{-1}\right]\right\}^{-1} = 1/\exp\left\{-\ln \overline{K} R^{-C_K} + \ln R^{C_K}\right\} = \overline{K} R^{-2C_K} \tag{4.85}$$

And Eq. (4.83) can be written as

$$K_{eff} = \exp\left(\ln \overline{K} - C_K \ln R\right) = \overline{K} R^{-C_K} \tag{4.86}$$

Eqs. (4.85) and (4.86) are clearly different in the dependence on R. Eq. (4.85) is exact for flow in one dimension but not for flow in higher dimensions.

An alternate approach that exploits the scaling properties of K field can be obtained when K is an isotropic multifractal field. From the scaling analysis presented in section 4.2 (see in particular Eq. (4.69)), $\underline{\bar{q}}(S) = \bar{K}(S) R^{-(2/D)C_K} \underline{J}$. Therefore the expression for the effective hydraulic conductivity is

$$K_{eff}(S) = \bar{K}(S) R^{-\frac{2}{D}C_K} \tag{4.87}$$

For D = 1, Eq. (4.87) reproduces Eq. (4.85), which for this case is known to be exact. For D = 2, Eq. (4.87) reproduces (4.86). Eq. (4.87) provides an expression for K_{eff} that shows its dependence on the space dimension D, the erraticity of the field C_K and the resolution to which the K field is developed R. It is interesting to note that Eq. (4.87) is a restatement of Matheron's (1967) conjecture that the effective conductivity of a D-dimensional flow system is

$$K_{eff}(S) = K_o \exp\left[\sigma_F^2\left[\frac{1}{2} - \frac{1}{D}\right]\right] = e^{m_F + \left(\frac{1}{2} - \frac{1}{D}\right)\sigma_F^2} \tag{4.88}$$

where $m_F = E[\ln K] = K_o$

A validation of Eq. (4.87) for two-dimensional flow in K fields with $C_K = 0.1$ and 0.3 is provided in Chapter 6.

4.4 Comparison of the current approach with the results of random electrical conductivity networks by Bin Lin et al. (1991) and Archangelis et al. (1985)

In the derivation of the distribution of the hydraulic gradient ∇H and specific discharge $\underline{q}$ fields we assumed that the hydraulic conductivity field K to be an isotropic lognormal multifractal field. The K field served as the input into the zero divergence Darcy equation. The distributions of the hydraulic gradient ∇H and specific discharge $\underline{q}$ fields were obtained through a formal analysis using the renormalization approach. The results of Bin Lin et al. (1991) and Archangelis et al. (1985) for random electrical networks also assumes that the random resistors have a multifractal distribution. Next, they assume that voltage drops (which is analogous to ∇H) across the network also have a multifractal distribution. Thus, the current distribution across the electrical network is also shown to have a multifractal distribution. The two parameter hierarchical model used in studying the multifractal properties of random resistor networks is found to be in good agreement with simulation data.

Another notable difference between this work and that of Bin Lin et al. (1991) and Archangelis et al. (1985) is that whereas we specify a continuous probability distribution for the hydraulic conductivity field and obtain the distributions of ∇H and $\underline{q}$, Bin Lin et al. (1991) and Archangelis et al. (1985) model the random resistor with a discrete

probability distribution. Specifically, they model the random resistor network with a binomial distribution.

Finally, in deriving the properties of the hydraulic gradient ∇H and specific discharge $\underline{q}$ fields, we took into account their random rotations. The rotation of the vector quantities such as voltage is not considered in the work of Bin Lin et al. (1991) and Archangelis et al. (1985).

CHAPTER 5 – SPECTRAL ANALYSIS OF THE HYDRAULIC GRADIENT AND SPECIFIC DISCHARGE FIELDS

Introduction

Spectral densities play an important role in the characterization of hydraulic conductivity and the analysis of subsurface flow. In chapter 2, we reviewed the linear perturbation method that relies heavily on spectral methods in deriving the statistical properties of the hydraulic gradient and specific discharge fields. Results of the linear perturbation method are quite robust for media with low variance of the log-conductivity field. In chapter 4, the flow characteristics were studied for a highly fluctuating field. The analysis was limited to a field with an isotropic lognormal multifractal hydraulic conductivity. Hence, this chapter begins in section 5.1 with a derivation of the spectral density tensors of scalar random measures and their logarithms under isotropic multifractality. These conditions are satisfied by the hydraulic conductivity field K. The spectral density tensors of homogeneous random vector measures under generalized scale invariance conditions are then analyzed in section 5.2. Results from section 5.2 will be used in section 5.3 to derive the spectral density tensors of the hydraulic gradient and specific discharge fields.

The findings in this chapter differ from results of the first-order perturbation analysis in several significant ways:

1. The linear perturbation analysis produces homogeneous hydraulic gradient ∇H and specific discharge $\underline{q}$ fields with scale-invariant anisotropy. For example, the first-order spectral density tensors of ∇H and $\underline{q}$ scale in exactly the same way along any straight line from the origin; hence these tensors have the same

anisotropy at both small and high wavenumbers. By constrast, we obtain spectral tensors that are anisotropic at low wavenumbers (large scale) and gradually become isotropic at high wavenumbers (small scales). The current analysis accounts for the effects of the rotation angles of the ∇H and $\underline{q}$ vectors. As one moves from low to high wavenumbers in the flow domain, the dispersion of these rotation angles increase and become locally isotropic. It is the effect of these rotation angles that produce scale-dependent anisotropy in the spectral density tensors of ∇H and $\underline{q}$. The effects of these rotation angles are not accounted for in the first-order analysis.

2. The spectral density tensors of the hydraulic conductivity K, log-conductivity F, hydraulic gradient ∇H and specific discharge $\underline{q}$ obtained from the first-order analysis decay as k^{-D} along any given direction from the origin; k is the wavenumber vector amplitude and D is the space dimension. The analysis presented in this chapter produces different results:
   - We find different decay exponents for the spectra of K and F, when the hydraulic conductivity field is a lognormal multifractal field.
   - The behavior of the spectral density tensors of ∇H and $\underline{q}$ is more complex: in the small to medium wavenumber range, the tensors do not behave as power functions of k. This is due to the effect of the rotation matrices discussed above. At sufficiently high wavenumbers, the fields ∇H and $\underline{q}$ become isotropic and the tensors decay as power laws of k, with exponents that differ from those of F and K.

5.1 Spectral Analysis of ∇H and $\underline{q}$: First-order and Second-Order Analyses

In the linear perturbation analyses (e.g. Gelhar and Axness, 1983) reviewed in Chapter 2, the log-conductivity F = ln(K) and the hydraulic head H are expressed as $F=\overline{F}+f$ and $H=\overline{H}+h$, where $\overline{F}=E[F]$, $\overline{H}=E[H]$ and f and h are zero mean fluctuations from the mean values. Darcy's equation is then expressed in terms of the perturbation terms as

$$\begin{aligned} q &= -K\nabla H \\ &= -\exp\left(\overline{F}+f\right)\nabla\left(\overline{H}+h\right) \\ &= K_o\left(1+f+\frac{f^2}{2}+\ldots\right)\left(\underline{J}_o-\nabla h\right) \end{aligned} \qquad (5.1)$$

Under the condition that the perturbations f and h are small so that the higher-order terms may be neglected, the mean value of q is

$$E[q]=K_o\underline{J}_o$$

where $K_o=\exp\left(\overline{F}\right)$ and $-\nabla\overline{H}(\underline{x})=\underline{J}_o$. It is also assumed that $\underline{J}_o=J_o\underline{e}_1$ where $\underline{e}_1$ is the unit vector in the x_1 direction. Since $H(\underline{x})$ and $\underline{q}$ are proportional to J_o and $\underline{q}$ is

proportional to E[K], one may further put $J_o = 1$ and $\overline{K} = E[K] = 1$. Thus the mean-corrected specific discharge $\underline{q}' = \underline{q} - E[\underline{q}]$ is given by

$$\begin{aligned} q' &= K_o\left(1 + f + \frac{f^2}{2} + ...\right)(\underline{J}_o - \nabla h) - K_o \nabla h \\ &= K_o(\underline{J}_o f - \nabla h) = K_o(\underline{e}_1 f - \nabla h) \end{aligned} \tag{5.2}$$

Also the flow equation, $\nabla^2 H + \nabla F . \nabla H = 0$, may be expressed in terms of $\overline{F}$, $\overline{H}$ and the perturbation terms f and h. When the higher order terms in f and h are ignored, this gives

$$\nabla^2 h = \underline{e}_1 . \nabla f = \frac{\partial f}{\partial x_1} \tag{5.3}$$

Gelhar and Axness (1983) used Eqs. (5.2) and (5.3) to derive the power spectra of various quantities from the power spectrum of the log hydraulic conductivity F = ln(K). They found

$$\begin{aligned} &\text{(i)} \quad S'_K(\underline{k}) = K_o^2 S_F(\underline{k}) \\ &\text{(ii)} \quad S'_h(\underline{k}) = e_1^2 k^{-2} S_F(\underline{k}) \\ &\text{(iii)} \quad S'_{\nabla H}(\underline{k}) = e_1^2 (\underline{e}\underline{e}^T) S_F(\underline{k}) \\ &\text{(iv)} \quad S'_{\underline{q}}(\underline{k}) = K_o^2 \left[\underset{i,j=1,...,D}{(\delta_{i1} - e_1 e_i)(\delta_{j1} - e_1 e_j)} \right] S_F(\underline{k}) \end{aligned} \tag{5.4}$$

where k is length of $\underline{k}$, $\underline{e} = \underline{k}/k$ is the unit vector in the direction of $\underline{k}$, and the primed sign denotes first-order approximation. There is some controversy as to the form of the prefactor K_o^2 in Eq. (5.4)iv; see Dagan (1984), Ababou (1988) and Gelhar (1995). The small perturbation approach has been applied extensively to the study of flow through heterogeneous formations. A general outline for this methodology was first presented by Beran (1968) and extensions were later provided by several authors, e.g. Schwydler, 1962; Matheron, 1967; Bakr et al, 1978; Sagar, 1978, Gutjahr et al, 1978; Dettinger and Wilson, 1981 and later by Gelhar and Axness, 1983 and coworkers (Gelhar et al., 1984; Gelhar, 1987).

In the case of a flow field with multifractal hydraulic conductivity K, the variance of K diverges and the geometric mean $K_o \to 0$. Therefore, the spectral densities in Eq. (5.4)i and (5.4)iv are nonzero only if one limits the scaling range of K. In Sec. 5.3, we find that the vanishing behavior of the spectrum of $\underline{q}$ is qualitatively correct, but that of K is not.

Another problem with the first-order analysis is that all the spectral densities in Eq. (5.4) have incorrect power-law exponents. This is quite clear in Eq. (5.4)i because when K is an isotropic lognormal multifractal field in $\mathbb{R}^D$ the exact spectral densities of f and K have the form $S_f(\underline{k}) \propto k^{-D}$ and $S_K(\underline{k}) \propto k^{-D+2C_K}$, respectively (these equations will be discussed in detail in the next section). The term $2C_K$ in the expression for $S_K(\underline{k})$ is a positive constant, which in practice might range between 0.2 and 0.8 depending on the erraticity of the K field. Therefore, the error in the decay exponent of

the first-order spectrum S_K' may be substantial. The exponents in Eqs. (5.4)i-iv contain similar errors.

Another problem with the first-order spectra of ∇H and $\underline{q}$ is that they have scale-invariant anisotropy. By contrast, sections 5.4 and 5.5 will discuss how the actual spectral tensors are anisotropic for small k and gradually become isotropic for large k.

A second-order spectral analysis of the hydraulic head fluctuation h has been made by Dagan (1985) and presented in Chapter 2. His results are shown in Chapter 2 for the case when the log-hydraulic conductivity has a spectral density of the type $S_f(\underline{k}) \propto k^{-\alpha}$. It is found that, in the case of multifractal K (when $\alpha = D$), the second-order correction to $S_h'(\underline{k})$ diverges and is therefore not useful.

A case that is pertinent to the present analysis and for which first-order theory is exact is when the hydraulic conductivity equals $K_1(\underline{x})$, the first term is the sequence of hydraulic conductivities $K_j(\underline{x})$ is used to analyze scaling issues. This case is important because the first-order theory is exact when the resolution to which the hydraulic conductivity field is developed r is close to 1; this means that the K field is almost deterministic and contains a low content of high frequency data. In this case, the fluctuations f and h are infinitesimal and the geometric mean K_o satisfies $K_o = \overline{K} = 1$. Further using the spectrum of F for isotropic lognormal K fields, $S_F(\underline{k}_o) = \frac{2}{S_D} C_K k_o^{-D}$, one obtains from Eqs. (5.4)iii and (5.4)iv that, for $\underline{k} = \underline{k}_o$,

$$\text{(i)}\quad \underline{S}_h(\underline{k}_o)=\left(\frac{2}{S_D}C_K k_o^{-D-2}\right)e_1^2$$

$$\text{(ii)}\quad \underline{S}_{\underline{q}}(\underline{k}_o)=\left(\frac{2}{S_D}C_K k_o^{-D}\right)\left(\underset{i,j=1,\ldots,D}{(\delta_{i1}-e_1e_i)(\delta_{j1}-e_1e_j)}\right) \tag{5.5}$$

where the prime signs have been omitted because these results are nonlinear. Because the first-order theory was obtained for K fields with mildly varying heterogeneities, the spectral results obtained for a deterministic field, where k has been set to k_o, as done in Eq. (5.5), produces exact results. The results in Eq. (5.5) serve as the starting point for deriving the spectral density tensors for ∇H and $\underline{q}$ in multifractal K fields. For this analysis, one needs to know how the spectral density tensors of ∇H and $\underline{q}$ change under rotation and isotropic contraction of the support. These transformations are presented in Sec 5.2.

5.2 Isotropically Multifractal Measures and their logarithms

An isotropic multifractal measure K(S), $S\subset\mathbb{R}^D$ with an associated measure density $\overline{K}(S)=K(S)/|S|$ satisfies the scale invariance condition

$$\overline{K}(S)\overset{d}{=}A_r\overline{K}(rS) \tag{5.6}$$

where $\overset{d}{=}$ denotes the equality of all finite dimensional distributions and A_r is a random variable independent of $\overline{K}(rS)$. The function $W_K(s)=\log_r\left(E\left[A_r^s\right]\right)$ is called the moment scaling function of K. If K is a lognormal multifractal measure, then A_r also has a lognormal distribution and

$$W_K(s)=C_K\left(s^2-s\right) \tag{5.7}$$

where $C_K=\frac{1}{2}\mathrm{Var}\left[\ln(A_r)\right]$ is a parameter with values between 0 and D.

In addition, the average measure density $\overline{K}(S)$ has Fourier representation (Yaglom, 1987)

$$\overline{K}(S)=\frac{1}{|S|}\int_{\mathbb{R}^D}\hat{I}_S(\underline{k})\hat{K}(d\underline{k}) \tag{5.8}$$

where $|S|$ is the volume of S, $\hat{I}_S(\underline{k})$ is the D-dimensional Fourier transform of the indicator function of S, and $\hat{K}(d\underline{k})$ is a complex measure in Fourier space. Since $\hat{I}_{rS}(\underline{k})=r^D\hat{I}_S(r\underline{k})$ and the volume of rS is $r^D|S|$, substitution of Eq. 5.8 into Eq. 5.6 gives

$$\begin{aligned}\frac{1}{|S|}\int_{\mathbb{R}^D}\hat{I}_S(\underline{k})\hat{K}(d\underline{k})&\overset{d}{=}r^D\frac{1}{r^D|S|}A_r\int_{\mathbb{R}^D}\hat{I}_S(r\underline{k})\hat{K}(d\underline{k})\\&\overset{d}{=}\frac{1}{|S|}A_r\int_{\mathbb{R}^D}\hat{I}_S(\underline{k}')\hat{K}(d\underline{k}'/r)\end{aligned} \tag{5.9}$$

where $\underline{k}' = r^D \underline{k}$. Eq. (5.9) must hold for S, hence, the spectral measure $\hat{K}(d\underline{k})$ must satisfy

$$\hat{K}(d\underline{k}) \overset{d}{=} A_r \hat{K}(d\underline{k}/r) \qquad r \geq 1 \tag{5.10}$$

Eq. (5.10) is a dual property of Eq. (5.6), $\overline{K}(S) \overset{d}{=} A_r \overline{K}(rS)$ in Fourier space. An important difference between the two scaling conditions is that K is multifractal under contraction, whereas $\hat{K}$ is multifractal under dilation. In addition, K is homogeneous, whereas $\hat{K}$ is non-homogeneous.

If the spectral density $S_K(\underline{k}) = \dfrac{E\left[\left|\hat{K}(d\underline{k})\right|^2\right]}{d\underline{k}}$ exists, then from Eq. (5.10)

$$S_K(\underline{k}) = r^{-D} E\left[A_r^2\right] S_K(\underline{k}/r) \tag{5.11}$$

Since $E\left[A_r^2\right] = r^{W_K(2)}$, then Eq. (5.11) can be written as

$$S_K(k\underline{e}) = k^{-D+W_K(2)} S_K(\underline{e}) \tag{5.12}$$

where $\underline{e}$ is any given unit vector.

In order to derive the spectral density of the logarithm of K, the sequence of low-passed fields $\overline{K}_j(\underline{x})$ obtained by eliminating all Fourier components of $\ln(\overline{K})$ with

wavenumbers $|k| > r^j k_o$ is considered. In other words, we consider a cascade of "bare" K fields with resolutions $r_j = (1+\varepsilon)^j$, where j = 1, 2, etc and $0 < \varepsilon \ll 1$. With the high-wavenumber components eliminated, the point values $\overline{K}_j(\underline{x})$ exist. The average value of $\overline{K}_j(\underline{x})$ in S is denoted by $\overline{K}_j(S)$.

If $\overline{K}(S) = \lim_{j\to\infty} \overline{K}_j(S)$ satisfies Eq. (5.6), then at least for large j,

$$\overline{K}_{j+1}(\underline{x}) \overset{d}{=} A_r \overline{K}_j(\underline{x}) \tag{5.13}$$

and

$$\ln\left(\overline{K}_{j+1}(\underline{x})\right) \overset{d}{=} \ln(A_r) + \ln\left(\overline{K}_j(r\underline{x})\right) \tag{5.14}$$

It follows that the spectral densities of $\ln\left(\overline{K}_{j+1}\right)$ and $\ln\left(\overline{K}_j\right)$ must satisfy

$$S_{\ln(\overline{K}_{j+1})}(\underline{k}) = r^D S_{\ln(\overline{K}_j)}(\underline{k}/r) \tag{5.15}$$

If as $j \to \infty$, $S_{\ln(\overline{K}_j)}$ converges to a finite limit $S_{\ln(\overline{K})}$ then this implies

(i) $S_{\ln(\overline{K})}(k\underline{e}) \propto k^{-D}$

or (5.16)

(ii) $S_{\ln(K)}(k\underline{e}) = k^{-D} S_{\ln(K)}(\underline{e})$

Eqs. (5.12) and (5.16) show that both S_K and $S_{\ln(K)}$ have a power law behavior along any direction in Fourier space, but have different decay exponents. In practice, the parameter C_K is expected to have values between 0.1 and 0.4 depending on how erratic the K field is, thus the two exponents might differ by 0.2 to 0.8. For Goggin's (1988) data analyzed in Chapter 3, we find $C_K = 0.25$, for which the two exponents in Eqs. (5.12) and (5.16) will differ by 0.5. This is an important result because according to first-order perturbation analysis the decay exponents are equal to D.

To determine the spectral density of F = lnK, one considers the sequence of low-passed fields $K_r(\underline{x})$ obtained by eliminating all Fourier components of ln(K) outside the range $k_o \le |\underline{k}| \le k_{max}$, where k_o is some positive constant. Having eliminated the high-wavenumber components, the point values $K_r(\underline{x})$ exist. The average value of $K_r(\underline{x})$ in Ω is denoted by $\overline{K}_r(\Omega)$.

Suppose that $\overline{K}(\Omega) = \lim_{r\to\infty} \overline{K}_r(\Omega)$ satisfies $\overline{K}(\Omega) \overset{d}{=} G_r \overline{K}(r\Omega)$. Then, at least for large r_1 and any $r \ge 1$,

$$K_{rr_1}(\underline{x}) \overset{d}{=} G_r K_{r_1}(r\underline{x}) \tag{5.17}$$

or

$$\ln\left(K_{r_1}(\underline{x})\right)\overset{d}{=}\ln(G_r)+\ln\left(K_{r_1}(r\underline{x})\right) \tag{5.18}$$

It follows that the spectral densities of $\ln\left(K_{r_1}\right)$ and $\ln\left(K_{r_1}\right)$ must satisfy $S_{\ln(K_{r_1})}(\underline{k})=r^{D}S_{\ln(K_{r_1})}(\underline{k}/r)$. If as $r\to\infty$ $S_{\ln(K_r)}$ converges to a finite limit $S_{\ln K}$, then this implies

$$S_{\ln K}(k\underline{e})\propto k^{-D} \tag{5.19}$$

In the isotropic case Eq. (5.19) gives

$$S_{\ln K}(\underline{k})=ck^{-D} \tag{5.20}$$

for some c and k=|k|. Since G_r and $K_{r_1}(r\underline{x})$ are independent, then from Eq. (5.18),

$$\mathrm{Var}\left[\ln\left(K_{r_1}(\underline{x})\right)\right]=\mathrm{Var}\left[\ln(G_r)\right]+\mathrm{Var}\left[\ln\left(K_{r_1}(r\underline{x})\right)\right] \tag{5.21}$$

The spectral density of K_{r1} is the same as $S_{\ln K}$ in Eq. (5.20) in the interval $k_o\le k\le r_1k_o$ and is zero otherwise. Therefore using Eq. (5.21),

$$\begin{aligned}\mathrm{Var}\left[\ln(G_r)\right]&=\mathrm{Var}\left[\ln\left(K_{r_1}(\underline{x})\right)\right]-\mathrm{Var}\left[\ln\left(K_{r_1}(r\underline{x})\right)\right]\\&=c\int_{r_1k_o\le k\le r_1k_o}k^{-D}d\underline{k}=cS_D\ln(r)\end{aligned} \tag{5.22}$$

where S_D is the surface area of a unit ball in R^D; hence $S_1 = 2, S_2 = 2\pi, \quad S_3 = 4\pi$. Hence $c = \frac{1}{S_D}\frac{\mathrm{Var}\left[\ln(G_r)\right]}{\ln(r)}$, where for G_e lognormal with mean value 1, $\mathrm{Var}\left[\ln(G_e)\right] = \ln E\left[G_e^2\right] = W_K(2) = 2C_K$. Hence $c=2C_K/S_D$, and hence

$$S_{\ln K}(\underline{k}) = \frac{2}{S_D} C_K k^{-D} \tag{5.23}$$

5.3 Spectral Energy Tensors under Generalized Scale Invariance

In order to derive the spectral tensors of the hydraulic gradient ∇H and specific discharge $\underline{q}$ fields we consider a cascade of these quantities associated with the sequence of low-passed $\overline{K}_j$ fields obtained by eliminating all Fourier components of $\ln\left(\overline{K}\right)$ with wavenumbers $|k| > r^j k_o$; where the K fields have a resolutions $r_j = (1+\varepsilon)^j$, j =1, 2, etc. and $\varepsilon \ll 1$. The analysis of the hydraulic gradient ∇H and specific discharge $\underline{q}$ requires knowledge of the renormalization properties of the spectral density tensors of homogeneous vector fields $\underline{V}_j(\underline{x})$ that satisfy a multifractal relation of the type

$$\underline{V}_{j+1}(\underline{x}) \overset{d}{=} A_r\left[\underline{R}_r \underline{V}_j\left(r\underline{R}_r^T \underline{x}\right)\right] \tag{5.24}$$

where A_r is a random variable and $\underline{R}_r$ is a random rotation matrix, independent of A_r. In Eq (5.24), the expression in brackets is a transformed version of $\underline{V}_j(\underline{x})$, obtained by spatially contracting by a factor r and rotating the field by $\underline{R}_r$. Denoting this transformed vector field by $\underline{V}_j'(\underline{x}) = \underline{R}_r \underline{V}_j\left(r\underline{R}_r^T \underline{x}\right)$, for any given rotation matrix $\underline{R}_r$, the spectral density of $\underline{V}_j'$, $\underline{S}_{\underline{V}_j'}(\underline{k})$ can be obtained from the spectral density tensor of $\underline{V}_j$ as

$$\underline{S}_{\underline{V}_j'}(\underline{k}) = r^{-D}\left[\underline{R}_r \underline{S}_{\underline{V}_j}\left(\frac{1}{r}\underline{R}_r^T \underline{k}\right)\underline{R}_r^T\right] \tag{5.25}$$

If the rotation matrix $\underline{R}_r$ is random, then the expectation on the right hand side of Eq. (5.25) must be taken with respect to $\underline{R}_r$. This gives

$$\underline{S}_{\underline{V}_j'}(\underline{k}) = r^{-D} \underset{\underline{R}_r}{E}\left[\underline{R}_r \underline{S}_{\underline{V}_j}\left(\frac{1}{r}\underline{R}_r^T \underline{k}\right)\underline{R}_r^T\right] \tag{5.26}$$

Finally, using Eq. (5.24) and $E\left[A_r^2\right] = r^{W(2)}$, the spectral density tensors $\underline{S}_{\underline{V}_j}$ and $\underline{S}_{\underline{V}_{j+1}'}$ are related as

$$\underline{S}_{\underline{V}_{j+1}'}(\underline{k}) = r^{-D+W(2)} \underset{\underline{R}_r}{E}\left[\underline{R}_r \underline{S}_{\underline{V}_j}\left(\frac{1}{r}\underline{R}_r^T \underline{k}\right)\underline{R}_r^T\right] \tag{5.27}$$

Having discussed the above properties of spectral tensors, a discussion on the nonlinear spectral analysis of ∇H and $\underline{q}$ follows.

5.4 Nonlinear Spectral Analysis of ∇H

The spectral analysis of the hydraulic gradient field ∇H and specific discharge field $\underline{q}$ is based on the multifractal scaling of these two parameters, which was derived in Chapter 4. Scaling relations obtained for ∇H_j and $\underline{q}_j$ at different resolution levels are

$$\begin{aligned} &\text{(i)}\quad \nabla H_{j+1}(\underline{x}) \overset{d}{=} A_r \underline{R}_r \nabla H_j\left(r\underline{R}_r^T \underline{x}\right) \\ &\text{(ii)}\quad \underline{q}_{j+1}(\underline{x}) \overset{d}{=} B_r \underline{R}_r \underline{q}_j\left(r\underline{R}_r^T \underline{x}\right) \end{aligned} \tag{5.28}$$

It follows from Eqs. (5.28)i and (5.27) and the independence of A_r and $\underline{R}_r$ that

$$\underline{S}_{\nabla H_{j+1}}(\underline{k}) = r^{-D} E\left[A_r^2\right] \underset{\underline{R}_r}{E}\left[\underline{R}_r \underline{S}_{\nabla H_j}\left(\underline{R}_r^T \underline{k}/r\right)\underline{R}_r^T\right] \tag{5.29}$$

As $j \to \infty$, ∇H_j tends to a non-degenerate random measure ∇H and $\underline{S}_{\nabla H_j}(\underline{k})$ converges to a spectral tensor $\underline{S}_{\nabla H}(\underline{k})$ that satisfies

$$\underline{S}_{\nabla H}(\underline{k}) = r^{-D+2\frac{C_K}{D}} \underset{\underline{R}_r}{E}\left[\underline{R}_r \underline{S}_{\nabla H}\left(\underline{R}_r^T \underline{k}/r\right)\underline{R}_r^T\right] \tag{5.30}$$

where $E\left[A_r^2\right] = r^{w_J(2)} = r^{2\frac{C_K}{D}}$ (for s = 2) has been substituted into Eq. (5.26). Further using the relation $\underline{\underline{S}}_{\nabla H}(\underline{k}) = \left(\underline{k}\underline{k}^T\right) S_h(\underline{k})$, the term in the brackets in Eq. (5.30) may be written as

$$\underline{\underline{R}}_r \underline{\underline{S}}_{\nabla H}\left(\underline{\underline{R}}_r^T \underline{k}/r\right)\underline{\underline{R}}_r^T = \left(\frac{\underline{k}}{r}\frac{\underline{k}^T}{r}\right) S_h\left(\underline{\underline{R}}_r^T \underline{k}/r\right) \tag{5.31}$$

On the right hand side of Eq. (5.31), all rotation matrices $\underline{\underline{R}}_r$ except the one in the argument of S_h have disappeared. This simplification came from the fact that ∇H is a potential field, that is, ∇H is the gradient of a scalar field. Substitution of Eq. (5.31) into Eq. (5.30) gives

$$\underline{\underline{S}}_{\nabla H}(\underline{k}) = r^{-D+2\frac{C_K}{D}} \left(\frac{\underline{k}}{r}\frac{\underline{k}^T}{r}\right) \underset{\underline{\underline{R}}_r}{E}\left[S_h\left(\underline{\underline{R}}_r^T \underline{k}/r\right)\right] \tag{5.32}$$

Equation (5.32) relates the spectral tensor of ∇H at wavenumber $\underline{k}$ to S_h at some smaller rotated smaller wavenumber $\underline{\underline{R}}_r^T \underline{k}/r$. For example, in 2D the rotation matrix $\underline{\underline{R}}_r = \begin{bmatrix} \cos(\alpha_r) & -\sin(\alpha_r) \\ \sin(\alpha_r) & \cos(\alpha_r) \end{bmatrix}$, where α_r is a random angle with symmetric distribution about zero.

In order to obtain an explicit expression for $\underline{S}_{VH}$ from Eq. (5.32), it is assumed that, for $\underline{k} = \underline{k}_o$ (at the low-wavenumber end of the scaling range), the spectral density of h is evaluated correctly by Eq. (5.5)i. Then, setting $\underline{k} = r\underline{k}_o$, Eq. (5.32) becomes

$$\underline{S}_{VH}(r\underline{k}_o) = r^{-D+\frac{2}{D}C_K}\left(\underline{k}_o\underline{k}_o^T\right)\left(\frac{2}{S_D}C_K k_o^{-D-2}\right)\underline{E}_{\underline{\alpha}_r}\left[e_{r_1}^2\right]$$

$$= \begin{cases} \left(k_o^{-1}C_K\right)r^{-1+C_K} & \text{for } D = 1 \\ \left(\frac{1}{\pi}k_o^{-2}C_K\right)r^{-2+C_K}\left[b_r e_1^2 + (1-b_r)e_2^2\right]\left(\underline{e}\underline{e}^T\right) & \text{for } D = 2 \end{cases} \qquad (5.33)$$

where e_i is the i^{th} component of the unit vector $\underline{e} = \underline{k}_o / k_o$, e_{r_1} is the first component of $\underline{R}_r^T\underline{e}$ and $b_r = E\left[\cos^2(\alpha_r)\right]$. From Chapter 4, it is known that for D = 2, the angle α_r has normal distribution with zero mean and variance $\frac{2}{D(D+2)}C_K \ln(r)$ and that for D = 3, the distribution of α_r does not have a simple analytical form but can be accurately approximated by D-dimensional Fisher distributions.

The spectral density of $h = H - \overline{H}$ follows directly from Eq. (5.33) and is given by

$$\underline{S}_h(r\underline{k}_o) = r^{-D-2+\frac{2}{D}C_K}\left(\frac{2}{S_D}C_K k_o^{-D-2}\right)\underset{\underline{\alpha}_r}{E}\left[e_{r_1}^2\right]$$

$$= \begin{cases} \left(k_o^{-3}C_K\right)r^{-3+C_K} & \text{for } D = 1 \\ \left(\frac{1}{\pi}k_o^{-4}C_K\right)r^{-4+C_K}\left[b_r e_1^2 + (1-b_r)e_2^2\right] & \text{for } D = 2 \end{cases} \qquad (5.34)$$

The spectral results in Eqs. (5.33) and (5.34) have some interesting features:

1. The exponents of r in the two equations give the asymptotic high-frequency decay of the spectral densities. They differ from the first-order exponents, which are –D for ∇H and –(D+2) for h (see Eqs. (5.22)ii and (5.4)), due to the term $\frac{2}{D}C_K$. This term depends on the space dimension D and the erraticity of the K field through the parameter C_K. In order for h to exist, C_K must be between 0 and D; see Kahane and Peyriere (1976) and Schertzer and Lovejoy (1996). Hence the exponent in r of Eq. (5.28) is between –D and –(D+2), which is the range of spectral exponents for fractional Brownian surfaces.
2. The terms in the square brackets for D = 2 and D = 3 are anisotropy factors. For example in the D = 2 case, for r = 1 (at low frequencies), $\alpha_r = 0$ and $b_r = 1$; hence the term in square brackets equals e_1^2 as in first-order theory. For $r \to \infty$ (at very high frequencies), the variance of α_r diverges, $b_r \to 0.5$, and the term in square brackets $\to 1$. Hence, at very high frequencies the h and ∇H have isotropic fluctuations. This transition of h and ∇H from anisotropy to isotropy as one goes

from low to high frequencies is not predicted by first-order theory, according to which the fluctuations of H and VH have anisotropy at all scales (see Eq. 5.4)

3. The prefactor terms in Eqs. (5.33) and (5.34) differ from the prefactor terms in the first-order theory. Equations (5.33) and (5.34) express the prefactor in terms of the low-wavenumber cutoff k_o and C_K, a parameter that depends on the erraticity of the hydraulic conductivity field. The prefactor in the first-order theory K_o^2 is obtained from the Taylor's series expansion of the F=lnK field whereas the prefactors in Eqs. (5.33) and (5.34) were obtained in an exact manner by introducing lower and upper bounds for the spectrum of the F=lnK field.

For D = 2 and C_K = 0.1 and 0.3, contour plots of $S_h(r\underline{k}_o)$ are shown in Figures 5.1 and 5.2 respectively. Due to the power-law behavior of the function, the spectra and its argument have been transformed logarithmically, so that the contours represent $\log_{10}(S_h(r\underline{k}_o))$ and the axes represent $\log_{10}\left(\frac{k}{k_o}\right)$. The plots in Fig. 5.1 are for the spectral density tensors

$$\begin{cases} S_h(r\underline{k}_o) = \left(\frac{1}{\pi}k_o^{-4}C_K\right) r^{-4+C_K}\left[b_r e_1^2 + (1-b_r)e_2^2\right] & \text{Nonlinear Theory} \\ \underline{S}_h(r\underline{k}_o) = \left(\left(\frac{1}{\pi}k_o^{-4}C_K\right) r^{-4}\right) e_1^2 & \text{Linear Theory} \end{cases}$$

The spectra are computed as follows. We write $e_1 = \frac{k_1}{k}$ and $e_2 = \frac{k_2}{k}$ and let $k = \underline{e}\,'10^{k'}$. Then for $k_1', k_2' = 0\,(\pm 0.0156) \pm 4$, the spectra $S_h'(\underline{k}') = \log_{10} S_h\left(\underline{k} = \underline{e}\,'10^{k'}\right)$ is calculated and contoured. Contour plots for the head spectra shown in Fig. 5.1 have a log spacing of –4. The innermost contours have a log-spectral value of –4 and decreases radially with a value of –4, so that the outermost contour has a value of –20.

From Figure 5.1 the following interesting features can be observed:

1. The spectral density from linear theory decays at a faster rate than the spectra from the nonlinear theory. The decay exponent is –4 for the linear spectra and $-4+C_K$ for the nonlinear spectra, and
2. The contour lines for the spectral density from linear theory have the same non-circular shape at all scales, whereas those from nonlinear theory exhibit anisotropy at large scales and isotropy at small scales. The transition from anisotropy to isotropy is faster for larger values of C_K.

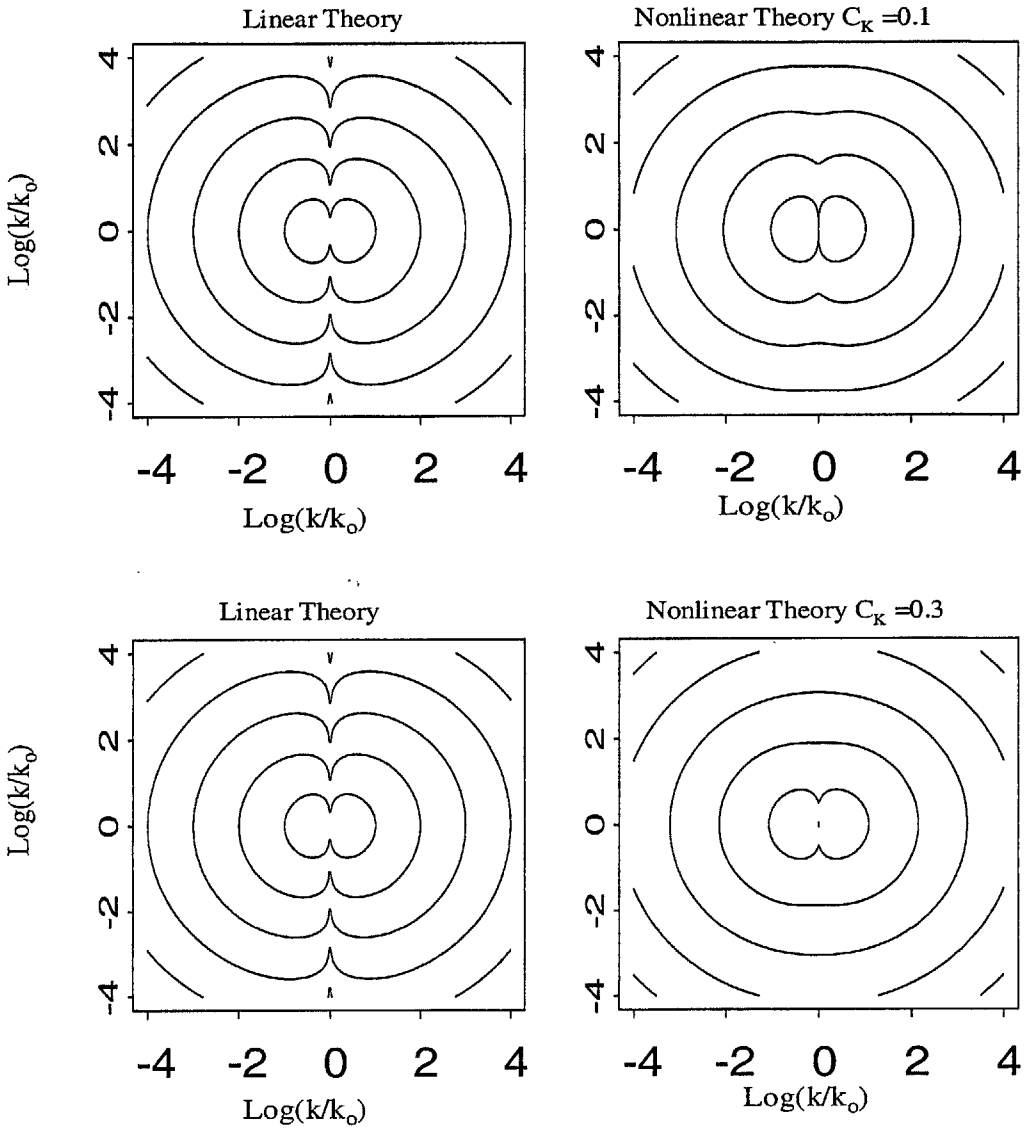

Figure 5.1 – Spectral contour of the head field for the linear and nonlinear theory

5.5 Nonlinear Spectral Analysis of Specific Discharge $\underline{q}$

The spectral analysis of the specific flow $\underline{q}$ follows closely that of the hydraulic gradient field ∇H with two main differences:

1. The hydraulic gradient field ∇H is conservative, i.e. its mean value does not depend on the resolution $r = k_{max} / k_o$ to which the conductivity field K is developed. The specific discharge $\underline{q}$, is however non-conservative, i.e. its mean value depends on r and approaches zero as $r \to \infty$. Also, the spectral density of $\underline{q}$ vanishes as $r \to \infty$; hence the spectral density tensors obtained here for $\underline{q}$ are for finite r.
2. The second difference is that ∇H is a potential field (it is the gradient of H), whereas $\underline{q}$ is a solenoidal field (due to the conservation of flow, $\underline{q}$ has zero divergence). The fact that $\underline{q}$ is not a potential field introduces some algebraic complications in the spectral analysis.

We begin by relating the spectral densities of $\underline{q}_{r_1}$ and $\underline{q}_{rr_1}$. From Eq. (5.28)ii we know that the scaling of $\underline{q}$ is

$$\underline{q}_{rr_1}(\underline{x}) \overset{d}{=} B_r \underline{R}_r \underline{q}_{r_1}\left(r\underline{R}_r^T \underline{x}\right) \tag{5.35}$$

where B_r is a random variable and $\underline{R}_r$ is a random rotation matrix. Also, from Eq. (5.25) we obtain

$$\underline{S}_{q_{rr_1}}(\underline{k}) = r^{-D} E\left[B_r^2\right] \underset{\underline{R}_r}{E}\left[\underline{R}_r \underline{S}_{q_{r_1}}\left(\underline{R}_r^T \underline{k}/r\right)\underline{R}_r^T\right] \tag{5.36}$$

where $E\left[B_r^2\right] = r^{2\frac{D-1}{D}C_K} r^{-\frac{4}{D}C_K}$. Eq. (5.36) is analogous to Eq. (5.29) for ∇H. The factor $r^{-\frac{4}{D}C_K}$ in the expression of $E\left[B_r^2\right]$ is the square of $\left|E\left[\underline{q}_r\right]\right| = r^{-\frac{2}{D}C_K}$ and results from the non-conservatism of $\underline{q}$. This factor is also responsible for the vanishing behavior of $\underline{S}_{q_r}$ as $r \to \infty$. To obtain a non-degenerate limit, we define conservative normalized flows as $\underline{q}_r'(\underline{x}) = r^{2C_K/D}\underline{q}_r(\underline{x})$. The spectral density tensors of the modified flows are given by $\underline{S}_{q_r'}(\underline{k}) = r^{4C_K/D}\underline{S}_{q_r}(\underline{k})$ and from Eq. (5.36) satisfy

$$\underline{S}_{q_{rr_1}'}(\underline{k}) = r^{-D+2C_K\frac{D-1}{D}} \underset{\underline{R}_r}{E}\left[\underline{R}_r \underline{S}_{q_{r_1}'}\left(\underline{R}_r^T \underline{k}/r\right)\underline{R}_r^T\right] \tag{5.37}$$

It follows that $\underline{S}_{q'}(\underline{k}) = \lim_{r\to\infty} \underline{S}_{q_r'}(\underline{k})$ renormalizes as

$$\underline{S}_{q'}(\underline{k}) = r^{-D+2C_K\frac{D-1}{D}} \underset{\underline{R}_r}{E}\left[\underline{R}_r \underline{S}_{q'}\left(\underline{R}_r^T \underline{k}/r\right)\underline{R}_r^T\right] \tag{5.38}$$

At the low-wavenumber end of the scaling range (for $k = \underline{k}_o$ with amplitude k_o), we assume that $\underline{S}_{q'}(\underline{k}_o)$ is given by Eq. (5.5)ii, which is obtained from first-order theory that

is asymptotically exact, as the variability of the K field tends to zero. When the resolution of the K field is unity or close to it, we can assume that Eq. (5.5)ii is exact; hence, we anchor the results to the exact form of the spectra given Eq. (5.5). Then for $\underline{k} = r\underline{k}_o$, Eq. (5.38) gives

$$\underline{S}_{\underline{q}'}(r\underline{k}_o) = \left(\frac{2}{S_D} C_K k_o^{-D}\right) r^{-D+2\frac{D-1}{D}C_K} \times \underset{\underline{R}_r}{E}\left\{\underline{R}_r\left[\underset{i,j=1,\ldots,D}{\left(\delta_{i1} - e_{r_i} e_{r_i}\right)\left(\delta_{j1} - e_{r_i} e_{r_j}\right)}\right]\underline{R}_r^T\right\} \tag{5.39}$$

where e_{r_i} is the ith component of the vector $\underline{e}_r = \underline{R}_r^T \underline{e}$ and $\underline{e}$ is the unit vector in the direction of $\underline{k}_o$. If K is multifractal down to resolution r_{max} and no further (meaning that the spectral density of F =ln(K) is zero beyond $r_{max}k_o$), the spectral density tensor of $\underline{q}$ is $\underline{S}_{\underline{q}}(\underline{k}) = r_{max}^{-4C_K/D}\underline{S}_{\underline{q}'}(\underline{k})$ for $k < r_{max} < k_o$ and $\underline{S}_{\underline{q}}(\underline{k}) = \underline{0}$ otherwise. This behavior of $\underline{S}_{\underline{q}}$ is a direct consequence of the spectrum of the log-conductivity F given in Eq. (5.23). The spectrum of F is constrained because as the resolution tends to infinity, the variance of the K field diverges and becomes non-conductive.

To obtain a more explicit form of $\underline{S}_{\underline{q}'}(\underline{k})$, one must evaluate the expectation term

$$\underset{\underline{R}_r}{E}\left\{\underline{R}_r\left[\underset{i,j=1,\ldots,D}{\left(\delta_{i1} - e_{r_i} e_{r_i}\right)\left(\delta_{j1} - e_{r_i} e_{r_j}\right)}\right]\underline{R}_r^T\right\} \tag{5.40}$$

in Eq. (5.39), where $\underline{R}_r$ is the random rotation matrix, e_{r_i} is the ith component of the vector $\underline{e}_r = \underline{R}_r^T \underline{e}$, and $\underline{e}$ is the unit vector in the direction of $\underline{k}_o$. The following is the derivation of an analytical expression for the matrix in Eq. (5.40) for the D = 2 case and a more manageable but not completely explicit expression for D = 3.

Two-dimensional case

Let $A_{ij} = \left[\left(\delta_{i1} - e_{r_i} e_{r_i}\right)\left(\delta_{j1} - e_{r_1} e_{r_j}\right)\right]$

for i=1 j=1

$$A_{11} = \left(1 - e_{r_1}^2\right)^2 = 1 - 2e_{r_1}^2 + e_{r_1}^4$$

for i=1 j=2

$$A_{12} = \left(1 - e_{r_1}^2\right)\left(-e_{r_1} e_{r_2}\right) = 0 - e_{r_1} e_{r_2} + e_{r_1}^3 e_{r_2}$$

for i=2 j=1

$$A_{21} = \left(0 - e_{r_1} e_{r_2}\right)\left(1 - e_{r_1} e_{r_2}\right) = 0 - e_{r_1} e_{r_2} + e_{r_1}^3 e_{r_2}$$

for i = 2 j = 2

$$A_{22} = \left(0 - e_{r_1} e_{r_2}\right)\left(0 - e_{r_1} e_{r_2}\right) = 0 - 0 + e_{r_1}^2 e_{r_2}^2$$

Thus in matrix form

$$A_{ij} = \underset{i,j=1,2}{\left[\left(\delta_{i1} - e_{r_1} e_{r_i}\right)\left(\delta_{j1} - e_{r_1} e_{r_j}\right)\right]} = \begin{bmatrix} 1 & 0 \\ 0 & 0 \end{bmatrix} - \begin{bmatrix} 2e_{r_1}^2 & e_{r_1} e_{r_2} \\ e_{r_1} e_{r_2} & 0 \end{bmatrix} + e_{r_1}^2 \begin{bmatrix} e_{r_1}^2 & e_{r_1} e_{r_2} \\ e_{r_1} e_{r_2} & e_{r_2}^2 \end{bmatrix}$$

$$= \left(1 - e_{r_1}^2\right) \begin{bmatrix} 1 & 0 \\ 0 & 0 \end{bmatrix} + e_{r_2}^2 \begin{bmatrix} 0 & 0 \\ 0 & 1 \end{bmatrix} - \underline{e}_{r_i} \underline{e}_{r_j}^T + e_{r_1}^2 \underline{e}_{r_i} \underline{e}_{r_j}^T$$

Using $\left(1 - e_{r_1}^2\right) = e_{r_2}^2$

$$A_{ij} = e_{r_2}^2 I - \underline{e}_{r_i} \underline{e}_{r_j}^T - e_{r_1}^2 \underline{e}_{r_i} \underline{e}_{r_j}^T = e_{r_2}^2 I - e_{r_2}^2 \underline{e}_{r_i} \underline{e}_{r_j}^T = e_{r_2}^2 \left(I - \underline{e}_{r_i} \underline{e}_{r_j}^T\right)$$

Therefore, the expectation in Eq. (5.40) becomes

$$\begin{aligned} \underset{\underline{R}_r}{E}\left\{\underline{R}_r \underset{i,j=1,\ldots,D}{\left[\left(\delta_{i1} - e_{r_1} e_{r_i}\right)\left(\delta_{j1} - e_{r_1} e_{r_j}\right)\right]} \underline{R}_r^T\right\} &= \underset{\underline{R}_r}{E}\left[e_{r_2}^2\right]\left(\underline{R}_r \underline{R}_r^T - \underline{R}_r \underline{e}_r \underline{e}_r^T \underline{R}_r^T\right) \\ &= \underset{\underline{R}_r}{E}\left[e_{r_2}^2\right]\left(\underline{I} - \underline{e}\underline{e}^T\right) \qquad (5.41) \\ &= \underset{\underline{R}_r}{E}\left[e_{r_2}^2\right] \begin{bmatrix} e_2^2 & e_1 e_2 \\ e_1 e_2 & e_1^2 \end{bmatrix} \end{aligned}$$

Using $e_{r_2} = -\sin\left(\alpha_r\right) e_1 + \cos\left(\alpha_r\right) e_2$ where α_r has normal distribution with zero mean and variance $\frac{1}{4} C_K \ln\left(r\right)$, and the fact that $E\left[\sin\alpha_r \cos\alpha_r\right] = 0$ due to symmetry of the distribution of α_r, one obtains $\underset{\underline{R}_r}{E}\left[e_{r_2}^2\right] = \left(1 - b_r\right) e_1^2 + b_r e_2^2$ where $b_r = E\left[\cos^2\alpha_r\right]$. Hence, in the 2D case, the matrix in Eq. (5.40) may be written explicitly as

$$\underset{\underline{R}_r}{E}\left\{\underline{R}_r\left[\underset{i,j=1,\ldots,D}{\left(\delta_{i1}-e_{r_i}e_{r_i}\right)\left(\delta_{j1}-e_{r_i}e_{r_j}\right)}\right]\underline{R}_r^T\right\}= \\ \left((1-b_r)e_1^2+b_re_2^2\right)\begin{bmatrix} e_2^2 & -e_1e_2 \\ -e_1e_2 & e_1^2 \end{bmatrix} \tag{5.42}$$

Three-dimensional case

In three-dimensional space, the matrix in brackets in Eq. (5.40) may be written as

$$\left[\underset{i,j=1,2,3}{\left(\delta_{i1}-e_{r_i}e_{r_i}\right)\left(\delta_{j1}-e_{r_i}e_{r_j}\right)}\right]=\begin{bmatrix}1&0&0\\0&0&0\\0&0&0\end{bmatrix}-\begin{bmatrix}2e_{r_i}^2 & e_{r_i}e_{r_2} & e_{r_i}e_{r_3}\\ e_{r_i}e_{r_2} & 0 & 0\\ e_{r_i}e_{r_3} & 0 & 0\end{bmatrix}+e_{r_i}^2\underline{e}_r\underline{e}_r^T \\ =\left(1-2e_{r_i}^2\right)\begin{bmatrix}1&0&0\\0&0&0\\0&0&0\end{bmatrix}-\begin{bmatrix}0 & e_{r_i}e_{r_2} & e_{r_i}e_{r_3}\\ e_{r_i}e_{r_2} & 0 & 0\\ e_{r_i}e_{r_3} & 0 & 0\end{bmatrix}+e_{r_i}^2\underline{e}_r\underline{e}_r^T \tag{5.43}$$

Using Eq. (5.43), the expectation in Eq. (5.40) becomes

$$\underset{\underline{R}_r}{E}\left\{\underline{R}_r\left[\underset{i,j=1,2,3}{\left(\delta_{i1}-e_{r_i}e_{r_i}\right)\left(\delta_{j1}-e_{r_i}e_{r_j}\right)}\right]\underline{R}_r^T\right\} \\ =E\left[\left(1-e_{r_i}^2\right)\underline{R}_{r_i}\underline{R}_{r_i}^T\right]-E\left[e_{r_i}e_{r_2}\left(\underline{R}_{r_i}\underline{R}_{r_2}^T+\underline{R}_{r_2}\underline{R}_{r_i}^T\right)\right] \\ =E\left[e_{r_i}e_{r_3}\left(\underline{R}_{r_i}\underline{R}_{r_3}^T+\underline{R}_{r_3}\underline{R}_{r_i}^T\right)\right]+E\left[e_{r_i}^2\right]\underline{e}\underline{e}^T \tag{5.44}$$

where $\underline{R}_{r_i}$ is the ith column of $\underline{R}_r$. (The various terms must now be expanded and the expectation dealt with in index notation.)

Substituting Eq. (5.41) into Eq. (5.38) the specific discharge spectrum for the two-dimensional case is obtained as

$$\underline{S}_{\underline{q}'}(r\underline{k}_o)=\left(\frac{1}{\pi}k_o^{-2}C_K\right)r^{-2+C_K}\left((1-b_r)e_1^2+b_re_2^2\right)\begin{bmatrix} e_2^2 & -e_1e_2 \\ -e_1e_2 & e_1^2 \end{bmatrix} \tag{5.45}$$

where $b_r=E\left[\cos^2(\alpha_r)\right]$ and α_r has normal distribution with mean zero and variance $\frac{1}{4}C_K\ln(r)$. It is worth noting that:

(i) Since $\underline{q}'$ has zero divergence, its spectral density tensor must satisfy $\sum_i k_i\left[\underline{S}_{\underline{q}'}(\underline{k})\right]_{ij}=0$ for each j and $\sum_j k_j\left[\underline{S}_{\underline{q}'}(\underline{k})\right]_{ij}=0$ for each i [Panchev, 1971, Eq. 9.4]. One can verify that Eq. 5.45 satisfies these conditions.

(ii) For $\underline{k}$ in the direction of k_1 (for $e_1 = 1$ and $e_2 = 0$), $S_{q_1'q_1'}(\underline{k})$ and $S_{q_2'q_2'}(\underline{k})$ vanish and $S_{q_2'q_2'}(r\underline{k}_o)$ becomes

$$S_{q_2'q_2'}\left(r\begin{bmatrix} k_o \\ 0 \end{bmatrix}\right)=(1-b_r)\left(\frac{1}{\pi}k_o^{-2}C_K\right)r^{-2+C_K} \tag{5.46}$$

The term $(1-b_r)$ in Eq. (5.46) is close to zero for small r (at low frequencies) and approaches 0.5 as $r\to\infty$. Contrary to linear theory, the spectral density $S_{q_2'q_2'}$ does

not vanish identically along k_1. The reason is the random rotation of the flow field at small scales.

(iii) Like the hydraulic gradient ∇H, the specific flow $\underline{q}$ is anisotropic at large scales but tends to be isotropic at small scales. The scale below which $\underline{q}$ may be considered isotropic is controlled by the term b_r and hence by C_K, which appears in the variance of α_r. For example, if one considers isotropy to be effectively realized when $b_r = 0.6$, then this requires $\mathrm{Var}[\alpha_r] = 0.9$ and a resolution $r_{iso} = e^{3.6/C_K}$. For example, $r_{iso} = 8103$ for $C_K = 0.4$. If r_{iso} exceeds the multifractal scaling range of the hydraulic conductivity, $r_{max} = k_{max} / k_o$, then complete isotropy is not observed, even at the smallest scales.

The spectral components $S_{q_1q_1}$, $S_{q_2q_2}$ and $S_{q_1q_2}$ are contour plotted in Figures 5.2a-c using a representation similar to Figure 5.1. In each figure, the nonlinear functions from Eq. (5.45) are compared with the linear spectral densities in Eq. (5.4) for C_K = 0.1 and C_K = 0.3. As in the case of the hydraulic head fluctuations, the main differences between the linear and nonlinear spectra are that the latter are flatter and consistent with the fact that, at small scales, $\underline{q}$ approaches isotropy (at large wavenumbers, the spectra $S_{q_1q_1}$ and $S_{q_2q_2}$ are identical except for a 90° rotation, and $S_{q_1q_2}$ is symmetrical). Both features (slow decay of the spectrum relative to the linear case and high-wavenumber isotropy) are more pronounced for higher values of C_K. The contours in Figs. 5.2 have a log spacing of –2. The innermost contours have a

log-spectral value of –2 and decrease outward with increments of –2. The decay exponent is –2 for the linear theory spectra and $-2 + C_K$ for the nonlinear spectra. Thus, we observe that the spectra of $\underline{q}$ for the nonlinear theory decays at a slower rate than the spectra from the linear theory. The difference in the rates of decay between the linear and nonlinear theory spectra becomes more pronounced as the C_K value increases.

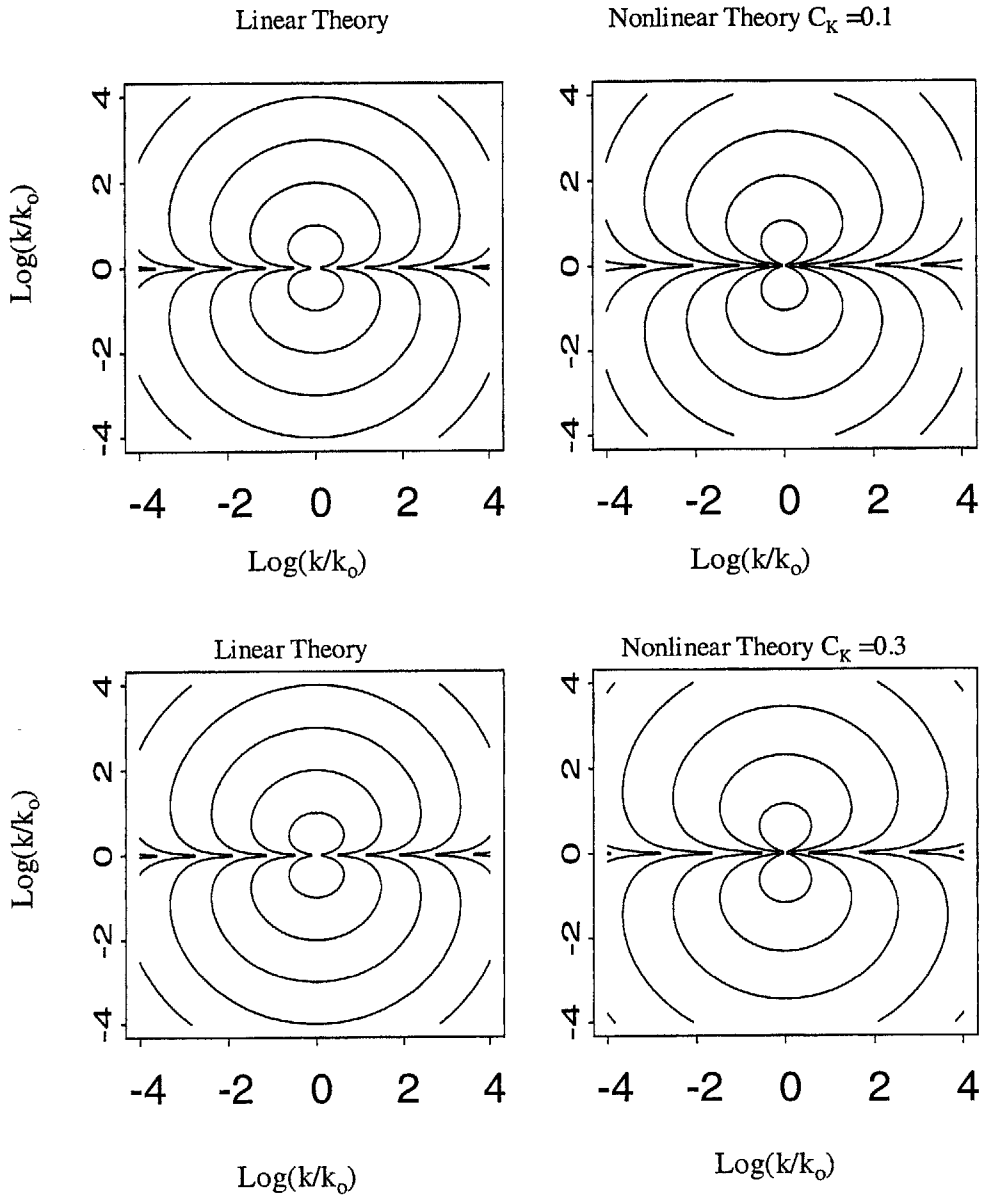

Figure 5.2a – Spectral contours of the longitudinal specific flow $S_{q_1q_1}$

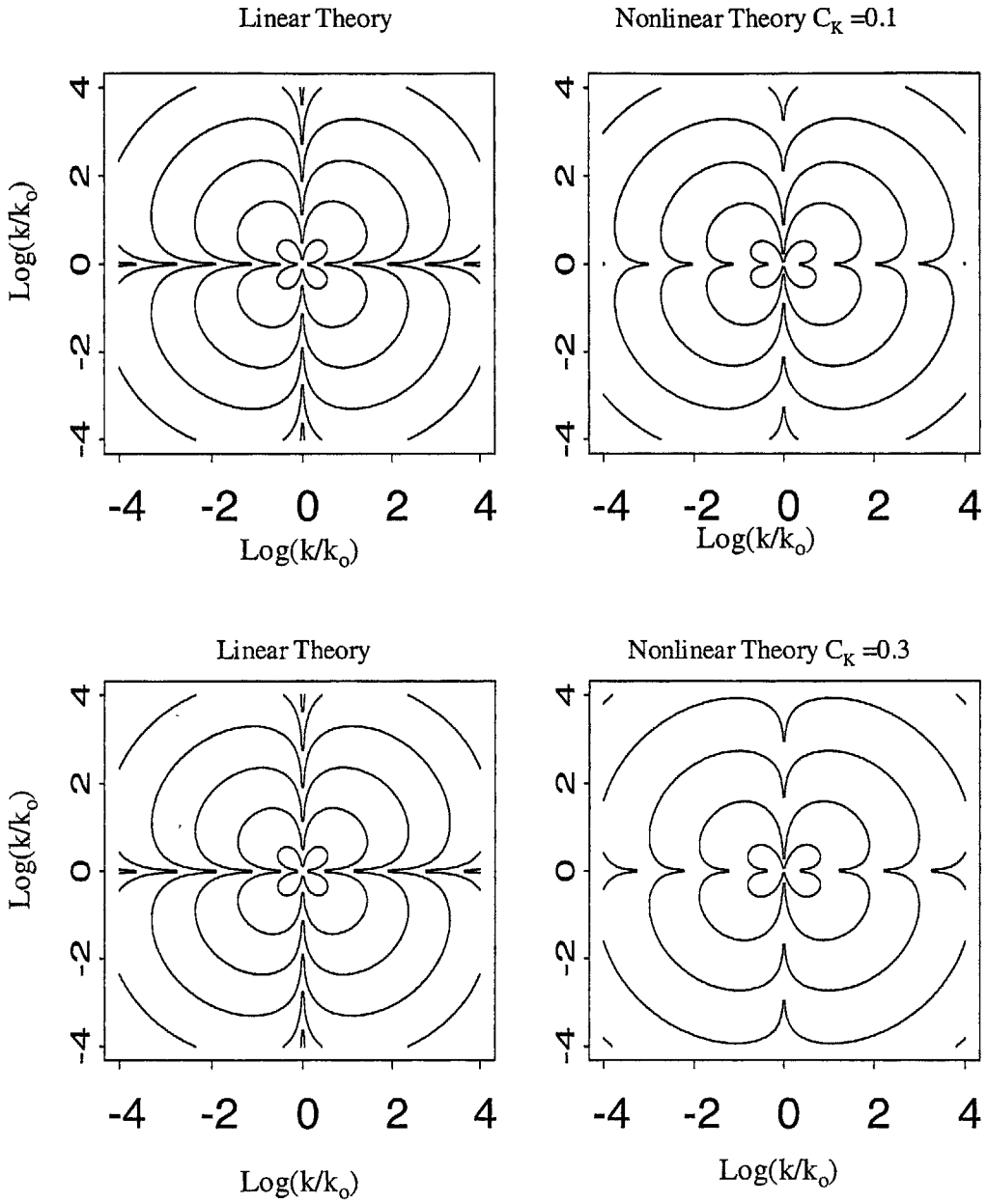

Figure 5.2b – Spectral contours of the transverse specific flow $S_{q_2q_2}$

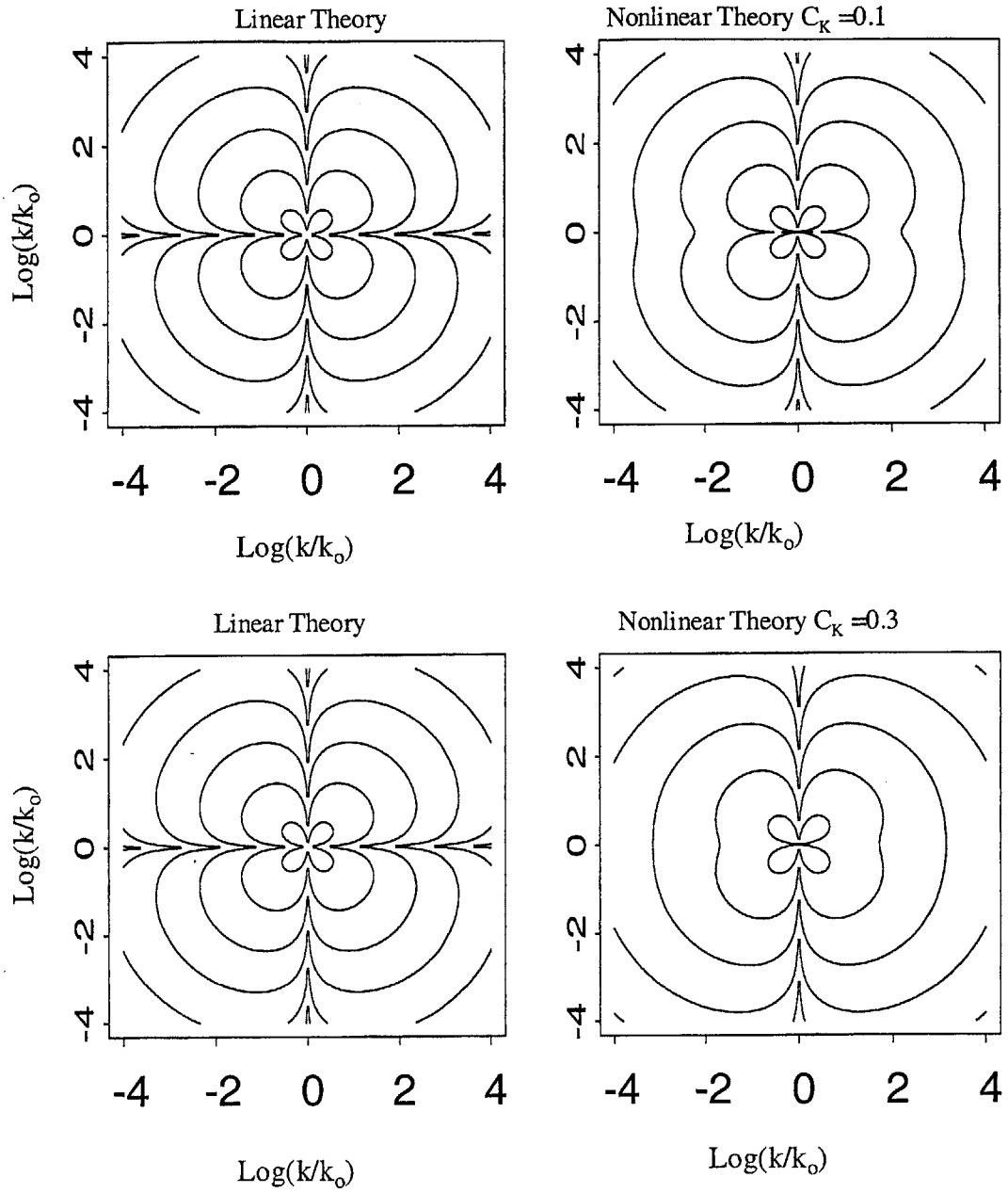

Figure 5.3c – Spectral contours of $S_{q_1q_2}$

CHAPTER 6: FLOW SIMULATIONS IN SATURATED AQUIFERS WITH MULTIFRACTAL HYDRAULIC CONDUCTIVITY

Introduction

In this chapter, the theoretical results of Chapter 4 are validated by performing two-dimensional simulations on a 512 x 512 grid. To produce hydraulic gradients and flows, boundary conditions of $H=1$ along $x_1=0$, $H=0$ along $x_1=1$, where H is the hydraulic head and no flow through the other two boundaries are imposed. Consequently, the average hydraulic gradient is oriented in the x_1 direction and coincides with the mean flow direction. The flow domain and the boundary conditions are illustrated in Fig. 6.1. Because of the simplicity of the flow domain, a finite difference approach is used in computing the head field H, which is then used to calculate the hydraulic gradient field ∇H. Using the hydraulic conductivity K field and the hydraulic gradient, the specific discharge field $\underline{q}$ is computed. Most of the validating procedures consist of computing the moments of the field and examining how these moments change scale ratio r. The scale ratio, also known as resolution r, is defined as the ratio between image size and pixel size in an image.

In general two types of validation are done: the first consists of creating a K field on a grid size of say 512 x 512, computing the associated ∇H and $\underline{q}$ fields, and then averaging these fields to obtain $\{K, \nabla H \text{ and } \underline{q}\}$ fields on coarser grid sizes. The

moments of the original field and the fields obtained through averaging are examined. This type of analysis is known in the multifractal literature as "partial dressing." The

second type of validation consists of examining the scaling properties of flow through K fields of different resolutions. For example if $\{K_{512}, K_{256}, K_{128}, K_{64}\}$ are K fields on grids of sizes 512x 512, 256 x 256, 128 x 128 and 64 x 64 respectively, and these fields serve as inputs into the program that computes the head fields, so that the associated hydraulic gradient field and specific discharge fields are respectively $\{\nabla H_{512}, \nabla H_{256}, \nabla H_{128}, \nabla H_{64}\}$ and $\{q_{512}, q_{256}, q_{128}, q_{64}\}$. Then, the scaling properties of the fields are examined by considering how the moments of the sets $\{K_{512}, K_{256}, K_{128}, K_{64}\}$, $\{\nabla H_{512}, \nabla H_{256}, \nabla H_{128}, \nabla H_{64}\}$ and $\{q_{512}, q_{256}, q_{128}, q_{64}\}$ change with resolution (or the grid size). This type of analysis is known in the multifractal literature as "bare scaling analysis."

Sections 6.1 through 6.5 examine the "partial dressing" of multifractal K fields. How one constructs multifractal K fields is discussed in Sec. 6.1. The computation of the scaling properties of these K fields is also discussed. Using the multifractal K fields as input into a finite difference program, the head field is calculated. Section 6.2 discusses the finite difference program used in computing the head field. Properties of the head field are discussed in section 6.3.

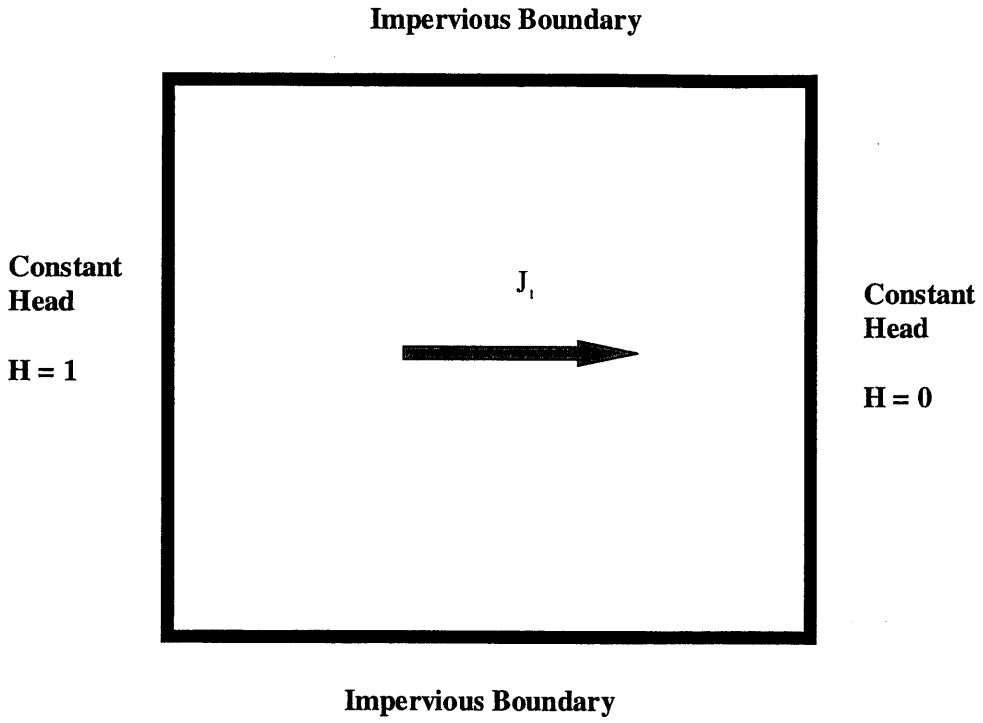

Figure 6.1 – An illustration of the flow domain and the imposed boundary conditions.

Section 6.3.2 discusses how the hydraulic gradient ∇H field is computed from the head field and what one can observe about its scaling properties. An interesting feature of the vector fields ∇H and $\underline{q}$ from a variable K field is that in addition to considering the scaling properties of their amplitudes, one has to consider their rotations. The statistical properties of these rotations are discussed in Sec. 6.5. The properties of the specific discharge are presented in Sec. 6.4.

The scaling of bare fields is discussed in section 6.6. Unlike the partially dressed field, where the mean value of $\underline{q}$ does not depend on the resolution r, in the "bare case" one observes a decrease in the mean value of $\underline{q}$ as the K fields are developed to higher resolutions. To explain this behavior Sec. 6.7 discusses the relation between the log hydraulic conductivity and the hydraulic gradient ∇H. The negative correlation between these fields is examined in detail. Finally, Sec. 6.8 considers the case of a K field with a high variability. In deriving the theoretical results of Chapter 4, it was assumed that the contribution of the term $\nabla F.\nabla h$ in the incremental flow equation (Eq. 4.7) was negligible compared to $\nabla^2 h$. Under this assumption, we obtained theoretical results for the case when $k_o \gg 1$ and $C_K \ll 1$, where k_o is the minimum wavenumber for the $F = \ln(K)$ spectrum and C_K is the codimension parameter that determines the variability of the K field. In Sec. 6.8 we consider flow through a K field with a C_K value close to unity to examine if the scaling results still hold or break down under this condition.

6.1 Construction of the K field and its scaling properties

The hydraulic conductivity field K that is input into the flow program is an isotropic lognormal multifractal field that satisfies the scale invariance condition

$$\overline{K}(S) \stackrel{d}{=} A_r \overline{K}(rS) \tag{6.1}$$

where $\stackrel{d}{=}$ denotes equality of all finite dimensional distributions and A_r is a random variable independent of $\overline{K}(rS)$, $\overline{K}(S)$ denotes the average value of K in regions S of $\mathbb{R}^D$ and $r \geq 1$. We consider the case when A_r has lognormal distribution, so that $F = \ln(K)$ is a Gaussian random field. Determining the multifractality of a scalar quantity like K consists of verifying that Eq (6.1) is satisfied. In Chapter 3 it was shown that Eq. (6.1) can be written as

$$E\left[\overline{K}(S)^s\right] = r^{W(s)} E\left[\overline{K}(rS)^s\right] \tag{6.2}$$

where $W(s)$ is commonly known as the moment scaling function. For a lognormal K field with $E[A_r] = 1$, $\ln(A_r)$ must have a mean value of $-C_K \ln(r)$ and variance $2C_K \ln(r)$, thus from the moments of the lognormal distribution [Johnson and Kotz, 1970, chapter 14], the moment scaling function $W(s)$ is

$$W(s) = C_K\left(s^2 - s\right) \tag{6.3}$$

W(s) is obtained by plotting $\log\left\{E\left[\overline{K}(S)^s\right]\right\}$ against $\log(r)$ for different values of s. For a D-dimensional K field with a given C_K value one can take the moments up to a value determined from the relation

$$W(s) \le D(s-1) \tag{6.4}$$

This relation ensures that the moments of $\overline{K}(S)$ are finite for $s < s_L$, where $s_L > 1$ satisfies

$$W(s) = D(s_L - 1) \tag{6.5}$$

and moments of $\overline{K}(S)$ of order $s \ge s_L$ diverge. As an example, for a two-dimensional K field with $C_K = 0.3$ the maximum value of s, $s_L = 6.67$. To study the scaling behavior of the multifractal K field, K fields with C_K values of 0.1 and 0.3 were generated.

The numerical simulation of lognormal multifractal measures is discussed in Schertzer and Lovejoy (1987), Wilson et al. (1991) and Pecknold et al. (1993). This thesis follows the same procedures outlined in these papers and numerical simulates an isotropic lognormal multifractal following these steps:

1. A Gaussian white noise $\Gamma_{r=512}$ with zero mean and variance $2C_K$ is generated over the discrete 512 x 512 grid.

2. $\Gamma_{r=512}$ is Fourier transformed an filtered with a $\sqrt{C_K}k^{-D/2}$ filter, where k is the amplitude of the wavenumber vector $\underline{k}$. Theoretical reasons for choosing this filter are provided in Schertzer and Lovejoy (1987), Eq. 36. The resulting field is Fourier transformed to yield a real space field.
3. The field in step 2 is normalized by subtracting $C_K \log(\text{size})$.
4. The field in step 3 is exponentiated to yield a multifractal field with a mean of approximately 1.

Following the steps outlined above, K fields with C_K values of 0.1 and 0.3 were generated. The K fields with $C_K = 0.1$ and 0.3 are shown in Figs. 6.2a and 6.2b. The K field with $C_K = 0.3$ is sparser and more variable than the $C_K = 0.1$ field. The scaling behavior of the K field is examined as follows:

1. The simulated K field with $E[K]=1$ on the 512 x 512 grid corresponds to the K field at a resolution of 512. To obtain the data at a resolution of 256 x 256, the original K field is averaged so that the average of four neighboring points on the original grid corresponds to a new single point on the 256 x 256 grid. In general, to obtain a new field with resolution $R = 2^N$ x 2^N where $N = 0, 1, 2,.....,8$ from the original 512 x 512 K field, the 512 x 512 K field is averaged over 2^{9-N} x 2^{9-N} neighboring points. To further explain this averaging procedure, consider the K field of resolution r = 4 in Fig. 6.3 being averaged to obtain a field

with r = 2. The averaging is done such that for the field with r = 4, the averaged values in the K field with r = 2 are obtained as follows:

$$K_1 = \frac{K_{11} + K_{12} + K_{21} + K_{22}}{4}$$

$$K_2 = \frac{K_{13} + K_{14} + K_{23} + K_{24}}{4}$$

$$K_3 = \frac{K_{31} + K_{32} + K_{41} + K_{42}}{4} \qquad (6.6)$$

$$K_4 = \frac{K_{33} + K_{34} + K_{43} + K_{44}}{4}$$

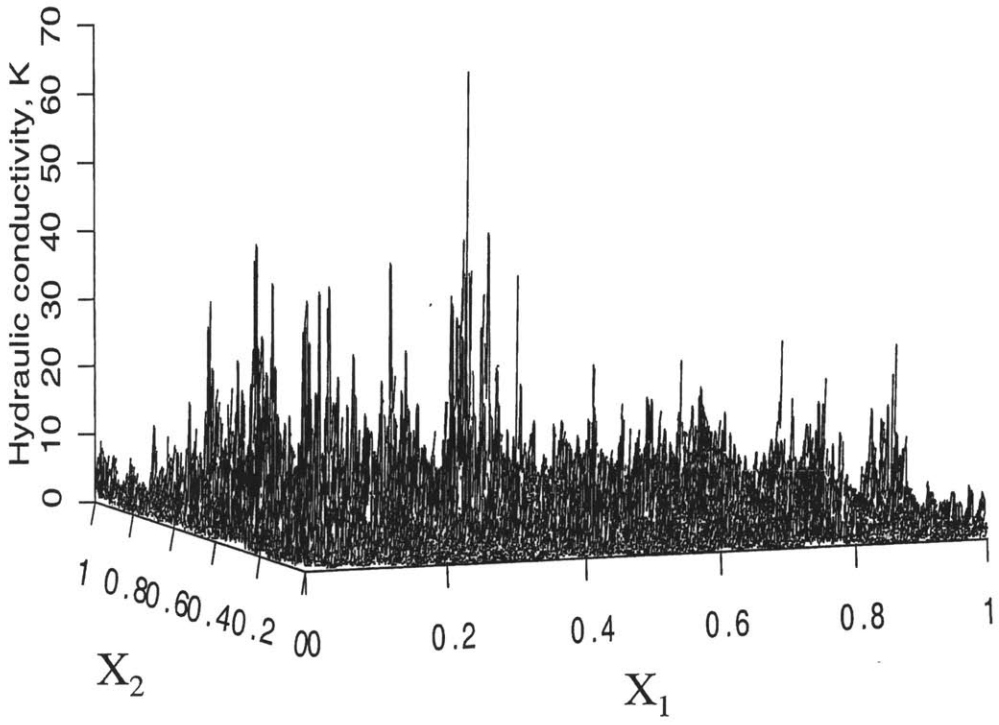

Figure 6.2a – A lognormal multifractal hydraulic conductivity field with $C_K = 0.1$

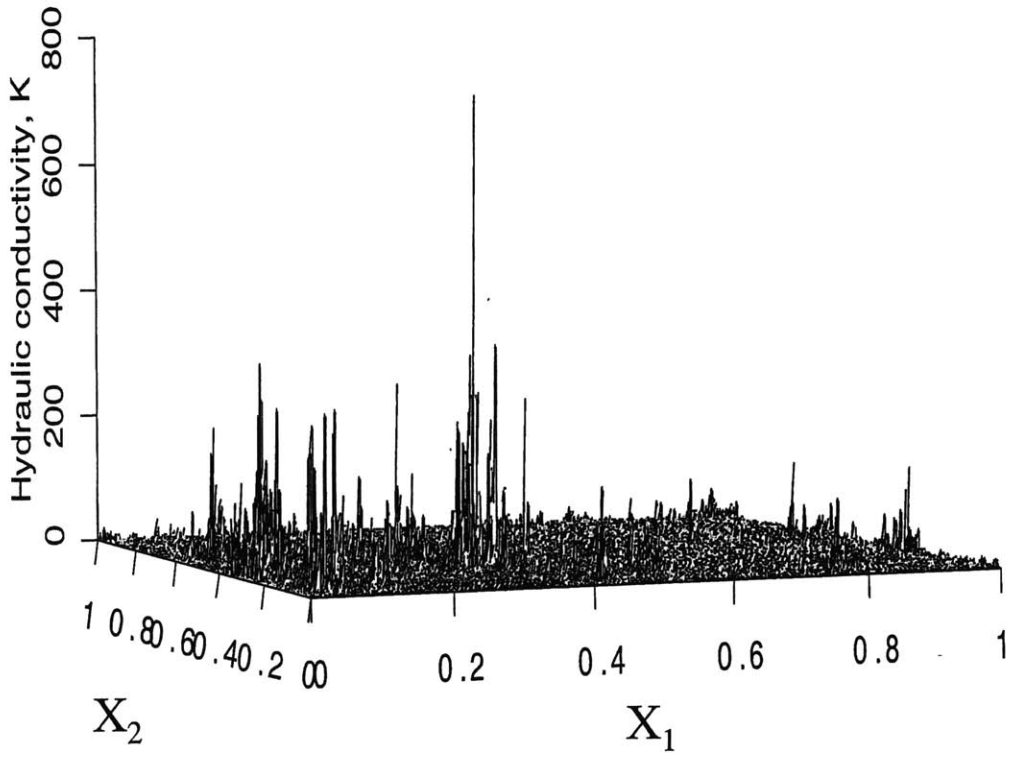

Figure 6.2b – A lognormal multifractal hydraulic conductivity field with $C_K = 0.3$

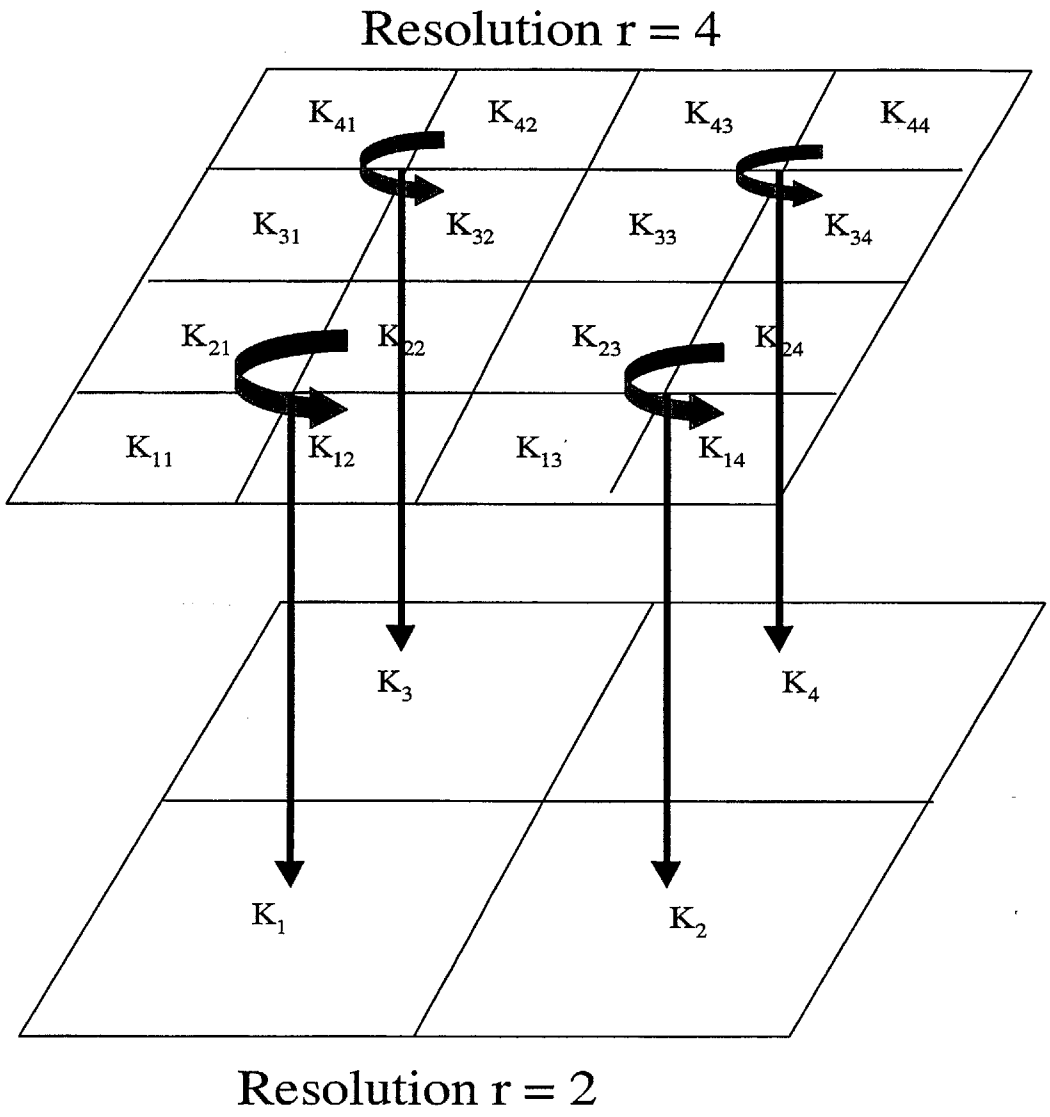

Figure 6.3 – An illustration of how a K field at resolution r = 4 is averaged to obtain a K field with resolution r = 2.

In the discussion that follows, we denote the field at resolution r with a subscript that shows the resolution of the field. So that the K fields obtained by averaging the K field at r = 512 to obtain fields with r = 256, 128, 64, 32, 16, 8, 4, 2 and 1 respectively are denoted as

$$K = \{K_{512}, K_{256}, K_{128}, K_{64}, K_{32}, K_{16}, K_8, K_4, K_2, K_1\} \tag{6.7}$$

2. To obtain the moments of the K field, Eq. 6.7 is exponentiated to the power s to obtain K^s and the spatial averages are taken. So that the s^{th} moment of the K field is

$$\langle K^s \rangle = \{\langle K_{512}^s \rangle, \langle K_{256}^s \rangle, \langle K_{128}^s \rangle, \langle K_{64}^s \rangle, \langle K_{32}^s \rangle, \langle K_{16}^s \rangle, \langle K_8^s \rangle, \langle K_4^s \rangle, \langle K_2^s \rangle, \langle K_1^s \rangle\}$$

where $\langle\ \rangle = \frac{1}{N}\sum_{j=1}^{N}$ denotes the spatial average of K and N is the number of elements.

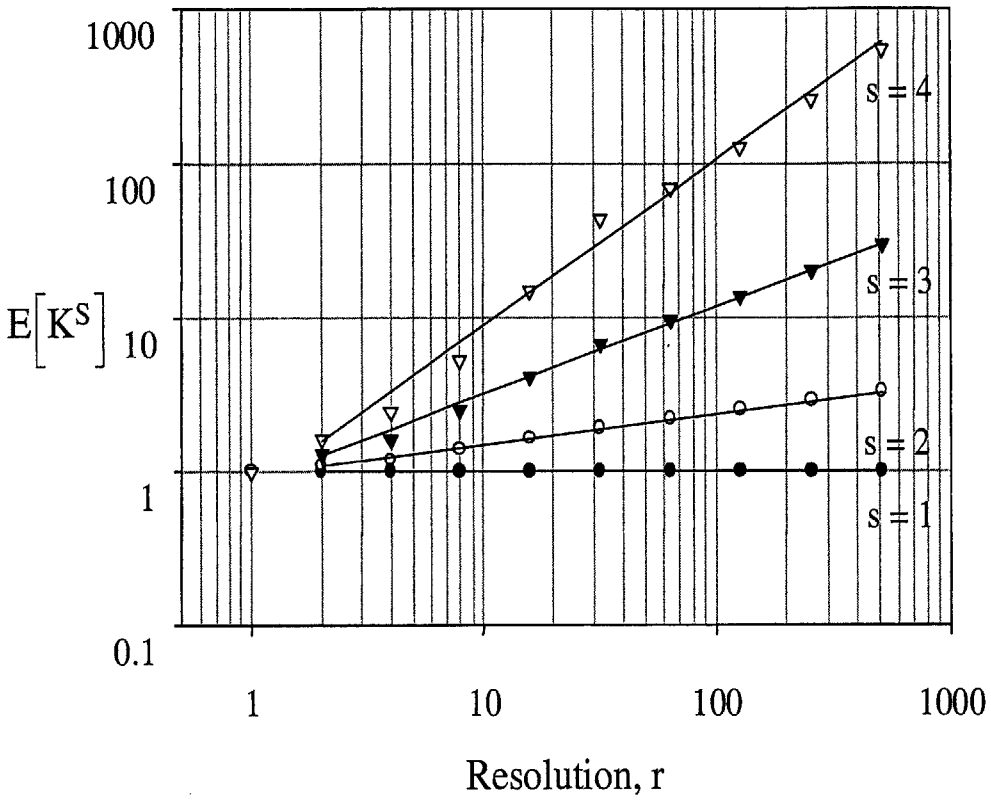

Figure 6.4 – The scaling of a lognormal hydraulic conductivity field K with C_K= 0.1. The straight lines on the graph are obtained by performing a linear regression against the data points.

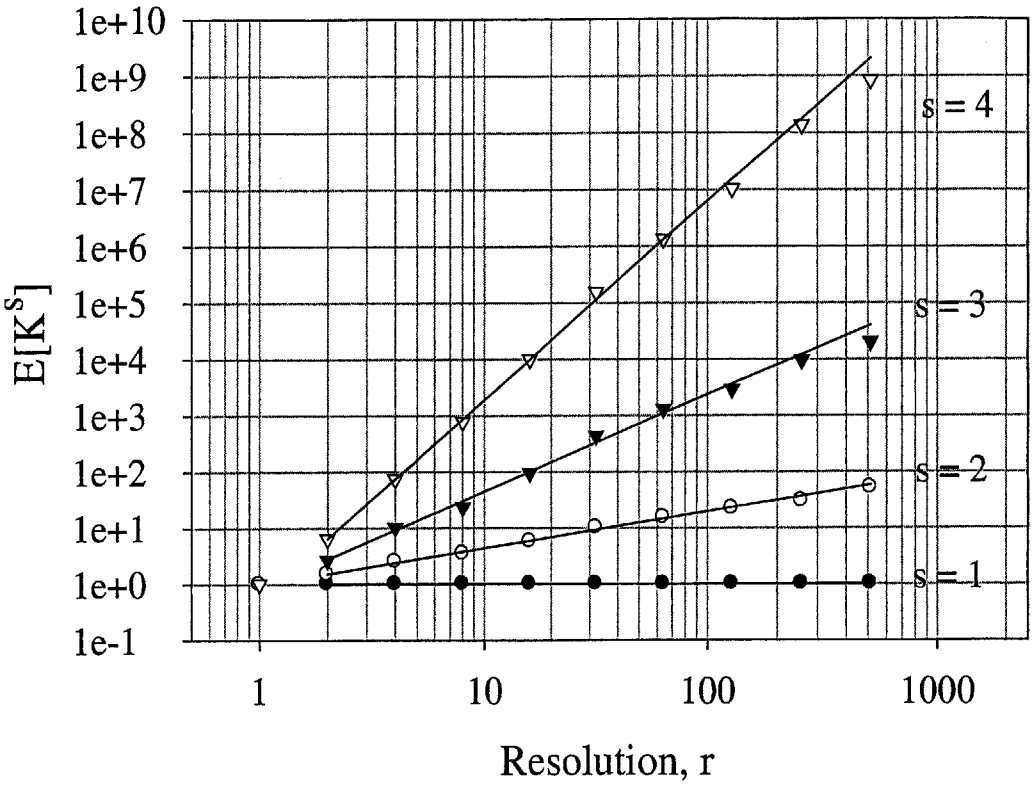

Figure 6.5 – The scaling of a lognormal hydraulic conductivity field K with $C_K = 0.3$. The straight lines on the graph are obtained by performing a linear regression against the data points.

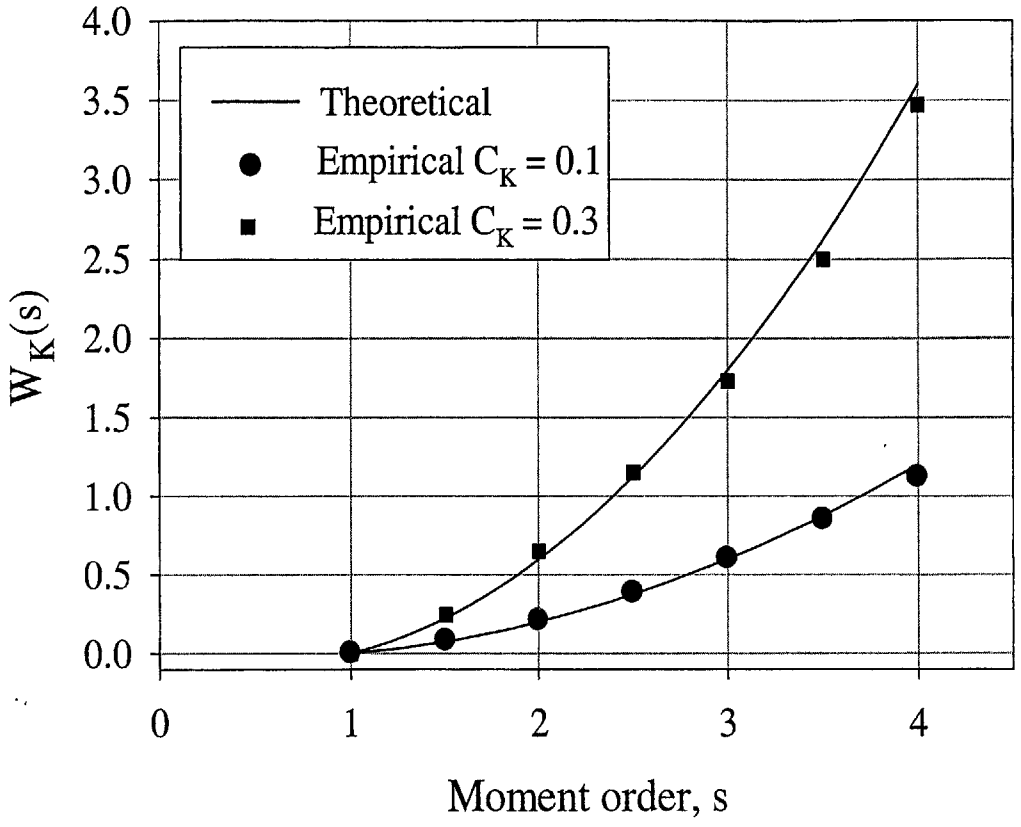

Figure 6.6 – Comparison between the results of the numerical (empirical) simulation and the theoretical scaling relations for K fields with $C_K = 0.1$ and 0.3.

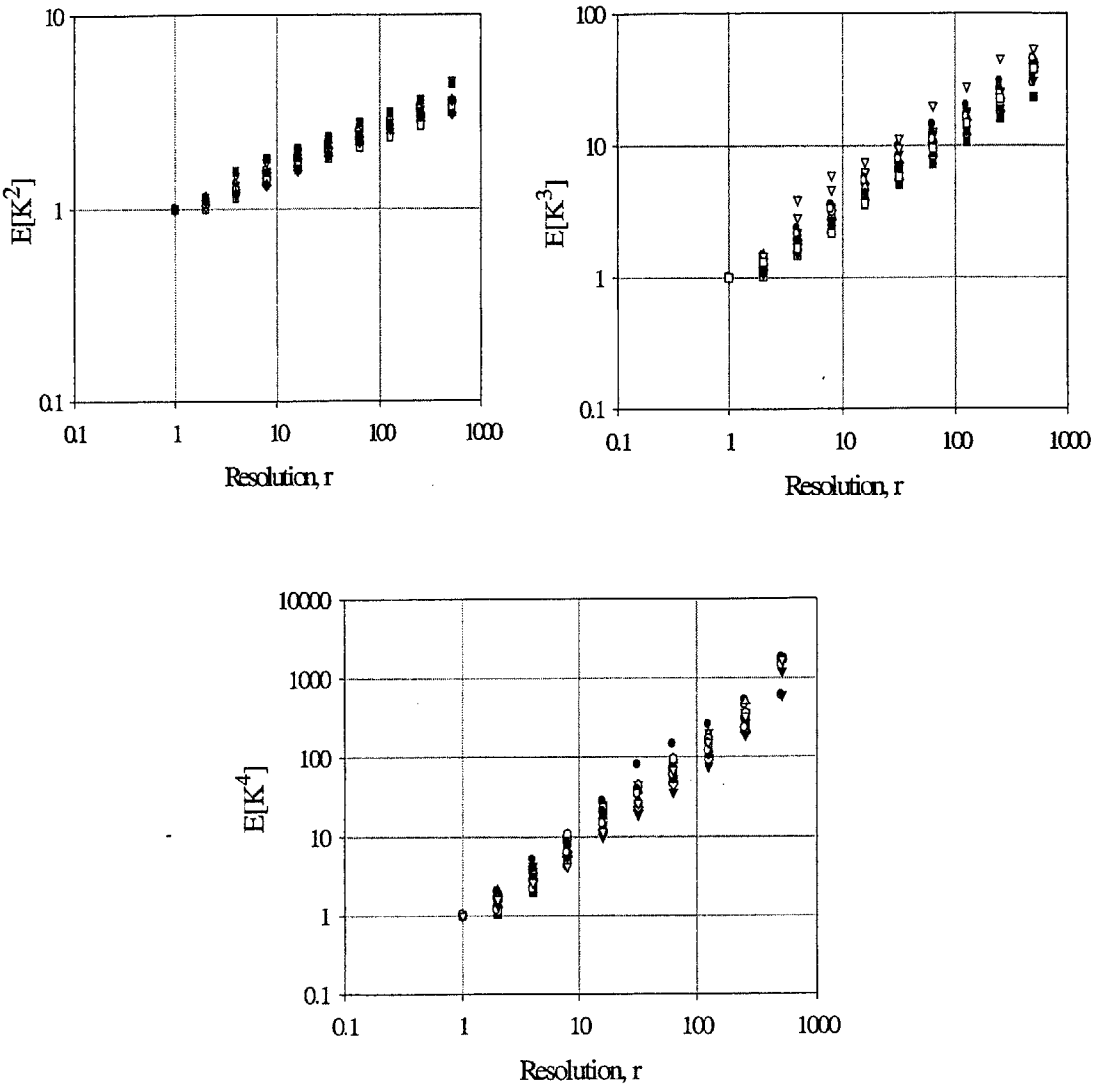

Figure 6.7 – The scaling moments for 20 simulations of lognormal multifractal K fields with $C_K = 0.1$. Moments for s = 1 have not been shown because they all have a value of 1. Due to the overlap of some points one cannot clearly see all the 20 points.

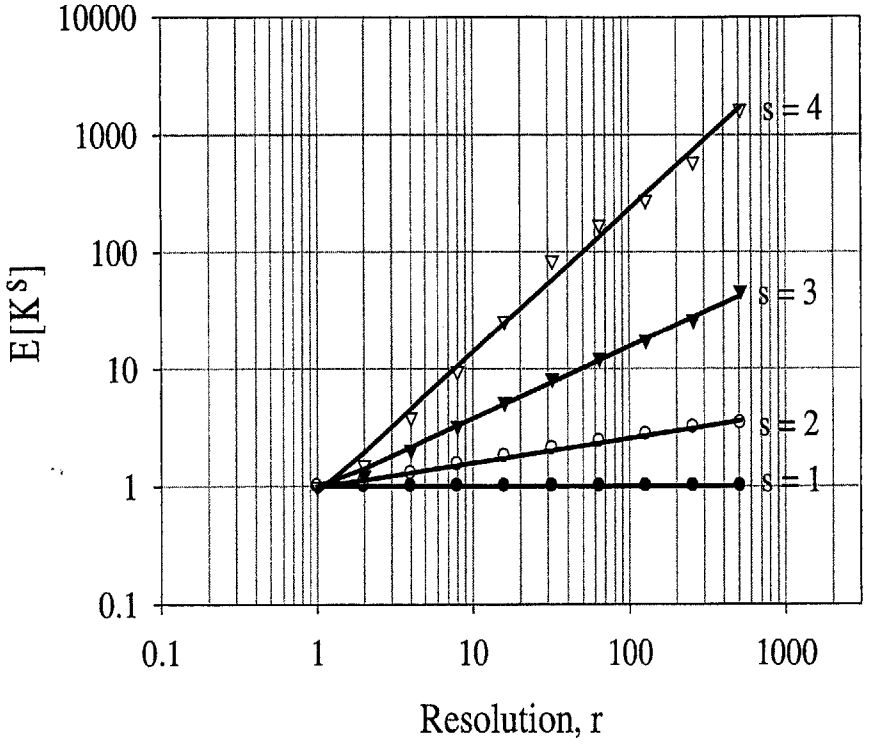

Figure 6.8 – The scaling moments of the average values of the moments shown in Figure 6.7. This is the average scaling moment of 20 realizations of K fields with $C_K = 0.1$.

The scaling of the K field with $C_K = 0.1$ and 0.3 obtained following the steps outlined above are shown in Figs. 6.4 and 6.5. The empirical $W(s)$, the slopes of the moments in Figs. 6.4 and 6.5, were obtained through linear regression of $\log\{E[K_r^s]\}$ versus $\log\{r\}$, where $r = \{512, 256, 128, 64, 32, 16, 8, 4, 2, 1\}$ and are shown in Fig. 6.6; for $C_K = 0.3$ the moments $q = 3$ and 4 are slightly less than the theoretical slopes predicted by Eq. 6.3. The discrepancy of the empirically obtained slopes from the theoretical can be attributed to the seed used in generating the K field. In fact, one cannot overemphasize the fact that the numerical simulations involve an inherent randomness and depending on the seed used one may obtain slightly varying results. Fig. 6.7 shows the results of 20 simulations performed to generate K fields with $C_K = 0.1$. Each K field was created with a different seed. It is interesting to observe the results are closely clustered. The slopes of the individual realizations are presented in Table 6.1. And the average value of the realizations is plotted in Fig. 6.8. The average slopes closely match the theoretical slopes for a K field with $C_K = 0.1$ given in Table 6.1.

Table 6.1 Slopes of $\log\{\langle K^s \rangle\}$ versus $\log\{\text{resolution}\}$ for K fields with $C_K = 0.1$

$W_K(2)$	$W_K(3)$	$W_K(4)$
0.219	0.627	1.32
0.210	0.629	1.26
0.213	0.613	1.15
0.200	0.600	1.23
0.220	0.615	1.19
0.290	0.820	1.43
0.180	0.600	1.20
0.210	0.530	1.15
0.200	0.620	1.18
0.230	0.600	1.20
0.200	0.560	1.10
0.210	0.560	1.09
0.200	0.610	1.21
0.214	0.590	1.19
0.210	0.612	1.15
0.195	0.609	1.19
0.199	0.607	1.20
0.189	0.594	1.19
0.215	0.599	1.24
0.204	0.604	1.19
Mean 0.210 Standard Deviation 0.02 Theoretical 0.2 Value	Mean 0.609 Standard Deviation 0.055 Theoretical 0.6 Value	Mean 1.20 Standard Deviation 0.07 Theoretical 1.2 Value

6.2 Computing the Head Field

A finite difference code was used in computing the head field. There is a vast literature on the application of the finite difference approach in simulating groundwater flow (for example Bear, 1992; Langtangen, 1999 among others). Moreover, the finite difference approach is extremely popular in the hydrologic community due to the availability of commercial software packages such as Modflow©, Visualflow© and similar packages. Due to the simple geometry of the flow domain used in this thesis, the finite difference code was implemented using Matlab©. Construction of the finite difference code begins with a discretization of the flow domain. For a 2D flow domain the zero divergence Darcy equation is expressed as [Bear, 1992]

$$\frac{\partial}{\partial x}\left(K\frac{\partial H}{\partial x}\right)+\frac{\partial}{\partial y}\left(K\frac{\partial H}{\partial y}\right)=0 \tag{6.8}$$

The first and second derivatives are expressed in approximate form. By subscripting the H and K variables with (i,j) to denote their values at node (i,j), the terms in Eq. (6.8) are approximated as

$$K\frac{\partial H}{\partial x}\simeq\frac{1}{2}\left(K_{i,j}+K_{i+1,j}\right)\left(\frac{H_{i+1,j}-H_{i,j}}{\Delta x}\right) \tag{6.9}$$

where Δx is the grid size in the x_1 direction and Eq. (6.9) is the flow in the x_1 direction from node (i, j) to node $(i+1, j)$. The flow from node $(i-1, j)$ to node (i, j) in the x_1 direction is approximated as

$$K\frac{\partial H}{\partial x} \simeq \frac{1}{2}\left(K_{i-1,j} + K_{i,j}\right)\left(\frac{H_{i,j} - H_{i-1,j}}{\Delta x}\right) \tag{6.10}$$

An approximation for the second derivative is then obtained as

$$\frac{\partial}{\partial x}\left(K\frac{\partial H}{\partial x}\right) = \frac{\left(K\frac{\partial H}{\partial x}\right)_{(i,j)\to(i+1,j)} - \left(K\frac{\partial H}{\partial x}\right)_{(i-1,j)\to(i,j)}}{\Delta x} \tag{6.11}$$

Substituting Eqs. (6.9) and (6.10) into Eq. (6.11) gives

$$\frac{\partial}{\partial x}\left(K\frac{\partial H}{\partial x}\right) \simeq \frac{\frac{1}{2}\left(K_{i,j} + K_{i+1,j}\right)\left(\frac{H_{i+1,j} - H_{i,j}}{\Delta x_1}\right) - \frac{1}{2}\left(K_{i-1,j} + K_{i,j}\right)\left(\frac{H_{i,j} - H_{i-1,j}}{\Delta x_1}\right)}{\Delta x_1} \tag{6.12}$$

Letting $A_i = \frac{1}{2}\left(\frac{K_{i+1,j} + K_{i,j}}{(\Delta x_1)^2}\right)$ and $B_i = \frac{1}{2}\left(\frac{K_{i,j} - K_{i-1,j}}{(\Delta x_1)^2}\right)$, Eq. (6.12) can be written as

$$\frac{\partial}{\partial x}\left(K\frac{\partial H}{\partial x}\right)=A_iH_{i+1,j}-(A_i+B_i)H_{ij}+B_iH_{i-1,j} \tag{6.13}$$

Likewise

$$\frac{\partial}{\partial y}\left(K\frac{\partial H}{\partial y}\right)=C_jH_{i,j+1}-(C_j+D_j)H_{ij}+D_jH_{i,j-1} \tag{6.14}$$

where $C_j=\frac{1}{2}\frac{K_{i,j+1}+K_{i,j}}{(\Delta x_2)^2}$ and $D_j=\frac{1}{2}\left(\frac{K_{i,j}-K_{i,j-1}}{(\Delta x_2)^2}\right)$

From Eqs. (6.13) and (6.14), Eq. (6.8) can be written as

$$(A_i+B_i+C_j+D_j)H_{i,j}=A_iH_{i+1,j}+B_iH_{i-1,j}+C_jH_{i,j+1}+D_jH_{i,j-1} \tag{6.15}$$

The goal is to obtain a solution for $H_{i,j}$ subject to the boundary conditions. Eq. (6.15) constitutes a discrete system of equations that can be written in matrix form as

$$[Q]\{u\}=\{B\} \tag{6.16}$$

where Q is the matrix of the coefficients of the head, u is the head field for which a solution is being sought and B is a vector of the boundary conditions. The Matlab© solver is used in solving Eq. (6.16). The numerical solution presented above should be consistent, converge, and be stable for the solver to be considered reliable [Bear, 1992].

The condition of consistency requires the numerical derivation to tend to the exact solutions when the finite intervals Δx_1 and $\Delta x_2 \rightarrow 0$. In regards to the condition of convergence, Bear [1992] says, "It is much more difficult to verify the condition of convergence.....In many applications, it is impossible to prove convergence in a rigorous way. Therefore it is usually sufficient if the numerical procedure has been verified against a variety of analytical solutions." The code used in this thesis has been tested against known deterministic solutions and thus convergence of the code may be assumed [Wang and Henderson, 1982 and Elfeki et al., 1997].

6.3 The Head Field

With the hydraulic conductivity K data (for example as shown in Fig. 6.2) as the input with the boundary conditions shown in Fig. 6.1, the hydraulic head field was computed. The hydraulic head for the K field in Fig. 6.2 is shown in Fig. 6.9. There are several interesting features about this head field, which was also observed for all the computed head fields:

1. First, it is observed that the imposed constant head boundary conditions tend to propagate towards the interior of the flow domain. At the top left corner of the hydraulic head field one observes a sustained head value close to the imposed value of 1. A similar behavior is observed at the lower right boundary, where low head values are sustained into the flow domain. This behavior can be attributed to the seed used because from Fig. 6.10 we notice that the head contours for $C_K = 0.3$ do

not exhibit the same behavior. This persistence of the imposed boundary conditions into the flow domain has been observed by other researchers, for example Ababou [1988].

2. The contour plots of the head fields obtained for K fields with C_K values of 0.1 and 0.3 are shown in Fig. 6.10. At first one notices the increasing wavy nature of the head contours as the C_K values increase. At a rather small distance away from the boundary, one can observe the effect of the imposed no flow condition. However, this effect diminishes rapidly as one moves to the interior of the flow boundary.

3. Another interesting observation about the head field is that compared to the K field, the head field seems less erratic. In contrast to the K field, the head fields exhibit a much longer range of correlation. The values of the K field (see Fig. 6.2) change quite rapidly as one moves from one location to the other, whereas the head field values change relatively slowly. One can observe from the head contours the clear demarcation of the various head values and the region each interval occupies. Contour plots for the K fields could not even be obtained because of the rapidly changing values from one location to the other, which makes it infeasible to triangulate the data and display it with contours as was done for the head field.

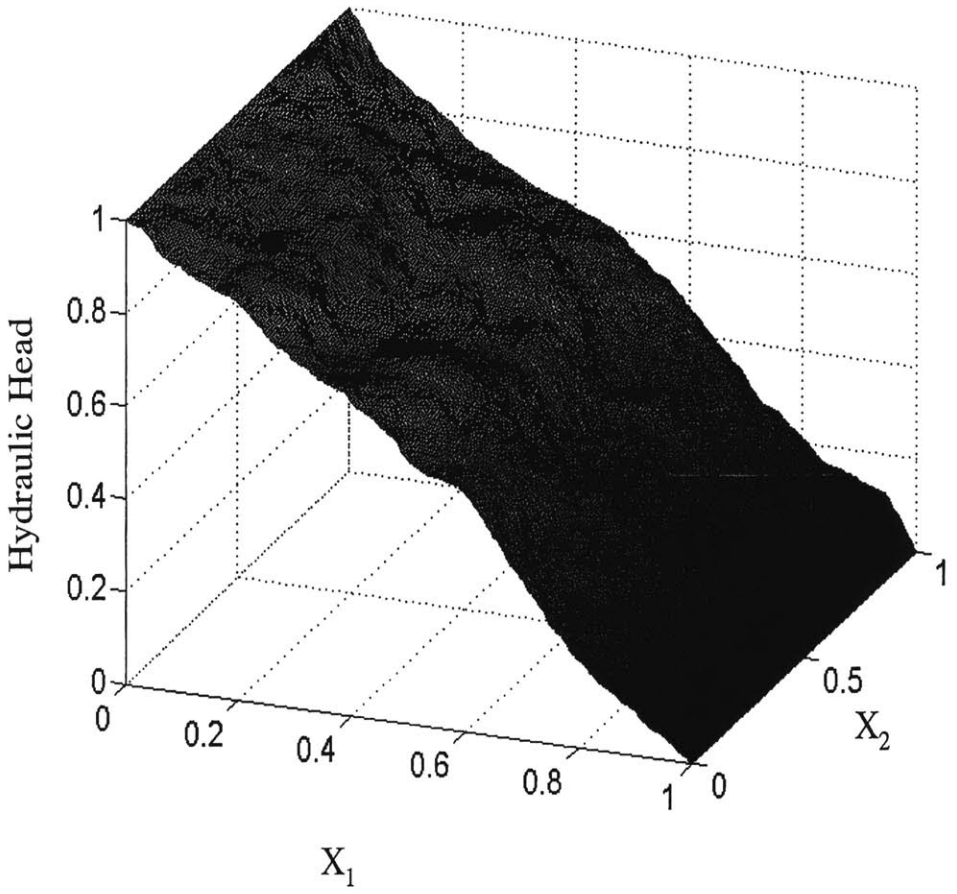

Figure 6.9a – A perspective view of the head field computed from a hydraulic conductivity field with $C_K = 0.1$

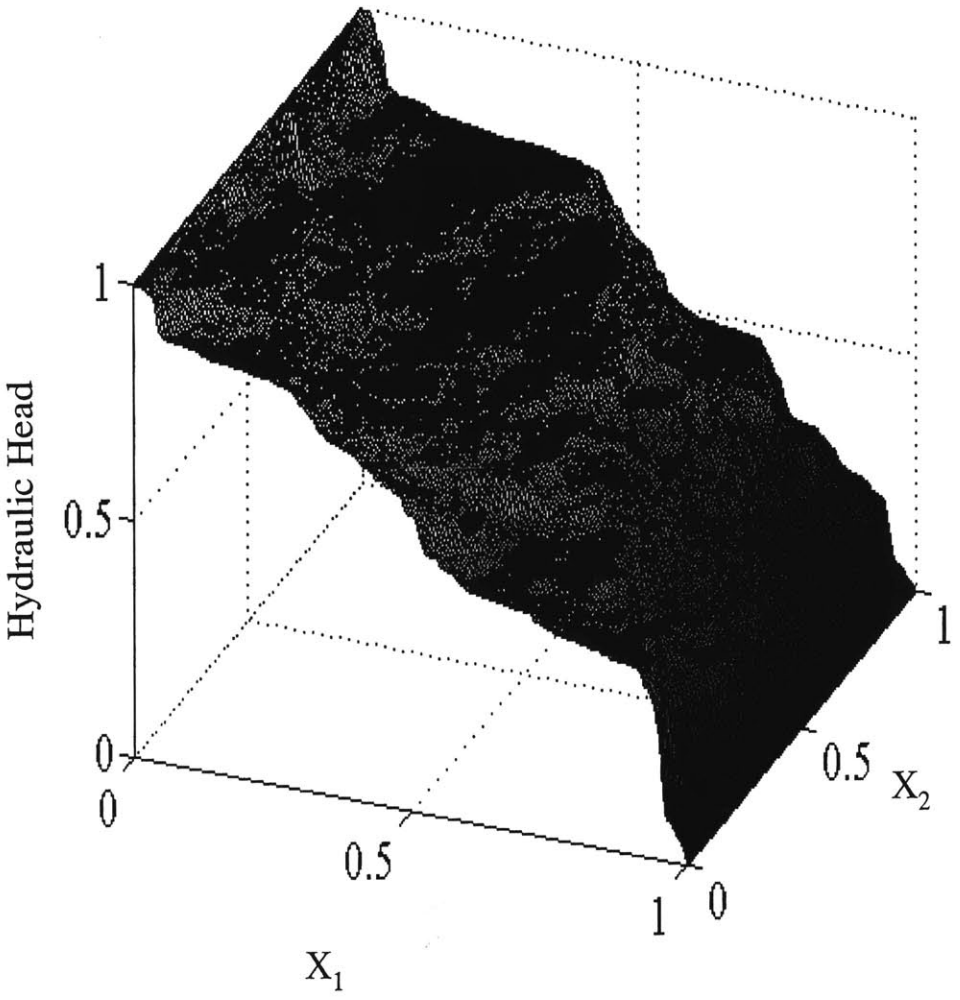

Figure 6.9b – A perspective view of the head field computed from a hydraulic conductivity field with C_K= 0.3

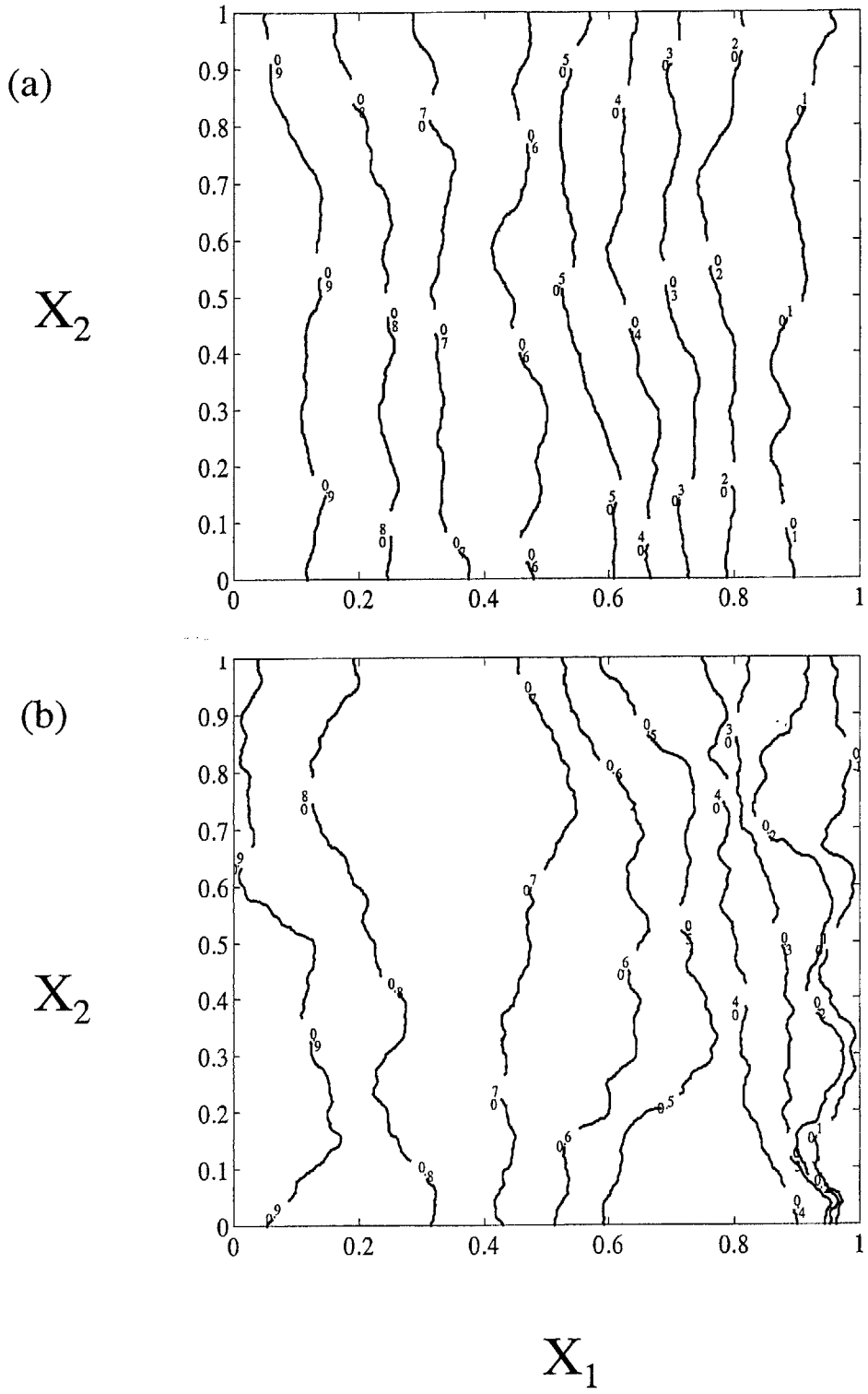

Figure 6.10 - The head contours from K fields with (a) C_K= 0.1 and (b) C_K= 0.3

An important consideration in the theoretical analysis in this study deals with the scaling properties of the hydraulic gradient field. The scaling properties of the hydraulic gradient ∇H are examined to study its behavior when flow occurs in an isotropic lognormal multifractal K field. In a fashion similar to one used in studying the scaling properties of the K field, the behavior of the slope of the $\log\left\{\left|\nabla H\right|^q\right\}$ versus log (resolution) is examined.

The notion of resolution as used in analyzing the data, corresponds to the number of quadrants over which the original data is divided and analyzed. One can gain a better understanding of this notion of resolution by looking at Fig. 6.12. This figure illustrates the hydraulic gradient data at resolutions r = 1, 2, 4 and 8. At resolution r = 1, the H data is distributed over one square block. A regression analysis is used in determining the components of the hydraulic gradient in the x_1 and x_2 directions. The equation of the plane has the form

$$H = J_1 x_1 + J_2 x_2 + \varepsilon \tag{6.17}$$

where ε is a zero mean residual term, $H(x_1, x_2)$ is the head field, J_1 and J_2 are the slopes of the plane in the x_1 and x_2 directions respectively and correspond to the

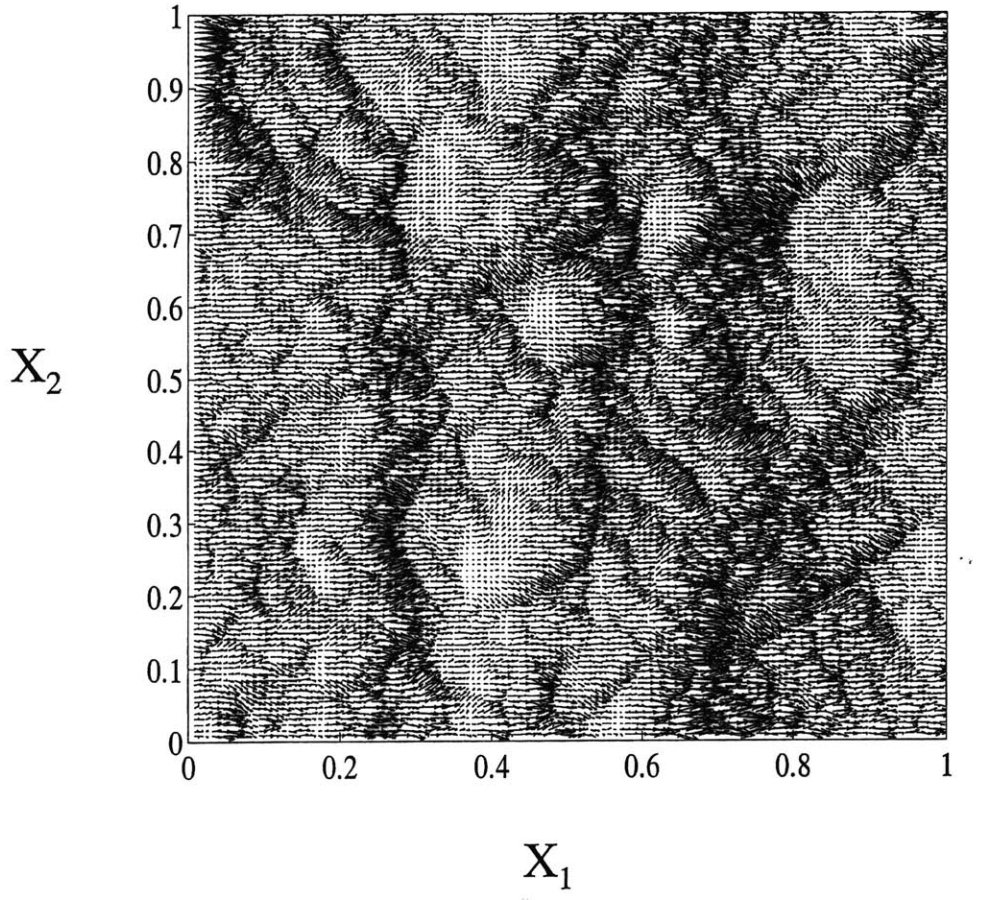

Figure 6.11 – The hydraulic gradient field computed from a K field with $C_K = 0.1$

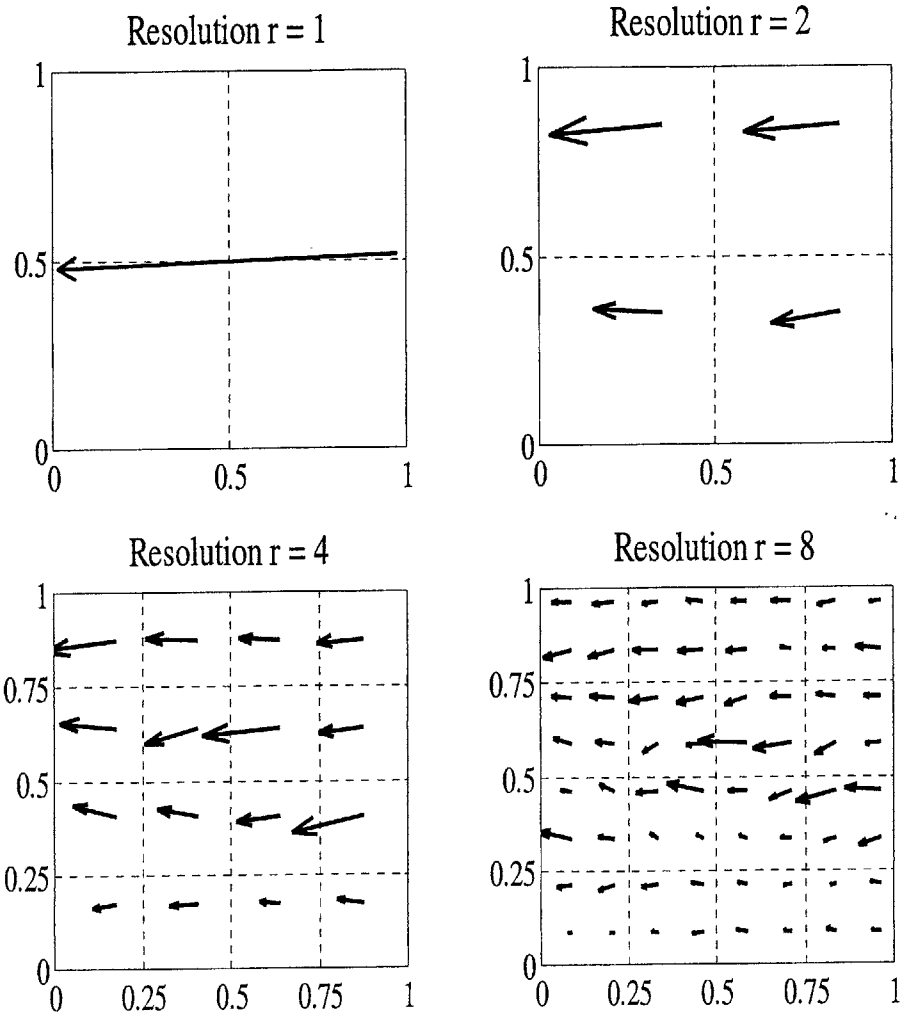

Figure 6.12 - An illustration of how the hydraulic gradient vectors change with resolution

components of the hydraulic gradients in these directions. A regression analysis performed according to Eq. 6.17 on the head field at r = 1 produced a $J_1 = -1.096$ and $J_2 = -0.0621$ so that the mean hydraulic gradient $J = \sqrt{J_1^2 + J_2^2} = 1.0978$. This mean hydraulic gradient exceeds the initially imposed J = 1. As discussed previously, the discrepancy between the numerically obtained J and the imposed value increases as the variance or C_K value of the K field increases because in variable K fields, the rotation of the flow vectors increase as the variability of the K field increases. Another interesting feature of the hydraulic gradient is that although it was initially imposed in the x_1 direction, the computed value shows a slight deviation or rotation away from the x_1 direction. The magnitude of this rotation angle α is computed as follows:

$$\alpha = \arctan\left(\frac{J_2}{J_1}\right) \tag{6.18}$$

In further discussions, the rotation angle at a resolution r will be denoted as α_r. Thus for r = 1 in Fig. 6.11 the mean hydraulic gradient J has an associated rotation angle $\alpha \approx 3.24°$.

To obtain the mean hydraulic gradient at different resolutions, the hydraulic head field H is divided into a number of squares corresponding to the resolution. For example as shown in Fig. 6.12 at r =2, the H field is subdivided into 4 squares, so that there are two r = 2 squares on either axis. Similarly, at r = 4, the H field is subdivided into 4^2 squares,

and at r = 8, the H field is subdivided into 8^2 squares. In general, when the H field is being analyzed to obtain the mean hydraulic gradient $J_r = |\nabla H_r|$ at a resolution r, the H field is subdivided into r^2 squares. Next, all the H values within each "subsquare" are analyzed as discussed in pt. 2 according to Eq. (6.17), to obtain the J_1 and J_2 values for each quadrant. Following this procedure, the mean hydraulic gradients were obtained for H field derived from the K field with $C_K = 0.1$ and the mean hydraulic gradients are displayed for r = 1, 2, 4 and 8 in Fig.6.12. A few interesting observations can be made about this figure: First of all, the mean hydraulic gradient at r = 1, does not coincide exactly with the imposed mean hydraulic gradient. The deviation of the computed mean hydraulic gradient from the x_1 direction can be attributed to the heterogeneity of the K field, which in turn causes the flow vectors to rotate and effectively increases the mean hydraulic gradient. Also, the heterogeneity of the K field results in a slight rotation of the mean hydraulic gradient at r = 1. As one goes from r = 1 to finer resolutions, there is an observed increase in the rotations of the hydraulic gradient vectors. The magnitude of the hydraulic gradient vectors tend to decrease with increasing resolution although their average value tends to remain the same as one goes from a coarser (small values of r) to finer (higher values of r) resolution. The rotations of the hydraulic gradient vectors tend to become more erratic as one moves from coarser to finer resolutions. The scaling of the hydraulic gradient vectors is next examined in detail.

6.3.2 Scaling of the hydraulic gradient

Using the procedure described above, the scaling of the hydraulic gradient fields for K fields with $C_K = 0.1$ and 0.3 were examined. The mean hydraulic gradient at each resolution is obtained and then exponentiated to the power s. The mean value of the exponentiated values are then taken and these are the plotted values in Figs. 6.13 and 6.14 for K fields with $C_K = 0.1$ and 0.3 respectively. From these Figures, one notices a significant deviation of the scaling behavior when r = 1. This corresponds to the mean hydraulic gradient over the whole flow domain. The lack of scaling of the mean hydraulic gradient at r = 1 may be attributed to the persistent behavior of the imposed constant hydraulic head boundaries, whose effects become pronounced at the larger scale or at coarse resolutions of r = 1. We observe that at a resolution of even r = 2, the effects of these boundary conditions do not seem to affect the scaling behavior of the hydraulic gradient fields for both $C_K = 0.1$ and 0.3. In computing the slopes of the moments of the mean hydraulic gradients at various resolutions, the values at r = 1 were excluded. Also it should be noted that although the head field was obtained on a 512 x 512 grid, the hydraulic gradient fields were obtained for resolutions up to r = 256. The hydraulic gradient field at a resolution of r = 512 was excluded from the analysis because a different numerical procedure would have been used in obtaining the hydraulic gradient values. Specifically, an approximate hydraulic gradient value at r =512 can be obtained

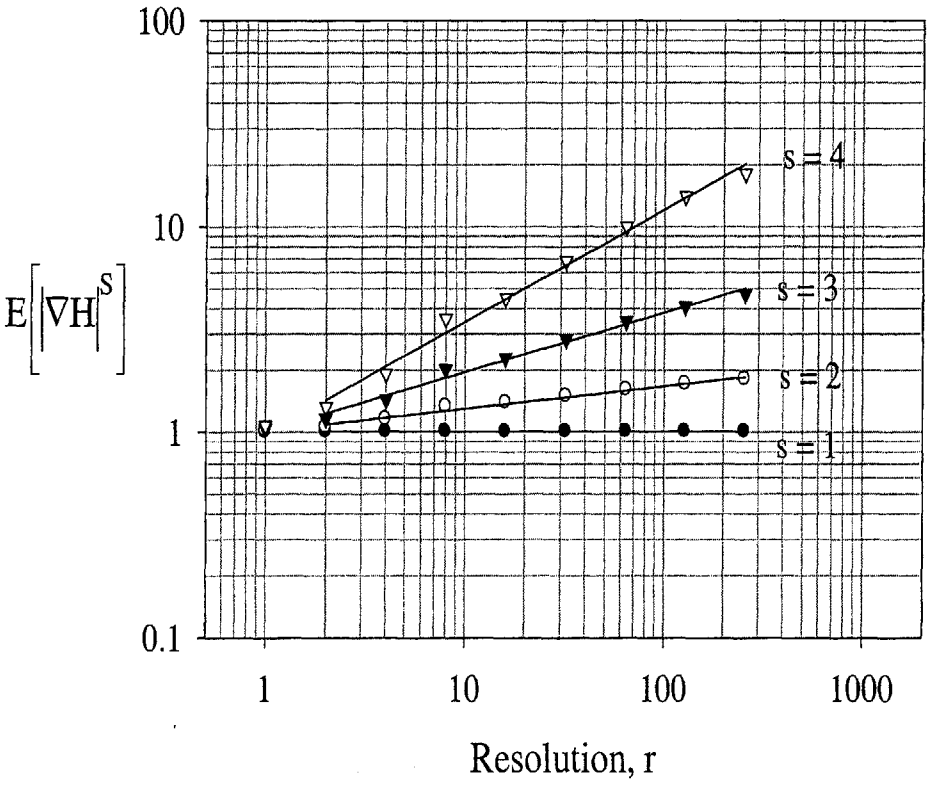

Figure 6.13 - The scaling of moments for the hydraulic gradient amplitude for $C_K = 0.1$.
The lines on the graph are obtained by performing a linear regression on the points.

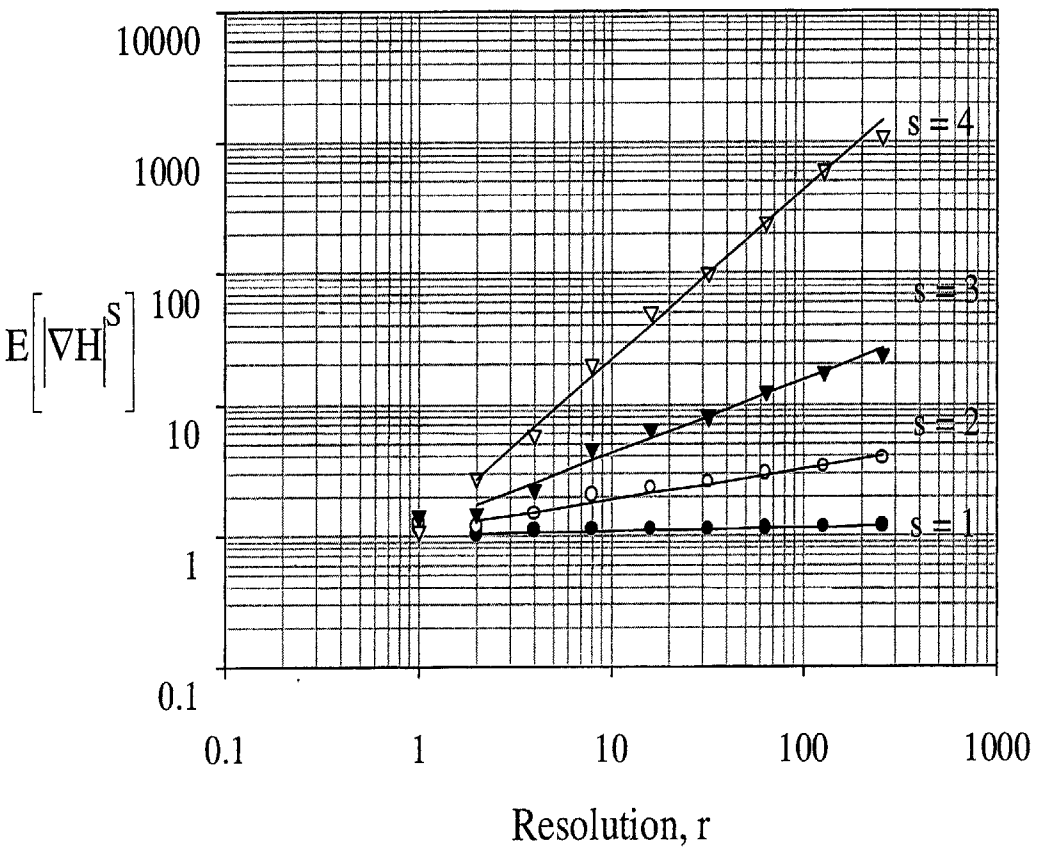

Figure 6.14 - The scaling of moments for the hydraulic gradient amplitude for $C_K = 0.3$. The lines on the graph are obtained by performing a linear regression on the points.

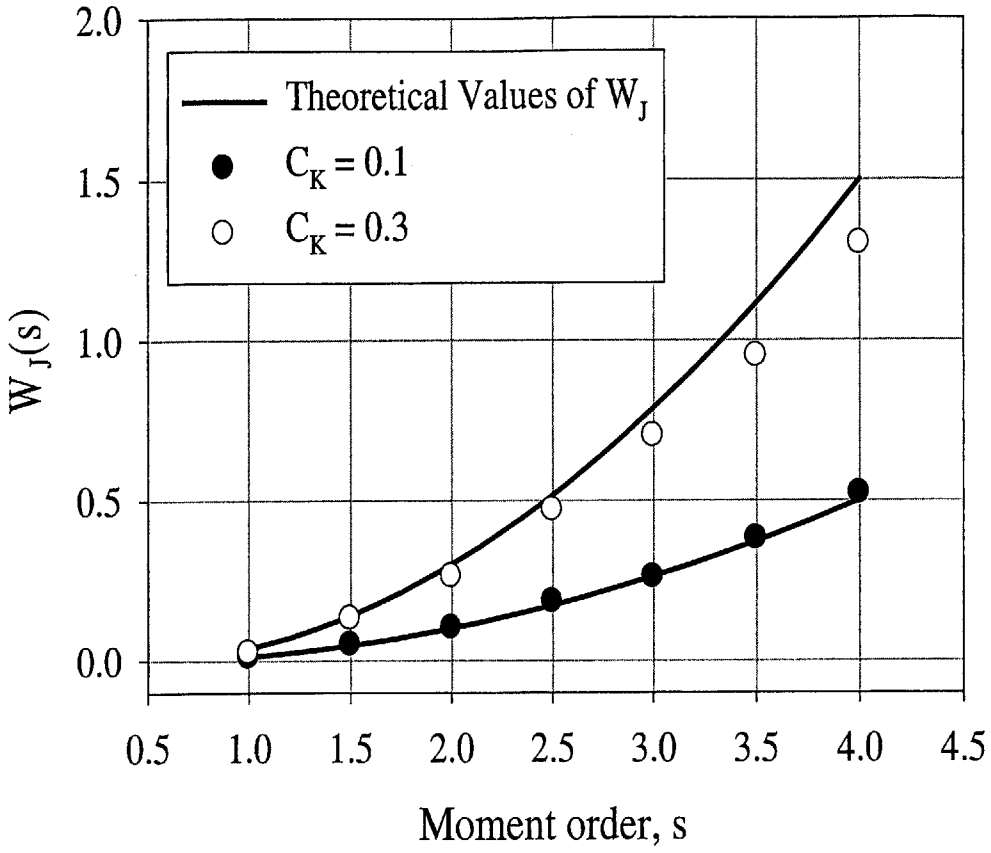

Figure 6.15 - Comparison of the numerically obtained scaling moments of the hydraulic gradient field with the theoretically derived values for fields with $C_K = 0.1$ and 0.3.

by taking the differences of the H values at unit intervals in the x_1 and x_2 directions. This approach is less accurate in determining the gradients than the linear regression method described above. Hence, to avoid differences in results by virtue of changing the estimation method, the hydraulic gradient values at r = 512 were excluded.

The slopes of the plots in Figs. 6.13 and 6.14 are shown in Fig. 6.15, which compares the theoretically obtained scaling moments of the mean hydraulic gradient with the numerically obtained values. The theoretical slopes of the hydraulic gradient field (or the moment scaling function) was obtained in Chapter 4 as:

$$W_J(s) = C_K\left[\frac{D-1}{D(D+2)}s + \frac{3}{D(D+2)}(s^2 - s)\right] \tag{6.19}$$

where D is the space dimension. Thus for K fields with $C_K = 0.1$ and 0.3 in a 2D space, $W_J(s) = C_K(0.125s + 0.375(s^2 - s)$. This theoretical curve is plotted in Fig.6.15 for $C_K = 0.1$ and 0.3, and compared to the slopes of the curves obtained through the numerical simulation. We observe that the numerical simulation results closely match of the theoretical derivations. To illustrate the type of variation one can observe for different simulations, the hydraulic gradient fields for the 20 K fields whose scaling is shown in Fig. 6.7 was computed and the scaling of the moments for the 20 ∇H fields is shown in Fig. 6.16. The data in Fig. 6.16 displays a close cluster for the different moments. The slopes of the lines shown in Fig. 6.16 are reported in Table 6.2. And the

scaling of the mean of the 20 simulations is shown in Fig. 6.17. From Table 6.2 and Fig. 6.17 we observe that both the individual simulations and their averaged values show a good agreement with the theoretical results.

From the numerically obtained hydraulic gradient data, the rotation angles of the hydraulic gradient vectors were also computed using Eq. (6.18). The properties of these rotation angles would be further discussed in Section 6.5. In the next section, the scaling of the specific discharge field is discussed.

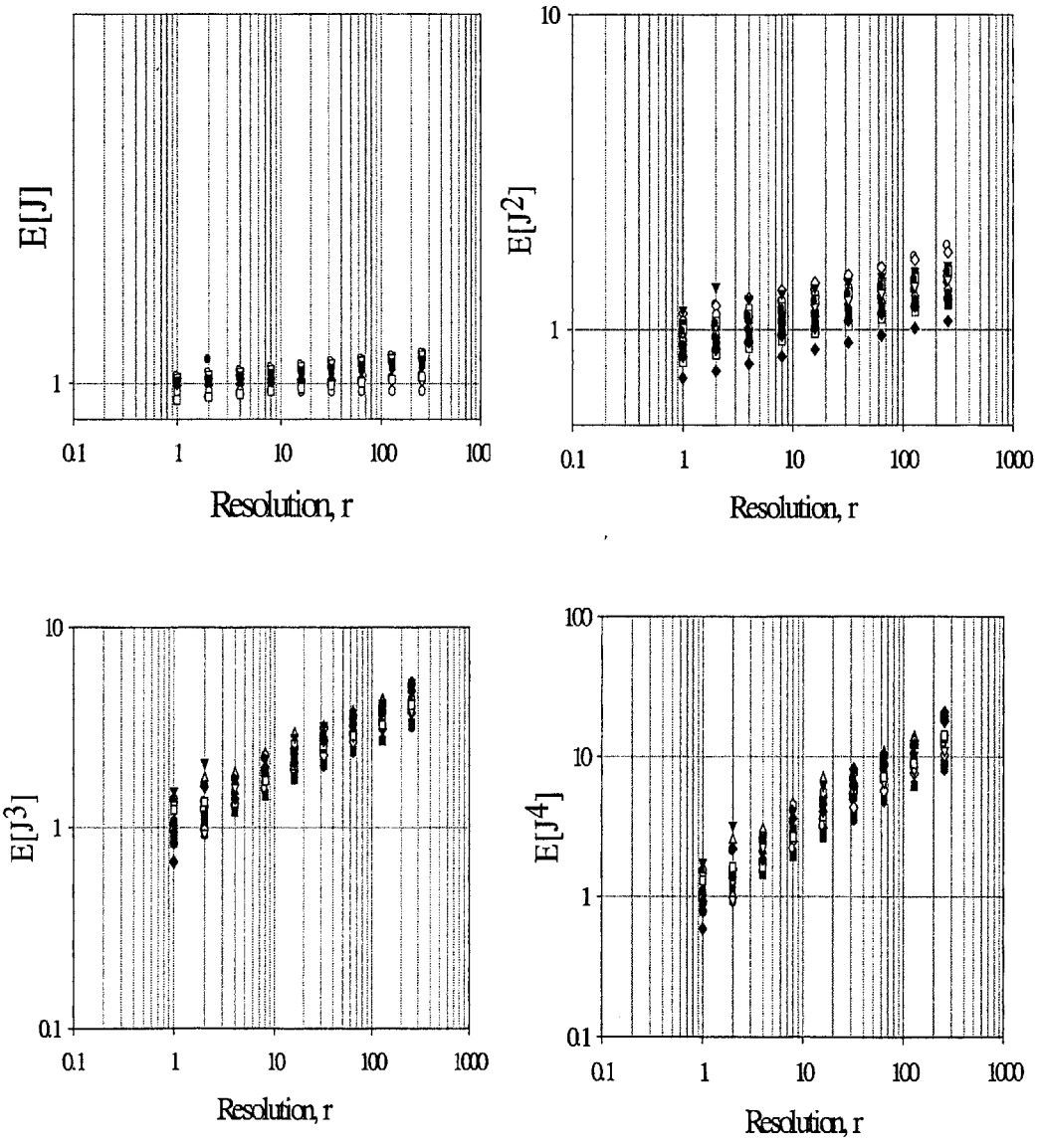

Figure 6.16 - Scaling of the amplitude of the hydraulic gradient field for the $C_K = 0.1$ fields shown in Fig. 6.7.

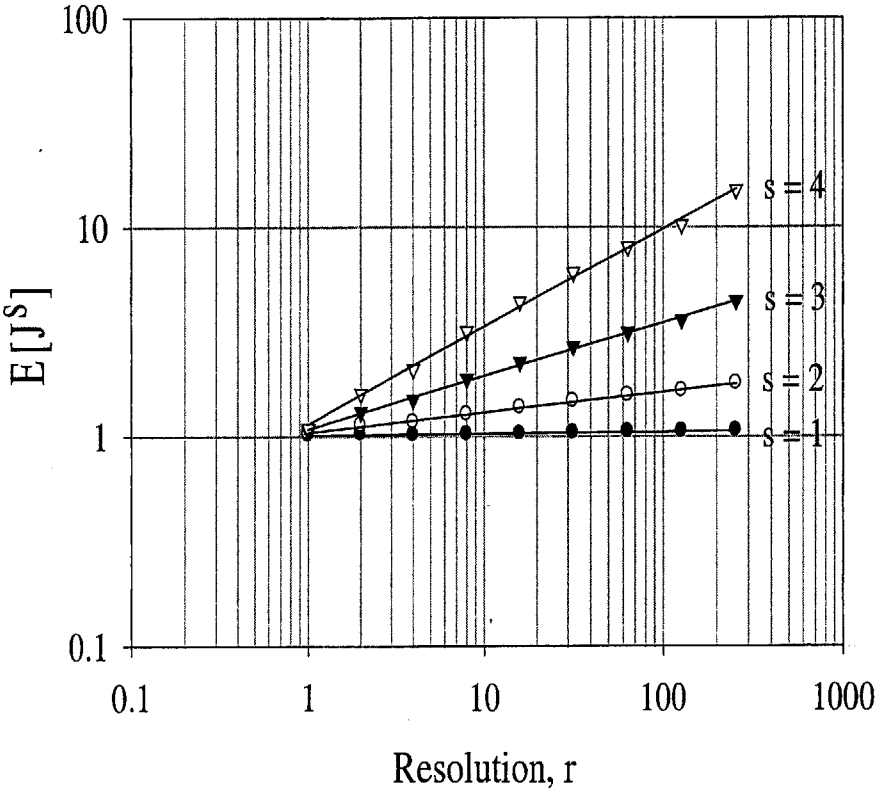

Figure 6.17 – The scaling of the average values of the hydraulic gradient amplitude shown in Fig. 6.16 for fields with $C_K = 0.1$.

Table 6.2 Slopes of $\log\{E[J^S]\}$ versus $\log\{\text{resolution}\}$ for K fields with $C_K = 0.1$

$W_J(1)$	$W_J(2)$	$W_J(3)$	$W_J(4)$
0.0131	0.1136	0.2891	0.5211
0.0002	0.0940	0.2670	0.5080
0.0050	0.0750	0.2040	0.4200
0.0170	0.0140	0.2750	0.5300
0.0080	0.0800	0.2120	0.4200
0.0139	0.0970	0.2400	0.4400
0.0164	0.1142	0.2780	0.4970
0.0155	0.1088	0.2830	0.5200
0.0146	0.1003	0.2410	0.4300
0.0140	0.1155	0.2910	0.5230
0.0050	0.0970	0.2400	0.4300
0.0080	0.0890	0.2300	0.4700
0.0100	0.1140	0.2620	0.4750
0.0060	0.0800	0.2200	0.4300
0.0100	0.1010	0.2614	0.5100
0.0151	0.1100	0.2630	0.5600
0.0070	0.0800	0.2300	0.4400
0.0150	0.1010	0.2500	0.4970
0.0110	0.1000	0.2600	0.5200
0.0120	0.1100	0.2811	0.5160
Mean 0.01084 Standard Deviation 0.0045 Theoretical 0.0125	Mean 0.0950 Standard Deviation 0.0024 Theoretical 0.1	Mean 0.254 Standard Deviation 0.0245 Theoretical 0.2625	Mean 0.483 Standard Deviation 0.045 Theoretical 0.5

6.4 Scaling of Specific Discharge Field

From the head field H and the hydraulic conductivity K, the specific discharge field is obtained approximately as follows

$$\text{(i)}\quad q_{x_1 i,j} = \sqrt{K_{i-1,j}K_{i,j}}\,\frac{\left[H_{i,j} - H_{i-1,j}\right]}{(\Delta x_1)}$$
$$\text{(ii)}\quad q_{x_2 i,j} = \sqrt{K_{i,j-1}K_{i,j}}\,\frac{\left[H_{i,j} - H_{i,j-1}\right]}{(\Delta x_2)} \qquad (6.20)$$

where Δx_1 and Δx_2 are the grid sizes in the x_1 and x_2 directions respectively. The magnitude of the flow field is obtained as $q = \sqrt{q_{x_1}^2 + q_{x_2}^2}$. The flow field for the K field with $C_K = 0.1$ (shown in Fig. 6.2) calculated using Eq. (6.20) is shown in Fig. 6.18. The specific discharge field, like the ∇H field, seems more erratic than the head field and less erratic than the K field. Unlike the hydraulic gradient field, where we fit a plane to the whole data set to determine the mean value at r = 1, the value of specific discharge field at r = 1 is obtained by simply taking the average value over the whole domain.

$$q_{r=1} = \langle |q| \text{ over the whole flow domain} \rangle \qquad (6.21)$$

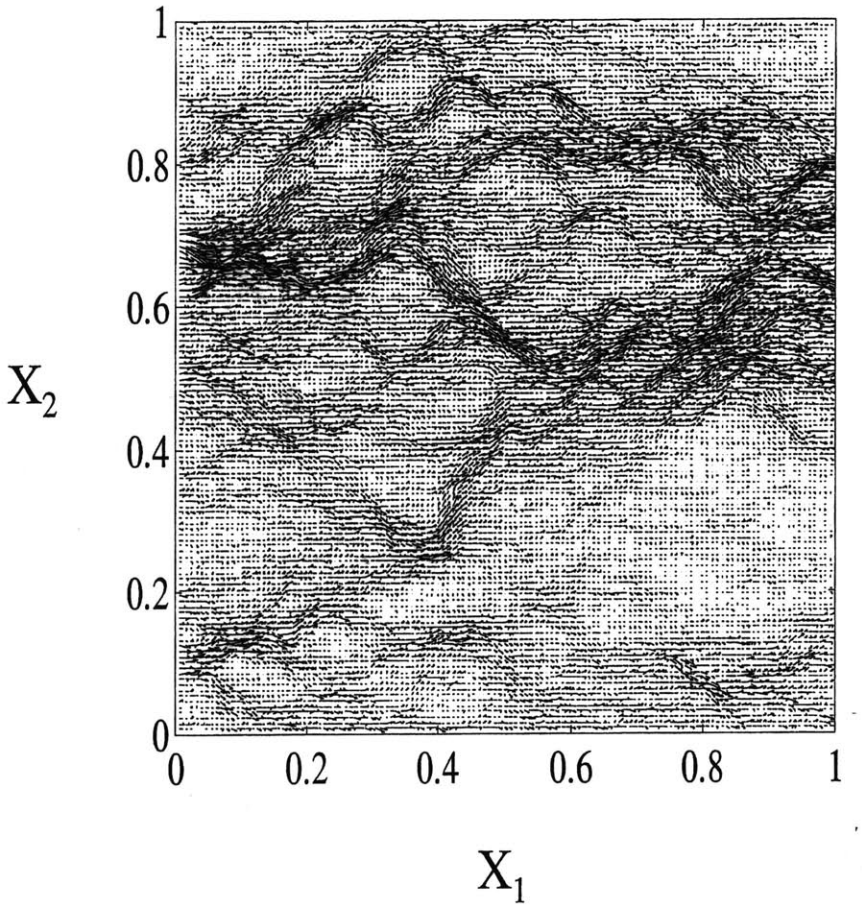

Figure 6.18a - The velocity field computed for a hydraulic conductivity field with $C_K = 0.1$

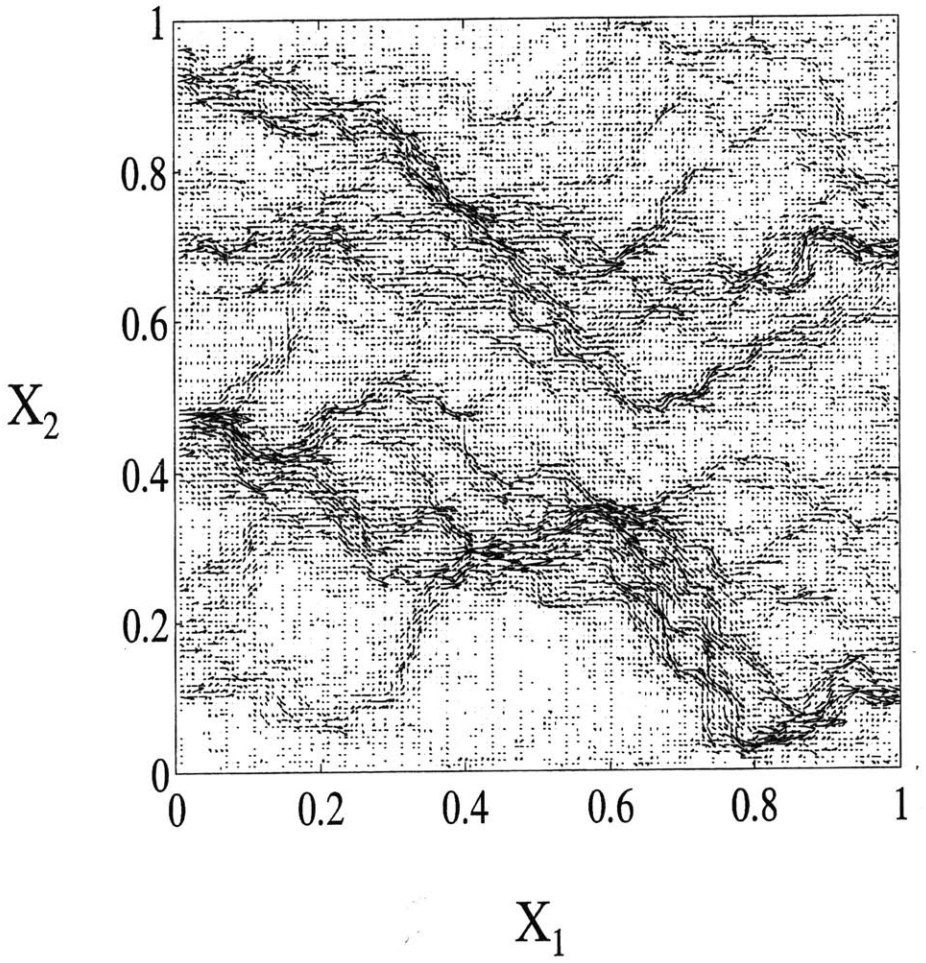

Figure 6.18b - The velocity field computed for a hydraulic conductivity field with $C_K = 0.3$

For r = 2, the flow field is divided into 2^2 squares. And the mean value of the magnitude of the specific discharge field within each square is taken, so that

$$q_{r=2} = \left(\langle q_{\in 1}\rangle, \langle q_{\in 2}\rangle, \langle q_{\in 3}\rangle, \langle q_{\in 4}\rangle\right) \tag{6.22}$$

where the subscript $\in 1$ denotes magnitude of the flow within sub square 1.

In general, at a resolution of r, the square flow field is divided into r^2 squares and the mean flow within each square is taken. Once the values of the mean flows at each resolution are obtained, the moments can be computed by simply exponentiating the mean values within each sub square. As an example, the higher moments s = 2, 3, or 4 of the flow field at resolution r =2, is obtained as follows,

$$\left\langle q_{r=2}^{s}\right\rangle = \left\langle \left(\langle q_{\in 1}\rangle\right)^{s}, \left(\langle q_{\in 2}\rangle\right)^{s}, \left(\langle q_{\in 3}\rangle\right)^{s}, \left(\langle q_{\in 4}\rangle\right)^{s} \right\rangle \tag{6.23}$$

The moments at various resolutions are obtained in a similar fashion. Figs. 6.19 and 6.20 show the moments obtained for velocity fields with C_K values of 0.1 and 0.3.
In both figures one notices that the linear scaling of the velocity field does not begin at the resolution of r = 512 at which the field was computed. Instead, the scaling begins at approximately r = 256 and continues to a resolution of about r = 2.

The theoretically derived expressions for the scaling of the moments of the velocity fields are as follows:

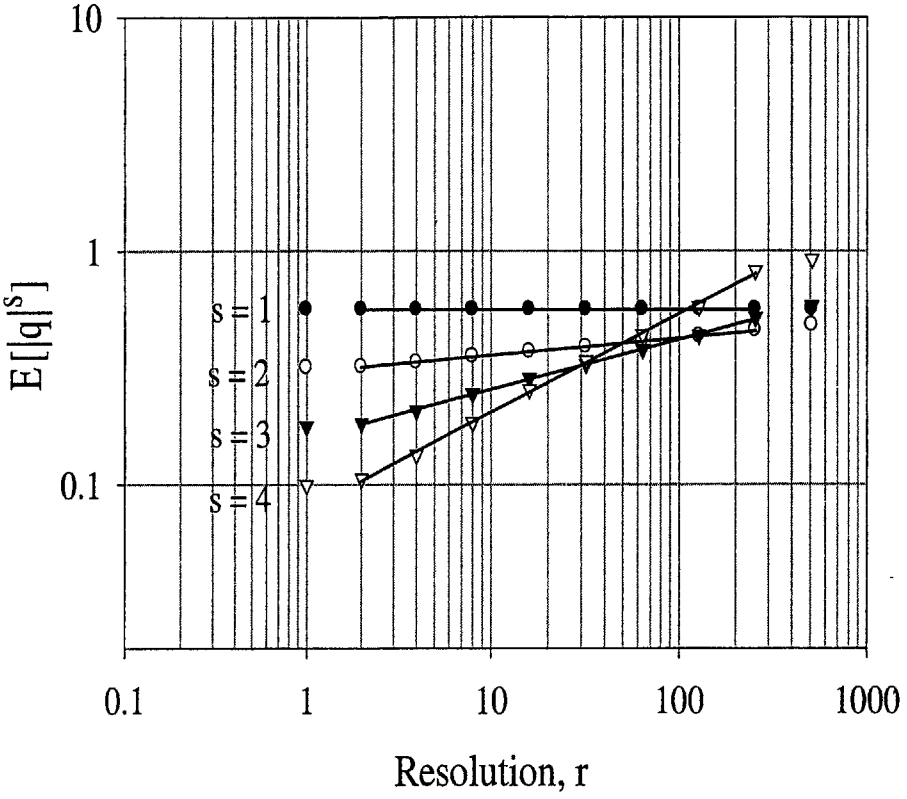

Figure 6.19 - Scaling of the magnitude of the velocity vectors for a field with $C_K = 0.1$

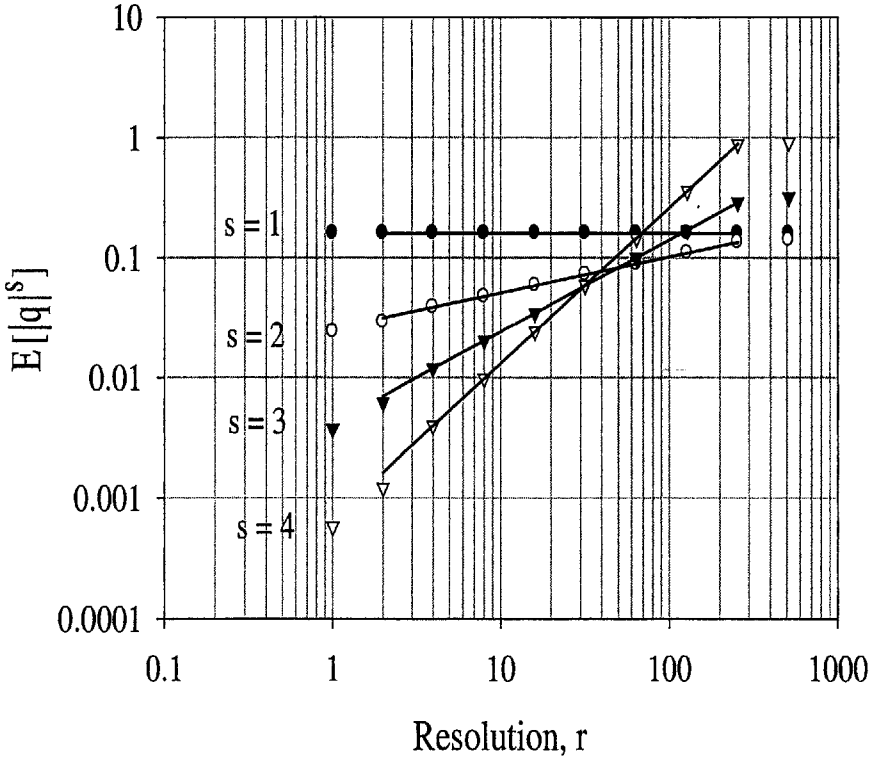

Figure 6.20 - Scaling of the magnitude of the velocity vectors for a field with $C_K = 0.3$

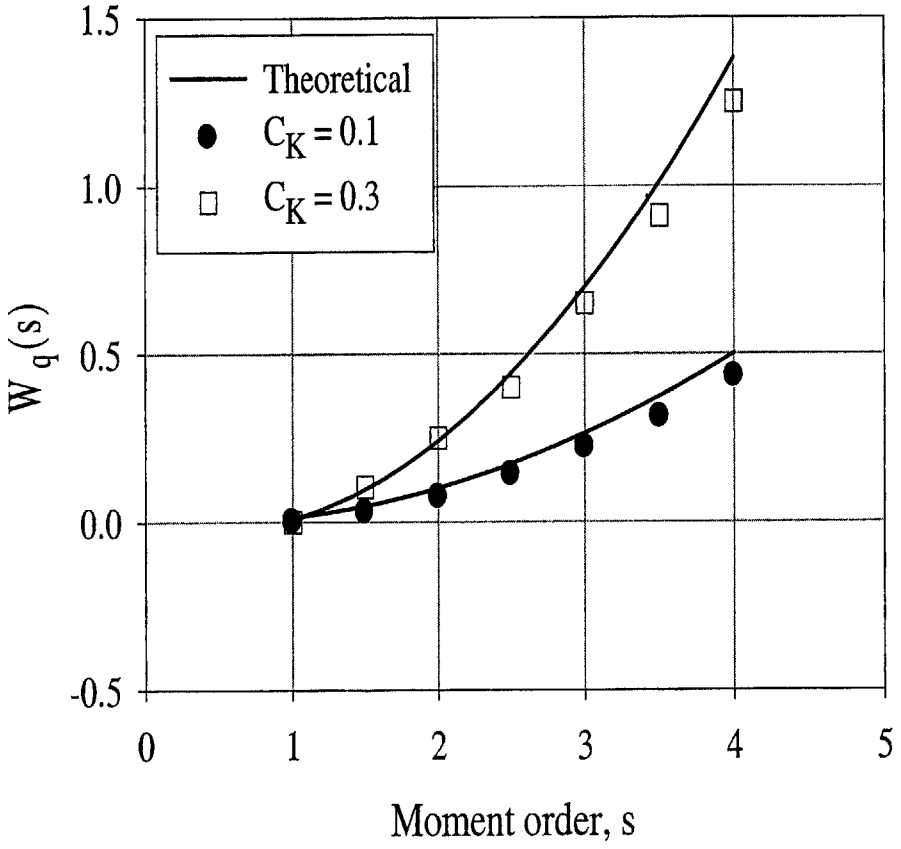

Figure 6.21 - Comparison between the theoretical and empirical scaling moments for the specific discharge amplitude for $C_K = 0.1$ and 0.3

$$\text{(i)}\quad E[\ln B_r]=\left[\frac{D-4}{D(D+2)}-1\right]C_K \ln(r)$$

$$\text{(ii)}\quad Var[\ln B_r]=\frac{2(D^2-1)}{D(D+2)}C_K \ln(\gamma r) \tag{6.24}$$

where $\gamma = 1+2C_K$ is a constant which accounts for the variability of the velocity field when r = 1. For a 2D field the initial moments of the velocity field are computed as

$$E\left[B_r^s\right] = \exp\left\{-0.25sC_K \ln r + 0.375s^2 C_K \ln \gamma r\right\}$$

The theoretical slopes shown in Fig. 6.21 are computed by performing a linear regression of $\log\left(E\left[B_r^s\right]\right)$ versus $\log(r)$ for each given value of s. Fig. 6.21 shows the computed theoretical slopes and the slopes of the velocity moments shown in Figs 6.19 and 6.20. The numerical scaling moments for the $C_K = 0.1$ field show a good agreement with the theoretically computed curve. Although the log of velocity moments of the $C_K = 0.3$ field display a linear dependence on the log resolution (see Fig. 6.19), the slopes of these lines are considerably less than the theoretical curve. The discrepancy is due to the seed used in generating the K field. To illustrate the type of randomness one can expect when simulating these flow fields, the moment scaling for the specific discharge amplitudes for the K fields with $C_K = 0.1$ was computed and is displayed in Fig. 6.23 and their average values are plotted in Fig. 6.24. Even though different seeds were used in creating the

velocity fields, the 20 velocity fields display a small variance of 0.001 for resolution r = 1.

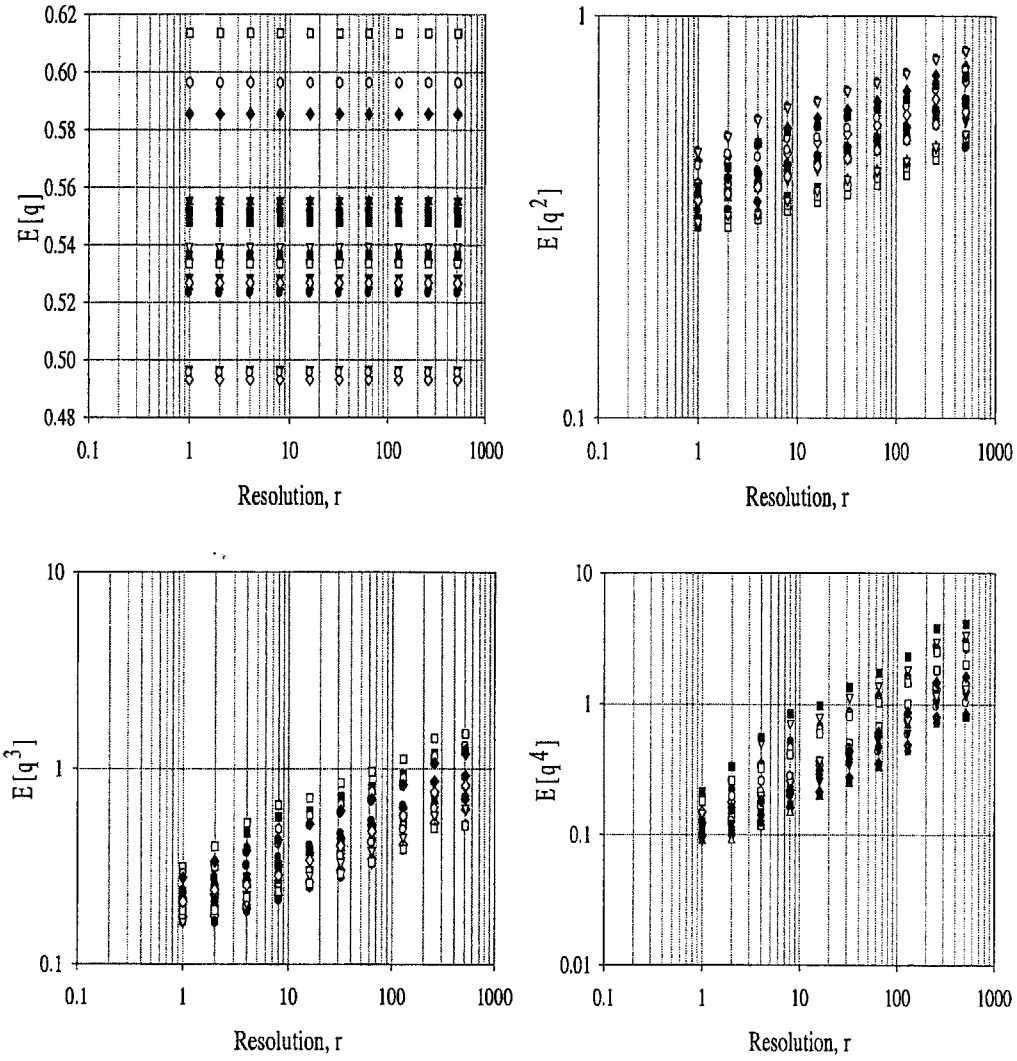

Figure 6.22 - The scaling of the specific discharge amplitudes for fields with $C_K = 0.1$

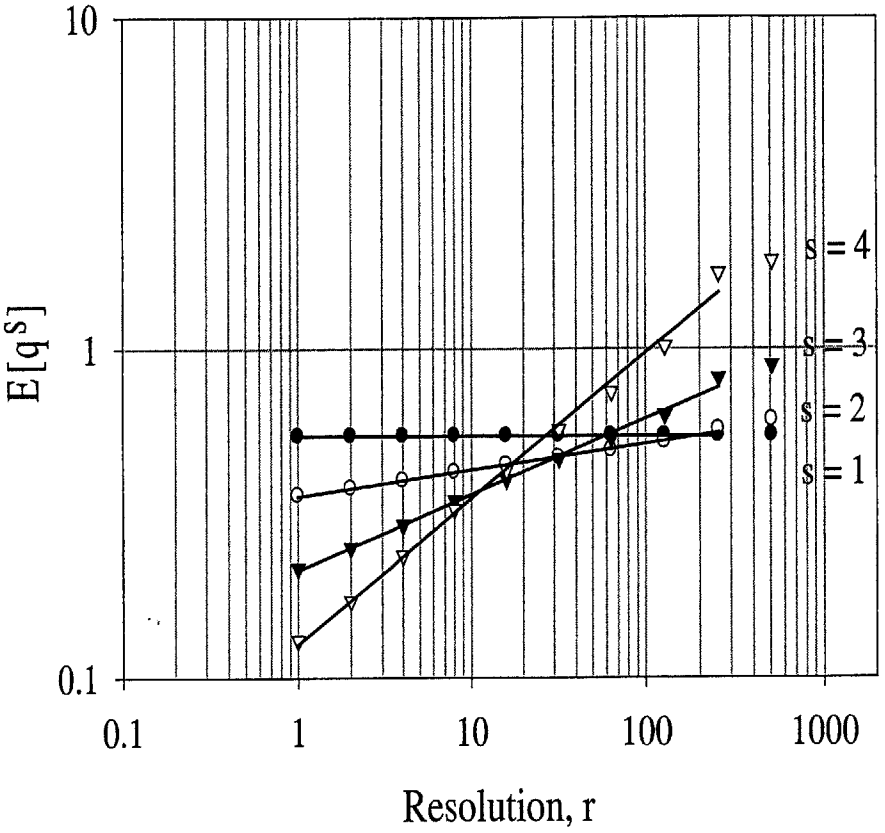

Figure 6.23 - The scaling of the average of the specific discharge amplitudes for fields with $C_K = 0.1$ shown in Fig. 6.22

Scaling of the inverse velocity field (Slowness)

The inverse of the velocity field is used in deriving the first passage time distribution and the plume concentrations for solute transport in multifractal K fields. The slowness $B_r^{'}$ is characterized as a lognormal random variable with the following mean and variance

$$E\left[\ln\left(B_r^{'}\right)\right]=\left[1-\frac{D-4}{D(D+2)}\right]C_K \ln(r)$$

$$\mathrm{Var}\left[\ln\left(B_r^{'}\right)\right]=\frac{2\left(D^2-1\right)}{D(D+2)}C_K \ln\left((1+2C_K)r\right) \tag{6.25}$$

The moments of the inverse velocity fields with $C_K = 0.1$ and 0.3 are shown in Fig. 6.24. Moments from the numerically simulated flow fields are shown as points (circles and triangles) and overlain with the theoretically computed moments from Eq. (6.25). Fig. 6.24 shows that the theoretically obtained results are valid.

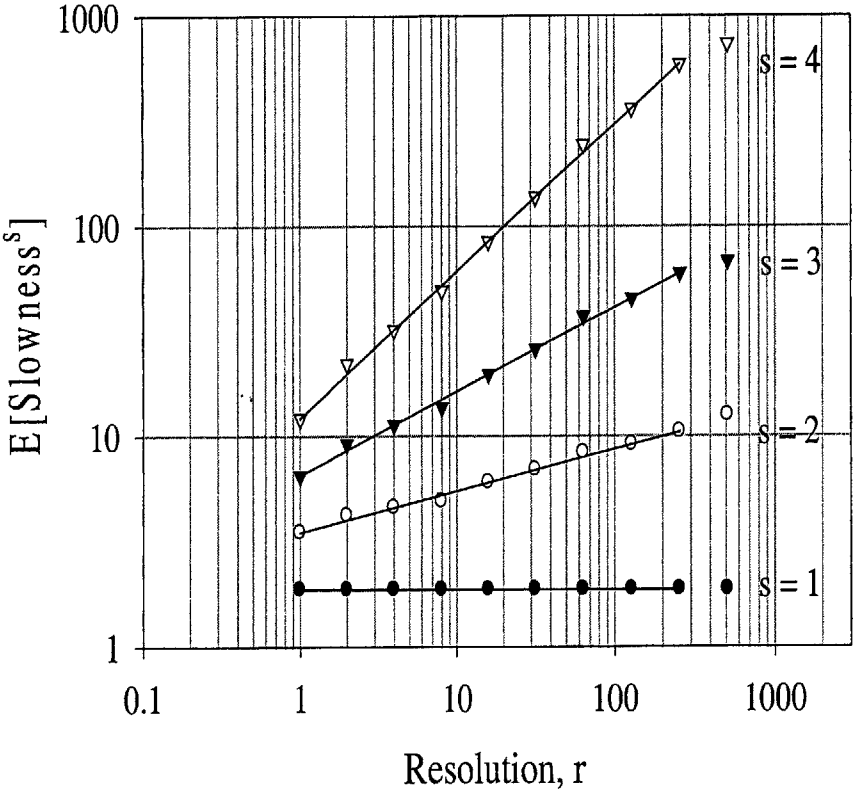

Figure 6.24a - The scaling of the slowness for a field with $C_K = 0.1$

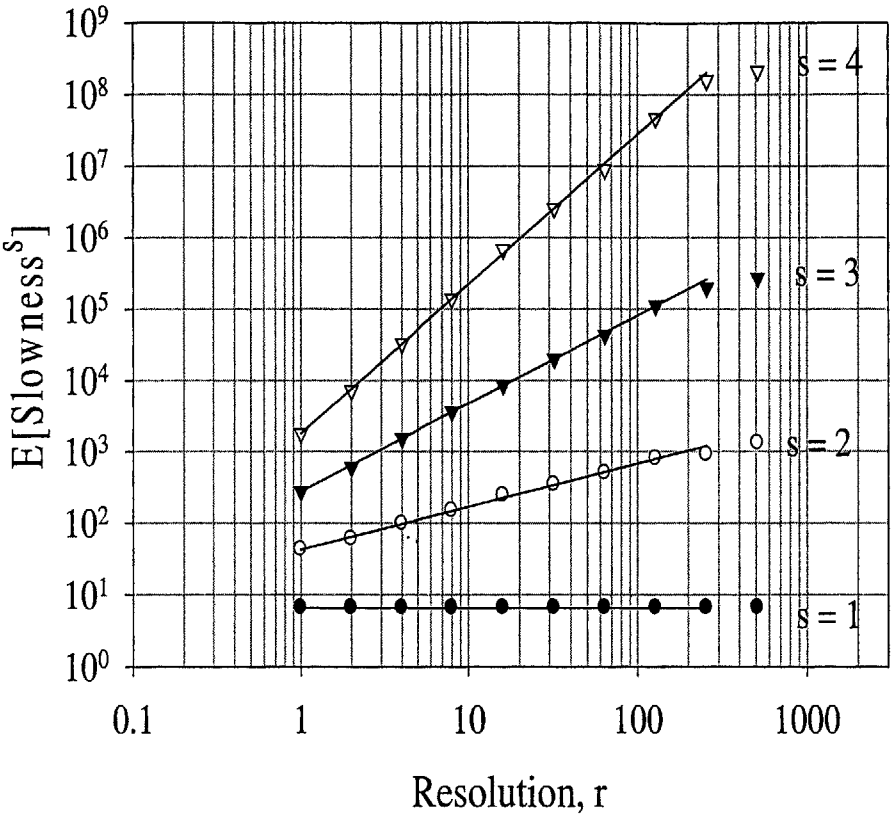

Figure 6.24b - The scaling of the slowness for a field with $C_K = 0.3$

The discussion so far has focused on the scaling properties of the K-field, the magnitude of hydraulic gradient and the velocity field. In discussing the scaling of the hydraulic gradient field, the computation of the rotation angles of the hydraulic gradient vectors was presented. We now present in detail the properties of the rotation angle, and the interaction of the hydraulic gradient and hydraulic conductivity field and how these in turn affect the flow field.

6.5 Properties of the rotation angle

The hydraulic gradient is a vector and its scale invariance properties involve a scaling of both its magnitude and its rotation vector. This property is better understood by discussing the transformation of the hydraulic gradient field shown in Fig. 6.12. At the large-scale r = 1 we have the mean vector in the $-x_1$ direction. When r = 2, the size of the domain has been reduced to half its original size, and one observes that vectors are about the mean direction. To obtain the hydraulic gradient at r = 1 one needs to multiply the magnitude of each vector by a random number and rotate each vector to align it in the direction of the hydraulic gradient vector at r = 1. The isotropic contraction of the support by a factor, rotating the vectors by a random quantity, and multiplying their magnitudes by a random quantity to obtain the original field is expressed mathematically as

$$\nabla H(S) \overset{d}{=} (J_r \underline{R}_r).\nabla H\left(r\underline{R}_r^T S\right) \tag{6.26}$$

where J_r is the magnitude of the hydraulic gradient ∇H, $\underline{R}_r$ is an orthogonal random matrix with first column equal to $\underline{e}_r$ that characterizes the random rotation of the first coordinate axis. For 1D flow, there is no rotation and for 2D flow the rotation matrix is completely defined by the vector $\underline{e}_r$. In Eq. (6.26) $\left(J_r \underline{R}_r\right)$ is independent of the random field $\nabla H\left(r\underline{R}_r^T S\right)$. To examine this assertion, the angle of rotation of the vectors α_r at each resolution are computed and plotted against the magnitude of the hydraulic gradient J_r and shown in Fig. 6.25.

Fig. 6.25 shows the apparent lack of correlation between the rotation angles α_r and the magnitude of the hydraulic gradient J_r. The plots of α_r versus J_r have an approximately circular shape, indicative of the lack of correlation between the two parameters.

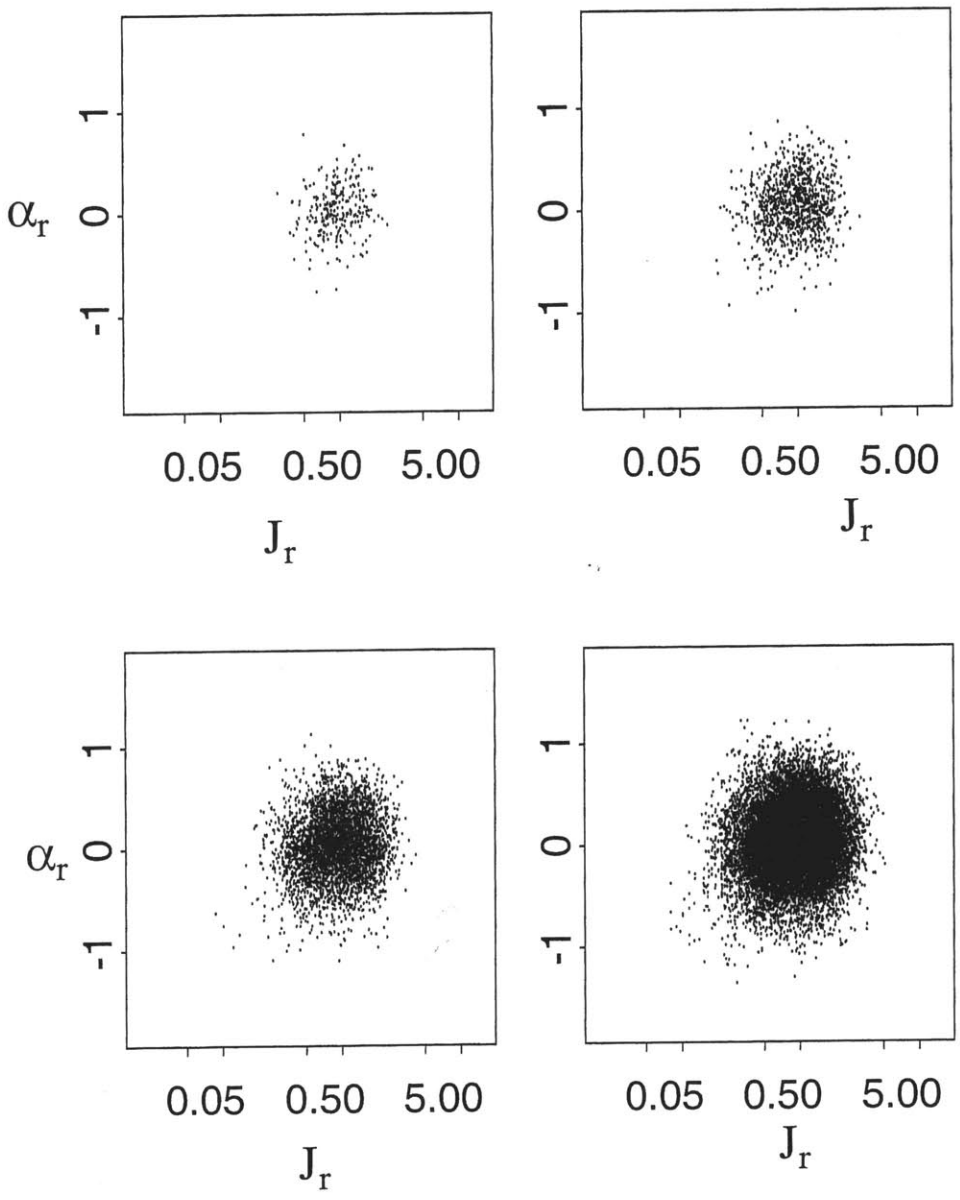

Figure 6.25 - A plot of the angle of rotation α_r versus the magnitude of the hydraulic gradient J_r for different resolutions for a field with $C_K = 0.1$

Theoretically the rotation angle α_r was characterized as a Brownian motion with independent increments as one moved from one scale or resolution to the other. To validate this assumption, the value of the rotation angle α_r beginning at the coarsest resolution r = 1 was taken and the rotation angles at the next finer resolution r = 2 was subtracted from it, to obtain the differences in the rotation angles. This differencing procedure was continued to the finest resolution of the simulation. Some of the results of the differencing are shown in Fig. 6.26. The results for the coarser resolutions are not shown because the points are so few that one cannot really determine the co relational properties by a visual inspection. However, the results for r = 16 to r = 256 is shown, and just like Fig. 6.25 shows a lack of correlation of the differences in the angles of rotation as one moves from a coarser scale to the next finer scale. Moreover, the theoretical variance of the rotation angle α_r as a function of the resolution was obtained as

$$\mathrm{Var}[\alpha_r] = \frac{2}{D(D+2)} C_K \ln(r) \tag{6.27}$$

so that for D = 2 and $C_K = 0.1$, $\mathrm{Var}[\alpha_r] = 0.025 \ln(r)$. To validate this result, the variance of the rotation angles was computed for each resolution and is shown in Fig. 6.27. The theoretical values were computed using Eq. (6.27) for r = 1, 2, 4, 8,

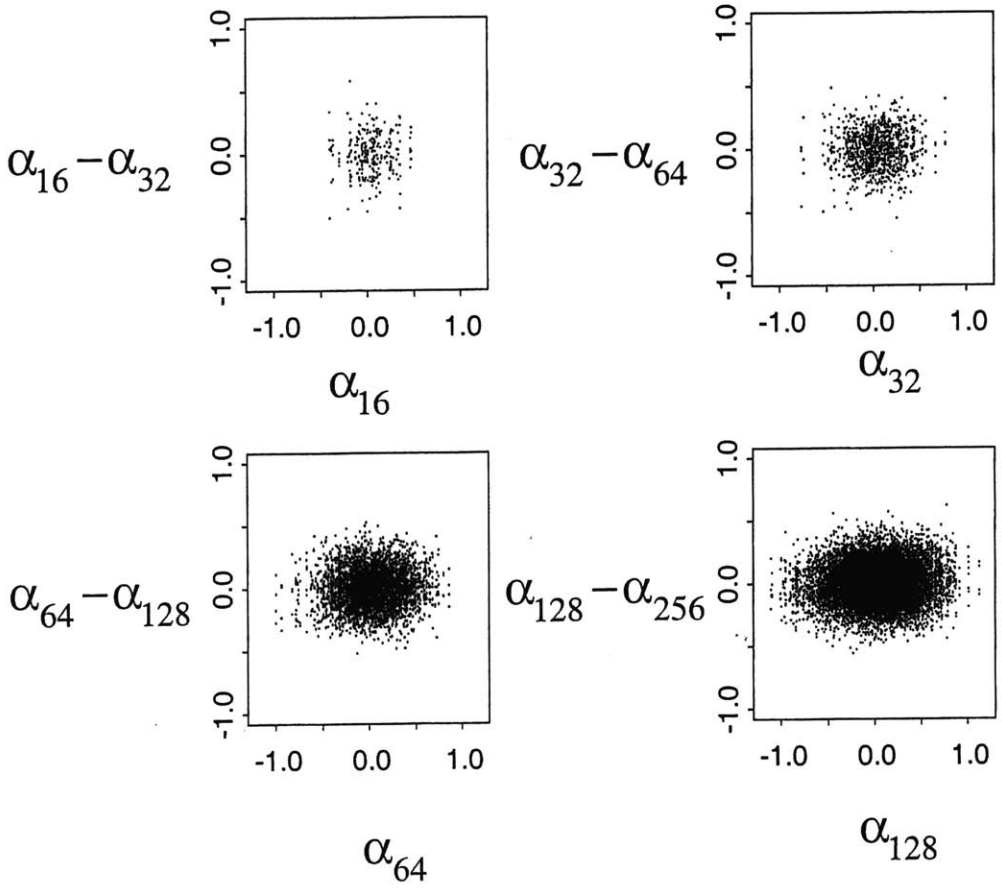

Figure 6.26 – The increments of the rotation angles as one moves from a coarser to a finer resolution versus the original rotation angles at the coarser resolution

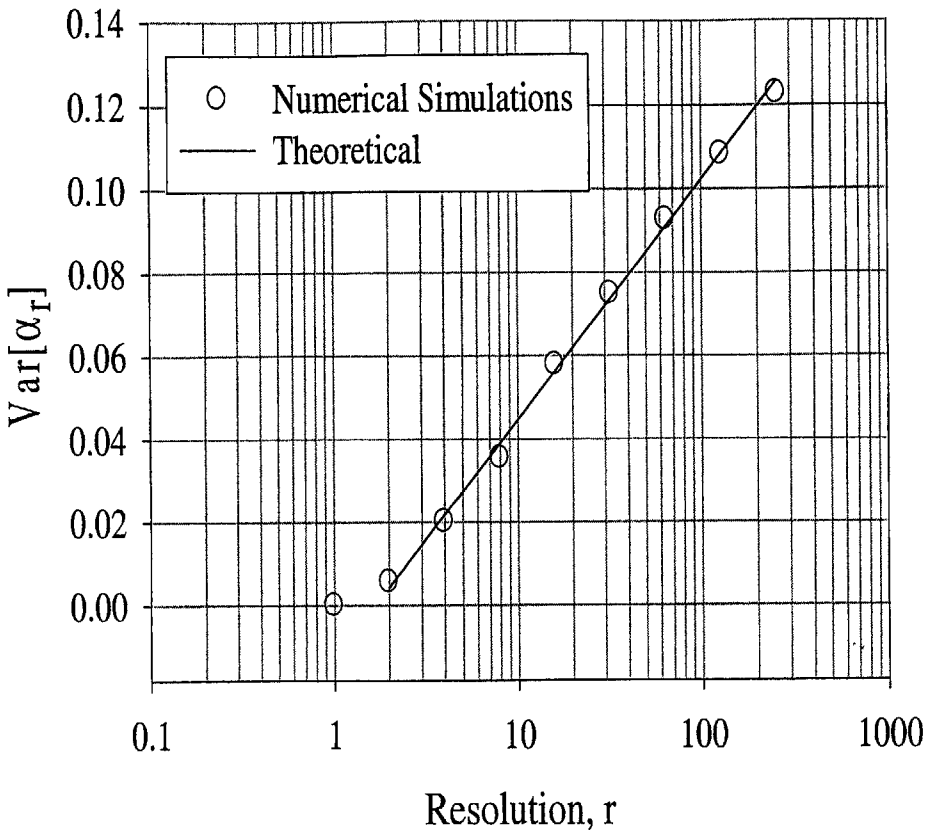

Figure 6.27 - A plot of the variance of the rotation angles of the hydraulic gradient vectors versus resolution

16, 32, 64, 128 and 256 and is shown as the straight line on Fig. 6.27. The theoretical curve was shifted in the positive x-axis by 0.013 to match the values of the $\mathrm{Var}[\alpha_r]$ from r = 2 to r = 256. The shift was made to ignore the values of the variance at the low resolutions that show a departure from the linear behavior of the higher r values. This departure from linearity of the $\mathrm{Var}[\alpha_r]$ values at low values of r is explained by the fact that a unit hydraulic gradient was imposed on the flow boundary.

Next we turn our attention to the distributional properties of the rotation angle α_r and J_r. In the theoretical derivation we found that both α_r and log J_r are normally distributed. A simple way to examine this assumption is to make a normal plot of the distributions of the two parameters. Fig. 6.28 shows the plot of the normalized values of $\ln(J_{256})$ and α_{256} on a normal probability paper. The $\ln(J_r)$ and α_r have been normalized to have mean 0 and 1 respectively for better reading and variance 1. Normality and independence $\ln(J_r)$ and α_r which are properties predicted by theory, are both confirmed.

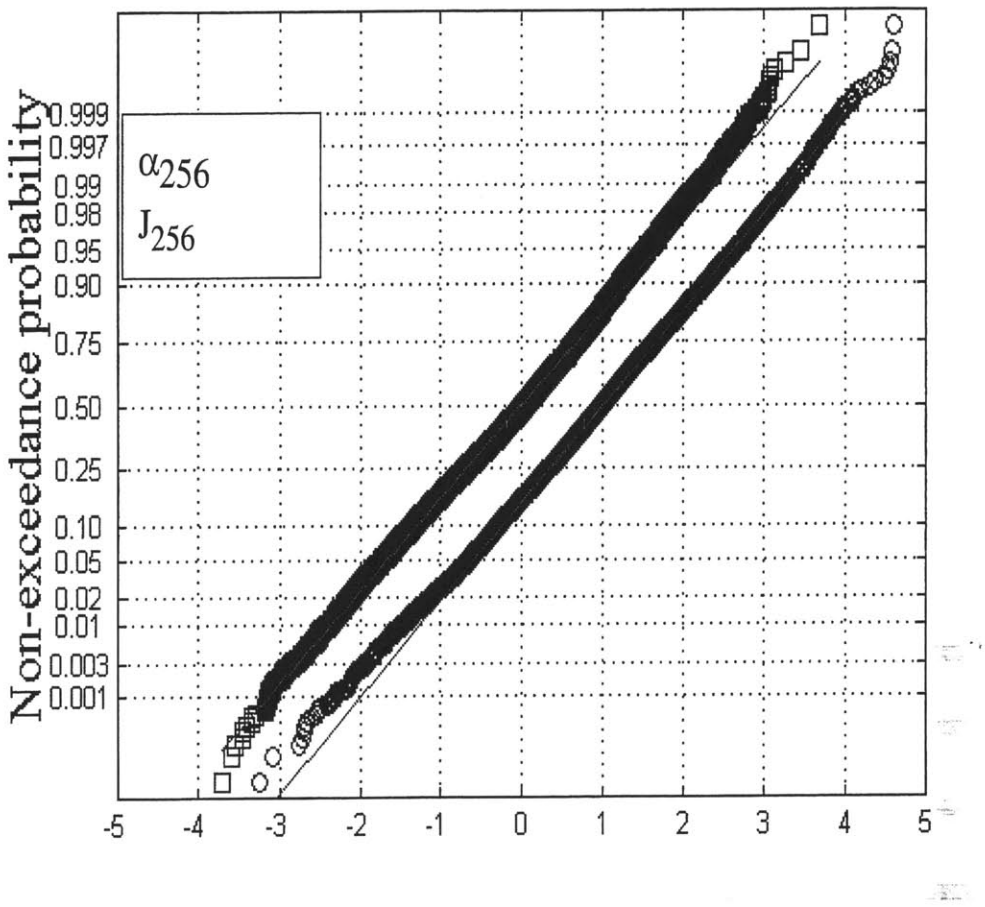

Figure 6.28 - A normal probability plot of the normalized values of $\ln(J_{256})$ and α_{256}. The values of α_{256} have a mean of 1 and variance 1 to better display the data.

6.6 Scaling of Bare Fields

The discussion so far has focused on how a hydraulic conductivity field K developed to a certain maximum resolution can be averaged or degraded to obtain K fields of coarser resolutions, and how these coarser fields and the original K field scale. For a K field developed to a certain resolution, the associated hydraulic gradient ∇H and specific discharge $\underline{q}$ fields are averaged to obtain coarser fields, and the higher moments of these fields are examined to determine the scaling properties of the K, ∇H and $\underline{q}$ fields. In the numerical cases presented, K fields were generated on a 512 x 512 grid, and the associated ∇H and $\underline{q}$ fields were computed. The scaling properties of the K field were analyzed by averaging the data on the 512 x 512 grid to obtain K fields on grid sizes of 256 x 256, 128 x 128, 64 x 64 etc. Similarly, the magnitude of the $\underline{q}$ field was averaged to obtain $|\underline{q}|$ fields on coarser grid sizes. The ∇H field was analyzed differently, by performing a linear regression on the H field on the 512 x 512 grid to obtain ∇H fields with different resolutions. This method of obtaining new fields by averaging the original field is called "partial dressing" in the multifractal literature. In this section, instead of averaging the 512 x 512 K field to obtain fields of different resolutions, the analysis is carried out on K fields originally developed to resolutions of 512, 256, 128 and 64. Thus five different K fields are generated, and for each field the ∇H and $\underline{q}$ are computed. Next, the scaling properties of the K, ∇H and $\underline{q}$ fields are examined. This type of analysis is known in the multifractal literature as "bare analysis."

In theory, the so-called bare analysis consists of examining the scaling properties of a field at different resolutions r. An approximate way to generate "bare fields" is to first generate the Gaussian white noise W_n over a large field, say 700 x 700 grid. We extract the inner r x r matrix and create a multifractal K field with resolution r. Steps used in creating the multifractal K field discussed in Sec. 6.1 are used in creating the multifractal field over the r x r grid.

Permeability K fields with resolutions of 512, 256, 128 and 64 and $C_K = 0.1$ were created using the above procedure. Subscripting the K fields with their resolutions, so that for example K_{512} denotes the field at resolution 512, the moments of the K fields were obtained as follows:

$$\langle K^s \rangle = \left\{ \langle K_{64}^s \rangle, \langle K_{128}^s \rangle, \langle K_{256}^s \rangle, \langle K_{512}^s \rangle \right\}$$

where s is between 0 and 4. For s = 1, 2, 3, and 4, the moments of the K fields are shown in Fig. 6.29. The slopes of the lines is obtained by performing a linear regression of $\log\left(E\left[K^s\right]\right)$ versus $\log(\text{resolution})$ and compared to the theoretical slope, which is $C_K\left(s^2 - s\right)$ in Fig. 6.30. The slopes obtained by linear regression closely match the theoretical results.

Using the bare K fields $\{K_{64}, K_{128}, K_{256}, K_{512}\}$ as inputs into the finite difference program, the associated head $\{H_{64}, H_{128}, H_{256}, H_{512}\}$ and specific discharge $\{q_{64}, q_{128}, q_{256}, q_{512}\}$ fields were computed. The hydraulic gradient field was computed following the procedures discussed in Sec. 6.3.

The moments of the magnitude of the hydraulic gradient for $\{K_{64}, K_{128}, K_{256}, K_{512}\}$ are computed as

$$\langle J^S \rangle = \left\{ \langle J^s_{32} \rangle, \langle J^s_{64} \rangle, \langle J^s_{128} \rangle, \langle J^s_{256} \rangle \right\}$$

where s has a value between 0 and 4. For s = 1, 2, 3 and 4 the computed moments of the magnitude of the hydraulic gradient for the bare fields is reported in Fig. 6.31. The slopes of the moments of $E[J^s]$ are obtained by performing a linear regression of $\log(E[J^s])$ versus $\log(\text{resolution})$ where resolution is $\{32, 64, 128, 256\}$. The slopes

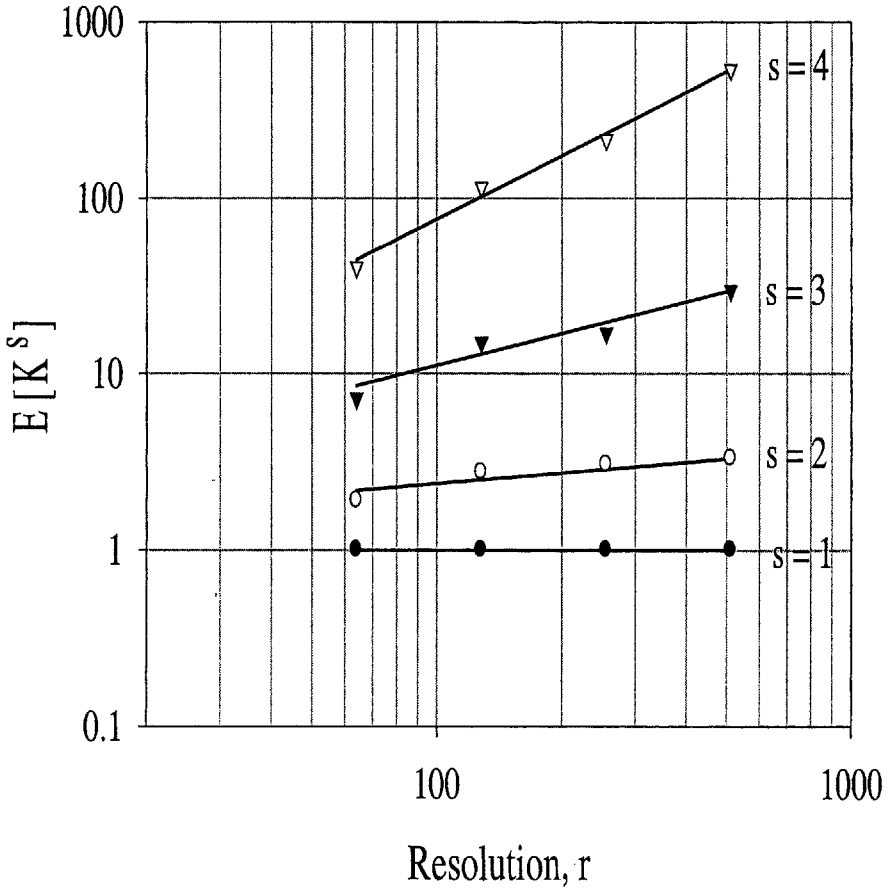

Figure 6.29- The scaling of K fields developed to resolutions of 64, 128, 256 and 512.

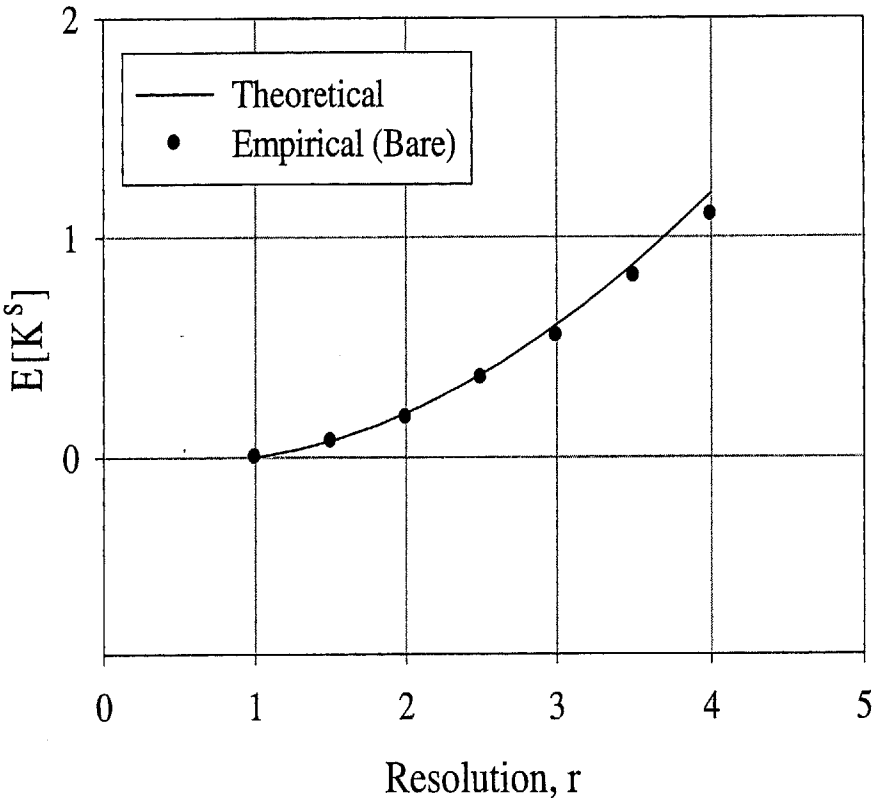

Figure 6.30 – Comparison the scaling of bare multifractal K fields and theoretical scaling of multifractal K fields with $C_K = 0.1$.

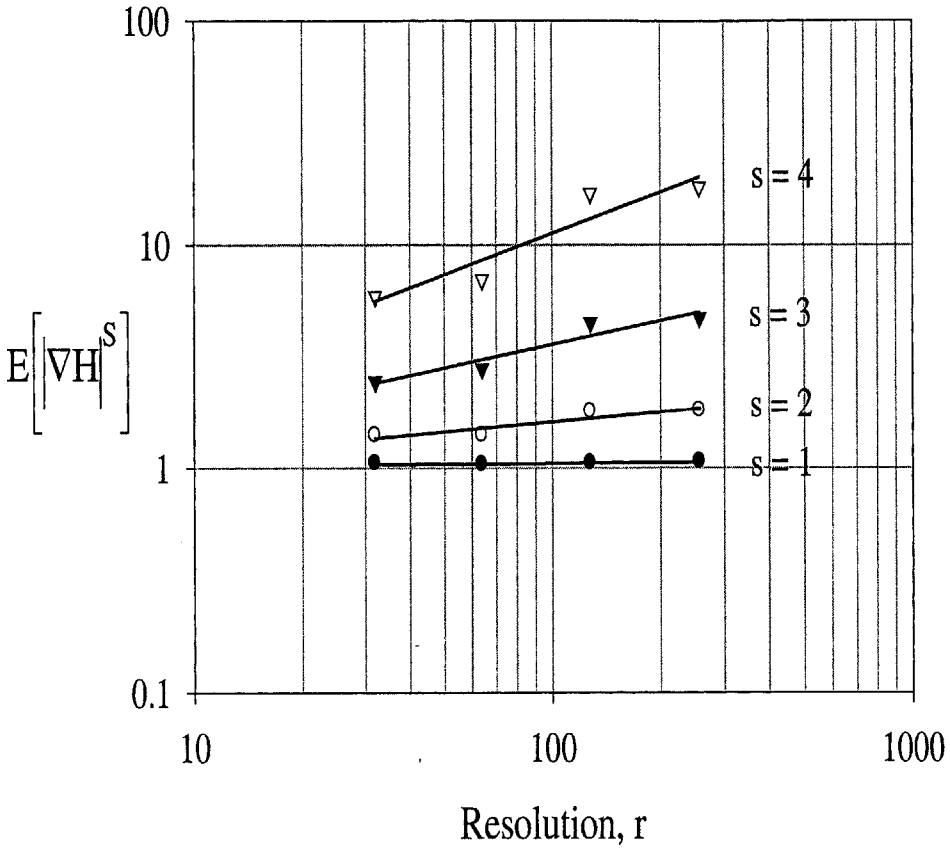

Figure 6.31 – The scaling of hydraulic gradient fields with resolutions 32, 64, 128 and 256 from K fields with $C_K = 0.1$.

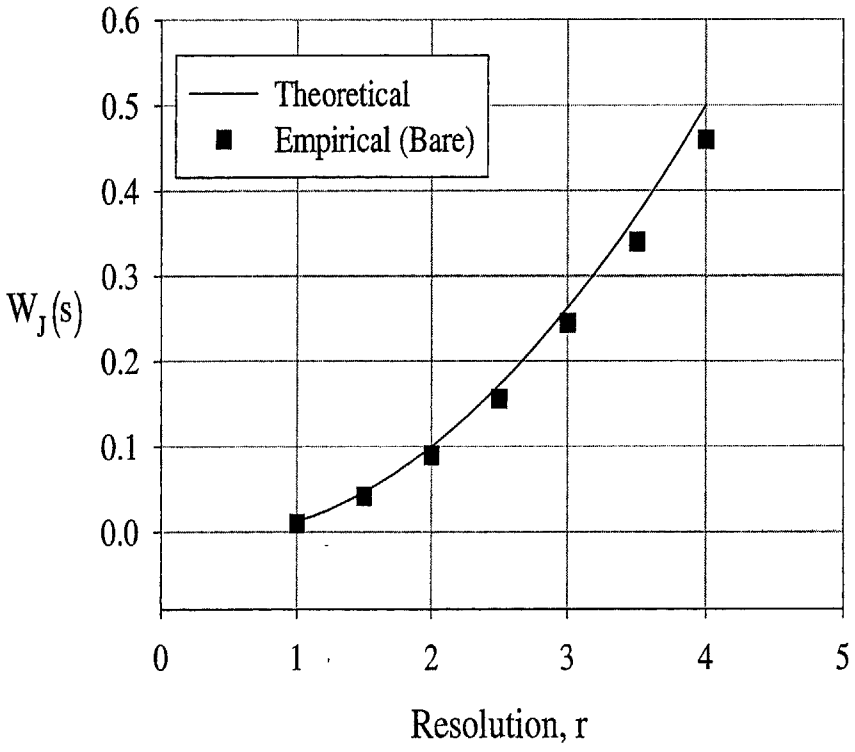

Figure 6.32 – Comparison of the scaling moments of the magnitude of the hydraulic gradient fields of K fields with $C_K = 0.1$ developed to resolutions of 64, 128, 256 and 512 with the theoretical moment scaling function $W_J(s) = C_K\left(0.125s + 0.375\left(s^2 - s\right)\right)$

obtained from the linear regression are juxtaposed on the theoretical slopes. The theoretical slopes for the magnitude of the hydraulic gradient is $W_J(s) = C_K\left(0.125s + 0.375\left(s^2 - s\right)\right)$. Just like the hydraulic conductivity field K, the slopes of the moments of the magnitude of hydraulic gradient field J closely matches the theoretical curves as can be seen in Fig. 6.32. Moreover, the slopes of the bare fields and the partially dressed fields for J are essentially the same because the hydraulic gradient field is conservative.

The moments of the specific discharge field are computed in a fashion similar to that of the hydraulic conductivity field K. The moments of the magnitude of the specific discharge field are computed as

$$\left\langle q^s \right\rangle = \left\{ \left\langle q^s_{64} \right\rangle, \left\langle q^s_{128} \right\rangle, \left\langle q^s_{256} \right\rangle, \left\langle q^s_{512} \right\rangle \right\}$$

For s = 1, 2, 3 and 4 the computed moments of $\left\langle q^s \right\rangle$ versus resolution is plotted in Fig.6.35. One observes that the expected value of specific discharge decreases as the resolution to which the field is developed increases. This is because the specific discharge field is non-conservative and its expected value vanishes as the resolution of the field tends to infinity. The slopes of the lines in Fig. 6.33 are obtained by performing a linear regression of $\log\left\{\left\langle q^s \right\rangle\right\}$ versus $\log\{\text{resolution}\}$. The slopes of the lines in Fig.

6.33 are compared with the theoretical slopes of $W_{q,b} = C_K\left[-0.875s + 0.375\left(s^2 - s\right)\right]$ for $C_K = 0.1$ in Fig. 6.34. The results of the numerical simulation confirm the theoretically obtained results.

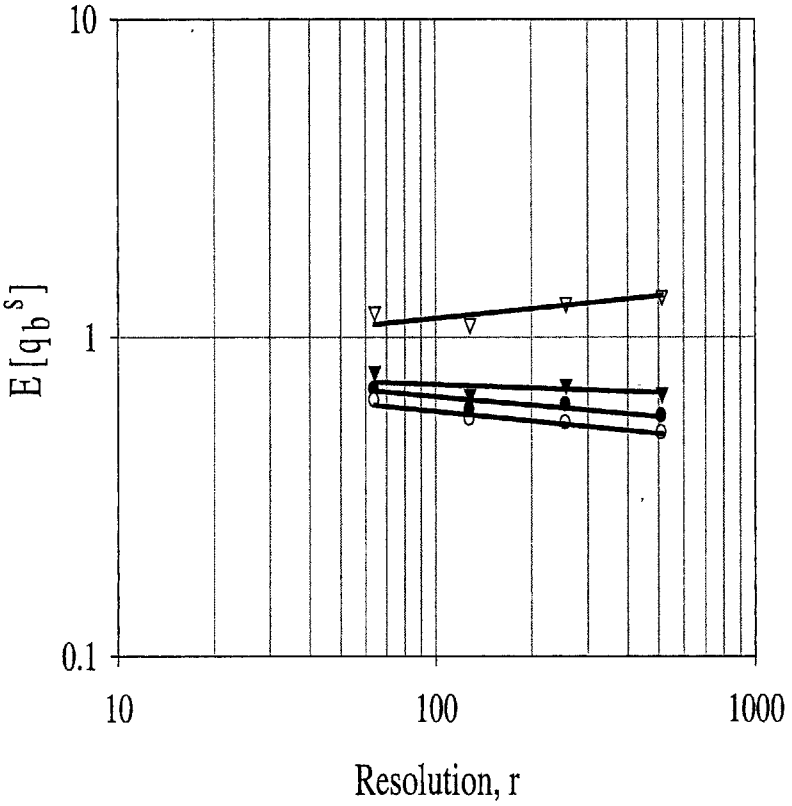

Figure 6.33 – The scaling of velocity fields obtained from K fields developed to resolutions of 64, 128, 256 and 512.

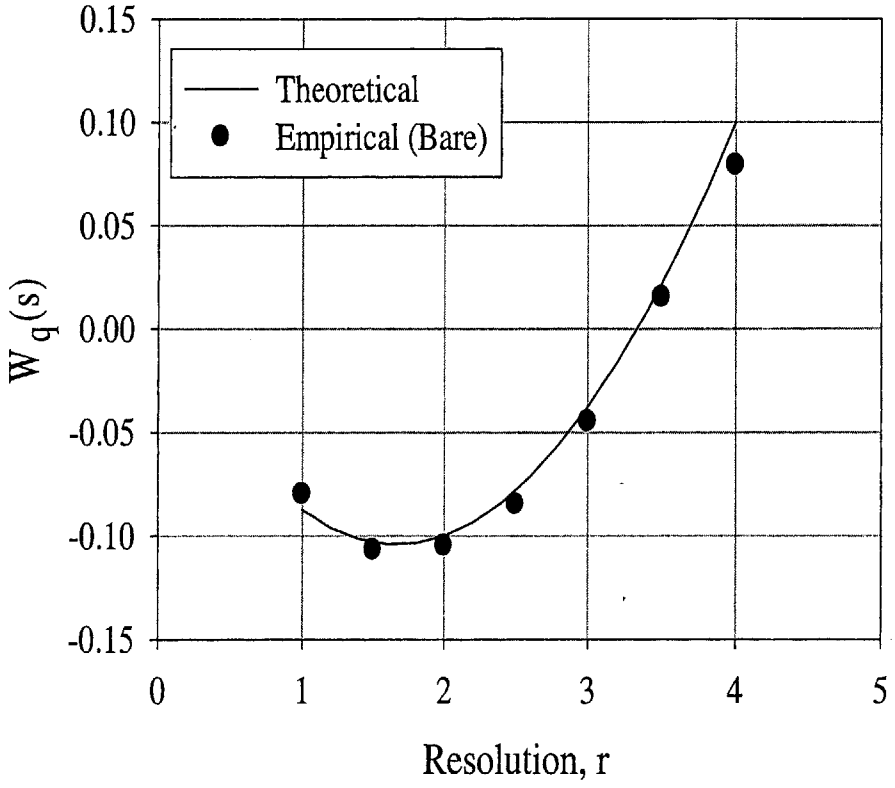

Figure 6.34 – Comparison of the slopes of lines in Fig. 6.33 with the theoretical scaling function $W_{q,b}(s) = C_K\left(-0.875s + 0.375\left(s^2 - s\right)\right)$.

6.7 The relation between the log conductivity F and the hydraulic gradient

In the previous section, the flow field was found to be non-conservative. What this means is that on the average, velocity fields developed on coarser grid, say a 256 x 256 grid will have a higher mean value than velocity fields developed on a finer grid, say a 512 x 512 grid if both fields are developed with the same C_K value. This vanishing behavior of specific discharge as the resolution increases results from the negative correlation coefficient ρ between the log conductivity $F_r = \ln K_r$ and the log hydraulic gradient amplitude $\ln(J_r)$ at any given location $\underline{x}$. The correlation coefficient ρ obtained from the theoretical derivation is independent of the resolution r and variance of the K field but varies with the space dimension D as $\rho = -\sqrt{\frac{D+2}{3D}}$. The log-conductivity versus the log hydraulic gradient amplitude for the K field with $C_K = 0.1$ are shown in Fig. 6.35. Section 6.1 discussed how to obtain the K fields at different resolutions and how one can obtain the amplitude of the hydraulic gradient field was presented in Section 6.3. Using the procedures in these sections, the values of the K and ∇H fields at different resolutions were computed and displayed in Fig. 6.35. The correlation coefficients are summarized in Table 6.3 and for D = 2 confirm the theoretical value of $\rho = -0.817$.

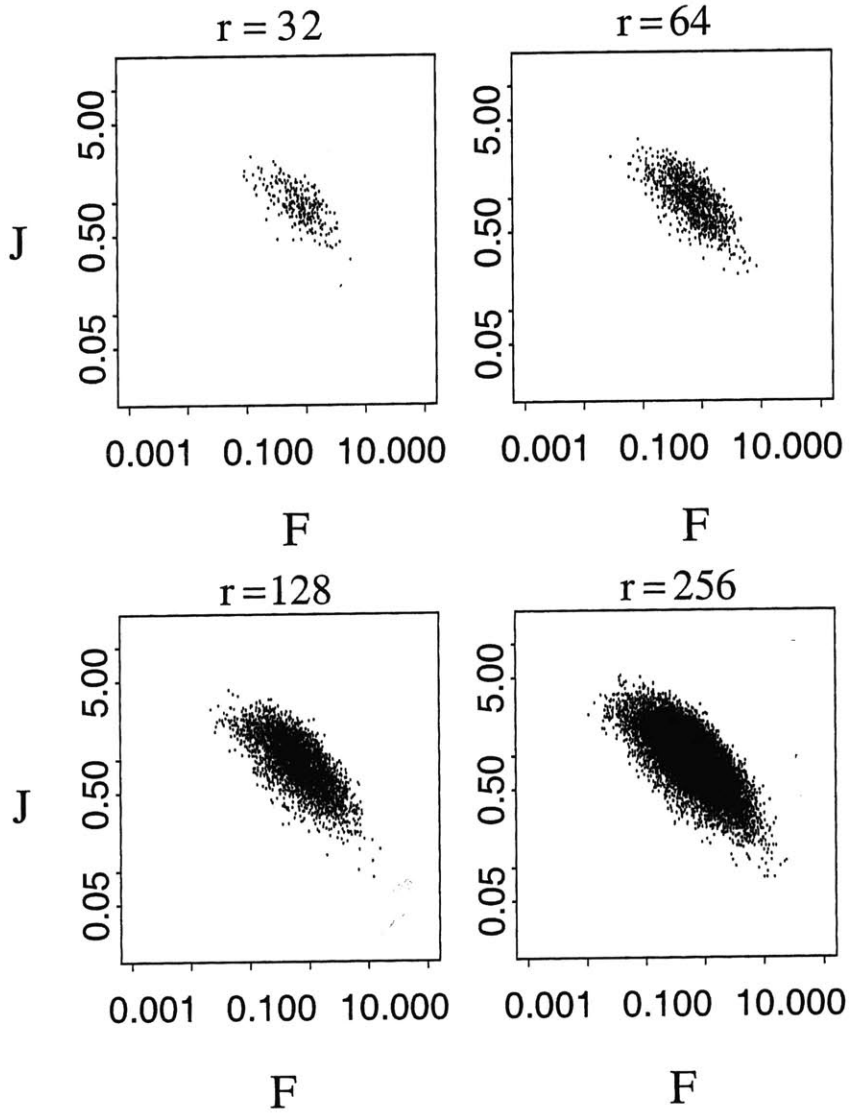

Figure 6.35 - A scatter plot of the log hydraulic conductivity F versus the log hydraulic gradient amplitude J.

Table 6.3 – Correlation coefficients between F_r and $\ln(J_r)$ for different resolutions r. The theoretical value for D = 2 is $\rho = -0.817$.

Resolution, r	Bare correlation coefficient ρ
32	-0.809
64	-0.813
128	-0.813
256	-0.815

Effective Hydraulic Conductivity

In the theoretical derivations of flow, it was found that the average flow depends on the resolution r to which the K field has been developed, the variability of the K field (C_K) and the space dimension D through the relation

$$E\left[\underline{q}_r(\underline{x})\right] = r^{-\frac{2}{D}C_K}[1,0,...,0] \tag{6.28}$$

The amplitude $r^{-\frac{2}{D}C_K}$ of $E\left[\underline{q}_r(\underline{x})\right]$ may be interpreted as the effective conductivity K_{eff} of the medium. To validate this result we take the K field on a grid size of 512 x 512, and degrade the K field through averaging to obtain K fields of sizes 256 x 256, 128x128 ....1x1. We denote these fields as $\{K_{512}, K_{256}, K_{128}, ..., K_1\}$. These K fields serve as inputs into the flow program. For each K field, the specific discharge field $\underline{q}_r$ and the mean hydraulic gradient $J = -|\nabla H|$ is computed. Next, we compute the projection of the flow field in the x_1 direction. In fact, one can simply take the x_1 component of the flow field. Then for each $\underline{q}_r$ we compute $q_m = E\left[q_{x_1}/J\right]$. Therefore, q_m is the flow in the direction of the mean hydraulic gradient for $J = \overline{K} = 1$. Using K fields with $C_K = 0.1$ and 0.3 and the procedure just described, the effective conductivity was computed for resolutions r = 1, 2, 4...512.

The results of the computations are presented in Fig. 6.36. The theoretical slopes in Fig. 6.36 are obtained by performing a linear regression of $\log\{K_{eff}\}$ versus

$\log\{\text{resolution}\}$ for the computed data. For the $C_K = 0.1$ and 0.3 fields the slopes of the lines are approximately –0.1 and –0.3 respectively. Results from the simulation validate the theoretical results.

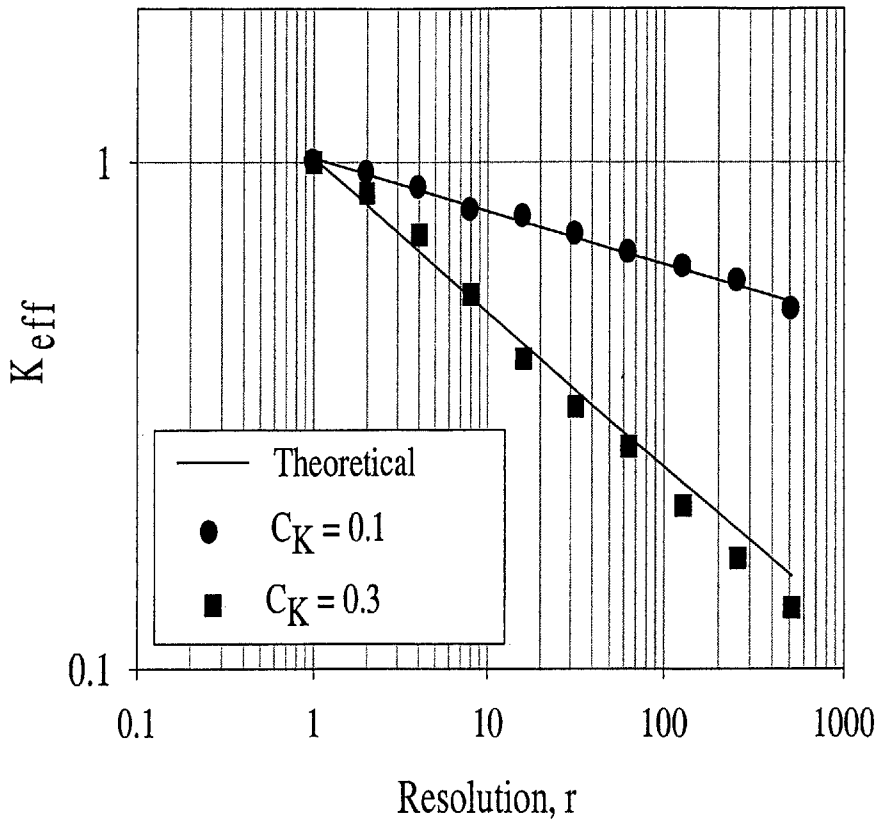

Figure 6.36 - The effective conductivity for K fields with $C_K = 0.1$ and 0.3

6.8 Flow simulation for a K field with a high variability $(C_K = 0.8)$

The simulations performed so far have validated the theoretical results. It is worth recalling that the theoretical results were obtained by considering the zero divergence flow equations for a cascade of "bare" K fields. The theoretical results were obtained by considering the behavior of the zero divergence Darcy equation as one moves from the deterministic solution at the large scale where $\{E[K]=1, \nabla F=0, J=-|\nabla H|=[1,0,0]$ and $\underline{q}=[1,0,0]\}$ to finer resolutions where higher frequency components are gradually added to the $F=\ln K$ field. When the scale of the problem is incremented by an infinitesimal amount so that the head field H is incremented by an amount h, then the hydraulic gradient at the finer scale can be written as $\nabla H = \begin{bmatrix} J_1 \\ 0 \\ 0 \end{bmatrix} + \nabla h$, where J_1 is the mean hydraulic gradient in the x_1 direction so that the flow equation at the finer scale can be written as

$$\nabla^2 h + \nabla F.\nabla h = -J_1 \frac{\partial F}{\partial x_1} \tag{6.29}$$

One of the assumptions made in the theoretical derivations in Chapter was that the contribution of the term $\{\nabla F.\nabla h\}$ is small relative to that of $\nabla^2 h$. To evaluate whether this ignored term has an influence on the scaling properties of the hydraulic gradient ∇H

and the specific discharge fields $\underline{q}$, we perform a numerical simulation on a square 512 x 512 grid and examine the scaling behavior of $|\nabla H|$ and $|\underline{q}|$ when the K field has a high variance. Specifically, an isotropic lognormal K field with a $C_K = 0.8$ for which the F = lnK field has a variance of 2*0.8*log(512) $\simeq 10$, which may be considered a significant variability for an F field, was simulated using the steps discussed in section 6.1. The scaling of the K field is presented in Fig. 6.37. A comparison of the slopes of the lines in Fig. 6.37 with the theoretical moment scaling function for the K field $W_K(s) = C_K(s^2 - s)$ for $C_K = 0.8$ are shown in Fig. 6.38. It is worth noting that one can only determine the s^{th} moment up to a value for which $W_K(s) \leq D(s-1)$, from which we obtain for D =2, $s \leq 2.5$ as the maximum moment for which one can consider the scaling of the field. Figs. 6.37 and 6.38 show that the K field scale as expected.

Figure 6.39 –

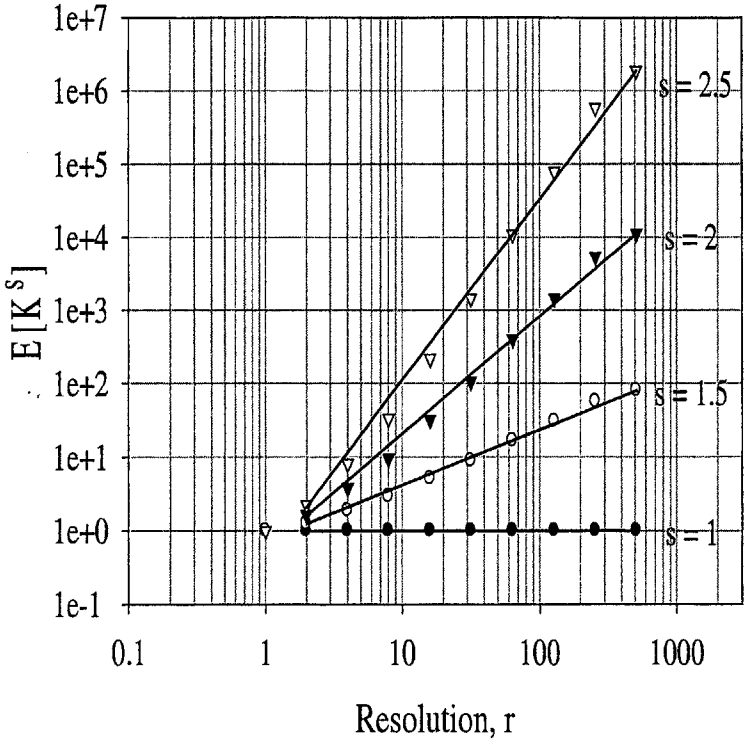

Figure 6.37 – The scaling of a K field with $C_K = 0.8$

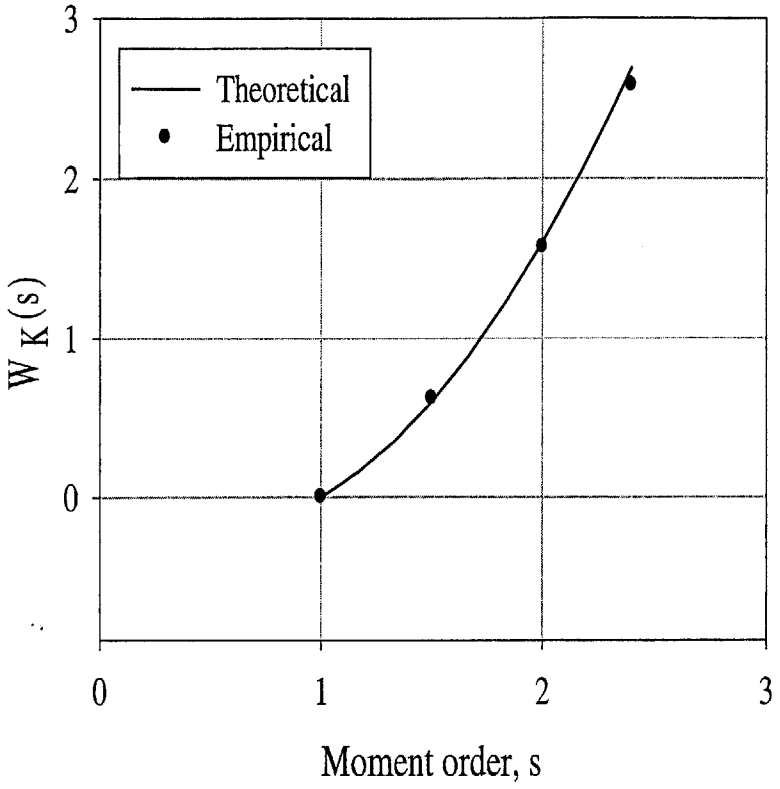

Figure 6.38 – A comparison of the moment scaling of a K field with $C_K = 0.8$ with the theoretical moment scaling function of $C_K(s^2 - s)$.

Using the K field with $C_K = 0.8$, the head field was computed and its contour displayed in Fig. 6.39. To examine the hydraulic gradient field, the procedures in Section 6.3.2 are used to analyze the scaling properties of the hydraulic gradient field. The hydraulic gradient field is graphically presented in Fig. 6.40. The scaling of the hydraulic gradient field is presented in Fig. 6.41. A comparison of the empirically obtained scaling moments is compared with the theoretical scaling moments in Fig. 6.42.

Finally, the specific discharge field was computed and its scaling moments computed and compared with the theoretical moment scaling function. Moments of the flow magnitudes are computed and presented in Fig. 6.43. In Fig. 6.43, one observes a linear behavior of the log the expected moments of the specific discharge magnitudes and the log of the resolution. The slopes of the lines in Fig. 6.43 are compared with the theoretical moments in Fig. 6.44 and we find a close agreement between the empirical and theoretical values. What these results demonstrate is that for at least fields with F = lnK variances up to a value of 10, the assumptions made in the derivation of the theoretical results seem valid. In fact attempts to perform flow simulations for K fields with $C_K \geq 1$ were made. Unfortunately, the solution of the head field did not converge, and hence the properties of these fields cannot be presented. The lack of convergence for these extremely high values of C_K may be due to the sparse nature of the K field for which the numerical method cannot obtain a suitable solution. Moreover, for an extremely high C_K value, the finite difference method may be limited in its applicability since the gradients of the K and the F = lnK fields become substantial. The interesting

conclusion one can draw from these simulations is that for K fields with variability up to $C_K = 0.8$, the assumptions made in the theoretical derivations seem valid.

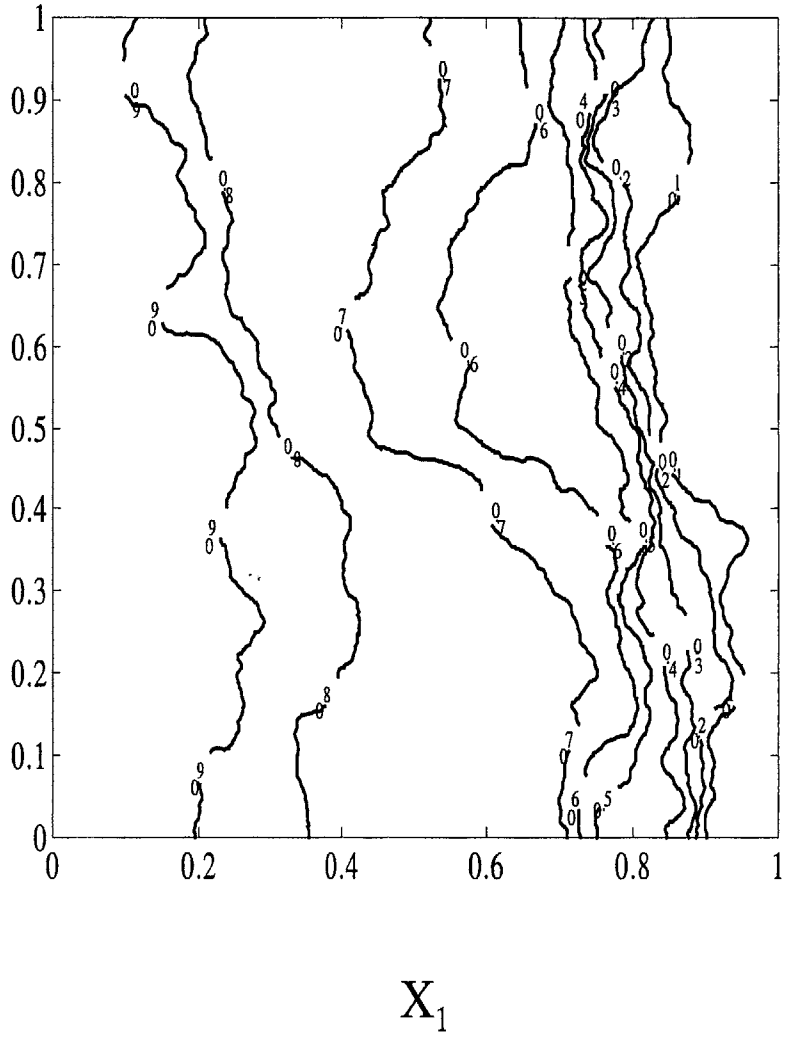

Figure 6.39 - A contour plot for the head field computed from a K field with $C_K = 0.8$

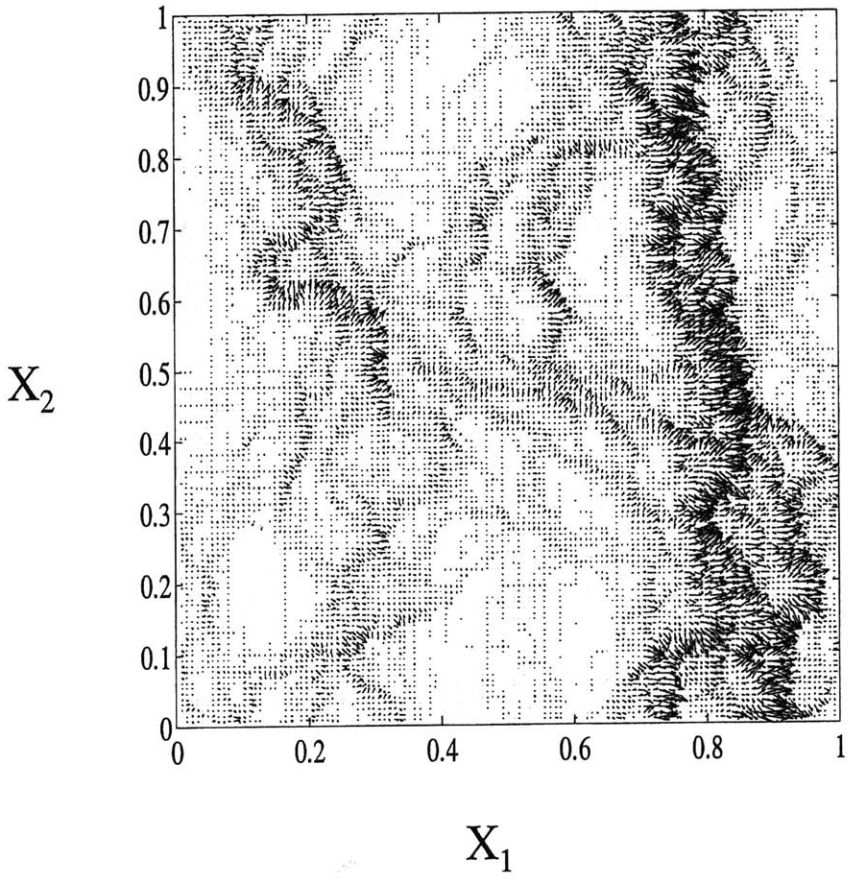

Figure 6.40 - The hydraulic gradient field computed for a K field with $C_K = 0.8$

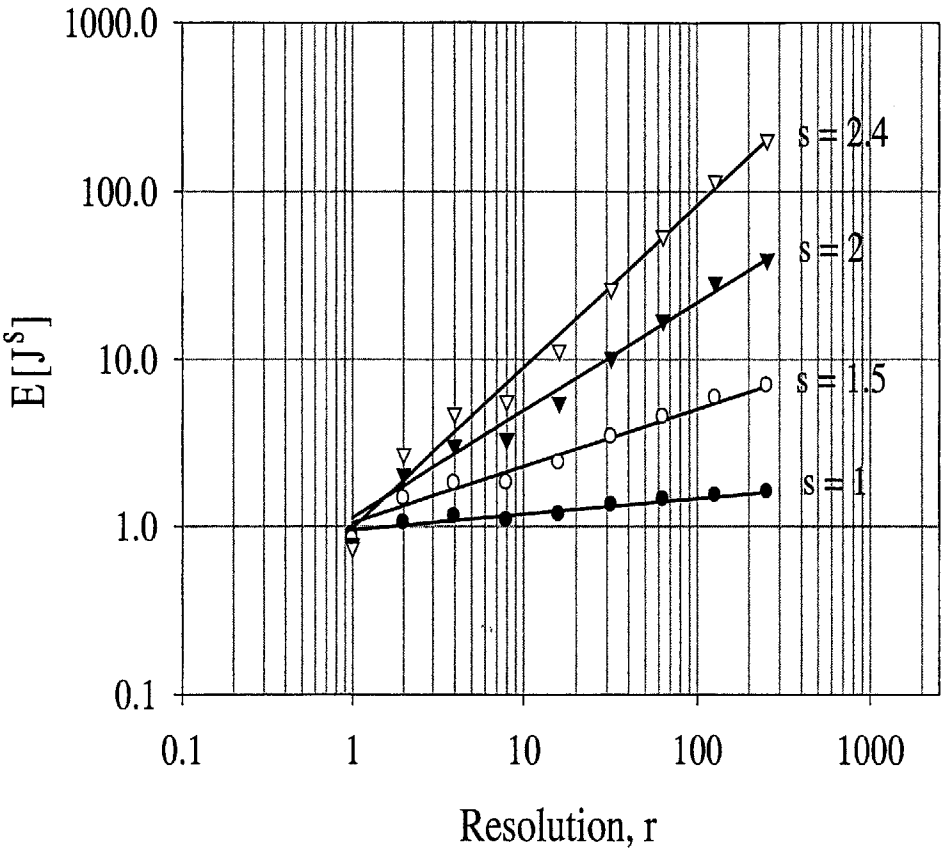

Figure 6.41 – The scaling of the hydraulic gradient amplitude for K fields with C_K=0.8.

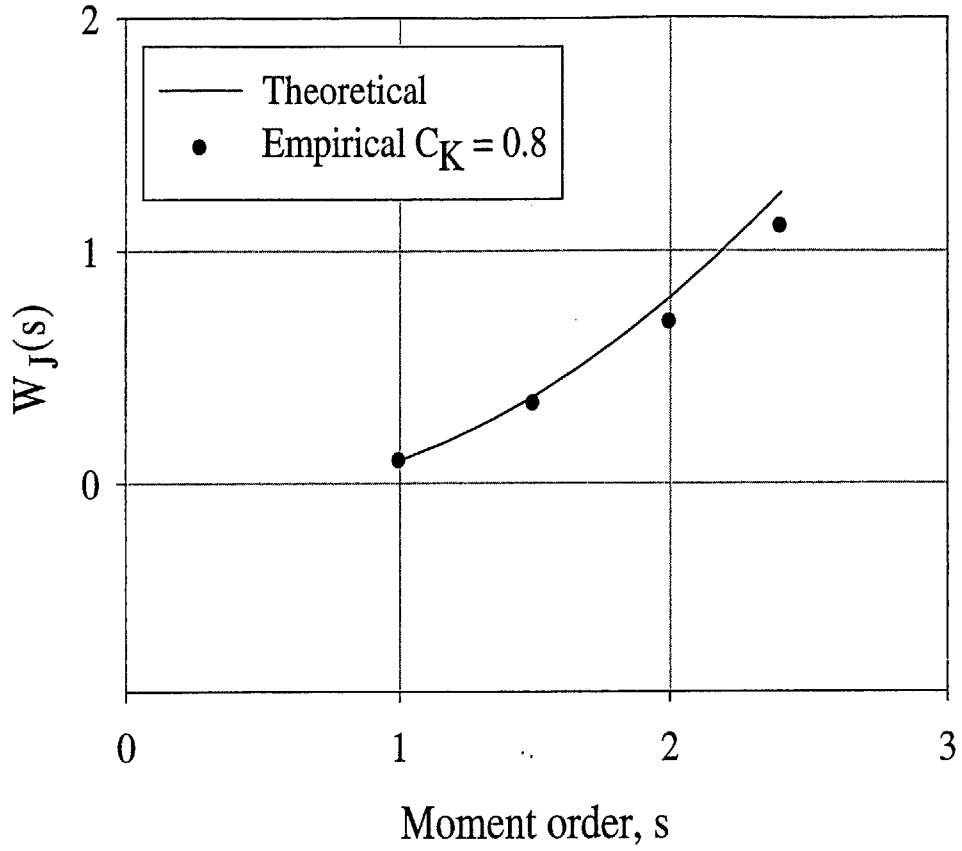

Figure 6.42 - A comparison of the moment scaling of the hydraulic gradient amplitude and the theoretical moment scaling function for a K field with $C_K = 0.8$.

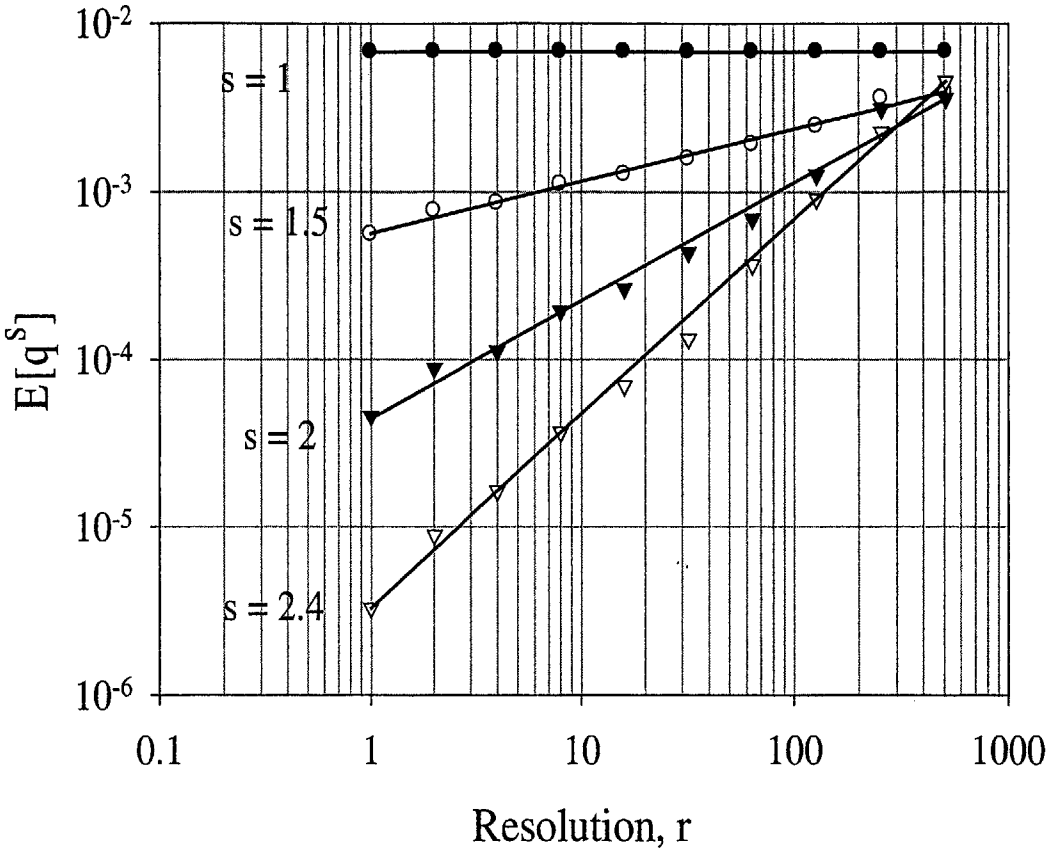

Figure 6.43 – The scaling of the hydraulic gradient amplitudes for a K field with $C_K = 0.8$

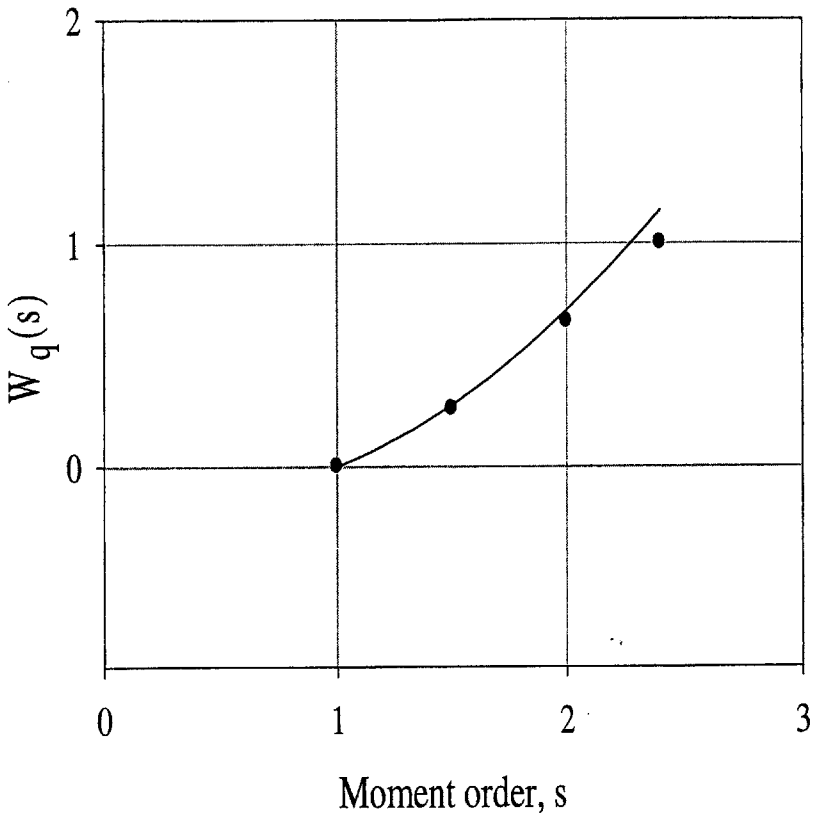

Figure 6.44 – A comparison of the moment scaling of the specific flow amplitude and the theoretical moment scaling function for a K field with $C_K = 0.8$

To illustrate the type of variability one would expect in simulating flow fields with a high variability as in the case of $C_K = 0.8$, several simulations were performed and the results are reported in Figure 6.45. The scaling of the specific flow is presented in Figure 6.45a and their average values are shown in Figure 6.45b. A comparison of the numerically obtained slopes of the specific flow and the theoretically predicted values are shown in Figure 6.45c. For this high variability field, we observe a good agreement between the numerical and theoretical results.

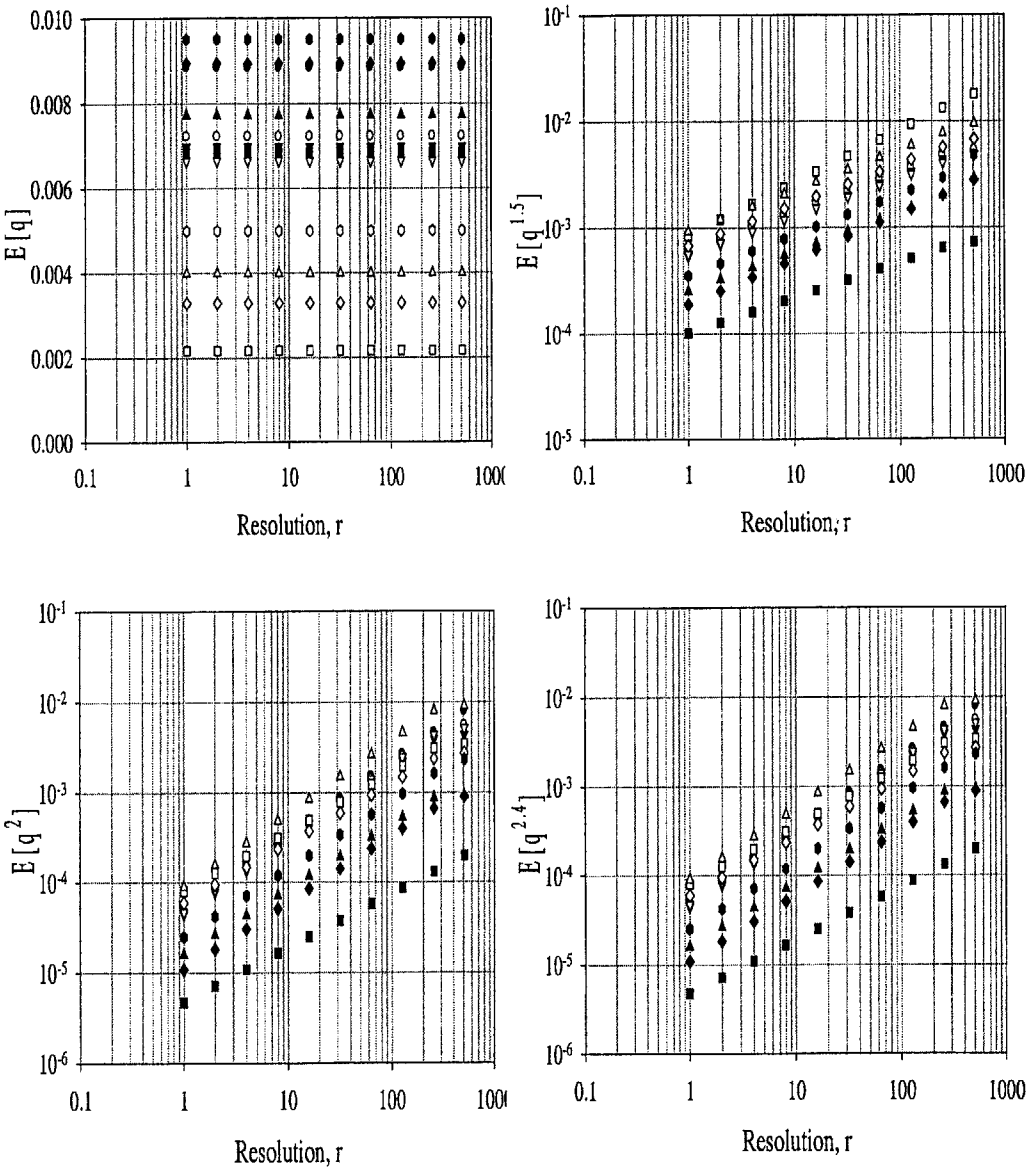

Figure 6.45a – The scaling of the specific flow amplitudes for fields with $C_K = 0.8$

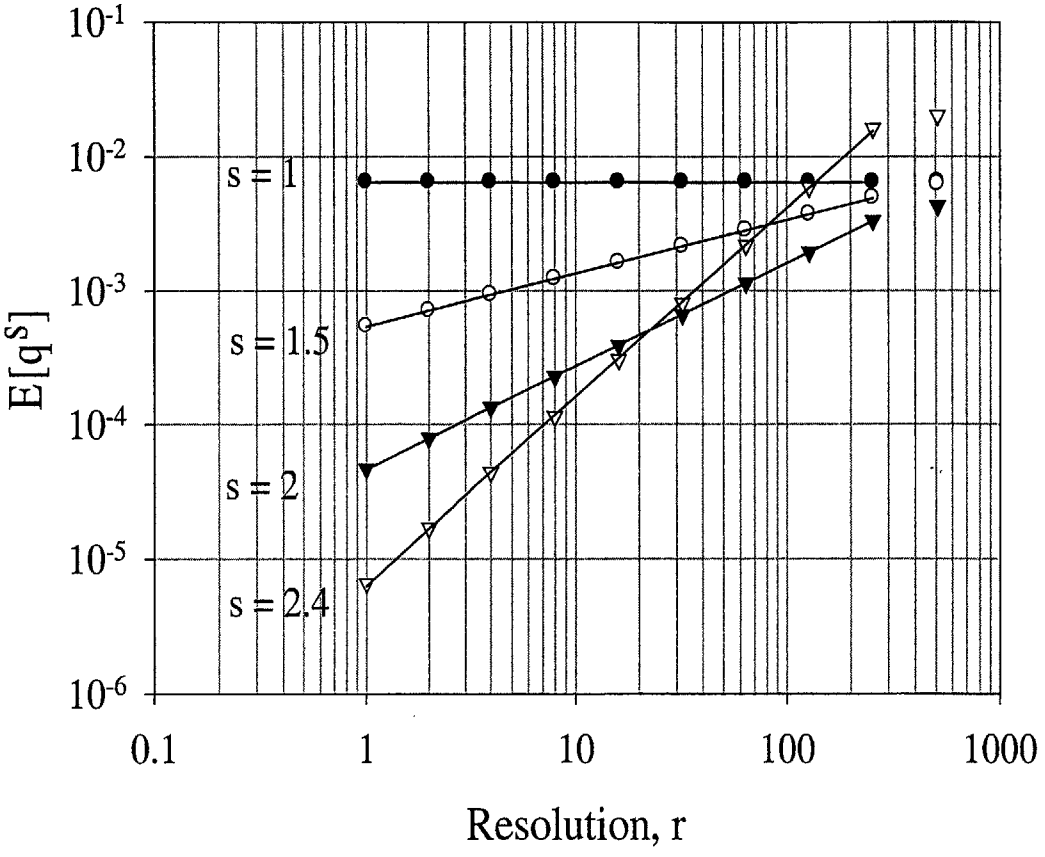

Figure 6.45b – The scaling of the average of the specific flow amplitudes for fields with $C_K = 0.8$ shown in Fig. 6.45a.

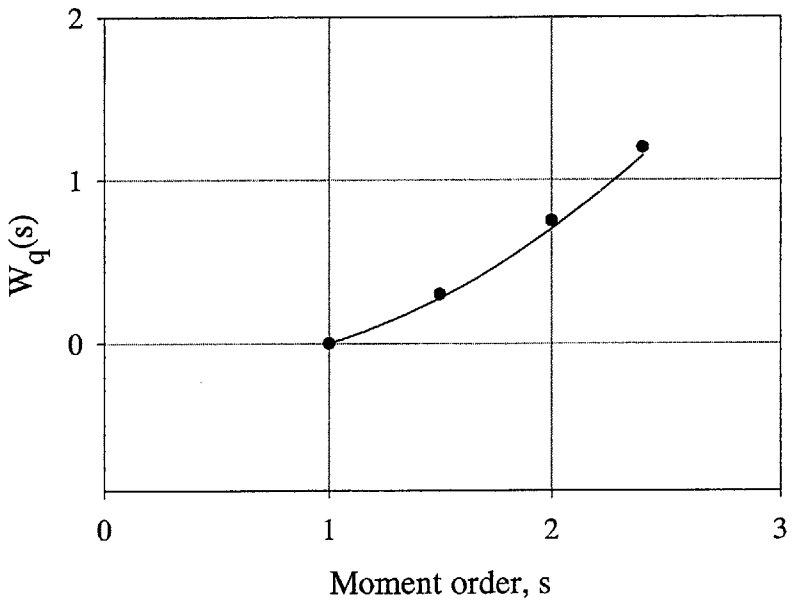

Figure 6.45c – Comparison between the theoretical and empirical scaling moments for the average specific flow amplitude for $C_K = 0.8$

CHAPTER 7 – SOLUTE TRANSPORT IN RANDOM POROUS MEDIA

Introduction

Understanding how solutes are transported in random porous media has occupied a central role in hydrology over the past three decades. One of the primary aims of solute transport research is to predict the extent of dilution or mixing of a solute as it moves with the flow. The mixing mechanisms of dispersion differ from one scale to another. At the molecular scale, thermodynamic diffusion causes mixing. At the microscopic scale, mixing is caused by velocity variations due to changes in the pore geometry (pore size and shape, the tortuosity of the flow paths, dead ends and the connectivity of the flow paths). At the macroscopic level, the mixing is to a large extent caused by velocity variations that are in turn governed by variations of hydraulic conductivity [Bear, 1972; Rajaram and Gelhar, 1993]. In general, the solute transport theories quantify the dilution of a solute in terms of their spatial moments and macrodispersivity that describes the growth rate of the second spatial moment with respect to distance. The moments and macrodispersivity definitions are presented below:

Denoting the concentration field in a single realization as $C(\underline{x},t)$ and the porosity as n, the spatial moments of the concentration field in a single realization are determined as follows [Gelhar, 1993; Rajaram and Gelhar, 1993, 1995]:

The total mass of the solute m

$$m = \int_{-\infty}^{+\infty} nC(\underline{x},t)d\underline{x} \tag{7.1}$$

Center of mass position for a single realization $\bar{x}$

$$\bar{x}_i(t) = \frac{n}{m}\int_{-\infty}^{+\infty} x_i C(\underline{x},t)d\underline{x} \qquad i = 1, 2, 3 \tag{7.2}$$

Second moment tensor for a single realization S_{ij}

$$S_{ij}(t) = \frac{n}{m}\int_{-\infty}^{+\infty} \left(x_i - \bar{x}_i(t)\right)\left(x_j - \bar{x}_j(t)\right)C(\underline{x},t)d\underline{x} \quad i, j = 1, 2, 3 \tag{7.3}$$

For inert solutes, the concentration field in any realization of steady flow at the macroscopic scale in a heterogeneous porous medium satisfies the advection – dispersion equation (ADE)

$$n\frac{\partial C}{\partial t} + q_i(\underline{x})\frac{\partial C}{\partial x_i} - \frac{\partial}{\partial x_i}\left(E_{ij}\frac{\partial C}{\partial x_j}\right) = 0 \qquad i, j = 1, 2, 3 \tag{7.4}$$

where $q_i(\underline{x})$ is the Darcy flow in the x_i direction

E_{ij} is the local bulk dispersion coefficient, equal to nD_{ij} and D_{ij} is the dispersion coefficient that includes both molecular diffusion and hydrodynamic dispersion.

Eq. (7.4) is derived from the principle of the conservation of mass (see for example Bear, 1972 pages 617 – 627). The solution of Eq. (7.4) is obtained through Laplace transform methods (see for example Sahimi, 1995) and is used in determining the dispersion coefficient of geologic samples in the laboratory or from pumping tests. These tests are based on the assumption that solute transport can be modeled with a single value of D. This is called the Fickian assumption. Additionally, plumes modeled with this approach are assumed to have smooth Gaussian shapes.

In the stochastic analysis of solute transport in random hydraulic conductivity fields K, a quantity of interest is the ensemble mean concentration field. Several researchers have obtained differential equations for the ensemble mean concentration for transport in random K fields (see for example Gelhar, 1993; Dagan, 1984; Koch and Brady, 1988). For uniform mean flow in the x_1 direction, these studies express Eq. (7.4) as follows:

$$n\frac{\partial \hat{C}}{\partial t}+\hat{q}_1\frac{\partial \hat{C}}{\partial x_i}-\frac{\partial}{\partial x_i}\left(\hat{q}_1 A_{ij}\frac{\partial \hat{C}}{\partial x_j}\right)=0 \qquad i,j=1,2,3 \tag{7.5}$$

where $\hat{q}_1$ is the uniform mean flow, A_{ij} is the macrodispersivity tensor and $\hat{C}$ is the ensemble mean concentration and is related to the single realization concentration field $C(\underline{x},t)$ through the following equations:

$$\hat{C}(\underline{x},t)=E\left[C(\underline{x},t)\right] \tag{7.6}$$

Center of mass of the ensemble average concentration $\hat{x}_i(t)$ in the ith direction

$$\hat{x}_i(t) = \frac{n}{m}\int_{-\infty}^{+\infty} x_i \hat{C}(\underline{x},t)d\underline{x} = \frac{\hat{q}_1 t}{n} \qquad i = 1, 2, 3 \tag{7.7}$$

Second moment $M_{ij}(t)$

$$M_{ij}(t) = \frac{n}{m}\int_{-\infty}^{+\infty}\left(x_i - \hat{x}_i(t)\right)\left(x_j - \hat{x}_j(t)\right)\hat{C}(\underline{x},t)d\underline{x} \tag{7.8}$$

$$i, j = 1, 2, 3$$

The macrodispersivity tensor A_{ij} is related to M_{ij} through the following equations [Gelhar, 1993; Dagan,]

$$A_{ij}(t) = \frac{n}{2\hat{q}_1}\frac{dM_{ij}}{dt} \tag{7.9}$$

which can be expressed in terms of displacement $\hat{x}_1$ as

$$A_{ij}(\hat{x}_1) = \frac{1}{2}\frac{dM_{ij}}{d\hat{x}_1} \tag{7.10}$$

Thus A_{ij} quantifies the dispersion of the ensemble mean concentration about the ensemble-mean center of mass position and it may be expected to be a reasonable estimate of the second moment growth rate in a single realization only under ergodic conditions (large initial solute size and at large displacements from the point of injection for instance). The second moment tensor M_{ij} is not equivalent to the ensemble average of the single realization second moment $\Sigma_{ij}(t)$, which is defined as

$$\Sigma_{ij}(t) = E\left[S_{ij}(t)\right] \tag{7.11}$$

where $S_{ij}(t)$ is defined in Eq. (7.3). The difference between $\Sigma_{ij}(t)$ and $M_{ij}(t)$ is well established in the literature on turbulent diffusion (e.g. Csanady, 1973, Rajaram and Gelhar, 1993 and 1995) and is expressed as

$$M_{ij}(t) = \Sigma_{ij}(t) + R_{ij}(t) \tag{7.12}$$

where

$$R_{ij}(t) = E\left[\left(\overline{x}_i(t) - \hat{x}_i(t)\right)\left(\overline{x}_j(t) - \hat{x}_j(t)\right)\right]$$

is a tensor whose component denotes the ensemble average of the product of the deviations of the center of mass in a realization in the i and j directions from the

ensemble mean center of mass locations in the same directions. In general, M_{ij} is larger than Σ_{ij}. For uniform mean flow in the x_1 direction, Eq. (7.12) may be written as

$$M_{ij}\left(\hat{x}_1\right)=\Sigma_{ij}\left(\hat{x}_1\right)+R_{ij}\left(\hat{x}_1\right) \tag{7.13}$$

From the theory of turbulent diffusion, macrodispersivity expressions have been obtained to relate M_{ij} and Σ_{ij} to the specific discharge spectra (see Neuman, 1987; Koch and Brady, 1988; Dagan, 1988; Gelhar, 1993; Rajaram and Gelhar, 1993 and 1995). These theories are reviewed in Chapter 2. These expressions are:

Ensemble macrodispersivity A_{ij}

$$A_{ij}\left(\hat{x}_1\right)=\frac{1}{2}\frac{dM_{ij}}{d\hat{x}_1}=\frac{n^2}{\hat{q}^2}\int_0^{\hat{x}_1}\int_{-\infty}^{+\infty}e^{\left(ik_1-\alpha k^2\right)}S_{q_iq_j}\left(\underline{k}\right)d\underline{k}d\xi \tag{7.14}$$

Plume-scale dependent macrodispersion (also known as relative dispersivity) A_{ij}^r

$$A_{ij}^r\left(\hat{x}_1,\Sigma_{ij}\right)=\frac{1}{2}\frac{d\Sigma_{ij}}{d\hat{x}_1}=\frac{n^2}{\hat{q}^2}\int_0^{\hat{x}_1}\int_{-\infty}^{+\infty}e^{\left(ik_1-\alpha k^2\right)\xi}\cdot\left\{1-e^{-k_ik_j\Sigma_{ij}\left(\hat{x}_1\right)}\right\}S_{q_iq_j}\left(\underline{k}\right)d\underline{k}d\xi \tag{7.15}$$

where α is the pore scale dispersion coefficient.

The rate of growth of Σ_{ij} in Eq. (7.15) involves two scales: the plume displacement $\hat{x}_1$ and the plume size Σ_{ij}. When the growth rate of M_{ij} is constant, the transport is described as Fickian. Non-Fickian or anomalous transport occurs when the growth rate of M_{ij} is time or space dependent [Elfeki et al., 1997]. The non-Fickian transport can also be classified to be either sub-diffusive (fractal dispersion) in which the growth of M_{ij} is slower than linearly with time or super-diffusive transport (also known as hyperdiffusion) in which M_{ij} grows faster than linearly with time [Elfeki et al., 1997; Bershadskii, 1999]. These mechanisms can be described mathematically as follows:

$$\begin{aligned} &\text{(i)} \quad M_{11} \sim t^{\lambda} \\ &\text{(ii)} \quad A_{11} \sim t^{\lambda-1} \end{aligned} \tag{7.16}$$

assuming a constant mean flow, Eq. (7.16) can be written as

$$\begin{aligned} &\text{(i)} \quad M_{11} \sim \hat{x}_1^{\lambda} \\ &\text{(ii)} \quad A_{11} \sim \hat{x}_1^{\lambda-1} \end{aligned} \tag{7.17}$$

where M_{11} is the variance in the longitudinal direction, A_{11} is the longitudinal macrodispersivity, t is the travel time from the point of injection and λ is an exponent describing the transport regime. When $\lambda = 1$ the transport is described as diffusive, $\lambda < 1$ describes sub-diffusive (fractal) dispersion and when $\lambda > 1$ the transport is described as

superdiffusive. Transport in heterogeneous media has been found to possess $1 \leq \lambda < 2$ [Arya et al., 1985; Hewett, 1986; Neuman, 1990 among others]. Moreover, field experiments (for example Rehfeldt and Gelhar (1992) for the Cape Cod site; Sudicky (1986) for the Borden site, Freyberg, 1986; Boggs et al., 1992) reveal that plumes have irregular shapes, different from the smooth Gaussian plumes predicted by the solution to the ADE. Recent developments in solute transport have aimed at addressing these two key issues:

1. Models that will describe the scale-dependent behavior of macrodispersivity
2. Models that will account for the asymmetry of plumes in heterogeneous porous media.

Scale-dependent macrodispersivity models by Gelhar and Axness (1983), Rajaram and Gelhar (1993 and 1995), Neuman and Zhang (1990) and Dagan (1987) among others, dual porosity models by Coats and Smith (1964) which is reviewed in Chapter 2, and more recently the continuous time random walk (CTRW) by Berkowitz et al. (2000), Margolin and Berkowitz (2000), Yanosky et al. (1999) have been posited to explain the asymmetry of concentration distributions and scale dependent behavior of macrodispersivity.

In the next section, we present results for macrodispersivity in multifractal porous media. Specifically, we compare macrodispersivities computed from specific discharge spectra from linear theory and nonlinear theory presented in Chapter 6. In Sec 7.3, we present a brief review of the CTRW model. The scaling features of flow through multifractal

porous media are exploited in Sec. 7.4 to derive expressions for the first passage time distribution and mean plume concentration. Sec. 7.5 presents a comparison of the model in Sec. 7.4 with the CTRW and two-phase models.

7.2 Ensemble and plume scale dependent macrodispersivity

To see the effect of nonlinearities in the flow equations on the macrodispersivity expressions in Eqs. (7.14) and (7.15), one may compare the functions of $A_{ij}\left(\hat{x}_1\right)$ and $A_{ij}^{r}\left(\hat{x}_1\right)$ for a 2D flow field through a hydraulic conductivity field K field when $S_{q_iq_j}\left(\underline{k}\right)$ in Eqs. (7.14) and (7.15) are taken to be

Linear Theory

$$S_{\underline{q}}\left(r\underline{k}_o\right)=\left(\frac{1}{\pi}k_o^{-2}C_K\right)r^{-2}\left[\begin{matrix}\left(\delta_{i1}-e_1e_j\right)\left(\delta_{j1}-e_1e_j\right)\\ i,j=1,\ldots,D\end{matrix}\right] \tag{7.18}$$

Nonlinear Theory

$$S_{\underline{q}}\left(r\underline{k}_o\right)=\left(\frac{1}{\pi}k_o^{-2}C_K\right)r^{-2+C_K}\left(\left(1-b_r\right)e_1^2+b_re_2^2\right)\left[\begin{matrix}e_2^2 & -e_1e_2\\ -e_1e_2 & e_1^2\end{matrix}\right]$$

where all the terms have been defined in Chapter 5: k_o is the minimum wavenumber for the $F=\ln\left(K\right)$ spectrum, r is the resolution to which the K field is developed, where e_i is the unit vector in the direction of x_i (for $i=1,2$), and $b_r=E\left[\cos^2\left(\alpha_r\right)\right]$, α_r being the

random rotation angle of the flow vectors that has a normal distribution with zero mean and variance $\frac{2}{D(D+2)} C_K \ln(r)$; see Chapters 4.

Substituting the spectra in Eq. (7.18) into Eq. (7.14) and assuming that the pore scale dispersion coefficient $\alpha = 0$, the ensemble longitudinal and transversal macrosdispersivities was computed for K fields with $C_K = 0.1$ and 0.3. Figures 7.1a and 7.1b compare the results of the nonlinear theory with the linear theory. For the results shown in Fig. 7.1, $k_o = 1$, because honoring the theoretical condition of $k_o \gg 1$ would have required a very fine discretization grid and made the computational demands prohibitive. The ensemble macrodispersivities A_{11} and A_{22} have been computed for non-dimensional distances given by $\text{distance}[L] * k_o \left[\frac{1}{L}\right]$. Reflecting the local isotropy of the flow field, the longitudinal and transversal macrodispersivities from nonlinear theory coincide at small distances. This feature is not captured by the linear perturbation approach. Another difference with the linear theory is that the macrodispersivities from nonlinear theory are larger at small distances, due to the increased high frequency content of the flow predicted by the nonlinear theory. Infact, we see from Figs. 7.1a and 7.1b that at small distances, the macrodispersivities for the nonlinear theory for $C_K = 0.3$ is larger than for $C_K = 0.1$ because the K field for $C_K = 0.3$ has higher frequency content than for the $C_K = 0.1$ field.

Plume-scale dependent macrodispersivity

The plume-scale macrodispersivities are computed for the linear and nonlinear theories by substituting Eq. (7.18) into Eq. (7.15). The growth of the plume second moment Σ_{ij} with mean travel distance is presented in Fig. 7.2, where the nondimensional plume second moment given by $\Sigma\left[L^2\right]*k_o^2\left[\frac{1}{L^2}\right]$ and the square parenthesis are the dimensions of Σ and k_o^2. The evolution of two plumes with initial Σs of $4x10^{-6}k_o^2$ and $.04k_o^2$ are shown in Figs. 7.2a and 7.2b. The initial plume size is given by the square root of the determinant of the initial Σs, so that for plumes with a circular configuration, initial Σs of $4x10^{-6}k_o^2$ and $.04k_o^2$ mean that the plumes have initial diameters of $0.002k_o$ and $0.2k_o$ respectively. From Fig. 7.2 we see that the plumes initially do not show any visible growth for small travel distances. This behavior can be explained by the fact that when a solute is introduced into a flow system, the initial solute locations are not correlated with the flow velocities. After some travel distance, the solute locations become correlated with the flow velocities, as a form of sorting occurs within the plume. The sorting is such that the higher velocities are at the front of the plume, whereas the slowest velocities are at the tail or end of the plume. The time and its equivalent mean travel distance it takes for the plume to undergo this sorting of velocities explains the lack of visible plume growth for short distances shown in Fig. 7.2. Moreover, we see from Fig. 7.2 that the sorting occurs faster in a plume with a smaller initial size ($0.002k_o$) than for a plume with a larger initial size ($0.2k_o$).

Unlike the power law growth of macrodispersivities in Fig. 7.1, the plume-scale dependent macrodispersivities in Fig. 7.3 display a nonlinear behavior with travel distance. This nonlinearity is because the growth rate of the plume at any mean travel distance depends on the longitudinal and transversal plume dimensions at an infinitesimally smaller travel distance before the location in consideration.

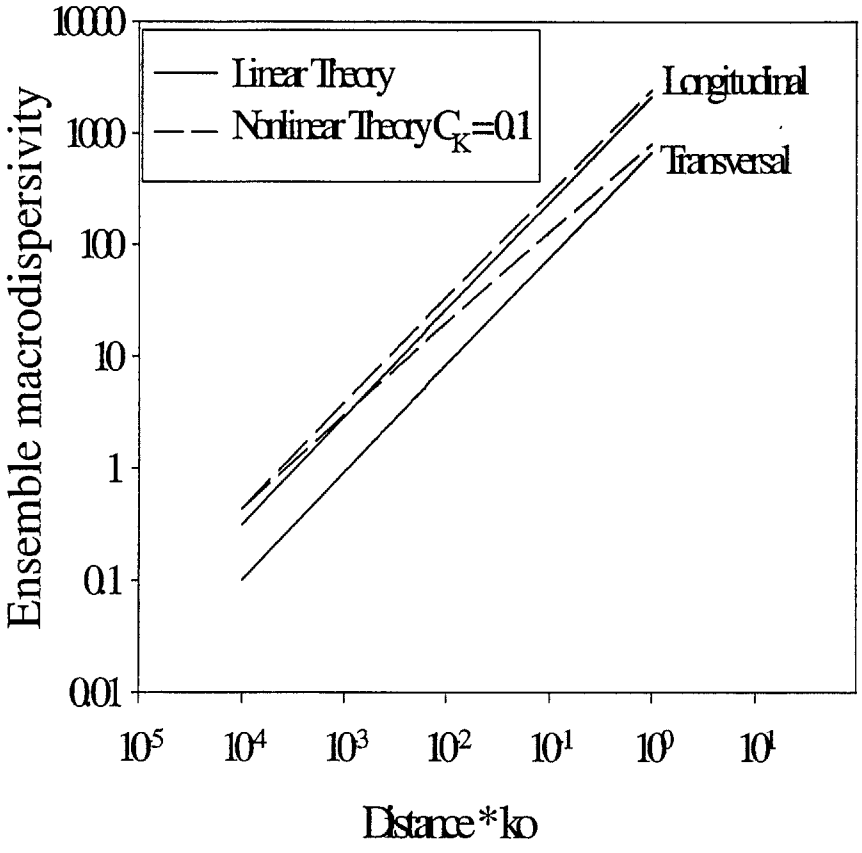

Figure 7.1a - Comparison of the linear and nonlinear ensemble macrodispersivities for $C_K = 0.1$

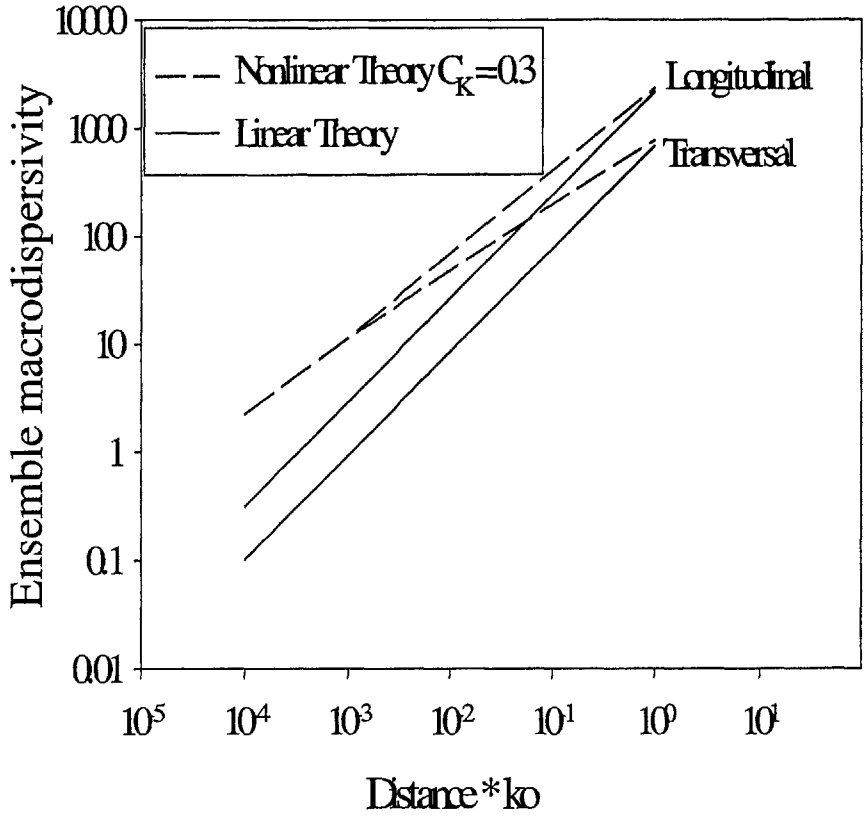

Figure 7.1b - Comparison of the linear and nonlinear ensemble macrodispersivities for $C_K = 0.3$

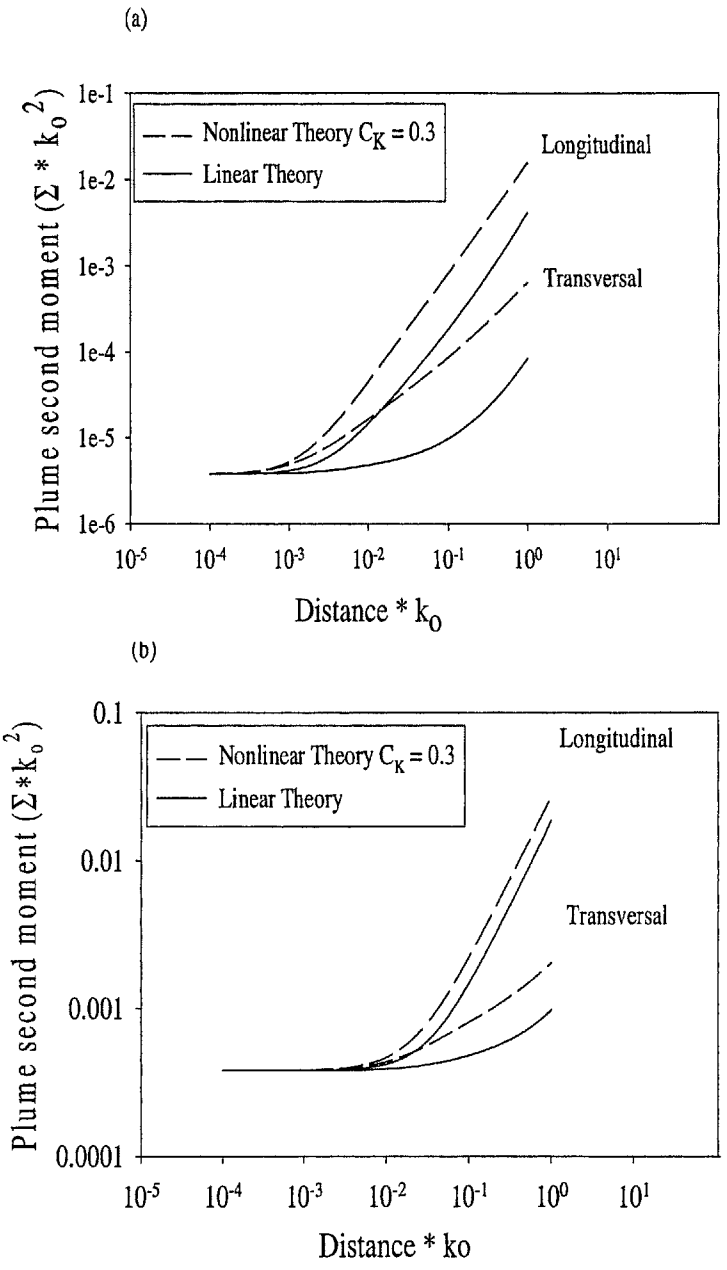

Figure 7.2 - Growth of plume second moments for linear and nonlinear theories for plumes with initial sizes of (a) .002/ko and (b) .2/ko

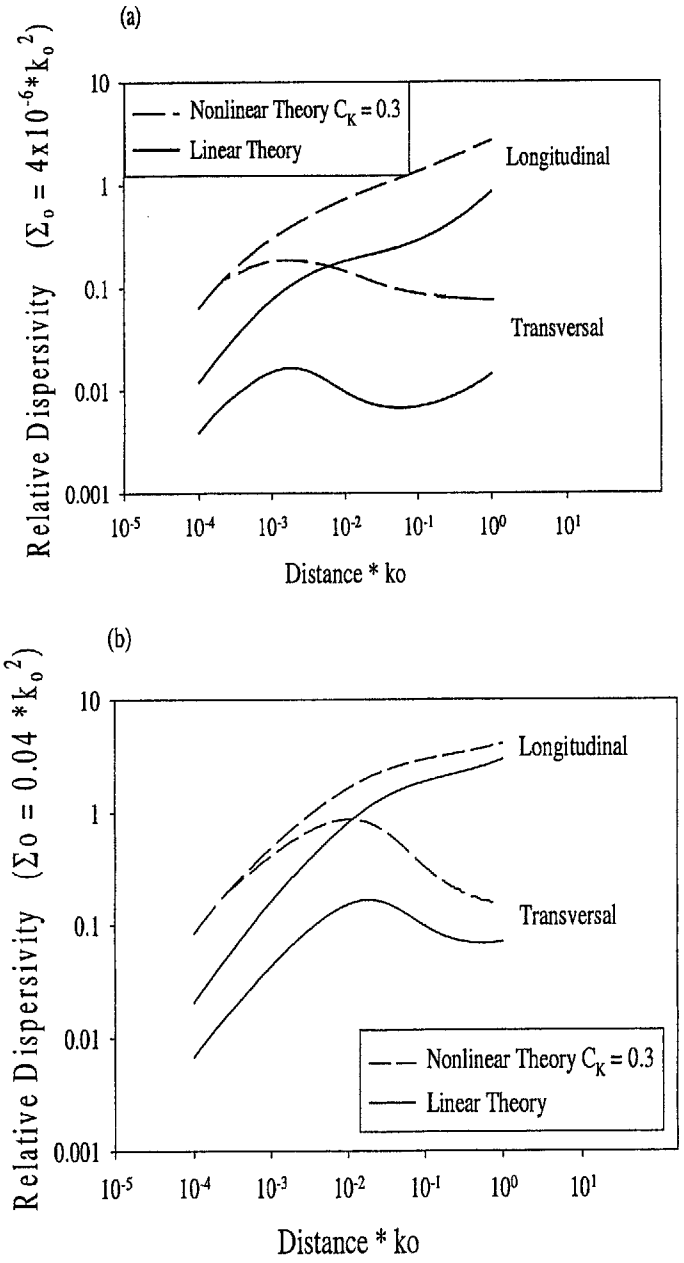

Figure 7.3 - Relative macrodispersivities for linear and nonlinear theories for plumes with initial sizes of (a) 0.002/ko and (b) 0.2/ko

From Fig. 7.3 it is clear that after a finite mean travel distance, the second moment of the plumes from the nonlinear theory are higher than those of the linear theory. This is because of the increased high frequency content of the flow predicted by the nonlinear theory and is reflected in the macrodispersivities shown in Figs. 7.3.

From Fig. 7.3, the plume-scale dependent macrodispersivities for the nonlinear theory at short distances are isotropic. This behavior is attributed to the rotations of the flow vectors that are accounted for in the spectral density tensors of the nonlinear theory.

The Evolution of a Plume with a flow field with multifractal K

To examine the behavior of the ensemble macrodispersivities for the linear and nonlinear spectra in Eq. (7.18) at small travel distances, we perform a simple scaling analysis and find that Eq. (7.14) is scale invariant under the scale transformations of the form:

$$\begin{cases} \hat{x}_1 \rightarrow \beta \hat{x}_1 \\ k_1 \rightarrow k_1 / \beta \\ k_2 \rightarrow k_2 / \beta \end{cases} \tag{7.19}$$

where $\beta > 1$. The above set of transformations means that we stretch the mean travel distance by a factor of β. In frequency space, this is equivalent to contracting the wavenumber vector by a factor of $1/\beta$, so that k_1 and k_2 are contracted by a factor of

$1/\beta$ in Eq. (7.19). Substituting the above transformations into Eq. (7.14) we find that the ensemble dispersivities have a power-law dependence on mean travel distance, i.e.

$$\begin{cases} A_{ij}\left(\hat{x}_1\right) \propto \hat{x}_1^{1-C_K} & \text{Nonlinear Theory} \\ A_{ij}\left(\hat{x}_1\right) \propto \hat{x}_1^{1} & \text{Linear Theory} \end{cases} \tag{7.20}$$

Thus, the ensemble second moments M_{ij} have the following power law dependence on mean travel distance

$$\begin{cases} M_{ij}\left(\hat{x}_1\right) \propto \hat{x}_1^{2-C_K} & \text{Nonlinear Theory} \\ M_{ij}\left(\hat{x}_1\right) \propto \hat{x}_1^{2} & \text{Linear Theory} \end{cases} \tag{7.21}$$

Eqs. (7.21) and (7.20) show that for transport in a multifractal K field, the linear theory predicts that the plume will grow at a faster rate than the in the nonlinear case.

Following the approach just presented, we derive an expression for two plumes of initial sizes Σ_{small} and Σ_{large}, where $\Sigma_{small} < \Sigma_{large}$ injected into a flow field with a multifractal K. Under the scale transformations in Eq. (7.19), we obtain the following scaling relations for the evolution of the plumes by substituting Eq. (7.19) into Eq. (7.15)

$$\Sigma_{Small}\left(\hat{x}_1\right)\overset{d}{=}\beta^{-2+C_K}\,\Sigma_{Big}\left(\beta\hat{x}_1\right)$$

$$A_{11-Small}\left(\hat{x}_1\right)\overset{d}{=}\beta^{-1+C_K}A_{11-Big}\left(\beta\hat{x}_1\right) \tag{7.22}$$

where $\overset{d}{=}$ denotes equality of distributions. Eq. (7.22) relates the second moment of a bigger plume Σ_{Big} that has traveled a distance $\beta\hat{x}_1$ to the second moment of a smaller plume Σ_{Small} that travels a smaller distance $\hat{x}_1$ in the same flow field with a multifractal K. In fact Eq. (7.22) can be used to predict the evolution of a larger plume traveling through a multifractal flow field. The evolution of a smaller plume through a multifractal flow field with the same C_K value can be used in predicting the behavior of a much larger plume.

In order to validate Eq. (7.22), two types of computations are performed: the first type of computation compares the evolution of two plumes computed from Eq. (7.15). The second type of computation is a numerical simulation of the transport of two plumes of different initial sizes migrating through a multifractal flow field. The transport code used in the simulation was developed by Feng (1997) and has been proven efficient for simulating transport in highly variable K fields.

First, we present results from computations from Eq. (7.15). For the computational results presented in Table 7.1, $k_o = 1$, $\Sigma_{Small} = 0.0004/k_o^2$ and $\Sigma_{Large} = 0.0064/k_o^2$ and the results are presented in non-dimensional form.

Table 7.1a- Evolution of plumes: $\beta = 2$, $C_K = 0.3$, $\Sigma_{Small} = 0.0004/k_o^2$, $\Sigma_{Large} = 0.04/k_o^2$

Travel Distance for Small Plume = $\hat{x}_1/k_o$	$\frac{\Sigma_{Small}(\hat{x}_1/k_o)}{k_o^2}$	Travel Distance for Large Plume = $\beta\hat{x}_1/k_o$	$\frac{\Sigma_{Large}(\beta\hat{x}_1/k_o)}{k_o^2}$	$\frac{\Sigma_{Large}(\beta\hat{x}_1/k_o)}{\Sigma_{Small}(\hat{x}_1/k_o)}$	Theoretical β^{2-C_K}
0.039	1.65×10^{-4}	0.078	5.41×10^{-4}	3.27	
0.049	2.09×10^{-4}	0.098	6.78×10^{-4}	3.25	
0.098	4.33×10^{-4}	0.195	1.41×10^{-3}	3.25	
0.195	9.36×10^{-4}	0.390	3.03×10^{-3}	3.24	
0.293	1.586×10^{-3}	0.586	5.12×10^{-3}	3.23	3.25
0.391	2.073×10^{-3}	0.781	6.68×10^{-3}	3.22	
				Mean = 3.24	

Table 7.1b- Ensemble macrodispersivity: $\beta = 2$, $C_K = 0.3$, $\Sigma_{Small} = 0.0004/k_o^2$, $\Sigma_{Large} = 0.04/k_o^2$

Travel Distance for Small Plume = $\hat{x}_1/k_o$	$A_{11\text{-Small}}\left(\hat{x}_1/k_o\right)$	Travel Distance for Large Plume = $\beta\hat{x}_1/k_o$	$A_{11\text{-Large}}\left(\beta\hat{x}_1/k_o\right)$	$\frac{A_{11\text{-Large}}\left(\beta\hat{x}_1/k_o\right)}{A_{11\text{-Small}}\left(\hat{x}_1/k_o\right)}$	Theoretical β^{1-C_K}
0.039	1.012	0.078	1.72	1.70	1.625
0.049	1.098	0.098	1.80	1.64	
0.098	1.205	0.195	2.00	1.66	
0.195	1.402	0.390	2.30	1.64	
0.293	1.532	0.586	2.45	1.60	
0.391	1.652	0.781	2.56	1.55	
				Mean = 1.63	

Table 7.1 shows a very good agreement between the computational results and the theoretical results in Eq. (7.22). In the second validation, we performed numerical transport simulations on a 512 x 512 grid. The velocity field serves as the input into the transport code, and the size, shape and initial location of the plume are defined and the transport computations are performed for different times. Figures 7.4a and b show the evolution of plumes with initial sizes of $\Sigma_o = \left(\frac{40}{512k_o} \right)^2$ in flow fields computed from K fields with $C_K = 0.1$ and 0.3 respectively. We observe in these figures that for the same travel time the plume in the $C_K = 0.1$ field travels further and spreads faster than the plume in the $C_K = 0.3$ field. The velocity field for the $C_K = 0.3$ field is sparser and has a lower mean value than the $C_K = 0.1$ field. Consequently, the plume travels faster in the $C_K = 0.1$ field. Similar computations were performed for plumes with initial sizes $\Sigma_o = \left(\frac{20}{512k_o} \right)^2$ and $\Sigma_o = \left(\frac{40}{512k_o} \right)^2$ in a flow field with $C_K = 0.3$. The averaged results for 15 simulations are presented in Table 7.2. For each simulation, the plumes were placed at different locations in the flow domain, so that the initial velocities varied from simulation to simulation and the center of mass and second moments for the various times are computed as the discrete versions of Eqs. (7.2) and (7.3) respectively

Center of mass in the x and y directions

$$\bar{x} = \frac{\sum_{i=1}^{N} C_i x_i}{\sum_{i=1}^{N} C_i} \quad \text{and} \quad \bar{y} = \frac{\sum_{i=1}^{N} C_i y_i}{\sum_{i=1}^{N} C_i} \tag{7.23}$$

Second spatial moments

$$S_{xx}(t) = \frac{\sum_{i=1}^{N} C_i \left(x_i(t) - \bar{x}\right)^2}{\sum_{i=1}^{N} C_i} \quad \text{and} \quad S_{yy}(t) = \frac{\sum_{i=1}^{N} C_i \left(y_i(t) - \bar{y}\right)^2}{\sum_{i=1}^{N} C_i} \tag{7.24}$$

For the 15 simulations the ensemble center of mass $\hat{x}$ and second moment Σ are obtained by averaging the values of $\bar{x}, \bar{y}, S_{xx}$ and S_{yy}:

$$\hat{x}_1 = \frac{\sum_{i=1}^{N} \bar{x}_i}{N} \quad \text{and} \quad \Sigma_{xx} = \frac{\sum_{i=1}^{N} S_{xxi}}{N} \tag{7.25}$$

From the results in Table 7.2, we find that there is a good agreement between the theoretical results of Eq. (7.22) and the results of the numerical simulations.

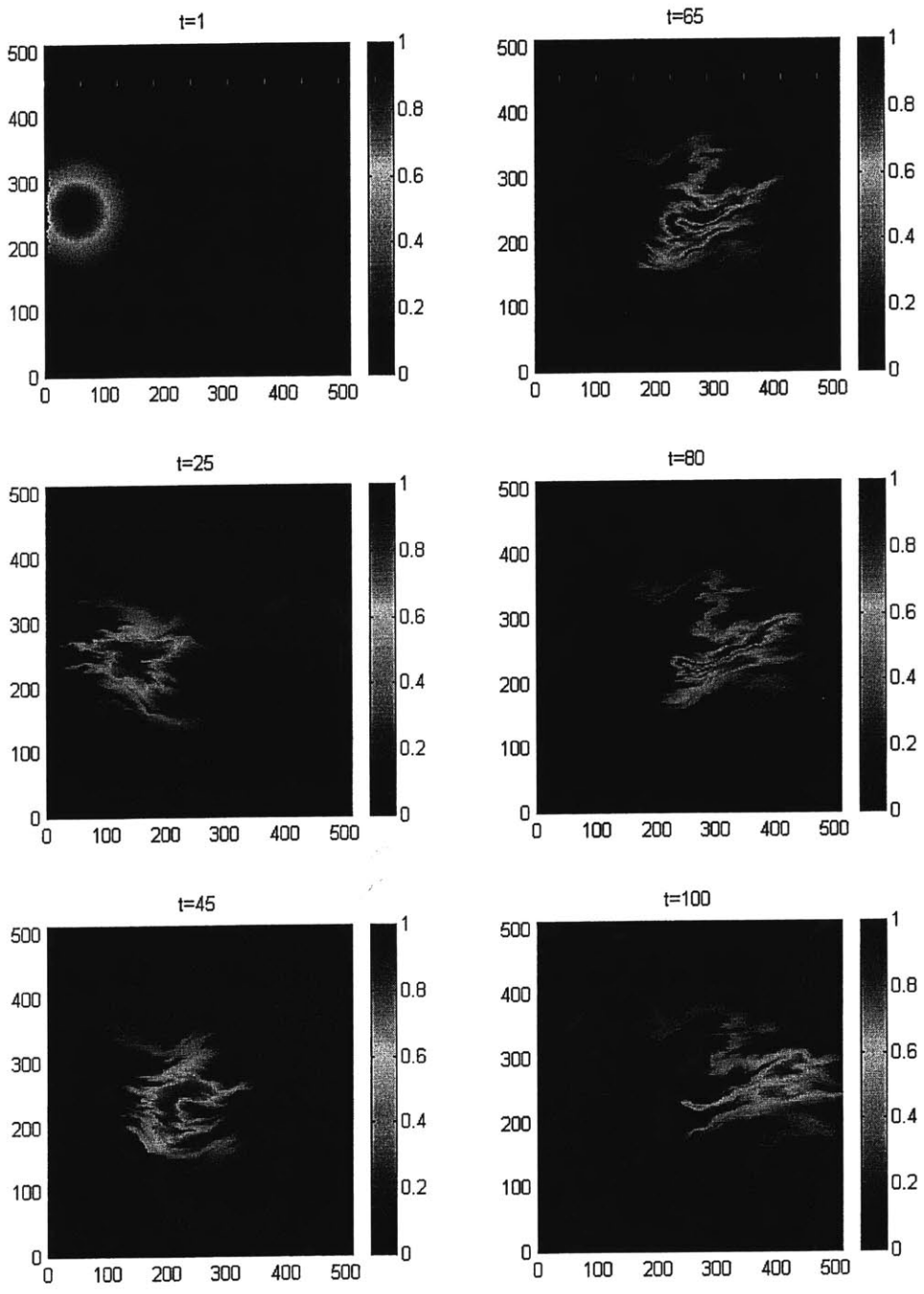

Fig 7.4 a - Evolution of a plume with initial size .1ko through a flow field with $C_K = 0.1$, kmax = 512, ko =1 and the times are t = time/kmax*E[V]

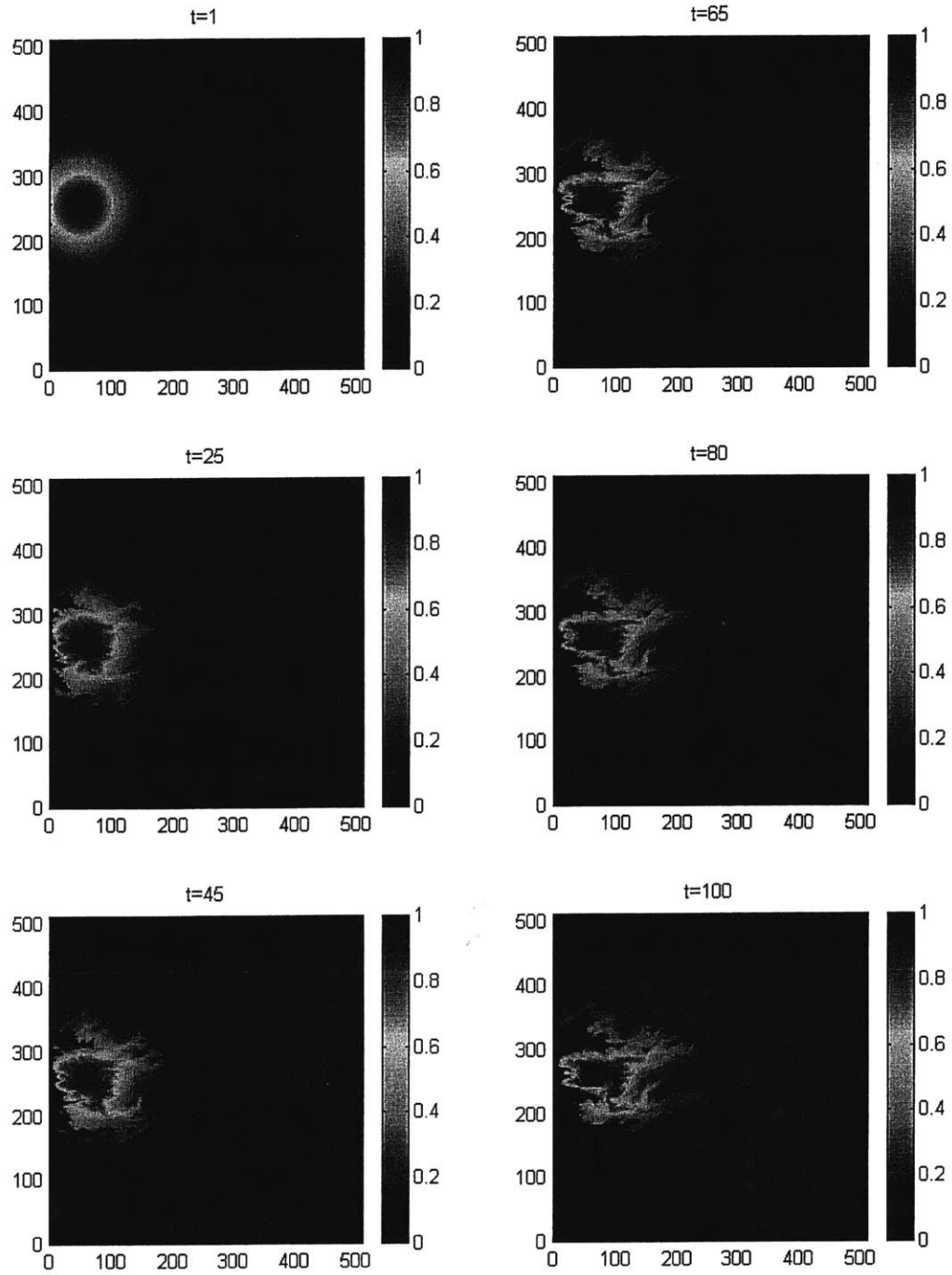

Fig 7.4b - Evolution of a plume with initial size .1ko through a flow field with $C_K = 0.3$, kmax = 512, ko =1 and the times are t = time/kmax*E[V]

Table 7.2 – The evolution of plumes with initial sizes $\Sigma_o = 0.0061k_o^2$ and $\Sigma_o = 0.0015k_o^2$, $\beta = 2$, $C_K = 0.3$ and $k_o = 1$

Distance*ko $\beta\hat{x}_1$	$\sqrt{\Sigma_{Large}(\beta\hat{x}_1)}$ *ko	Distance*ko $\hat{x}_1$	$\sqrt{\Sigma_{Small}(\hat{x}_1)}$ *ko	$\frac{\sqrt{\Sigma_{Large}(\beta\hat{x}_1)}}{\sqrt{\Sigma_{Small}(\hat{x}_1)}}$	Theoretical Ratio = $\beta^{1-C_K/2}$
0.0781	0.0826	0.0391	0.0453	1.82	
0.1563	0.0975	0.0781	0.0538	1.81	
0.2343	0.1128	0.1172	0.0613	1.84	1.8025
0.3125	0.1198	0.1563	0.0666	1.79	
				Mean = 1.815	

The results in Table 7.2 show that during the migration of a plume, there can be a significant degree of overlap of the subplumes. The small and big plumes are evolved from the same initial point. However, we find that for the same ensemble mean travel distance, the smaller plume grows at a faster rate than the larger plume. Thus, if one is to consider the smaller plume to be a subplume of the larger one, then by comparing the rates of evolution, one can conclude that within the larger plume, the smaller subplumes overlap. The results of the simulation in Table 7.2 do not provide information on the evolution of the mean concentration field. However, it can be used as a predictive tool in determining the evolution of a larger plume in a flow field with a multifractal hydraulic conductivity within which the evolution of a smaller plume has been studied.

7.3 – A review of the continuous time random walk (CTRW) model

The CTRW model by Benson et al. [2000], Berkowitz and Scher [2000] obtains a solution for the Fractional Fokker-Planck equation (FFPE). The FFPE is a generalization of the Fokker-Planck equation that is used in studying the dynamic behavior of particles driven by Gaussian noises. For the FFPE the driving source is a Levy stable motion L(t) instead of a Brownian motion. Specifically for an $\alpha-$stable Levy motion with skewness β $(-1 \le \beta \le 1)$ and for a small time t the FFPE is given by

$$\frac{\partial p}{\partial t} = -\frac{\partial}{\partial x} vp + \left(\frac{1}{2} + \beta/2\right)\frac{\partial^\alpha}{\partial x^\alpha}\mathcal{D}p + \left(\frac{1}{2} - \beta/2\right)\frac{\partial^\alpha}{\partial(-x)^\alpha}\mathcal{D}p \qquad (7.26)$$

where v is the drift of the process, i.e. the mean advective velocity, $\mathcal{D}$ is a constant dispersion coefficient, p is the transition probability that quantifies the probability that a particle that starts out at position y at time t will be at y' at time t'.

For a large number of independent solute "particles" the transition probability can be replaced by the expected concentration C [Benson et al., 2000]. Further, since the particle motions are iid, Eq. 7.23 simplifies to

$$\frac{\partial C}{\partial t} = -v\frac{\partial C}{\partial x} + \left(\frac{1}{2} + \beta/2\right)\mathcal{D}\frac{\partial^\alpha C}{\partial x^\alpha} + \left(\frac{1}{2} - \beta/2\right)\mathcal{D}\frac{\partial^\alpha C}{\partial(-x)^\alpha} \qquad (7.27)$$

where the dimensions of $\mathcal{D}$ are $L^\alpha T^{-1}$. For Gaussian and lognormal distributions $\alpha = 2$ and the classical ADE is recovered, since $d^2/dx^2 = d^2/d(-x)^2$. Solutions to Eq. (7.27) are obtained through Laplace transforms [for example Berkowitz et al., 2000] or Fourier transforms [e.g. Benson et al., 2000]. The solution of Eq. (7.27) in Fourier space obtained by Benson et al. is

$$\hat{C}(k,t) = \exp\left[\frac{1}{2}(1-\beta)(-ik)^\alpha \mathcal{D}t + \frac{1}{2}(1+\beta)(ik)^\alpha \mathcal{D}t - ikvt\right] \qquad (7.28)$$

This Fourier transform does not have a closed-form inverse. For a symmetric distribution $\beta = 0$, writing $\mathcal{B} = |\cos(\pi\alpha/2)|\mathcal{D}$ and using the identities $i = e^{i\pi/2}$ and $e^{i\theta} = \cos\theta + i\sin\theta$, Eq. (7.28) can be written as

$$\hat{C}(k,t) = \exp\left(-\mathcal{B}t|k|^{\alpha} - ikvt\right) \tag{7.29}$$

Eq. (7.29) is the probability density of a symmetric $\alpha-$stable variable C, with mean $\mu = vt$ and dispersion parameter $\sigma = (\mathcal{B}t)^{1/\alpha}$ and is known as the first passage time distribution (FPTD) or the first exit time distribution. The FPTD is the probability of a particle leaving a given range before a given time.

Berkowitz et. al. (2000) obtain the solution of Eq. (7.27) in Laplace space as

$$\begin{cases} FPTD(L,\tau) = \mathcal{L}^{-1}\left[\exp\left(bu^{\alpha}\right)\right] & \text{for } 0 < \alpha < 1 \\ FPTD(L,\tau) = \mathcal{L}^{-1}\left[\exp\left(-\ell u + bu^{\alpha}\right)\right] & \text{for } 1 < \alpha < 2 \end{cases} \tag{7.30}$$

where L is the distance between the inlet, origin or point of injection of the solute particles and the exit or outlet plane, u is the Laplace variable, $b \equiv b_{\beta}L/\langle\ell\rangle$ is a non-dimensional measure of L and b_{β} is proportional to the dispersion coefficient in Eq. (7.27), $\langle\ell\rangle$ is the mean displacement of a single transition, and $\tau = vt/\langle\ell\rangle = t/\langle\iota\rangle$ is a non-dimensional time.

Solutions to Eq. (7.30) are obtained by expanding the exponential terms and integrating term by term to yield

$$\mathrm{FPTD}(L,\tau)=\tau^{-1}\sum_{j=0}^{\infty}\frac{\left(-b/\tau^{\alpha}\right)^{j}}{\Gamma(j+1)\Gamma(-j\alpha)} \qquad \text{for } 0<\alpha<1 \tag{7.31}$$

where $\Gamma(x)$ is the gamma function and $1/\Gamma(-j\alpha)=0$ for integer values of $j\alpha$.

Writing $x=b/\tau^{\alpha}$, and since for $j\neq 0$ $\dfrac{1}{\Gamma(1-\alpha j)}\equiv\dfrac{1}{\pi}\Gamma(\alpha j)\sin(\pi\alpha j)$, Eq. (7.31) can be written as

$$\mathrm{FPTD}(L,\tau)=\frac{1}{\tau\pi}\sum_{j=0}^{\infty}(-x)^{j}\sin(\pi j\alpha)\frac{\Gamma(j\alpha+1)}{\Gamma(j+1)} \qquad \text{for } 0<\alpha<1 \tag{7.32}$$

Eq. (7.32) can only be evaluated numerically for small values of x, because of the j exponent. For large x, Eq. (7.32) can be approximated by (Scher and Montroll, 1975)

$$\mathrm{FPTD}\simeq\frac{1}{\tau}\frac{1}{\sqrt{2\pi(1-\alpha)}}\left(\sqrt{\alpha x}\right)^{\frac{1}{1-\alpha}}\exp\left(-\left(\frac{1-\alpha}{\alpha}\right)(\alpha x)^{\frac{1}{1-\alpha}}\right) \tag{7.33}$$

It is often more convenient to examine breakthrough data in terms of the cumulative FPTD (CFPTD) curves. CFPTDs are defined as

$$CFPTD = \int_0^t FPTD(t')dt' \tag{7.34}$$

The following expressions are obtained for the CFPTD for $0 < \alpha < 1$ (Berkowitz et al., 2000). Similar to the FPTD solutions, the same two cases introduced by x arise.

for up to moderate values of x

$$CFPTD = 1 + \frac{1}{\pi}\sum_{j=1}^{\infty}(-x)^j \sin(\pi j\alpha)\frac{\Gamma(j\alpha)}{\Gamma(j+1)} \tag{7.35}$$

for large x (>>1)

$$CFPTD = \frac{\exp\left\{-\left(\frac{1-\alpha}{\alpha}\right)[\alpha x]^{\frac{1}{1-\alpha}}\right\}}{\sqrt{2\pi(1-\alpha)(\alpha x)^{\frac{1}{1-\alpha}}}}$$

Solutions for the FPTD and CFPTD for $1 < \alpha < 2$ are obtained following the same methodology used in obtaining Eqs. (7.31) - (7.33), so that

for small to moderate values of h

$$\text{(i)}\quad \text{FPTD} = \frac{1}{\pi\alpha\langle t\rangle b^{1/g}}\sum_{j=0}^{\infty}(-h)^j\frac{\Gamma\left(\frac{j+1}{\alpha}\right)}{\Gamma(j+1)}\sin\frac{\pi(j+1)}{\alpha}$$

where $h \equiv (\ell-\tau)/b^{1/\alpha}$

for large positive h FPTD is approximated by

$$\text{(ii)}\quad \text{FPTD} \simeq \frac{(h/\alpha)^{(2-\alpha)/[2(\alpha-1)]}}{b^{1/\alpha}\langle t\rangle\sqrt{2\pi\alpha(\alpha-1)}}\exp\left\{-(\alpha-1)\left(\frac{h}{\alpha}\right)^{\alpha/\alpha-1}\right\}$$

for large negative h

$$\text{(iii)}\quad \text{FPTD} \simeq \frac{1}{\pi\langle t\rangle b^{1/\alpha}h}\sum_{j=0}^{\infty}(-h)^{-j\alpha}\sin(\pi j\alpha)\frac{\Gamma(j\alpha+1)}{\Gamma(j+1)} \qquad (7.36)$$

Note that in this case there are three functional forms for the FPTD solution over the complete range of h, whereas only two functional forms arise in the FPTD solutions for $0<\alpha<1$. The cumulative FPTDs for $1<\alpha<2$ are

$$\text{CFPTD} = \frac{1}{\alpha}+\frac{1}{\pi\alpha}\sum_{j=1}^{\infty}(-h)^j\sin\left(\frac{\pi j}{\alpha}\right)\frac{\Gamma(j/\alpha)}{\Gamma(j+1)} \qquad (7.37)$$

for large positive h,

$$\text{(i)}\quad \text{CFPTD}=\frac{\exp\left\{-(\alpha\text{-}1)(h/\alpha)^{\alpha/(\alpha-1)}\right\}}{\sqrt{2\pi\alpha(\alpha-1)(h/\alpha)^{\alpha/(\alpha-1)}}} \tag{7.38}$$

for large negative h

$$\text{(ii)}\quad \text{CFPTD}=1+\frac{1}{\pi}\sum_{j=1}^{\infty}(-h)^{-j\alpha}\sin(\pi j\alpha)\frac{\Gamma(j\alpha)}{\Gamma(j+1)}$$

Figs. 7.5 and 7.6 show the cumulative FPTD for $0<\alpha<1$ and $1<\alpha<2$ respectively. The curves become sharper and less disperse as α increases, and again, the curves are asymmetric with long tails.

The CTRW model resolves one problem associated with applying the ADE to model flow in heterogeneous media, which is the lack of symmetry predicted by the ADE. The first term in Eq. (7.27) serves as a transitional term that moves the plume with an average velocity through the medium. The variance of the plume is described by the second and third terms which like the ADE, model the plumes' spread with a Fickian dispersion and captures the asymmetry through the $\alpha-$parameter.

The CTRW model fails to describe the observed and measured scale-dependent dispersion or non-Fickian dispersion. Scale-dependent dispersion is a feature of highly heterogeneous media. Thus, whereas the CTRW model tries the resolve the issues

associated with the observed asymmetry of plumes, it fails to resolve the observed scale-dependent dispersion.

An additional shortcoming of the CTRW model is that it fails to directly relate the media properties to the parameters of the flow model. Thus, a fitted model does not really provide one with information about the properties of the media and vice-versa. Conversely, given the measured properties of a flow field one cannot relate these properties to the parameters of the CTRW model. However, the CTRW model provides a conceptual model to describe the asymmetry of plumes in heterogeneous media.

In the next section, we exploit the scaling features of the velocity field when flow occurs in a multifractal K field to derive a model that describes the scale-dependent dispersion and the asymmetry of the breakthrough curves. The theoretical derivations are presented next and results obtained are compared with the CTRW and two-phase models.

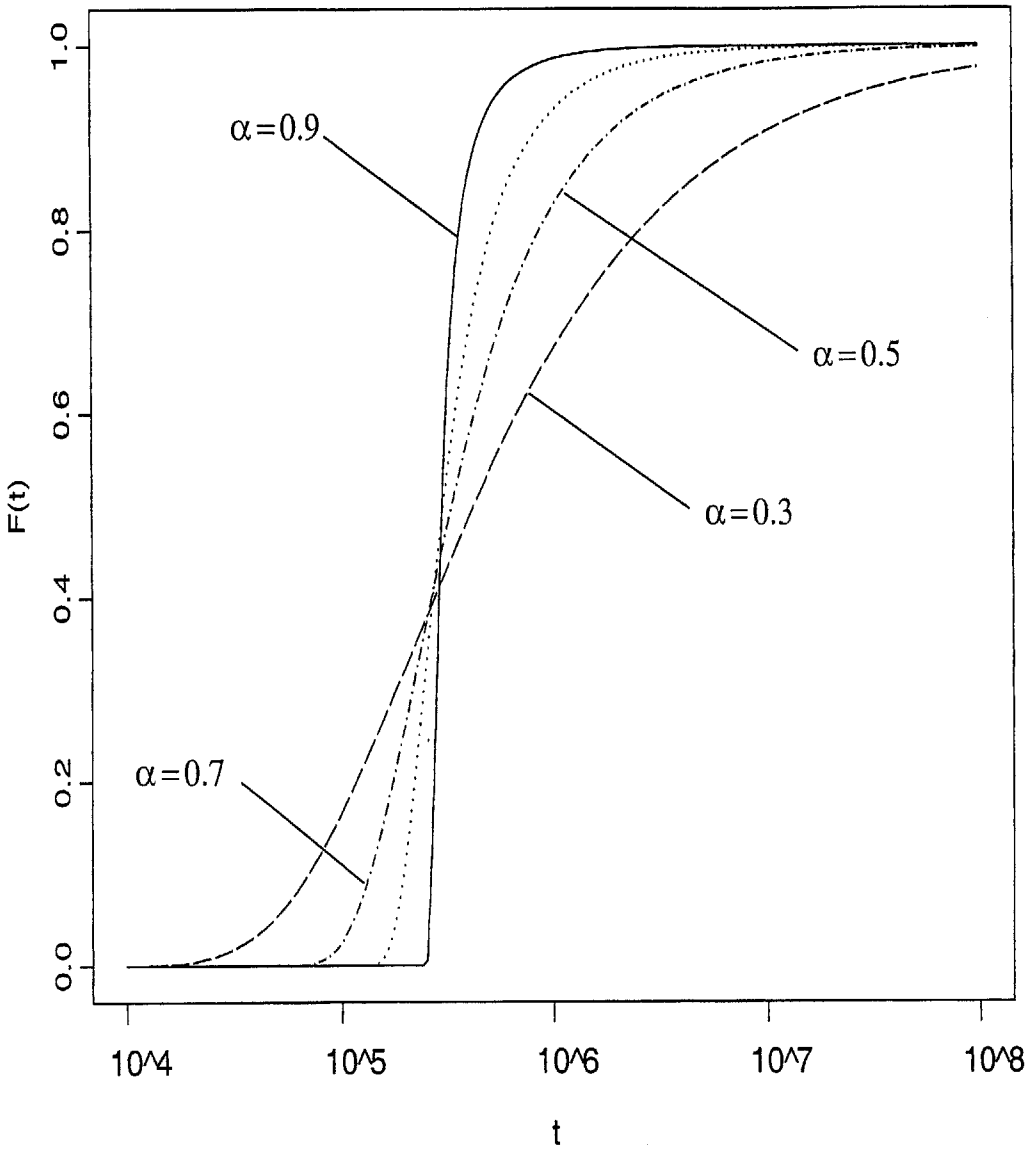

Figure 7.5- Cumulative FPTD for $0 < \alpha < 1$ for the CTRW model

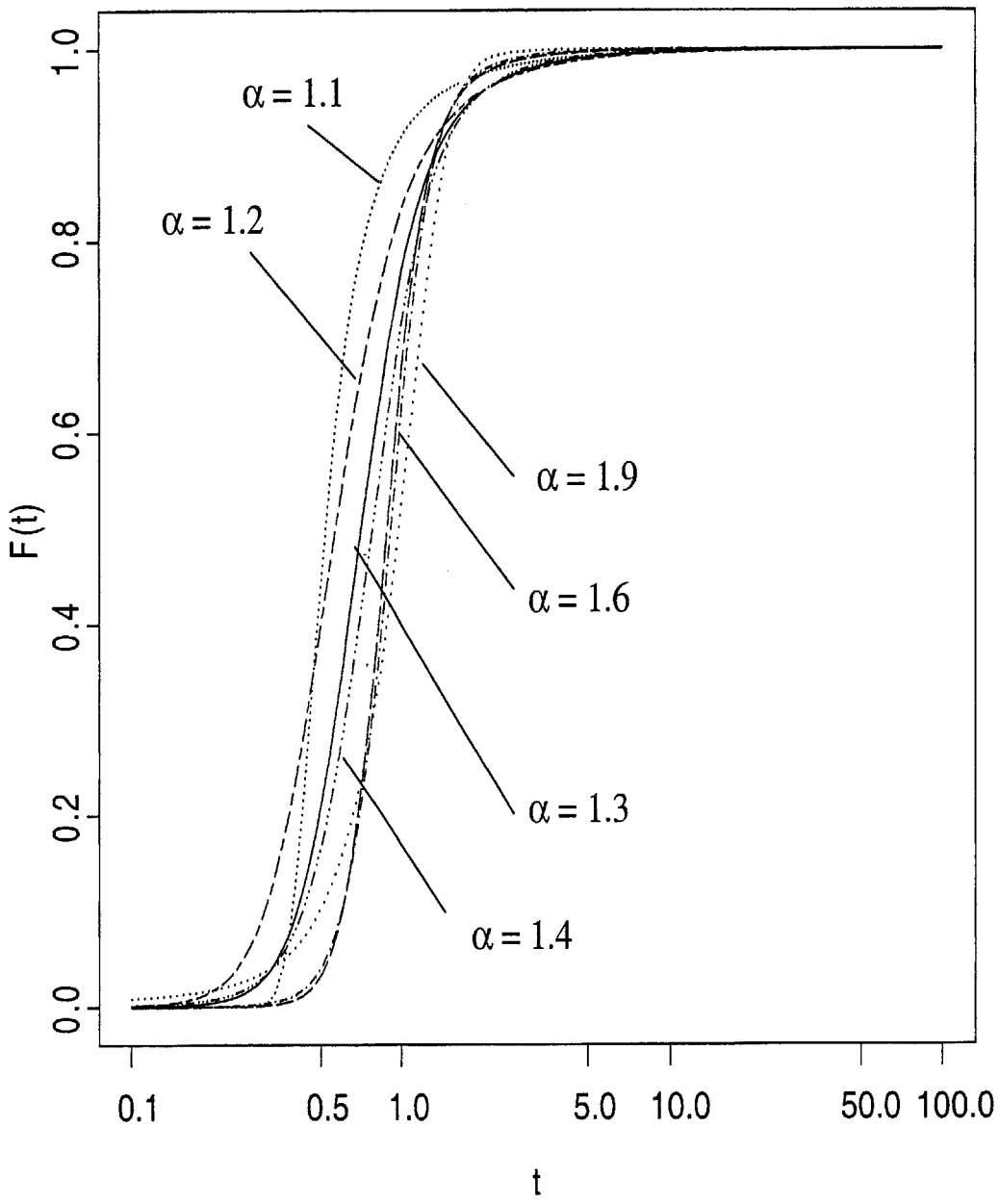

Figure 7.6 - Cumulative FPTD for $1 < \alpha < 2$ for the CTRW model

7.4 Scaling properties of the Velocity Field

For an isotropic lognormal field that has been developed to a finite resolution r, i.e. when $K(\underline{x}) = K_r(\underline{x})$ with a spectral density

$$S_{\ln(K)}(\underline{k}) = \left(\frac{2}{S_D} C_K\right) k^{-D} \qquad k_o \le k \le k_{max}$$

where k is the amplitude of the wavenumber vector $\underline{k}$, C_K is the codimension parameter that determines the variability of the K field and S_D is the surface area of a D-dimensional sphere.

Ignoring the rotations, the associated velocity field $\underline{V}_r(\underline{x})$ has been found to possess the following scaling relation with good approximation

1. Bare point velocities: $\underline{V}_{r_l}(\underline{x}) \overset{d}{=} \gamma_{r_l} . B_{r_l} . \underline{V}_r(r_l \underline{x}) \quad r, r_l \ge 1$

2. Bare average velocities: $\overline{\underline{V}}_{r_l}(\Omega) \overset{d}{=} \gamma_{r_l} . B_{r_l} . \overline{\underline{V}}_r(r_l \Omega)$ (7.39)

where $\gamma_{r_l} < 1$ is a deterministic non-conservation factor, $\overline{\underline{V}}_r(\Omega)$ is the average of $\underline{V}_r(\underline{x})$ inside the region Ω and B_{r_l} is a lognormal random variable with the following parameters:

$$\begin{cases} E\left[\ln\left(B_r\right)\right]=\left[\dfrac{D-4}{D(D+2)}-1\right]C_K \ln(r) \\ Var\left[\ln\left(B_r\right)\right]=\dfrac{2\left(D^2-1\right)}{D(D+2)}C_K \ln(r) \end{cases} \tag{7.40}$$

For partially dressed velocity fields, one can assume in approximation that a scaling relation similar to the above equation applies to the partially dressed average velocity $\overline{V}$ along flow lines. This means that

$$\overline{V}(\Delta)\overset{d}{=}B_r'.\overline{V}(r\Delta) \tag{7.41}$$

where Δ is a flow line segment and B_r' is a lognormal random variable with the following parameters.

$$\begin{aligned} E\left[\ln\left(B_r'\right)\right]&=\left[\frac{D-4}{D(D+2)}-1\right]C_K \ln(r) \\ Var\left[\ln\left(B_r'\right)\right]&=\frac{2\left(D^2-1\right)}{D(D+2)}C_K \ln(\gamma r/\Delta) \end{aligned} \tag{7.42}$$

where γ is a factor that was introduced to account for the variability of the flow field when r = 1. It has been found through simulation that $\gamma \approx 1+2C_K$.

The scaling of slowness vector (inverse velocity fields) is considered next $\underline{S}(\underline{x})=\left[1/V_1(\underline{x}),...,1/V_D(\underline{x})\right]$, where D is the spatial dimension. It follows from Eq. (7.41) that

$$(i)\ \underline{S}_{r_1}(\underline{x})\overset{d}{=}\frac{1}{\gamma_{r_1}}.\frac{1}{B_{r_1}}.\underline{S}_r(r_1\underline{x})$$

and (7.43)

$$(ii)\ \bar{\underline{S}}_{r_1}(\Omega)\overset{d}{=}\frac{1}{\gamma_{r_1}}.\frac{1}{B_{r_1}}.\bar{\underline{S}}_r(r_1\Omega)$$

In the partially dressed case, the $\underline{S}$ field is conservative in the mean. By analogy with the velocity, one may expect that when the rotations are ignored then the following approximate scaling relation will hold

$$\bar{\underline{S}}(\Omega)\overset{d}{=}\frac{\left[1/B_r'\right]}{E\left[1/B_r'\right]}.\bar{\underline{S}}(r\Omega)\overset{d}{=}B_r'.\bar{\underline{S}}(r\Omega) \qquad (7.44)$$

This equation has been validated numerically in Chapter 6.

Assuming that the above equation holds along flow lines, then

$$\bar{S}(\Delta) \overset{d}{=} B_r' . \bar{S}(r\Delta)$$

where B_r' has the properties of Eq. (7.42).

The first passage time distribution and the mean plume concentration depend on the marginal distribution of $\bar{S}(\Delta)$. If the time for a generic particle to travel a distance Δ along a flow line is denoted as T_Δ, then this time is related to the average slowness in Δ as

$$T_\Delta = \int_0^\Delta \frac{dx}{V(x)} = \Delta . \bar{S}(\Delta) \tag{7.45}$$

Taking the log of the left and right hand side of Eq. (7.45) one obtains

$$\ln(T_\Delta) = \ln(\Delta) + \ln(S_\Delta) \tag{7.46}$$

Hence the mean and variance of $\ln(T_\Delta)$ are

$$\begin{cases} E[\ln(T_\Delta)] = \ln(\Delta) + E[\ln(S_\Delta)] \\ Var[\ln(T_\Delta)] = Var[\ln(S_\Delta)] \end{cases} \tag{7.47}$$

And the distribution of T_Δ is

$$P(T_\Delta < t) = P\left(\Delta \bar{S}(\Delta) < t\right) = P\left(\bar{S}(\Delta) < t/\Delta\right)$$

$$F_{T_\Delta}(t) = F_{\bar{S}(\Delta)}(t/\Delta)$$

Figures 7.7 and 7.8 show the probability and cumulative distribution functions (PDF and CDF) for the slowness and first passage times respectively. The plots show the decrease in variance of slowness and the first passage time as distance from the point of injection Δ increases. In reality, the variance of FPTD increases as Δ increases as can be seen from Eq. (7.45). The transformation into log-space conceals this increase in the variance of FPTD because of the discarded Δ term in Eq. (7.47). The increase in the variance of FPTD does not go on indefinitely as can be seen in Figs. 7.10a and 7.10b. The variance of the FPTD for the flow with $C_K = 0.1$ increases up to a distance (Δ / k_o) of 0.7 and starts decreasing while the FPTD for the flow with $C_K = 0.3$ increases up to a distance of 0.9. The decrease in the variance of the FPTD at long travel distances is a result of the truncated spectrum of log-conductivity used in obtaining the distribution of the slowness. Thus, the large-scale fluctuations of S are not totally accounted for in the model. From Fig. 4.1 we see that between the line perpendicular to the k_o axis and the spectrum of $F = \ln(K)$, one can add a significant amount of variance to the velocity or slowness spectrum to account for the large-scale fluctuations in S. This additional component will eliminate the decrease in the variance of FPTD at large travel distances.

Another insight into why the FPTD variance decreases at long travel distances can be gained from sampling theory (see for example, Oppenheim et al., 1989 pages 109-

110). If the flow paths are idealized as sine functions (see Fig. 7.11a) and we sample the slowness or velocity at intervals of Δ, then a plot of the variance of the mean velocity $\overline{V}$ or mean slowness $\overline{S}$ as a function of Δ is shown in Fig. 7.11b. From this figure we see that the variance of $\overline{V}(\Delta)$ and $\overline{S}(\Delta)$ are not monotonic decreasing functions of Δ. Consequently, the variance of FPTD, which is a product of Δ^2 and $\mathrm{Var}[S(\Delta)]$ is not a monotonic increasing function of Δ.

The first passage time distribution can be used to derive the mean plume concentration.

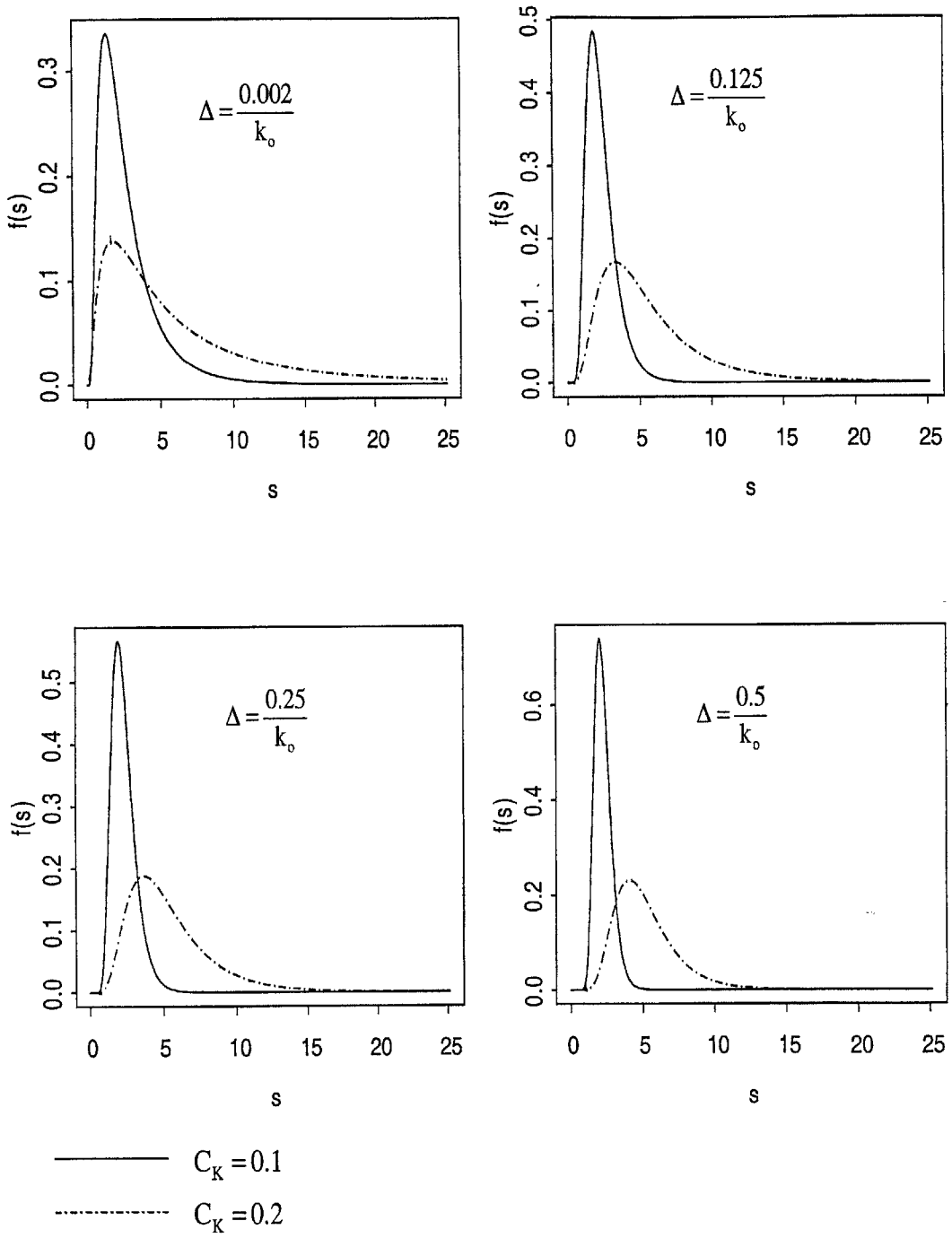

Figure 7.7a - PDF of Slowness for CK = 0.1 and 0.2, ko = 1 and kmax =512

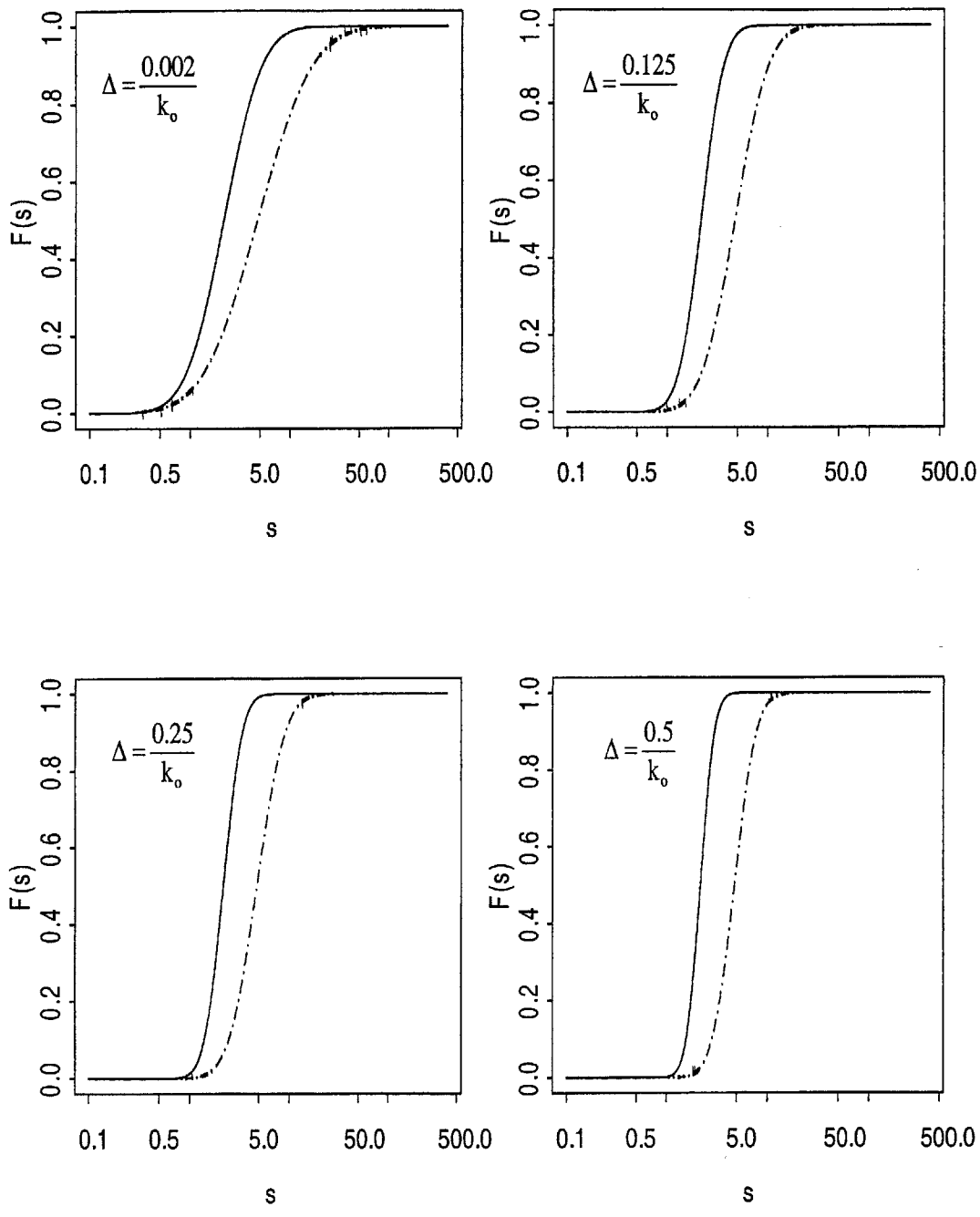

Figure 7.7b - CDF of Slowness for C_K = 0.1 and 0.2, k_o = 1 and k_{max}=512

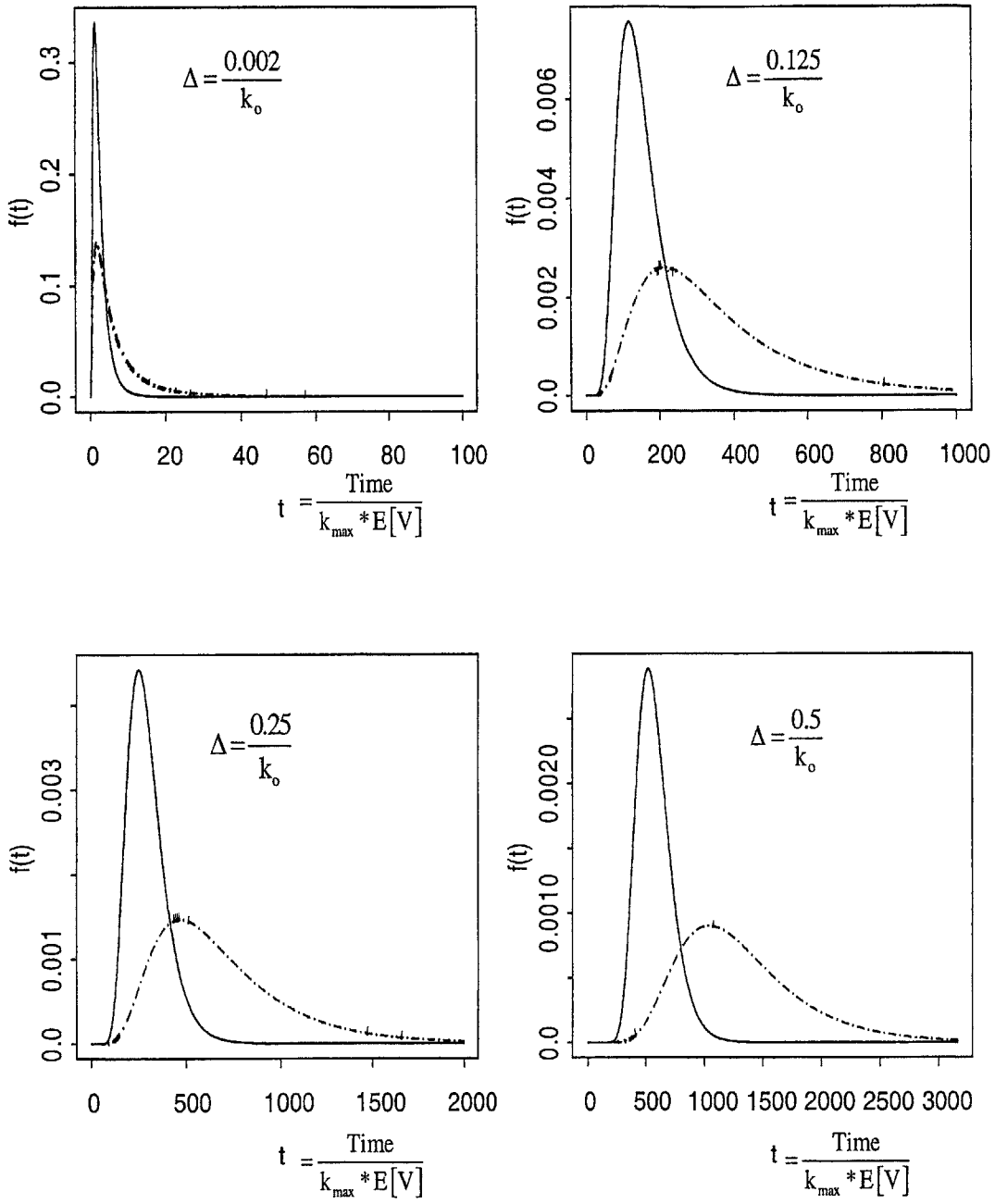

Figure 7.8a - PDF of FPTD for CK = 0.1 and 0.2, $k_o = 1$ and $k_{max} = 512$

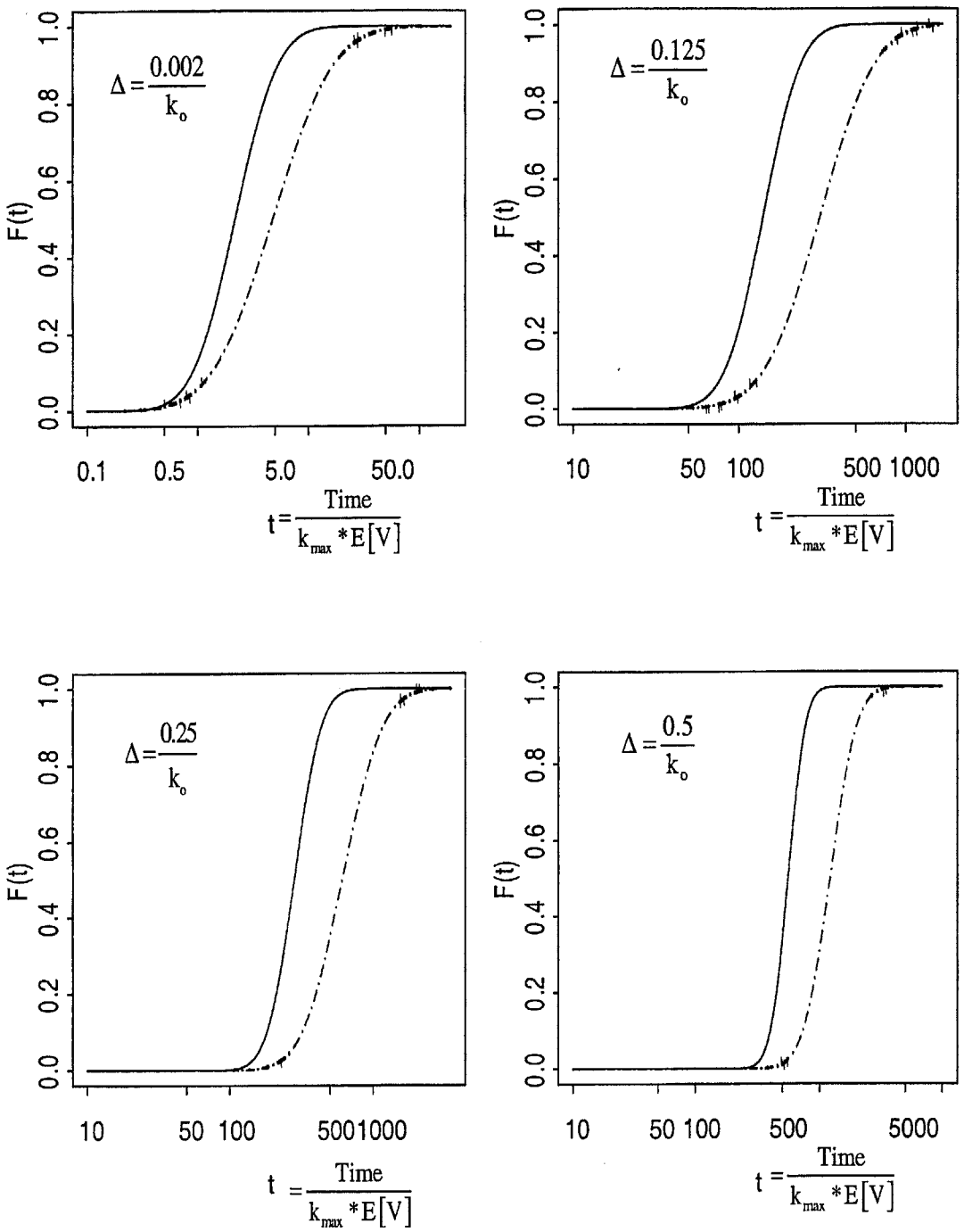

Figure 7.8b - CDF of FPTD for CK = 0.1 and 0.2, ko=1 and kmax = 512

Mean Plume Concentration

For the mean plume concentration, denote by $X(t)$ the location at time t of a particle released at x = 0 at time 0. Then

$$\text{(i)}\ F_{X(t)}(x) = P[X(t) < x] = P[T_x > t]$$

$$= P[\ln T_x > \ln t] = \Phi\left(-\frac{\ln t - m_{\ln T_x}}{\sigma_{\ln T_x}}\right) \qquad (7.48)$$

$$\text{(ii)}\ F_{X(t)}(x) = 1 - F_{S(x)}(t/x)$$

Figure 7.9 shows the PDF and CDF for the mean plume concentration at various fixed times for $C_K = 0.1$ and 0.2. For large times and the lower value of C_K the plume tends towards a Gaussian distribution. As the mean travel distance $E[x] \to 1$,

$E[T(1)] = E[S] = \frac{1}{E[V_\infty]}$, where $E[V_\infty]$ is the asymptotic average velocity and is smaller than the average velocity of flow $E[V]$. Thus as $E[x] \to 1$ the average mobility of the solute decreases over time as the particles tend to be trapped in low-velocity areas.

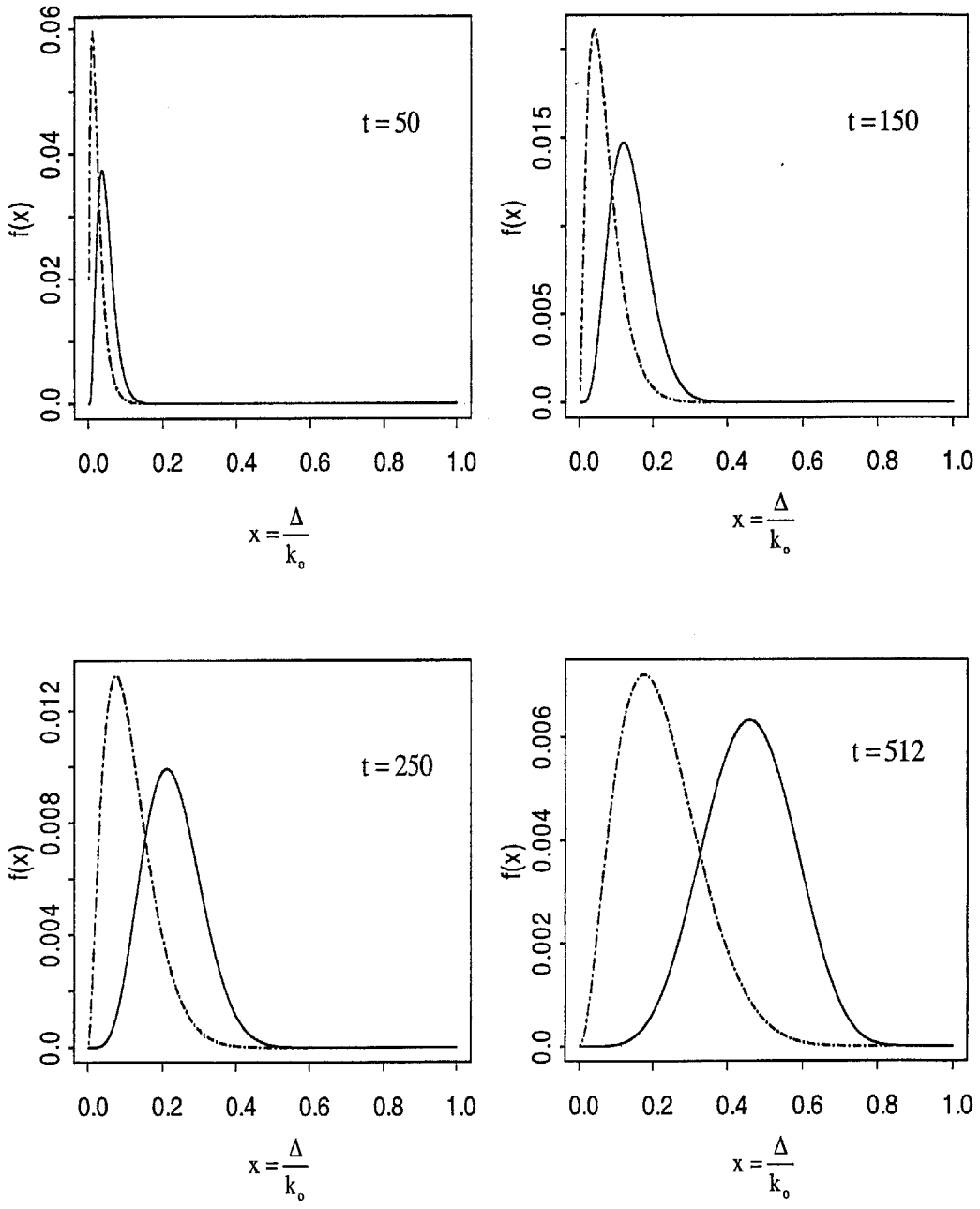

Figure 7.9a - PDF of particle location for $C_K = 0.1$ and 0.2, ko=1 and $k_{max} = 512$

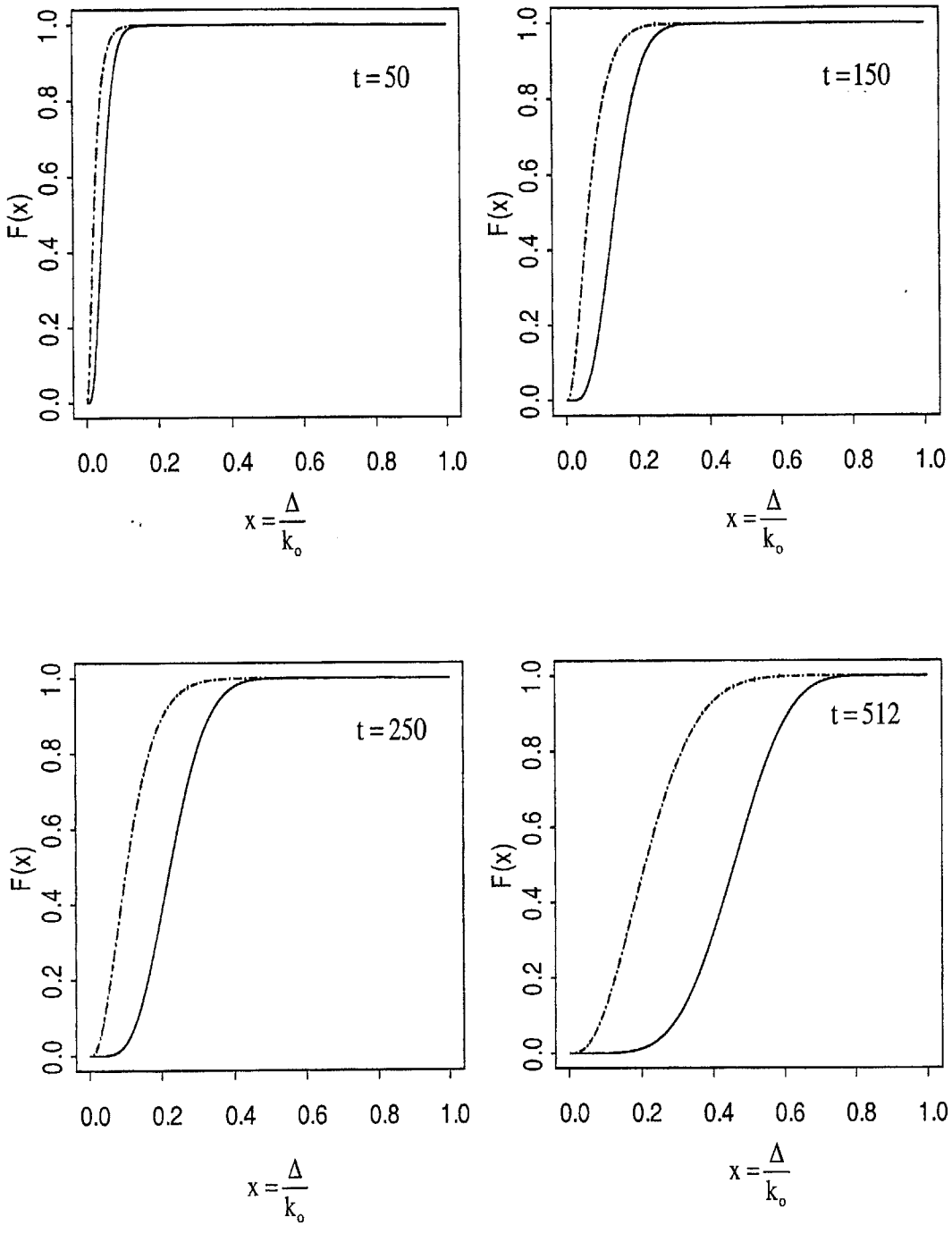

Figure 7.9b - CDF of particle location for $C_K = 0.1$ and 0.2, ko=1 and kmax=512

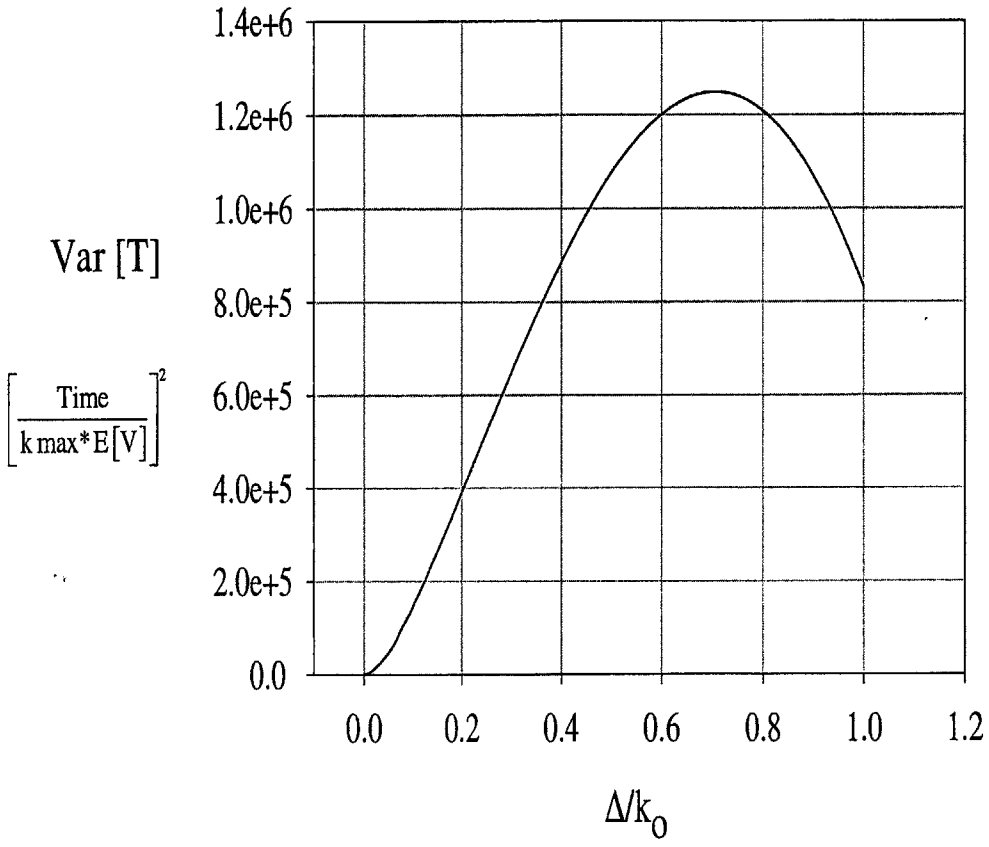

Fig. 7.10a - Variance of the first passage time for a flow field with $C_K = 0.1$, $k_{max} = 1024$, $k_o=1$

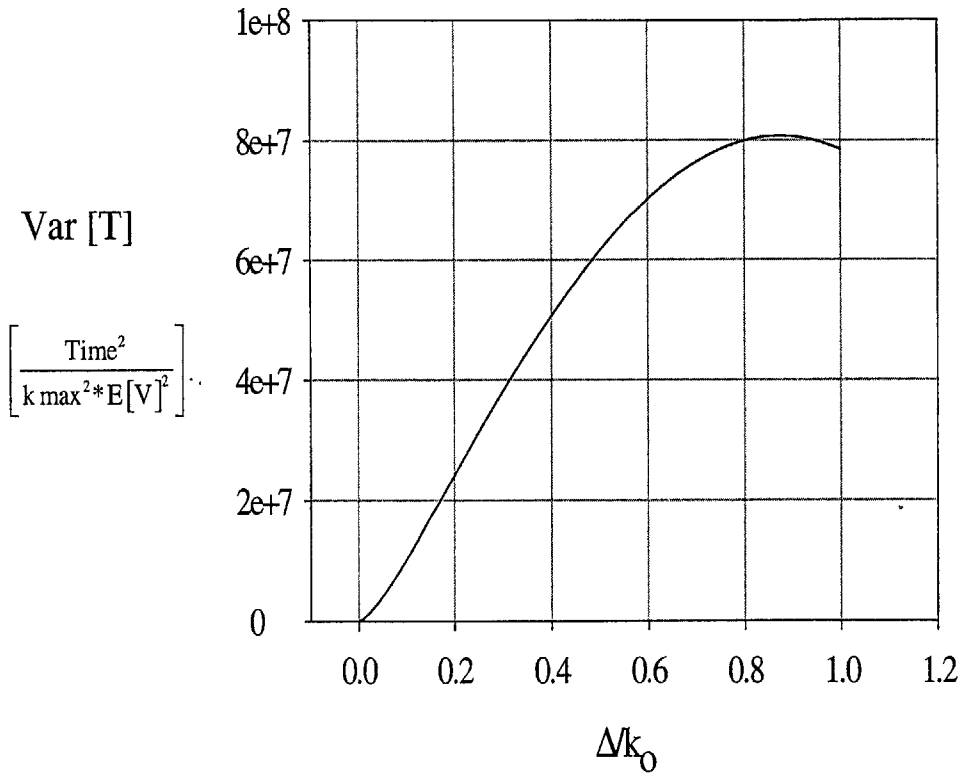

Fig 7.10b - Variance of the first passage time for a flow field with C_K = 0.3, kmax = 1024, ko=1

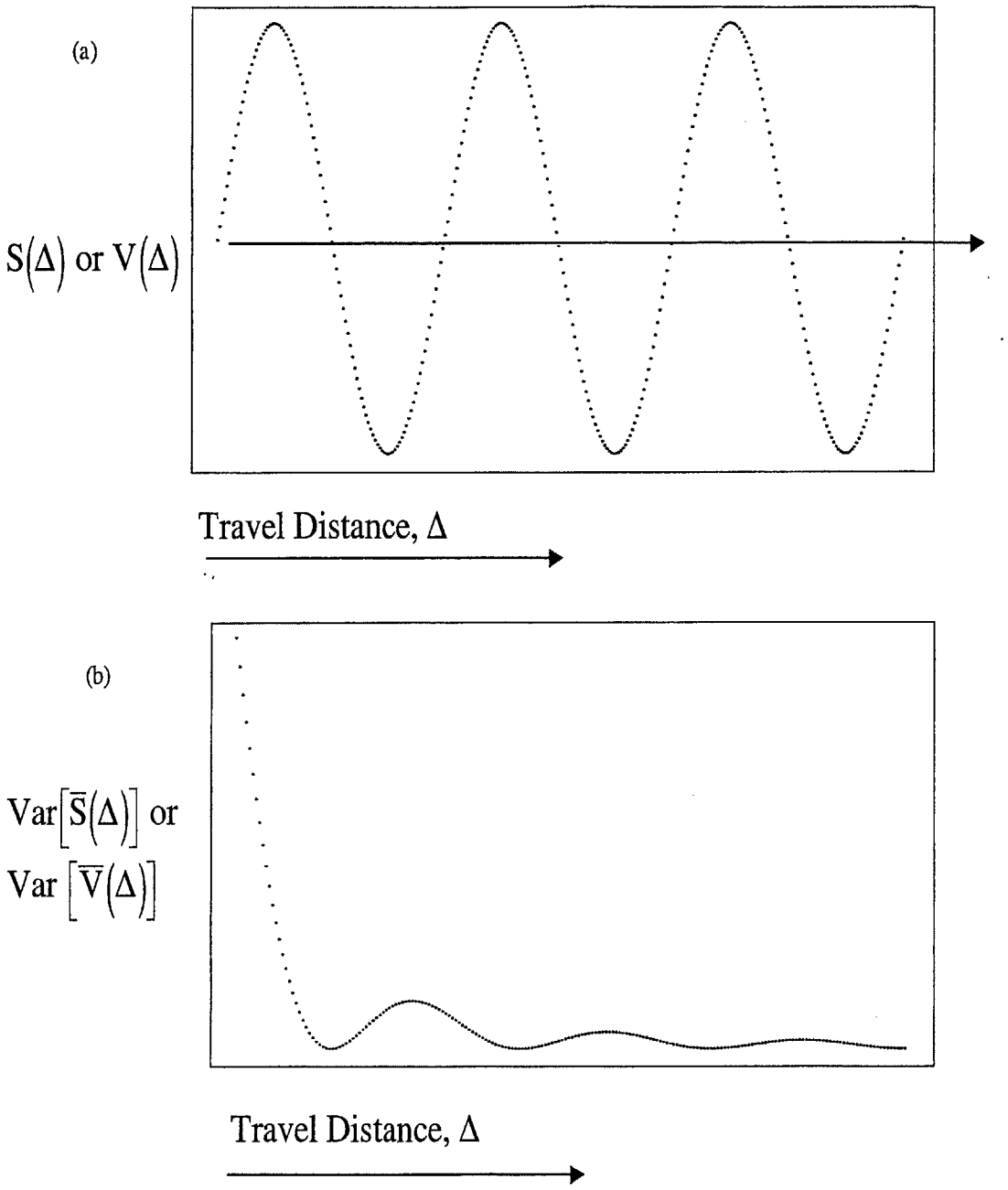

Fig 7.11 - (a) The flow path idealized as a sine function (b) Variance of the mean slowness at different sampling intervals along the sine curve in (a).

7.5 Comparison of the Nonlinear Theory Model, the CTRW and the Two-Phase Models.

In this section, the nonlinear theory model is compared with the CTRW and the two-phase models. Three types of comparisons are made:

1. First, a comparison of the three models is made with some "real world" data in Figures 7.12 and 7.13. In Figure 7.12, the models are fitted to data obtained from the Mobile site by Huyakorn et al., 1986. The concentration data has a lognormal distribution and thus we see that the nonlinear and two-phase models provide a better fit to the data than the CTRW model. The CTRW model is particularly suitable for asymmetric distributions of FPTD as shown in Figs. 7.13. Figure 7.13 plots data from a flow cell by Silliman and Simpson (1986). The flow cell is two-phase packing consisting of fine and coarse sand that are arranged into two vertical blocks through water flows horizontally. The CTRW and the two-phase models provide a better fit to the data than the NL model, and show the suitability of the CTRW and the two-phase model for asymmetric FTPD that result from inhomogeneous media.

2. Next, data obtained from numerical simulations of transport of a non-reactive solute in multifractal fields are compared to the NL and CTRW models. Data from these simulations are generated using the transport code described in Sec.

7.2. To compute the FPTD, transport was simulated in a flow field with $C_K = 0.1$ and at a distance of $0.12/k_o$ from the point of injection, the total amount of the solute C_{tm} that has transversed a distance of $0.12/k_o$ is computed. The ratio of C_{tm} to the total mass of the solute at various evolution times for the plume constitutes the FPTD. The FPTD of the numerical simulations shown in Fig.7.14 is average of seven FPTD curves. The CTRW and NL models are fitted to the data in Fig. 7.14 through nonlinear regression and are shown in Fig. 7.14. Both models provide a good fit to the data. The CTRW model provides a better fit for the lower half of the breakthrough curves while the NL model provides a better fit for the upper half of the curves.

3. Finally, using the theoretical formulations of the NL theory in Eq. (7.47) the FPTD are computed for flow fields with $C_K = 0.04$ and 0.4 for travel distances $0.001/k_o$ and $0.1/k_o$. These plots are shown in Figs. 7.15 and 7.16 and are compared with the best fit of the CTRW model. The CTRW model was initially fit to the breakthrough curve in the near field to obtain the α value. The CTRW model assumes the value of α to be constant for a given flow field. Hence, the α value obtaining through regression in the near field is used to compute the FPTD curve in the far field. From Figures 7.15 and 7.16, we see that the CTRW model provides a good fit to the data in the near field. However, in the far-field, the upper parts of the CTRW curves show a slight deviation from the NL FPTD curves. This is because the transport is non-Fickian: the variance of the FPTD

changes with travel distance. This feature is captured by the NL model, whereas the CTRW models the transport with a constant variance.

These comparisons show in what situations a CTRW, two-phase or the NL model may be appropriate. The CTRW model determines parameters by fitting to breakthrough curves obtained in field experiments. The model parameters are then used in predicting the FPTD at different locations in the flow field. The two-phase model, like the CTRW model is Fickian and is suitable for modeling asymmetric Fickian transport. The CTRW is particularly useful for modeling transport in inhomogeneous media. The CTRW and two-phase models are not suitable for modeling non-Fickian transport. When the flow field has a multfractal hydraulic conductivity, with known spectral properties (e.g. C_K, k_o and k_{max}), the NL model can be used to predict how a solute will evolve. The parameters of the NL model have a direct connection with the physical properties of the flow field. The CTRW model is a conceptual model whose parameters cannot be determined from the material properties in a flow domain.

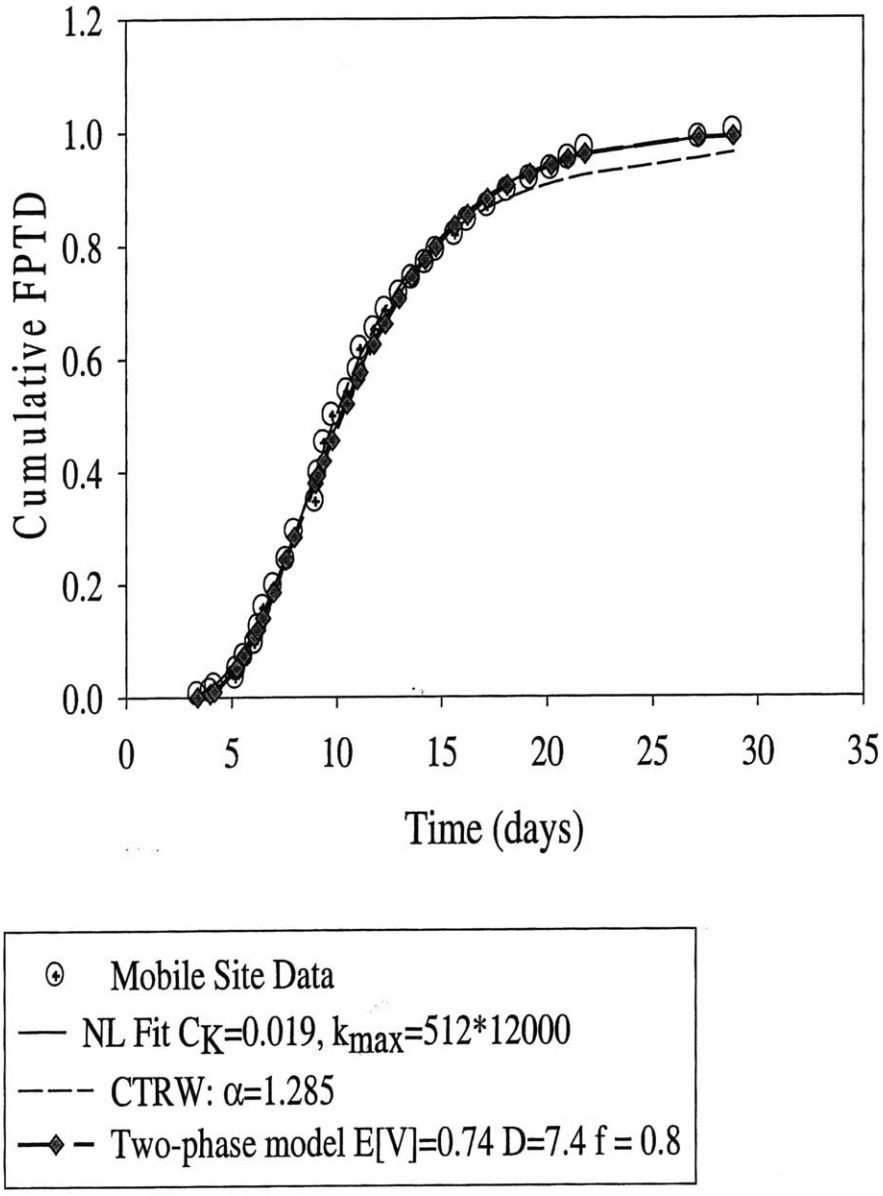

Figure 7.12 - Comparison of models and their fit to the Mobile Site data by Huyakorn et al. (1986)

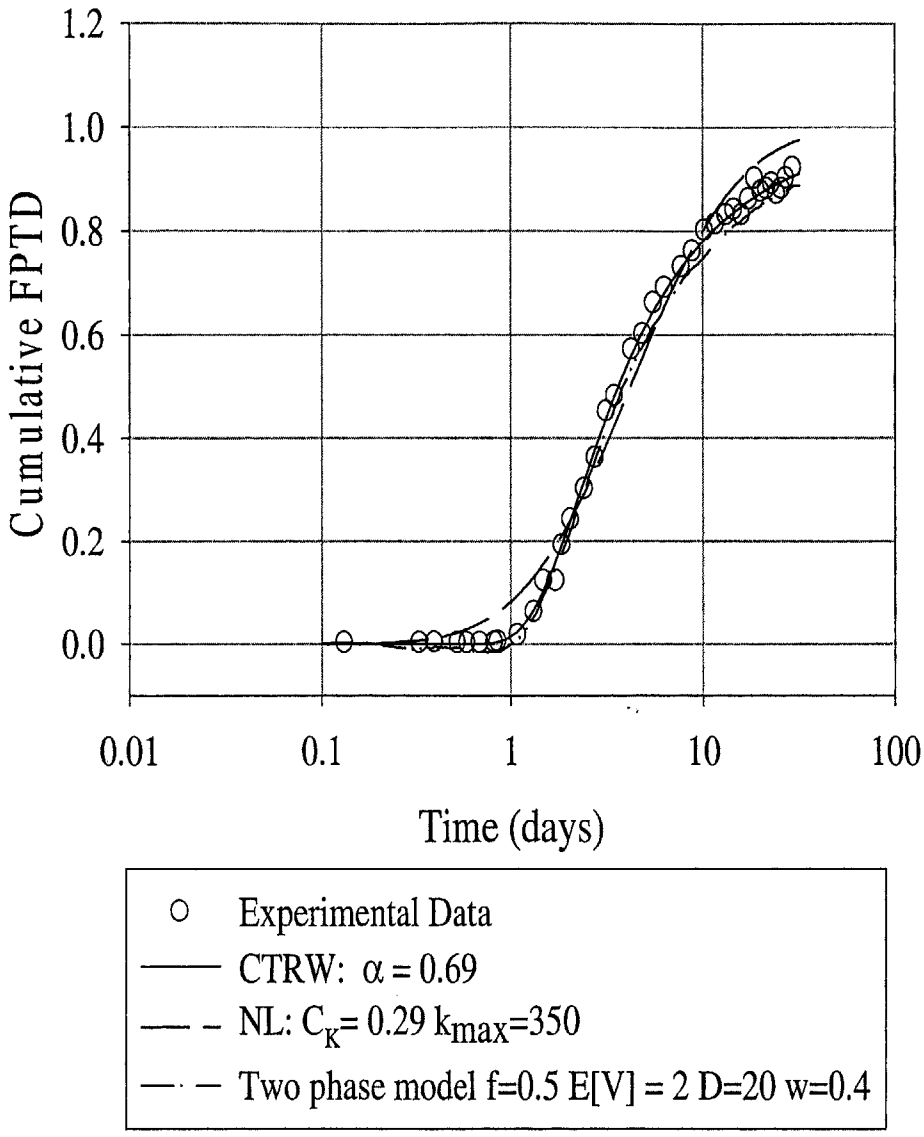

Figure 7.13 - Comparing the models to experimental data from Berkowitz and Scher (2000)

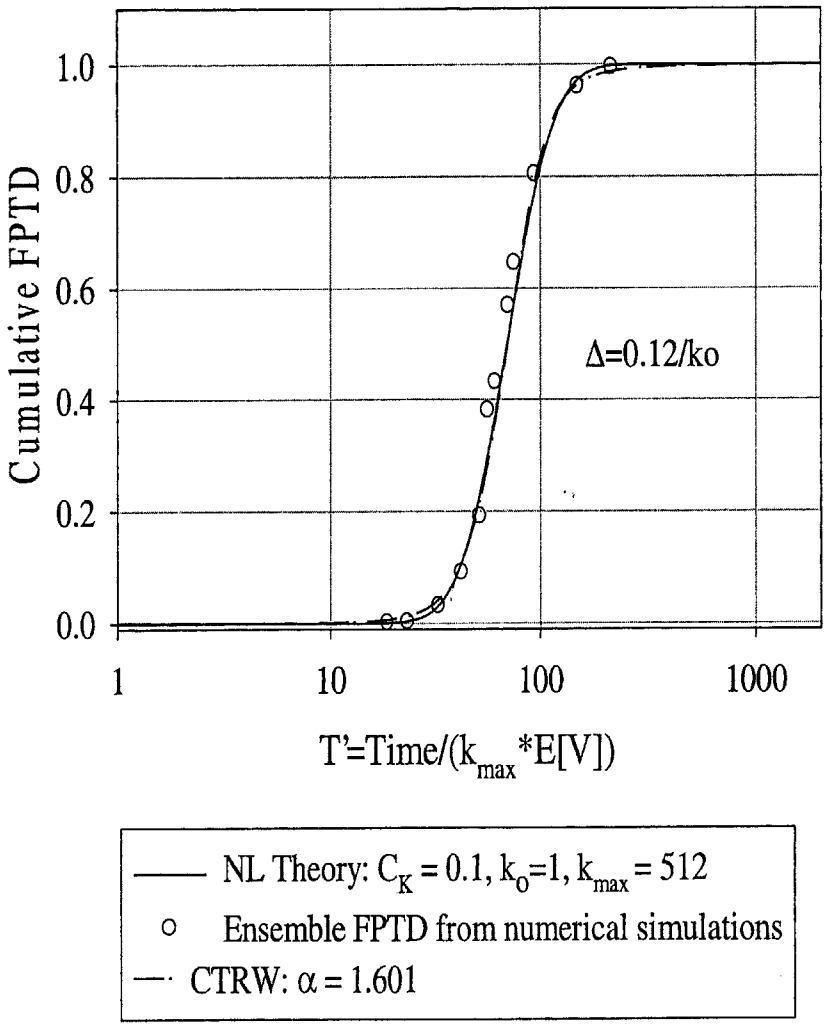

Figure 7.14 - FPTD for the CTRW and NL models fitted to data obtained from numerical simulations in fields with multifractal hydraulic conductivity with $C_K = 0.1$, $k_o = 1$ and $k_{max} = 512$

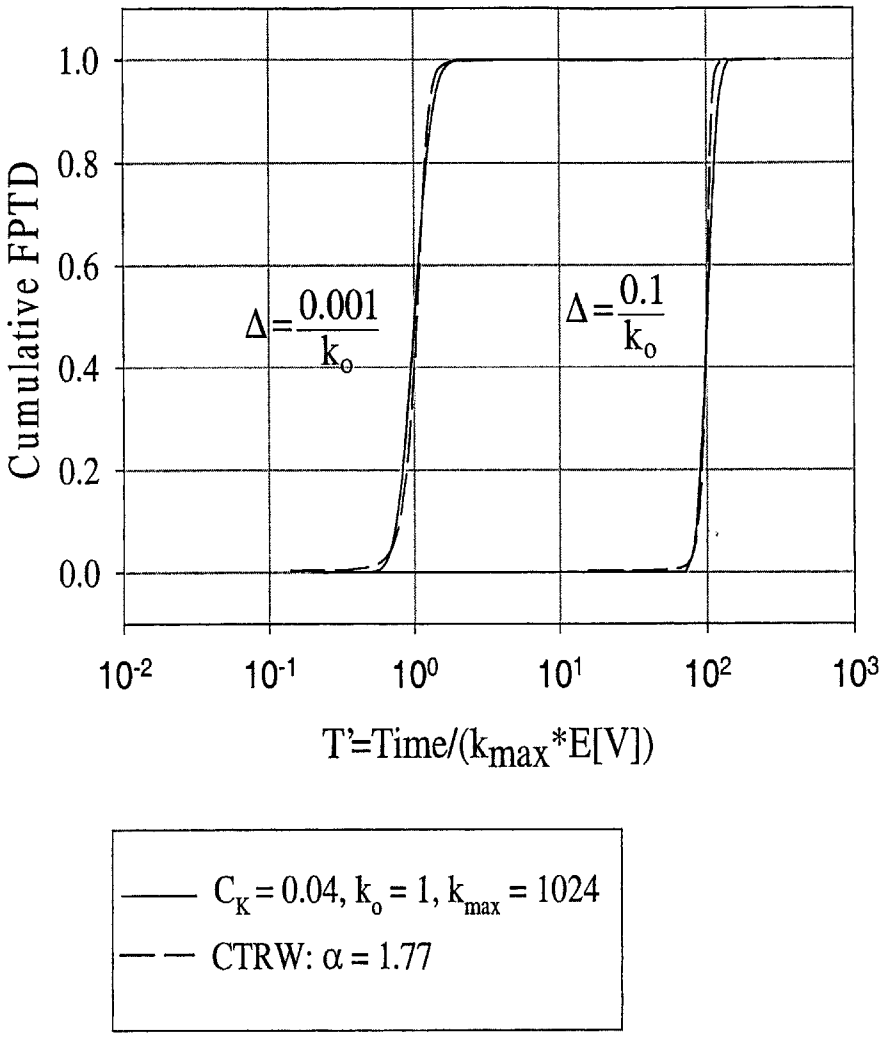

Figure 7.15 - Comparison of the CTRW and nonlinear theory (NL). The CTRW model was fitted to the NL model in the near field and using the the fitted parameters was compared to the NL model in the far field.

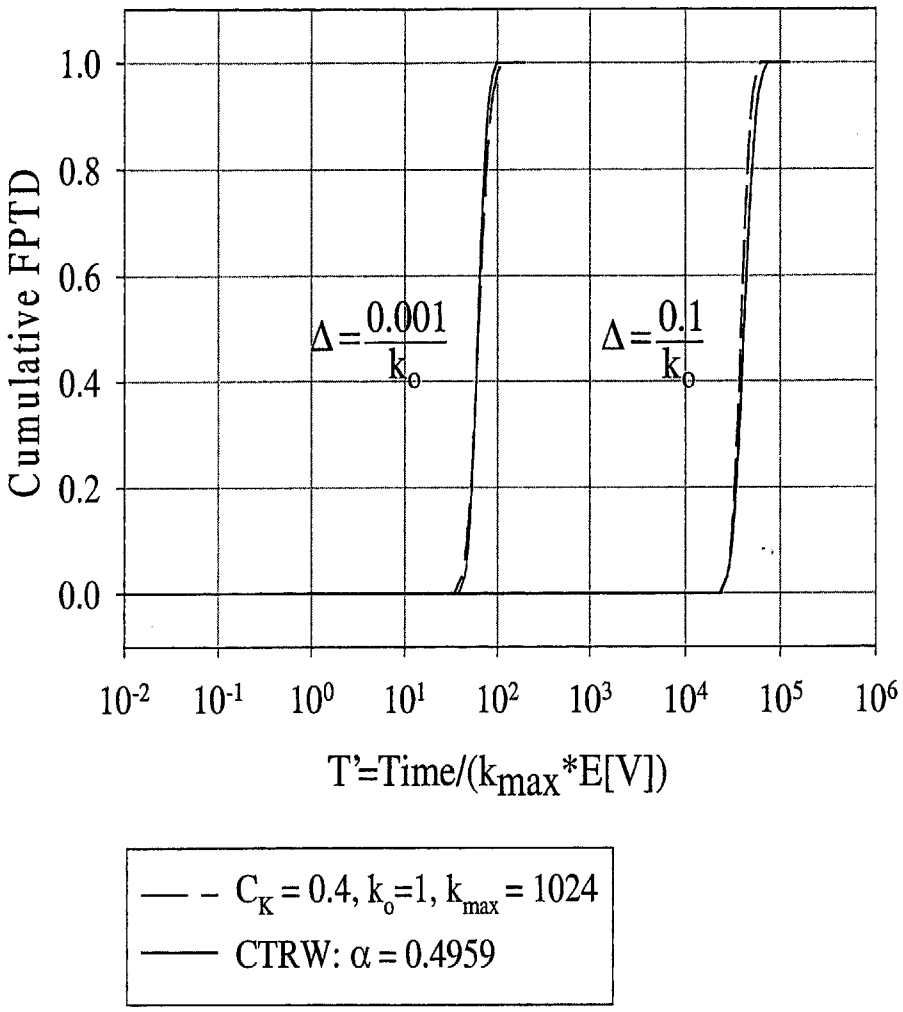

Figure 7.16 - Comparison of the CTRW and nonlinear theory (NL). The CTRW model was fitted to the NL model in the near field and using the fitted parameters was compared to the NL model in the far field.

Scaling of Concentration Variance

For sub-diffusive and superdiffusive transport, the plume concentration has a scaling described by

$$\left\langle \sigma_c^2(t) \right\rangle \sim t^{\lambda} \tag{7.49}$$

Assuming a constant mean flow, Eq. (7.49) can be written as

$$\left\langle \sigma_c^2\left(\overline{x}\right) \right\rangle \sim \overline{x}^{\lambda}$$

where λ is different from 2. For $\lambda > 2$, the transport is described as superdiffusive [Bershadskii, 1999]. However transport in heterogeneous porous media, has been found to possess $1 \le \lambda < 2$ [Arya et al, 1985, Hewett, 1986, Neuman, 1990 among others]. Table 7.3 provides some values of λ obtained by various authors. Using Eq. (7.48), the concentration variances for various times were computed. These computations are shown in Fig. 7.17. The computations show that for multifractal media $\lambda \simeq 2 - C_K$. Ensemble macrodispersivity computations in Figs. 7.1a and 7.1b agree with the computations in Fig. 7.17. Slopes of the ensemble longitudinal macrodispersivities for small travel distances are exactly $1 - C_K$ and have values slightly above $1 - C_K$ for long travel distances. Thus, results of the ensemble macrodispersivities in Fig. 7.1 support the scaling behavior of the concentration moments in Fig. 7.17.

Table 7.3 – Values of λ obtained by various authors

Author	λ value
Arya et al. [1985]	$1<\lambda<2$
Philip [1986]	$1<\lambda<2$
Neuman [1990]	$\lambda=1.75$
Hewett [1986]	$1.4<\lambda<1.6$

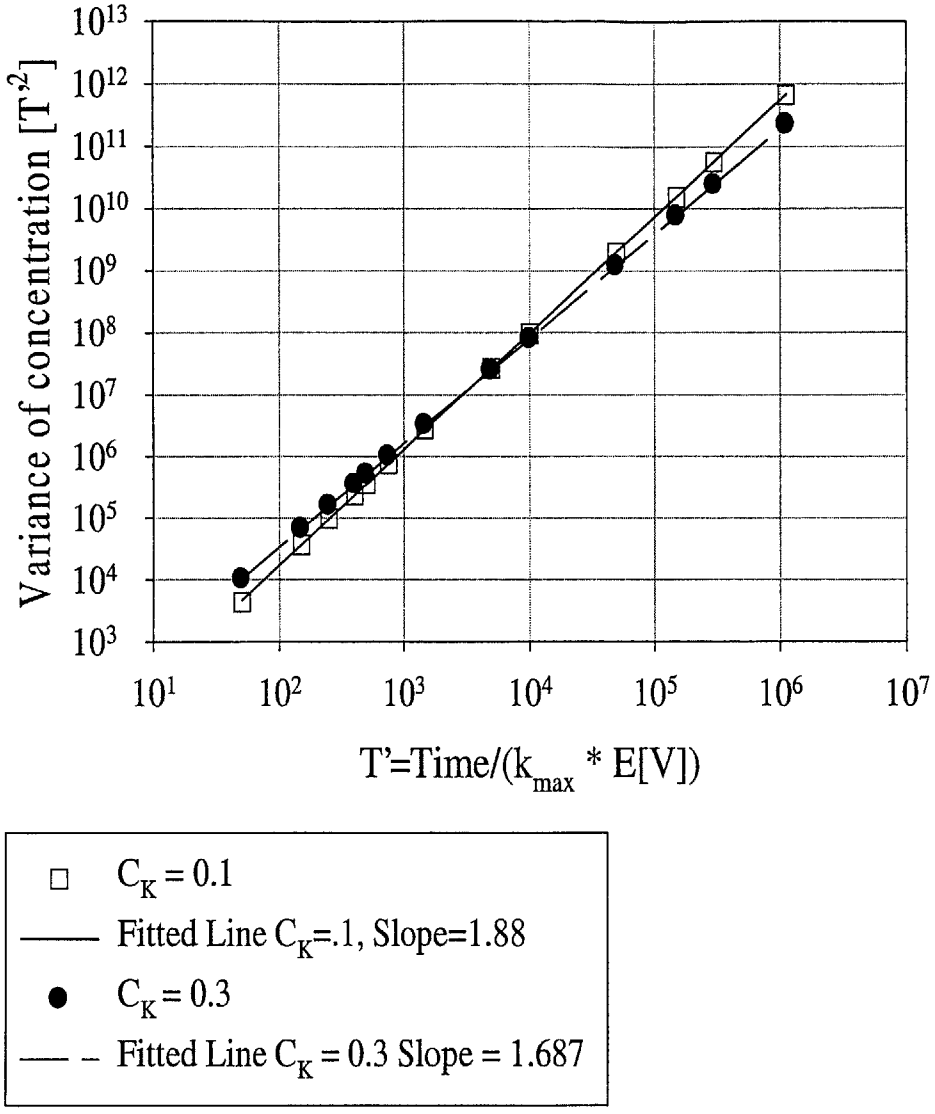

Figure 7.17 - Concentration variance versus time

CHAPTER 8: FLOW IN AQUIFERS WITH HOMOGENEOUS ANISOTROPIC LOGNORMAL HYDRAULIC CONDUCTIVITY FIELDS.

Introduction

This chapter extends previous work on flow through random porous media for which the hydraulic conductivity K was assumed isotropic, lognormal and multifractal to include anisotropic lognormal multifractal K fields. For anisotropic K fields, the material properties vary with direction. A commonly studied example of an anisotropic K field is the stratified aquifer, for which the K perpendicular to the bedding is different from that parallel to bedding [see for example Gelhar, 1993]. Usually the K field for anisotropic media is expressed as a second order symmetric tensor [Bear, 1972]

$$\underline{K} = \begin{bmatrix} K_{11} & K_{21} & K_{31} \\ K_{12} & K_{22} & K_{32} \\ K_{13} & K_{23} & K_{33} \end{bmatrix}$$

with the property that $K_{ij} = K_{ji}$ and $i, j = 1,\ 2$ and 3. In general, the flow velocity is at an arbitrary angle with respect to any normal to any plane, so that it can be decomposed into three components on each plane. For example, the specific flow in the plane normal to the x_2 axis is

$$q_{21} = K_{21}\frac{\partial h}{\partial x_2}$$

$$q_{22} = K_{22}\frac{\partial h}{\partial x_2}$$

$$q_{23} = K_{23}\frac{\partial h}{\partial x_2}$$

where the first subscript refers to the plane and the second subscript refers to the direction of flow. Similarly, there are three components of flow for the x_1 and x_2 axes. The total flow in the x_2 direction is given by:

$$\begin{aligned} q_{x_2} &= q_{12} + q_{22} + q_{32} \\ &= K_{12}\frac{\partial h}{\partial x_1} + K_{22}\frac{\partial h}{\partial x_2} + K_{32}\frac{\partial h}{\partial x_3} \end{aligned}$$

Current approaches (e.g Gelhar and Axness, 1983; Neuman, 1994 and Ababou, 1995) in deriving the statistical properties of flow through anisotropic porous media obtain the expected specific flow via averaged expressions of Darcy's law (Eq. 1.1). The expected specific flow is

$$E[q_i] = \overline{K}_{ij} J_j \qquad (8.1)$$

where $\overline{K}_{ij}$ is the effective permeability tensor which is also denoted as K_{eff}. The approach of Gelhar and Axness is reviewed in Sec. 2.3. For anisotropic media, the

integral $F_{ij} = \int_{\underline{k}} \frac{k_i k_j S_{ff}(\underline{k})}{k^2} d\underline{k}$ in Eq. 2.41 is evaluated using the anisotropic version of the log conductivity spectrum S_{ff}. As an example, a hydraulic K field with an exponential covariance function has a log-conductivity spectrum

$$S_{ff}(\underline{k}) = \frac{\sigma_f^2 \lambda_1 \lambda_2 \lambda_3}{\pi^2 \left(1 + \lambda_1^2 k_1^2 + \lambda_2^2 k_2^2 + \lambda_3^2 k_3^2\right)}$$

where λ_i is the correlation distance in the x_i direction. Gelhar and Axness (1983) have evaluated expressions for a stratified medium with isotropy on the plane of stratification $(\lambda_1 = \lambda_2 > \lambda_3)$, a 2D anisotropic field obtained by taking $\lambda_3 \to 0$ and the general case $\lambda_1 \neq \lambda_2 \neq \lambda_3$ for which the integrals were evaluated numerically. Ababou (1995) accounts for anisotropy by modifying Matheron's expression for K_{eff} (Eq. 2.49) to include the correlation lengths

$$K_{eff}^{ii} = K_o \exp\left(\sigma_f^2 \left[\frac{1}{2} - \frac{1}{D} \frac{\lambda_h}{\lambda_i} \right] \right) \quad i=1, 2, 3 \qquad (8.2)$$

where λ_h is the harmonic mean of the correlation lengths in the principal directions of anisotropy. Neuman proposes the same K_{eff} expression as Eq. 8.2 with β replacing $\frac{\lambda_h}{\lambda_i}$. Neuman does not however explain how the value of β can be determined.

Rajaram and Gelhar (1995) presented an expression for S_{ff} for an anisotropic K field that is has some form of scale invariance (fractional Gaussian noise fGn or fractional Brownian motion fBm)

$$S(\underline{k}) = C \Big/ \left(k_1^2 + k_2^2 + \mu k_3^2\right)^{(m+3)/2} \qquad 0 < m < 2 \tag{8.3}$$

where C is a constant and the wavenumber k_3 is scaled by the factor μ. Molz et al. (1997) obtain an expression similar to Eq. (8.3) for anisotropic fBm/fGn K fields of the form,

$$S(\underline{k}) = \frac{C k_3^{\alpha-1}}{\left(k_1^2 + k_2^2 + \left(\rho k_3^{\alpha}\right)^2\right)^{\beta/2}} \tag{8.4}$$

where C, α, β and ρ are constants. Molz et al. (1997) discuss different conceptual models for the anisotropic K field. For example, a fGn could characterize the vertical variations while the horizontal variations are described by fBm.

This chapter is organized as follows. In Sec. 8.1, the marginal distribution of the hydraulic gradient for fields with homogeneous anisotropic lognormal hydraulic conductivity is derived. Unlike the isotropic case, no closed-form solutions are obtained. However, expressions for the spectral density and covariance of the hydraulic gradient ∇H are obtained and these can be evaluated numerically. The complication with the anisotropic case arises from the characterization of the rotations of the ∇H vectors. These

vectors are not uniformly distributed as in the isotropic case but are dependent on the angle of inclination of the large-scale mean hydraulic gradient. The approach used in obtaining the results follow the renormalization method used in Chapter 4. We begin with the known deterministic values of ∇H under mean field conditions, when the hydraulic conductivity K is fixed to its mean value. Higher Fourier components are then progressively added to $F = \ln(K)$ and the corresponding effects on the distribution of ∇H are determined. The desired marginal distributions are obtained in the limit as the variance of F is totally accounted for. Sec. 8.2 presents an approximate scheme for dealing with geometric anisotropy.

8.1 MARGINAL DISTRIBUTION OF THE HYDRAULIC GRADIENT ∇H FOR HOMOGENEOUS ANISOTROPIC LOGNORMAL HYDRAULIC CONDUCTIVITY

Let Ω be a region in D-dimensional space where the hydraulic conductivity is an anisotropic multifractal field. The goal is to determine the marginal distribution of the hydraulic gradient $\nabla H(\underline{x}_o)$ at a generic point $\underline{x}_o$ of Ω, when Ω is subjected to a large-scale unit hydraulic gradient. For reasons of convenience, the point $\underline{x}_o$ at which the distribution of ∇H is sought is located at the center of Ω. The distribution of $\nabla H(\underline{x}_o)$ is obtained by solving a cascade of nested flow problems at increasing resolution r. At the coarsest level r = 1, the log-conductivity in Ω is $F_1 = 0$ and the hydraulic head and normal flow q_n on the boundary are equal to their spatial average values. This gives the mean field solution $\nabla H_1(\underline{x}_o) = -\underline{e}$ and $\underline{q}_1(\underline{x}_o) = -\underline{e}$, where $\underline{e} = [1,0,...,0]$ is the unit vector in the first coordinate direction. We then progressively increase the resolution r,

each time obtaining the hydraulic gradient $\nabla H_{r+dr}(\underline{x}_o)$ inside contracted regions of size Ω/r, centered at $\underline{x}_o$. This field is obtained by subjecting Ω/r to a mean large-scale hydraulic gradient equal to $\nabla H_r(\underline{x}_o)$, assuming that the log-conductivity inside Ω/r is $F_{r+dr}(\underline{x}) = F_r(\underline{x}_o) + F_{[r,r+dr)}(\underline{x})$. It is assumed that the quantities at resolution r, F_r and ∇H_r, are constants inside Ω/r and therefore are evaluated at $\underline{x}_o$, whereas $F_{[r,r+dr)}$ and $\nabla H_{[r,r+dr)}$ are allowed to vary spatially. In particular, one obtains the conditional distribution of $\nabla H_{r+dr}(\underline{x}_o) | \nabla H_r(\underline{x}_o)$. An attractive feature of this approach is that $\nabla H_r(\underline{x}_o)$ is a Markov process in the resolution parameter r. Therefore, the process is completely defined by its initial state $\nabla H_1(\underline{x}_o) = -\underline{e}$ for r = 1 and the conditional distribution $\nabla H_{r+dr}(\underline{x}_o) | \nabla H_r(\underline{x}_o)$. Using these initial conditions and conditional distribution, the marginal distribution of $\nabla H_r(\underline{x}_o)$ for any r and the desired asymptotic distributions of $\nabla H(\underline{x}_o) = \lim_{r \to \infty} \nabla H_r(\underline{x}_o)$ can be obtained. In addition, it is assumed that in spaces of dimension D >1, zero-mean high-frequency fluctuations of the head and flow along the boundary affect the hydraulic gradient and flow only in a narrow region close to the boundary. Details of the analysis are presented next.

To characterize the conditional random field $\nabla H_{r+dr}(\underline{x}_o) | \nabla H_r(\underline{x}_o)$ in a region of size Ω/r around $\underline{x}_o$, when the region is subjected to a large-scale mean hydraulic gradient $\nabla H_r(\underline{x}_o)$, one begins by rotating the coordinate axes such that the new x_1 axis has the direction of $-\nabla H_r(\underline{x}_o)$. Using a superscript R to denote all quantities in this rotated reference, we write $\nabla H_r(\underline{x}_o)$ and $\nabla H_{r+dr}(\underline{x})$ as

$$\begin{cases} \nabla H_r^R(\underline{x}_o) = -\left|\nabla H_r(\underline{x}_o)\right|\underline{e} \\ \nabla H_{r+dr}^R(\underline{x}) = -\left|\nabla H_r(\underline{x}_o)\right|\underline{e} + \nabla H_{[r,r+dr]}^R(\underline{x}) \end{cases} \tag{8.5}$$

where $\underline{e} = [1,0,...,0]$. Then the zero divergence flow equation in Ω/r is

$$\nabla^2 H_{[r,r+dr]}^R(\underline{x}) + \left[-\left|\nabla H_r(\underline{x}_o)\right|\underline{e} + \nabla H_{[r,r+dr]}^R(\underline{x})\right].\nabla F_{[r,r+dr]}(\underline{x}) = 0 \tag{8.6}$$

or

$$\nabla^2 H_{[r,r+dr]}^R(\underline{x}) + \nabla H_{[r,r+dr]}^R(\underline{x}).\nabla F_{[r,r+dr]}(\underline{x}) = \left|\nabla H_r(\underline{x}_o)\right|\frac{\partial F_{[r,r+dr]}(\underline{x})}{\partial x_1} \tag{8.7}$$

One can relate the $\nabla H_{[r,r+dr]}$ in Eq. (8.7) to the solution of a simpler problem. Let $\nabla H'_{[r,r+dr]}(\underline{x})$ be the hydraulic gradient field in Ω/r when the log-conductivity in Ω/r is given by $F_{[r,r+dr]}(\underline{x})$ and a unit large-scale mean hydraulic gradient is applied in the direction of the negative x_1 axis. The random field $\nabla H'_{[r,r+dr]}$ satisfies

$$\nabla^2 H'_{[r,r+dr]}(\underline{x}) + \nabla H'_{[r,r+dr]}(\underline{x}).\nabla F_{[r,r+dr]}(\underline{x}) = \frac{\partial F_{[r,r+dr]}(\underline{x})}{\partial x_1} \tag{8.8}$$

Comparison with Eq. (8.7) shows that

$$\nabla H^{R}_{[r,r+dr]}(\underline{x}) \overset{d}{=} \left|\nabla H_r(\underline{x}_o)\right| . \nabla H'_{[r,r+dr]}(\underline{x}) \tag{8.9}$$

where $\overset{d}{=}$ denotes equality in distribution. Therefore, from Eq. (8.5), and recalling that we are considering the hydraulic gradient at point $\underline{x}_o$ we have

$$\nabla H^{R}_{r+dr}(\underline{x}_o) \overset{d}{=} -\left|\nabla H_r(\underline{x}_o)\right| \left(\underline{e} - \nabla H'_{[r,r+dr]}(\underline{x}_o)\right) \tag{8.10}$$

It is important to note that $\nabla H'_{[r,r+dr]}(\underline{x}_o)$ in Eq.(8.8) is independent of $\nabla H_r(\underline{x}_o)$ because $F_{[r,r+dr]}$ is independent of F_r. Hence, the process $\nabla H_r(\underline{x}_o)$ is Markovian in the resolution parameter r.

In the anisotropic case, the transition $\nabla H_r(\underline{x}_o) \rightarrow \nabla H_{r+dr}(\underline{x}_o)$ in Eq. (8.10) has the form

$$\nabla H^{R}_{r+dr}(\underline{x}_o) \overset{d}{=} -\left|\nabla H_r(\underline{x}_o)\right| . \left[\underline{e} - \left(\nabla H'_{[r,r+dr]}(\underline{x}_o) \middle| \underline{\alpha}_r\right)\right] \tag{8.11}$$

where $\underline{\alpha}_r$ is the unit vector in the direction of $\nabla H_r(\underline{x}_o)$, , and $\nabla H'_{[r,r+dr]}(\underline{x})$ is the hydraulic gradient due to $F_{[r,r+dr]}$ for a unit large-scale hydraulic gradient equal to $-\underline{\alpha}_r$. What is new relative to the isotropic case is that now $\nabla H'_{[r,r+dr]}(\underline{x}_o)$ depends on the direction of $\nabla H_r(\underline{x}_o)$. To fully characterize the transition structure of the Markov

process $\nabla H_r(\underline{x}_o) \rightarrow \nabla H_{r+dr}(\underline{x}_o)$, the marginal distribution of $\nabla H'_{[r,r+dr]}$ is needed. This distribution is obtained by closely following the analysis in Sec 4.1 of Chapter 4. The term $\nabla H'_{[r,r+dr]}(\underline{x}).\nabla F_{[r,r+dr]}(\underline{x})$ in Eq. (8.8) is infinitesimal of higher-order and may be neglected. If $\underline{R}_r$ is an orthogonal matrix with first column equal to $\underline{\alpha}_r$, then using the superscript R to denote quantities in the rotated reference $\underline{x}^R = \underline{R}_r^T \underline{x}$, then $\left(\nabla H'^R_{[r,r+dr]}\left(\underline{x}^R\right)|\underline{R}_r\right)$ satisfies

$$\left(\nabla^2 H'^R_{[r,r+dr]}\left(\underline{x}^R\right)|\underline{R}_r\right) = \frac{\partial F^R_{[r,r+dr]}\left(\underline{x}^R\right)}{\partial x_1^R} \tag{8.12}$$

Eq.(8.12) is written in Fourier space as

$$-k^2 \hat{H}^R_{[r,r+dr]}\left(d\underline{k}^R \,|\, \underline{R}_r\right) = ik_1 \hat{F}_{[r,r+dr]}\left(d\underline{k}^R\right) \tag{8.13}$$

where $\hat{H}$ and $\hat{F}$ are the spectral measures of H' and F and $k^2 = k_1^2 + \ldots + k_D^2$. Eq. (8.13) is approximate because the random function $H_{[r,r+dr]}\left(\underline{x}^R \,|\, \underline{R}_r\right)$ with spectral measure in Eq. (8.13) does not satisfy the boundary conditions. Under the assumptions stated at the beginning of this section, the effect of this approximation should be small for D > 1. Hence, the spectral measure of the gradient field $\nabla H'_{[r,r+dr]}$ satisfies

$$\nabla \hat{H}'_{[r,r+dr]}\left(d\underline{k}^R \,|\, \underline{R}_r\right) = \left(\underline{k}' k_1'\right) \hat{F}_{[r,r+dr]}\left(\underline{R}_r d\underline{k}^R\right) \tag{8.14}$$

where $\underline{k}' = \underline{k}/k$ is the unit vector in the direction of $\underline{k}$ and k_1' is its first component. Eq. (8.14) implies that the spectral density tensor of $\nabla H^{'R}_{[r,r+dr]}$ is

$$\underline{\underline{S}}^{R}_{\nabla H'[r,r+dr]}\left(\underline{k}^{R} \mid \underline{R}_r\right) = \left(\underline{k}'^{R}\underline{k}'^{R^T}\right)\left(k_1'^{R}\right)^2 .S_F\left(\underline{R}_r \underline{k}^{R}\right) \tag{8.15}$$

Therefore, the covariances among the components of $\nabla H^{'R}_{[r,r+dr]}$ are (omitting the subscript $[r, r+dr]$),

$$\begin{aligned} \mathrm{Cov}\left[\nabla H_i'^{R}, \nabla H_j'^{R} \mid \underline{R}_r\right] &= \int_{\mathbb{R}^D} S_{\nabla H'^{R},ij}\left(\underline{k}^{R} \mid \underline{R}_r\right) d\underline{k}^{R} \\ &= E\left[U_1^2 U_i U_j \mid \underline{R}_r\right] .S_{F_{rad}}\left(rk_o\right) \end{aligned} \tag{8.16}$$

where $\left(\underline{U} \mid \underline{R}_r\right)$ is the unit random vector with probability density on the unit spherical surface proportional to $S_F\left(rk_o \underline{R}_r \underline{U}\right)$, $S_{F_{rad}}$ is the radial spectral density function of F and is equal to $\int_{\mathbb{R}^D} S_F\left(\underline{R}_r \underline{k}^{R}\right) d\underline{k}^{R}$, and $S_{\nabla H'^{R},ij}$ is the $(i,j)^{th}$ component of the spectral tensor in Eq. (8.15).

Finding the expectation terms in Eq. (8.16) is the biggest challenge. In general, these expectations depend on both r and $\underline{\alpha}_r$. However, in some cases the expectations depend only on $\underline{\alpha}_r$ or some component of $\underline{\alpha}_r$. Specifically,

1. If the log-conductivity field F has a power-law spectrum with geometric anisotropy so that its spectrum $S_F(\underline{k}) \propto |\underline{Ak}|^{-\alpha}$ for some positive definite matrix $\underline{A}$ and some $\alpha > D$, then $S_F(r\underline{k}) = r^{-\alpha} S_F(\underline{k})$ and the expectation terms in Eq. (8.16) do not depend on r.
2. If in addition F is isotropic in sub-space spanned by the first D-1 coordinate axes, then the expectation terms depend only on the first component of $\underline{\alpha}_r$.

The latter case corresponds to a stratified geology with isotropic conductivity on the stratification planes. In this case, it is possible to numerically evaluate the expectation terms in Eq. (8.16). An alternate approach is to calculate the moments

$$Q_{mnkl}(r) = E\left[U_m U_n U_k U_l \,|\, \underline{R}_r = \underline{I}\right], \quad m, n, k, l = 1,...,D \tag{8.17}$$

in the unrotated reference (in cases 1 and 2 above, these moments do not depend on r) and then find the moments in Eq. (8.16) using the relation $(\underline{U}|\underline{R}_r) = \underline{R}_r^T (\underline{U}|\underline{I})$ or in scalar notation and with the summation convention, $(U_i|\underline{R}_r) = c_{ij}(U_j|\underline{I})$. Then,

$$E\left[U_1^2 U_i U_j \,|\, \underline{R}_r\right] = \sum_{\substack{m,n,k,l \\ =1,...,D}} c_{1m} c_{1n} c_{ik} c_{jl} . Q_{mnkl}(r) \tag{8.18}$$

This corresponds to the method of Gelhar and Axness (1983) reviewed in Chapter 2 (see Eq. 2.46). An important difference between Gelhar and Axness' approach and

the present work is that they evaluate the large-scale mean hydraulic gradient whereas the present work evaluates the distribution of the hydraulic gradient at a point within the aquifer.

8.2 AN APPROXIMATE SCHEME TO DEAL WITH GEOMETRIC ANISOTROPY

Suppose the hydraulic conductivity K has geometric anisotropy inside the region of interest, Ω. This means that, for some positive-definite matrix $\underline{A}$, the scaled field $K'(\underline{x}) = K(\underline{A}\underline{x})$ is isotropic. The approximation consists of replacing the actual problem $\{K, \Omega\}$ with the scaled problem $\{K', \Omega'\}$ where $K'(\underline{x}) = K(\underline{A}\underline{x})$ and $\Omega' = \{\underline{x} : \underline{A}\underline{x} \in \Omega\}$. To be specific, consider the case when Ω is a D-dimensional rectangle with sides parallel to the principal directions of anisotropy of K. The coordinate axes are chosen to be aligned with the principal directions. Constant hydraulic head is specified on the faces of Ω orthogonal to the first coordinate axis and no flow conditions are imposed on the rest of the boundary. In this case, also the scaled region Ω' is a rectangle with sides parallel to the coordinate axes.

In order to show under which conditions this approximation may be accurate, the flow equation

$$\nabla^2 H + \nabla F . \nabla H = 0 \qquad (8.19)$$

is considered for the two problems, first for the one-dimensional case and then more in general for any spatial dimension D.

One-dimensional problem

Suppose that a one-dimensional tube of length L is down-scaled by a factor s. $F(x)$ and $H(x)$, $0 \le x \le L$, are the log conductivity and the hydraulic head in the original problem, in which a large-scale unit hydraulic head is applied by setting $H(0)=L$ and $H(L)=0$. The corresponding functions for the scaled problem are $F_s(x)$ and $H_s(x)$, $0 \le x \le L/s$. The boundary conditions for the latter problem are $H(0)=L/s$ and $H(L/s)=0$. The following relations hold among quantities in the original and scaled problems:

$$\begin{cases} F_S(x)=F(sx) \\ \nabla F_S(x)=s\nabla F(sx) \end{cases}$$

$$\begin{cases} \nabla H_s(x)=\nabla H(sx) \\ \nabla^2 H_s(x)=s\nabla^2 H(sx) \\ H_s(x)=\dfrac{1}{s}H(sx) \end{cases} \qquad (8.20)$$

Notice that:

1. if F and H satisfy Eq. (8.19) under the original boundary conditions, F_s and H_s satisfy Eq. (8.19) under the boundary conditions of the scaled problems.

2. the flow $q = -K.\nabla H$ is the same in the two cases; hence the effective hydraulic conductivity has the same distribution in the two problems, irrespective of the scaling factor s.

D-Dimensional Problem

Consider now a D-dimensional rectangle Ω with side lengths $L_i, i = 1,...,D$, specified hydraulic head values $H = L_1$ on the face $x_1 = 0$ and $H = 0$ on the face at $x_1 = L_1$. The flow domain Ω is downscaled by a factor s_i along the i^{th} coordinate direction, to make the K field inside Ω isotropic. Hydraulic heads $H_s = L_1 / s_1$ at $x_1 = 0$ and $H_s = 0$ at $x_1 = L_1 / s_1$ are applied. The flow equation for the scaled problem is

$$\nabla^2 H_s(\underline{x}) + \nabla F_s(\underline{x}).\nabla H_s(\underline{x}) = 0 \tag{8.21}$$

The log-conductivity and its gradient are related to the corresponding quantities in the original problem as

$$\begin{cases} F_s(\underline{x}) = F(\underline{Sx}) \\ \nabla F_s(\underline{x}) = \underline{S}\nabla F(\underline{Sx}) \end{cases} \tag{8.22}$$

where $\underline{S} = \mathrm{diag}\{s_i\}$. It is contended that, if the flow line directions are tightly distributed along the first coordinate direction, then an accurate approximation to $\nabla H_s(\underline{x})$ is

$$\begin{aligned} &\nabla H_s(\underline{x}) \approx s_1 \underline{S}^{-1}.\nabla H(\underline{S}\underline{x}) \\ \Rightarrow\ &\nabla^2 H_s(\underline{x}) \approx s_1 \nabla^2 H(\underline{S}\underline{x}) \end{aligned} \tag{8.23}$$

It is easy to verify that ∇F_s in Eq. (8.22) and ∇H_s in (8.23) satisfy Eq. (8.21) and the boundary conditions for the scaled problem. Eq. (8.23) is an approximation because ∇H_s in that equation is not necessarily a gradient field (the gradient of a scalar field H_s). The scaled hydraulic gradient field ∇H_s in Eq. (8.23) is a gradient field in two special cases: 1. when $\underline{S} = s\underline{I}$ (isotropic scaling) and 2. When the flow lines are parallel to the x_1 axis (one-dimensional flow). Therefore Eq. (8.23) is expected to be accurate if the flow is nearly one-dimensional, in both the original and scaled problems. Typically, but not always, isotropic conductivity requires larger downscaling in the direction of x_1 than in the other directions. Since downscaling more in the x_1 direction that in the other coordinate directions increases the sinuosity of the flow lines, the approximation is expected to be accurate if the variance of the rotation angles σ_α^2 in the isotropic problem is small with respect to 1.

To validate the scaling relations in Eqs. (8.22) and (8.23) numerical simulations were performed on the plane. An anisotropic K field with spectral density of $F = \ln K$ given by

$$S_F(\underline{k}) = \frac{C}{a_1 k_1^2 + a_2 k_2^2}$$

where a_1 and a_2 are coefficients that determine the correlation of the K field in the x_1 and x_2 directions respectively, C is a constant that determines the level of the spectral density. For a $F = \ln K$ field with a known variance σ_F^2, the value of C can be determined from the relation

$$\sigma_F^2 = \int_{\underline{k}} S_F(\underline{k}) d\underline{k}$$

For various values of a_1 and a_2 presented in Table 8.1, the flow field was computed and the effective conductivity K_{eff} was calculated and compared to the K_{eff} obtained from an isotropic K field but with an aspect ratio that corresponds to a_1 and a_2. The numerical simulations show that the approximate relations in Eqs. (8.22) and (8.23) are accurate.

Table 8.1 - A comparison of K_{eff} from an anisotropic K field with $\sigma_F^2 = 1.11$ compared to the K_{eff} from an isotropic K field with $C_K = 0.1$ but on a rectangle with aspect ratio determined by a_1 and a_2.

Aspect Ratio $\frac{a_1}{a_2}$	K_{eff} computed from anisotropic spectral density	K_{eff} computed from an isot on a rectangle
2	0.734 0.656 0.654 0.720 0.639	0.709 0.683 0.694 0.723 0.673
	Mean K_{eff} = 0.681	Mean K_{eff} = 0.696
10	0.874 0.863 0.893 0.842 0.869	0.914 0.880 0.792 0.832 0.841
	Mean K_{eff} = 0.868	Mean K_{eff} = 0.852
100	0.915 0.978 0.987 0.962 0.956	0.980 0.990 0.993 0.985 0.989
	Mean K_{eff} = 0.960	Mean K_{eff} = 0.987
0.5	0.487 0.443 0.461 0.451 0.478	0.501 0.492 0.464 0.488 0.493
	Mean K_{eff} = 0.464	Mean K_{eff} = 0.488

CHAPTER 9 – SUMMARY AND CONCLUSIONS

9.1 SUMMARY

This research has studied the properties of the hydraulic gradient ∇H and specific discharge $\underline{q}$ when the hydraulic conductivity K is an isotropic lognormal multifractal field. For these K fields, their $F = \ln(K)$ spectrum is

$$S_F(\underline{k}) = \begin{cases} \frac{2}{S_D} C_K k^{-D} & k_o \le k \le k_{max} \\ 0 & \text{otherwise} \end{cases} \qquad (9.1)$$

where k is the amplitude of the wavenumber vector $\underline{k}$, S_D is the surface area of the unit D-dimensional sphere so that $S_1 = 2$, $S_2 = 2\pi$ and $S_3 = 4\pi$, C_K is the so-called codimension parameter of the K field that determines the level of the spectrum of F and k_o and k_{max} define the limits of the multifractal scaling of K. The results are derived under certain conditions and assumptions explained in section 4.1 of Chapter 4.

The approach used to derive the renormalization properties of ∇H and $\underline{q}$ are different from the perturbation methods that are standard in the field of stochastic subsurface flow. Instead of the perturbation expansions, the flow equations (Eqs. 1.1 and 1.2) are solved by considering a cascade of hydraulic gradient and flow fields at different resolutions $r \ge 1$. The fields at resolution r are obtained by using a log-conductivity F_r in which all Fourier components with wavenumbers $k > rk_o$ have been filtered out; hence, the spectral density of F_r is given by Eq. 9.1 with $k_{max} = rk_o$. Using subscript r to denote quantities

derived under $F = F_r$, the hydraulic gradient ∇H_r and specific flow $\underline{q}_r$ satisfy the Darcy and no-divergence conditions

$$\begin{cases} \underline{q}_r = -K_r \nabla H \\ \nabla^2 H_r + \nabla F_r . \nabla H_r = 0 \end{cases} \tag{9.2}$$

The random fields ∇H_r and $\underline{q}_r$ for different resolution r are compared using Eq. (9.2) and the assumptions above which have been found to be accurate. The main results of the thesis are summarized next.

In Chapter 2, the linear perturbation method was reviewed and shortcomings of this approach were discussed. The linear perturbation method is asymptotically correct, as the variance of the log-conductivity σ_F^2 tends to zero. However, for hydraulic conductivity fields with a σ_F^2 greater than one, several authors (see for example, Dagan, 1985; Deng and Cushman, 1995 and 1998; Hsu and Neuman, 1997 among others) have found that the inclusion of second order terms has significant effects on the spectra of ∇H and $\underline{q}$ when the variance of $F = \ln(K)$ exceeds unity. Despite these insights into the behavior of the flow field when σ_F^2 is greater than one, the computational approach used makes it extremely difficult to incorporate higher order terms. Numerical solutions of the flow equations by Bellin et al. (1992) and Lent and Kitanidis (1996) revealed results that differed significantly from the linear perturbation approach. However, the numerical methods do not provide any predictive tools in studying flow behavior in heterogeneous media.

Lately there have been efforts in studying flow when K has some form of scale-invariance; more specifically these models have resorted to fractal descriptions of porous media properties. Reliance on these self-similar models was in part to explain the scale dependent nature of measured aquifer dispersivities. However, the theoretical descriptions relied on the linear perturbation approach and failed to capture the behavior of media with high log-conductivity variance.

In this thesis, the hydraulic conductivity is modeled with a more realistic and general form of self-similar model – the multifractal. In addition, the scaling properties of the multifractal hydraulic conductivity field are exploited to obtain a nonlinear solution of the flow equations. Properties of the multifractal field are described in Chapter 3. The group of transformations that describe the symmetries of scalar multifractals like K is discussed in Chapter 3. Moreover, properties of vector fields that are invariant under more complex space and field transformations (also known as generalized scale invariance GSI, see Lovejoy and Schertzer 1985 and Schertzer and Lovejoy, 1996) are reviewed. The final section of Chapter 3 discusses the one-dimensional spectra of K data from Mount Simon aquifer (Ababou and Gelhar, 1990) and from Northern Arizona by Goggin (1988). Results of the data analysis show that modeling the hydraulic conductivity with a spectrum of the type in Eq. 9.1 is not outside the range of what one may observe in nature. When applicable, multifractality of K is an important property. We know that homogeneous multifractal fields are generated through a multiplicative cascade process, which then suggests the basic genetic mechanism of geologic formations with

multifractal K. In addition, when the K field is modeled as a multifractal it allows one to exploit its scaling properties to obtain a nonlinear solution of the flow equations. Moreover, the application of this thesis extends beyond the field of hydrology and are applicable for example in studying random resistor electrical networks.

In Chapter 4 the distributional properties of the hydraulic gradient ∇H and specific discharge $\underline{q}$ fields were obtained. The results show that the ∇H and $\underline{q}$ fields derive their multifractal properties from the hydraulic conductivity field K and have scale invariance properties related to those of K. The type of scale invariance displayed by ∇H and $\underline{q}$ involves not only space contraction and multiplication of the fields by a random variable as in the case of K, but also random rotation of the fields and their supports. The probability distributions of the random amplitude factor and random rotation that describe the scaling properties of ∇H and $\underline{q}$ depend on the space dimension D and the multifractal parameter of K, the so-called co-dimension C_K.

At large scales the fields ∇H and $\underline{q}$ are anisotropic due to the fact that the hydraulic gradient applied to the entire aquifer has a particular direction. At smaller scales, the rotational component in the scaling relations of ∇H and $\underline{q}$ causes these fields to approach isotropy. This means that from measuring ∇H and $\underline{q}$ inside a very small region, an observer would be unable to determine the direction of the hydraulic gradient at large scales. This transition from anisotropy to isotropy as one goes from large to small scales affects the spectral density tensors of ∇H and $\underline{q}$ and the macrodispersivities in ways that cannot be assessed through conventional perturbation analysis.

The hydraulic gradient and specific discharge differ sharply in their amplitude scaling properties. The expected amplitude of ∇H increases with the resolution, whereas the expected amplitude of $\underline{q}$ decreases with increasing r. The reason for the decrease of $E[q] = E\left[\left|\underline{q}\right|\right]$ with r is that the log conductivity F and the log of the hydraulic gradient amplitude $\ln(J) = \ln(|\nabla H|)$ are negatively correlated. The correlation coefficient ρ between the log conductivity and the log hydraulic gradient amplitude is not dependent on the resolution or erraticity of the field but on the spatial dimension under consideration, as indicated through the analytical expression obtained for the correlation coefficient. Specifically, ρ = -1, -0.817 and –0.745 for D = 1, 2, and 3 respectively.

Another important result of this thesis is the variation of the effective hydraulic conductivity K_{eff} with the size of the region considered, or more precisely with the range R of scales below that of the region over which the K field is multifractal. An analytical expression for K_{eff} in terms of R, the codimension parameter C_K and the space dimension D was obtained. The result is the same as Matheron's (1967) conjecture.

The analytical results have been validated through two-dimensional simulations over 512 x 512 grids in Chapter 6. All the numerical results closely match the theoretical predictions. This includes the so-called moment scaling functions of $J = |\nabla H|$ and $q = |\underline{q}|$, which characterize the scaling properties of these two quantities.

Chapter 6 continues the flow analysis by deriving the consequence of the multifractality of ∇H and $\underline{q}$ on the spectral density tensors of these fields. The spectral density tensors

of these fields are obtained and contrasted with results of the linear perturbation approach. In contrast to the linear perturbation method, the nonlinear analysis accounts for the rotations of the ∇H and $\underline{q}$ vectors. The results indicate that the linear perturbation approach produces spectral density tensors that have incorrect decay exponents along any given direction in Fourier space and incorrectly characterizes the anisotropy of ∇H and $\underline{q}$ as being scale invariant. The results in Chapter 6 show that ∇H and $\underline{q}$ are anisotropic at large scales because of the boundary conditions but become progressively isotropic at small scales. This scale-dependent behavior is important for computing the macrodispersivities.

Chapter 7 deals with issues related to transport in isotropic lognormal multifractal K fields. First, the ensemble macrodispersivities and plume-scale dependent macrodispersivities are computed and compared with results of the linear theory. Reflecting the scale-dependent anisotropy of the spectral density of $\underline{q}$, results for the nonlinear produce isotropic macrodispersivities at small travel distances. However, the macrodispersivities become anisotropic over large travel distances. The macrodispersivities from the linear theory by contrast are anisotropic at all travel distances. The second part of Chapter 7 exploits the scaling properties of the velocity field and its inverse to obtain expressions for the first passage time distribution and mean plume concentration when the flow and transport occur in a saturated aquifer with an isotropic lognormal multifractal K. Results obtained from the nonlinear approach are compared with the continuous time random walk (CTRW) and two-phase models. There are some significant differences in these models. First, the nonlinear model is more suitable for modeling transport in homogeneous media, whereas the CTRW and two-

phase models are more suited for transport in non-homogeneous media. Secondly, the nonlinear model is non-Fickian in nature; that is, it is capable of characterizing the evolution of a plume whose dispersion coefficient or macrodispersivity changes with mean travel time or distance. The CTRW and two-phase models are Fickian models and require a constant dispersion coefficient as an input.

Chapter 8 extends the results of Chapter 4 to consider flow in anisotropic multifractal fields. The approach used in deriving the marginal distribution of the hydraulic gradient $\nabla H(\underline{x}_o)$ at a generic point $\underline{x}_o$ in the flow domain is similar to the approach used in the isotropic case in Chapter 4. One begins from known deterministic values of $\nabla H(\underline{x}_o)$ under mean field conditions when the hydraulic conductivity K is fixed to its mean value. Higher Fourier components are progressively added to $F = \ln(K)$ and the corresponding effects on the distributions of $\nabla H(\underline{x}_o)$ are determined. The marginal distribution of $\nabla H(\underline{x}_o)$ is obtained in the limit as the variance of F is totally accounted for. Unlike the isotropic case we are unable to obtain closed form solutions for the marginal distribution of $\nabla H(\underline{x}_o)$ because the rotations of the hydraulic gradient vectors are not uniformly distributed and depend on the angle of inclination of the unit large scale hydraulic gradient $\underline{\alpha}_r$. Approximate results are however obtained for geometrically anisotropic K fields. For these fields, approximate results for parallel and series configurations are obtained for the two-dimensional case. However, estimates of the effective hydraulic conductivity can be obtained for the three-dimensional case only through numerical simulations.

9.2 CONCLUSIONS

The major conclusions of this research are:

1. When flow occurs in a field with an isotropic lognormal multifractal hydraulic conductivity K, the resulting hydraulic gradient ∇H and specific discharge $\underline{q}$ fields are also multifractal. These results are obtained through a novel solution approach used in solving the zero divergence Darcy equation.

2. For flow on a plane, the rotation angles of ∇H and $\underline{q}$ which are the same can be characterized as a Brownian motion on a sphere. This distribution measures the change in the local flow direction that results when higher wavenumber components are added to the log-conductivity. In the 3D case, the Brownian motion on the sphere does not have a simple analytical form. These rotation angles play an important role in the spectral density tensors of ∇H and $\underline{q}$.

3. Accounting for the rotation angles, the spectral density tensors of ∇H and $\underline{q}$, unlike the results of the linear perturbation approach, have a scale dependent anisotropy. The spectral density tensors of this thesis are isotropic at small scales and become anisotropic at large scales. The rate at which the spectral tensors become isotropic depends on the variability of the K field. This scale-dependent behavior is important for the evaluation of macrodispersivities, which are anisotropic at large travel distances and nearly isotropic locally.

4. The spectral density tensors obtained from the analysis in this thesis show that the linear perturbation theory produces incorrect decay exponents for the spectral density tensors along any given direction in Fourier space.

5. The results of this thesis provide further support for Matheron's 1967 conjecture for effective hydraulic conductivity, which is known to be accurate at least for fields with a log-conductivity variance $\sigma_F^2 < 1$, for K isotropic lognormal, and for D = 1 and 2.

6. Exploiting the scaling properties of the inverse velocity field, expressions for the first-passage time distribution and mean plume concentration were obtained. These models are particularly suitable for describing transport in heterogeneous media that displays scale-dependent dispersion and have long tail distributions, such as those observed in field experiments.

7. The scale-invariant properties of the K field allow one to obtain approximate closed-form expressions for parallel and series configurations in geometrically anisotropic K fields.

8. Beyond the applications to hydrology, the results of this thesis present, for the first time a formal analysis of how parameters in a scale-invariant system can inherent their scaling properties from one of the variables. This is particularly pertinent to the study of random resistor networks, which are mathematically similar to the flow problem analyzed in this thesis.

9.3 RECOMMENDATIONS FOR FUTURE RESEARCH

The following are recommendations to extend the present work and help improve our understanding of flow and transport in highly heterogeneous media:

1. The present work has applied the renormalization method in obtaining the key results. This method is valid when K is multifractal, which means that the log-conductivity $F = \ln(K)$ has a power spectral density of the type $S_F(\underline{k}) \propto k^{-D}$, where D is the space dimension. In certain cases spectra of F that decay like $k^{-\alpha}$ with α smaller or larger that D have been observed. The associated K fields are not multifractal, although they may have the multiplicative structure of multifractal fields. Research needs to be done to consider this more general case, in addition to highly heterogeneous K fields which do not have a power-law type spectra. The solution approach developed in this thesis can be applied in studying flow through heterogeneous porous media that does not have a multifractal K field but has spectral density of F=lnK of a more general form.
2. An issue not addressed in the study of transport through multifractal porous media is the lack of macroscopic ergodicity, in the sense that the plume geometry and path of transport are highly dependent on the characteristics of the K field in the region of injection. One would expect that the initial velocity field in the vicinity of injection would determine the evolutionary nature of the solute. The average velocity field in the region of injection depends on the resolution to which the flow field has been developed. How

the resolution affects the velocity field that in turn determines the migrational properties of the solute need to be further studied.

3. Field data for hydraulic conductivity are scarce. The recent development of the air-permeameter should allow for an extensive sampling of K-data from sites of interest. These additional field studies in various rock formations are required in order to understand the geologic media within which multifractality of K may apply and the processes that create such fields. In chapter 3, some empirical data was presented to illustrate some ranges of frequencies within which multifractality can be observed in nature. One would expect geologic formations such as sedimentary and some types of metamorphic formations to exhibit multifractality over certain scales. Obtaining extensive field data in various formations and analyzing them would allow one to better understand the processes that generate these fields.

4. Another area that will require much fieldwork is the application of the transport models developed in this thesis to real-world situations. Understanding what parameters to measure and how these relate to those of the theoretical model will be important in accurately predicting solute spreading in a highly heterogeneous medium and in helping with predictions of the risk of contamination downstream.